

ISTANBUL TECHNICAL UNIVERSITY ★ GRADUATE SCHOOL OF SCIENCE
ENGINEERING AND TECHNOLOGY

**EXPERIMENTAL INVESTIGATION OF FLEXIBILITY EFFECTS IN
FLAPPING WING AERODYNAMICS**



Ph.D. THESIS

Onur SON

Department of Aeronautics and Astronautics Engineering

Aeronautics and Astronautics Engineering Programme

NOVEMBER 2018

ISTANBUL TECHNICAL UNIVERSITY ★ GRADUATE SCHOOL OF SCIENCE
ENGINEERING AND TECHNOLOGY

**EXPERIMENTAL INVESTIGATION OF FLEXIBILITY EFFECTS IN
FLAPPING WING AERODYNAMICS**



Ph.D. THESIS

**Onur SON
(511102105)**

Department of Aeronautics and Astronautics Engineering

Aeronautics and Astronautics Engineering Programme

Thesis Advisor: Prof. Dr. N. L. Okşan ÇETİNER-YILDIRIM

NOVEMBER 2018

İSTANBUL TEKNİK ÜNİVERSİTESİ ★ FEN BİLİMLERİ ENSTİTÜSÜ

**ÇIRPAN KANAT AERODİNAMİĞİNDE ESNEKLİK ETKİLERİNİN
DENEYSEL OLARAK İNCELENMESİ**



DOKTORA TEZİ

**Onur SON
(511102105)**

Uçak ve Uzay Mühendisliği Anabilim Dalı

Uçak ve Uzay Mühendisliği Programı

Tez Danışmanı: Prof. Dr. N. L. Okşan ÇETİNER-YILDIRIM

KASIM 2018

Onur Son, a Ph.D. student of ITU Graduate School of Science Engineering and Technology student ID 511102105, successfully defended the dissertation entitled “EXPERIMENTAL INVESTIGATION OF FLEXIBILITY EFFECTS IN FLAPPING WING AERODYNAMICS”, which he prepared after fulfilling the requirements specified in the associated legislations, before the jury whose signatures are below.

Thesis Advisor : **Prof. Dr. N. L. Okşan ÇETİNER-YILDIRIM**
Istanbul Technical University

Jury Members : **Prof. Dr. Fırat Oğuz EDİS**
Istanbul Technical University

Assoc. Prof. Dr. İlyas KANDEMİR
Gebze Technical University

Prof. Dr. Alim Rüstem ASLAN
Istanbul Technical University

Prof. Dr. Hüseyin AKILLI
Çukurova University

Date of Submission : 14 September 2018

Date of Defense : 01 November 2018





To my family,



FOREWORD

I am grateful to my supervisor N. L. Okşan Çetiner-Yıldırım for guiding me since my undergraduate days. She was always there when I have a problem, question or in need of help. I feel very lucky to work with her in my early academic career.

Trisonic Laboratory has been my second home and I have known great people under the roof of it. İdil Fenercioğlu with her positive high energy, always keep our work group's mood high. Berk Zaloğlu, “the motor control guy”, made it possible to give desired motions to the wings. Murat Sarıtaş, one of the best PIV experts in these lands, became a great lab neighbor, especially during my thesis writing days.

I also would like to thank my officemate Hasan Tabanlı, for his support and friendship. During our assistantship days, we have together live through hard and struggled days, but succeeded to overcome them backing each other. I also would like to express my thanks to Banu Yılmaz for her help and for contributions to gather the post process codes into one “marcus” code.

I want to thank to the technicians of the laboratory Aliosman Tabanlı and Murat Tarhan for their assistance to produce models and other technical works.

I also want to extend my thanks to the other professors of the Trisonic Laboratory; Duygu Erdem, Hayri Acar, and Bülent Yüceil.

I would specially like to thank thesis steering committee members Fırat Oğuz Edis and İlyas Kandemir for the fruitful discussions and for their valuable inputs on the thesis progress meetings.

I would like to also acknowledge the support of the thesis work by TUBITAK Grant 112M682 (Investigation of Flow Structures and Unsteady Loading for a Wing in Periodic or Transient Flapping Motion).

Finally, I want to express my gratitude to my mother, my father and my brother. I know how big devotions you have made for my education. I cannot pay you back all you have done for me. As my appreciation and gift to you, I hope this achievement will make you happy and proud.

September 2018

Onur SON

TABLE OF CONTENTS

	<u>Page</u>
FOREWORD	ix
TABLE OF CONTENTS	xi
ABBREVIATIONS	xiii
SYMBOLS	xv
LIST OF TABLES	xvii
LIST OF FIGURES	xix
SUMMARY	xxiii
ÖZET	xxvii
1. INTRODUCTION	1
1.1 Purpose of Thesis	3
1.2 Literature Review	4
1.2.1 Perching	4
1.2.2 Harmonic motion	7
1.2.3 Flexible wings	13
1.3 Definition of Major Parameters.....	22
1.4 Outline of the Thesis	23
2. EXPERIMENTAL SETUP	25
2.1 Flow System	25
2.2 Motion System	26
2.3 Models	28
2.3.1 3D printed model	30
2.3.2 Material properties determination	31
2.4 Force Measurements	33
2.5 DPIV Measurements and Post Processing	34
3. RESULTS	37
3.1 Perching of a Rigid Wing.....	37
3.1.1 Effect of aspect ratio	37
3.1.1.1 Force measurement results	38
3.1.1.2 DPIV results	40
3.1.2 Effect of leading edge and trailing edge shape	49
3.1.3 Effect of planform shape	51
3.2 Effect of Flexibility for Perching	57
3.2.1 Force measurement results	58
3.2.2 DPIV results	61
3.3 Plunging of a Rigid Wing.....	69
3.3.1 Force measurement results	70
3.3.2 DPIV results	79
3.4 Effect of Flexibility for Plunging	84
3.4.1 Airfoil shape characteristics	84
3.4.2 Force measurement results	93
3.4.3 DPIV results	112

4. CONCLUDING REMARKS AND RECOMMENDATIONS	125
4.1 Summary of Major Contributions	125
4.2 Recommendations for Further Study.....	128
REFERENCES	131
CURRICULUM VITAE.....	139



ABBREVIATIONS

3D	: Three-dimensional
AR	: Aspect Ratio
AVT	: Applied Vehicle Technology
BC	: Before Christ
CCD	: Charge Coupled Device
DPIV	: Digital Particle Image Velocimetry
LEV	: Leading Edge Vortex
MAV	: Micro Air Vehicle
NACA	: National Advisory Committee for Aeronautics
NATO	: North Atlantic Treaty Organization
NIOPLEX	: Non-Intrusive Optical Pressure and Loads Extraction for Aerodynamic Analysis
PhD	: Doctor of Philosophy
RPM	: Revolutions per minute
STO	: Science and Technology Organization
TEV	: Trailing Edge Vortex
TUBITAK	: Scientific and Technological Research Council of Turkey
TV	: Tip Vortex
UAV	: Unmanned Air Vehicle
VI	: Virtual Instrument



SYMBOLS

a	: Amplitude of the motion
a_{LE}	: Leading edge amplitude
a_{TE}	: Trailing edge amplitude
b	: Thickness
c	: Chord length
C(k)	: Theodorsen function
C_D	: Drag coefficient
C_L	: Lift coefficient
C_P	: Power input coefficient
C_T	: Thrust coefficient
d	: Horizontal distance between vortex cores
E	: Elastic modulus (Young modulus)
EI	: Flexural stiffness
f	: Frequency of the flapping motion
f_n	: Natural frequency of the wing
F_x	: Force component in the freestream direction
F_y	: Force component perpendicular to the freestream direction
h	: Position function of the plunge oscillation
I	: Second moment of area
k	: Reduced frequency
Re	: Reynolds Number
s	: Span length
St	: Strouhal number
t	: Time
t*	: Convective time
T	: Thrust force
u	: Horizontal component of velocity
U, U_∞	: Freestream velocity
v	: Vertical component of velocity
η	: Efficiency

μ	: Dynamic viscosity
v	: Velocity of the leading edge
ρ	: Density
ρ_{wing}	: Density of wing material
Φ_{TE}	: Phase between the trailing edge and the leading edge
Φ_x	: Phase between the motion and F_x
Φ_{x1}	: Phase between maximum position of the plate and first thrust peak
Φ_{x2}	: Phase between minimum position of the plate and second thrust peak
Φ_y	: Phase between the motion and F_y



LIST OF TABLES

	<u>Page</u>
Table 2.1 : Wing material properties.....	30
Table 2.2 : Sensor ranges and resolution.....	34
Table 3.1 : Motion parameters of the plunging wing.....	70





LIST OF FIGURES

	<u>Page</u>
Figure 1.1 : Perching trajectory (Cory and Tedrake, 2008).....	4
Figure 1.2 : Perching maneuver of a bird (Url-1).....	5
Figure 1.3 : Knoller-Betz effect for a plunging foil (Jones and Platzner, 2009).	7
Figure 1.4 : Strouhal Number range of selected aquatic animals swimming at their maximum speed (Triantafyllou et al., 1991).....	8
Figure 1.5 : Drag producing wake (Jones et al., 1998).....	9
Figure 1.6 : Zero drag wake (Jones et al., 1998).....	9
Figure 1.7 : Thrust producing wake (Jones et al., 1998).....	10
Figure 1.8 : Deflected wake (Jones et al., 1998).....	10
Figure 1.9 : Vortices in the wake of a fish (Lighthill, 1969).	11
Figure 1.10 : MAV with membrane fixed wing (Ifju et al., 2002).	14
Figure 1.11 : Flexible wing application as a control surface for improved agility (Garcia et al., 2003).	15
Figure 1.12 : LEV patterns in (a) positively cambered flexible wing, (b) rigid wing, (c) negatively cambered flexible wing (Zhao et al., 2010).....	18
Figure 2.1 : Water Channel at Trisonic Laboratory.....	25
Figure 2.2 : Position signal for the fast and the slow pitch-up motions.....	27
Figure 2.3 : Position and trigger signal for plunging motion ($a=10$ mm, $f=0.5$ Hz). 27	27
Figure 2.4 : Flexible wing mounting.....	28
Figure 2.5 : Free oscillation and damping of the 3D Printed wing.....	29
Figure 2.6 : 3D Printed model.....	30
Figure 2.7 : Deflection of the beam.	31
Figure 2.8 : Wing and the mass attached to trailing edge.	32
Figure 2.9 : Displacement vs applied force for the lexan wing.	32
Figure 2.10 : Displacement vs applied force for 3D printed wing.....	33
Figure 2.11 : ATI NANO-17 IP68 Force/Torque (F/T) sensor.	34
Figure 2.12 : PIV system overview (Url-2).	35
Figure 3.1 : Different aspect ratio wings.....	37
Figure 3.2 : C_L and C_D variation as a function of time in fast motion.	38
Figure 3.3 : C_L and C_D variation as a function of time in slow motion.	39
Figure 3.4 : Vortex formations together with the streamlines in fast motion, (a) AR=4 (with endplate/symmetry plane; the gap is 2 mm), (b) AR=4 (without endplate/symmetry plane), (c) AR=4 (with endplate/symmetry plane; the gap is 8 mm), (d) AR=2 (without endplate/symmetry plane), (e) AR=6 (with endplate/symmetry plane; the gap is 2 mm).....	42
Figure 3.5 : Vortex formations together with the streamlines in slow motion, (a) AR=4 (with endplate/symmetry plane; the gap is 2 mm), (b) AR=4 (without endplate/symmetry plane), (c) AR=4 (with endplate/symmetry plane; the gap is 8 mm), (d) AR=2 (without endplate/symmetry plane), (e) AR=6 (with endplate/symmetry plane; the gap is 2 mm).....	44

Figure 3.6 : Streamlines at the tip, mid, and root sections of the AR=4 plate (with endplate/symmetry plane; the gap is 2 mm) in fast motion.	46
Figure 3.7 : Streamlines at the tip, mid, and root sections of the AR=4 plate (with endplate/symmetry plane; the gap is 2 mm) in slow motion.....	47
Figure 3.8 : Streamlines at the tip, mid, and root sections of the AR=6 plate (with endplate/symmetry plane; the gap is 2 mm) in fast motion.	48
Figure 3.9 : Round and sharp edge plates.	49
Figure 3.10 : C_L variation with respect to time and vorticity contours together with streamlines for the flat plate with round and sharp edges in slow motion.	50
Figure 3.11 : C_L variation with respect to time and vorticity contours together with streamlines for the flat plate with round and sharp edges in fast motion.	50
Figure 3.12 : Sketch of different planform wings: (from left to right) rectangular, elliptic, trapezoidal (isosceles), two triangular wings (angled from trailing edge and leading edge), trapezoidal (right) and Zimmerman...	51
Figure 3.13 : Force Coefficient comparisons for fast (top) and slow motions (bottom).....	52
Figure 3.14 : Vortex formations together with the streamlines in fast motion (a) rectangular wing, (b) triangular (angled from leading edge), (c) triangular (angled from trailing edge), (d) Zimmerman, (e) elliptic, (f) trapezoidal, (g) trapezoidal isosceles.	53
Figure 3.15 : Vortex formations together with the streamlines in slow motion, (a) rectangular wing, (b) triangular (angled from leading edge), (c) triangular (angled from trailing edge), (d) Zimmerman, (e) elliptic, (f) trapezoidal, (g) trapezoidal isosceles.	54
Figure 3.16 : Vortex formations together with the streamlines in fast motion for three cross-sections along the span. Top row $t=3.75s$, bottom row $t=20s$	56
Figure 3.17 : Vortex formations together with the streamlines in slow motion for three cross-sections along the span. Top row $t=7s$, bottom row $t=8.5s$.	57
Figure 3.18 : Lift coefficient variation for the fast pitch-up motion (Upper graph: time axis focused on the motion phase).....	58
Figure 3.19 : Drag coefficient variation for the fast pitch-up motion (Upper graph: time axis focused on the motion phase).....	59
Figure 3.20 : Lift coefficient variation for the slow pitch-up motion (Upper graph: time axis focused on the motion phase).....	60
Figure 3.21 : Drag coefficient variation for the slow pitch-up motion (Upper graph: time axis focused on the motion phase).....	61
Figure 3.22 : Vorticity contours and streamlines for rigid wing in fast pitch-up motion.	62
Figure 3.23 : Vorticity contours and streamlines for lexan wing in fast pitch-up motion.	63
Figure 3.24 : Vorticity contours and streamlines for printed wing in fast pitch-up motion.	64
Figure 3.25 : Vorticity contours and streamlines for acetate wing in fast pitch-up motion.	65
Figure 3.26 : Vorticity contours and streamlines for rigid wing in slow pitch-up motion.	66

Figure 3.27 : Vorticity contours and streamlines for lexican wing in slow pitch-up motion.	67
Figure 3.28 : Vorticity contours and streamlines for printed wing in slow pitch-up motion.	68
Figure 3.29 : Vorticity contours and streamlines for acetate wing in slow pitch-up motion.	69
Figure 3.30 : Freestream and force directions.....	70
Figure 3.31 : Position of the plate, measured F_y force and Theodorsen solution for $k=1.57$ and $a/c=0.2$	71
Figure 3.32 : Contribution of non-circulatory and circulatory force components to the total lift force for four different reduced frequencies.	73
Figure 3.33 : Phase lag between F_y and the motion.	74
Figure 3.34 : Position of the plate and measured F_x force for $k = 1.57$ and $a/c = 0.2$	75
Figure 3.35 : Phase lag between F_x and the motion.	76
Figure 3.36 : Thrust coefficients (C_T), power input coefficients (C_P) and efficiencies (η) (lower left: full scale, lower right: thrust producing cases only). ...	77
Figure 3.37 : Efficiencies (η) with respect to Strouhal number.	78
Figure 3.38 : Vortical structures around the plate plunging at an amplitude of $a/c = 0.1$	80
Figure 3.39 : Horizontal distance between vortex cores.	81
Figure 3.40 : Time-averaged velocity profile in the near-wake and distribution of $u - U_\infty$ for the plate plunging at an amplitude of $a/c = 0.1$	82
Figure 3.41 : Comparison of two different LEV shedding mechanisms in a motion cycle.	83
Figure 3.42 : Airfoil shapes for the lexican wing.	85
Figure 3.43 : Airfoil shapes for the printed wing.....	86
Figure 3.44 : Airfoil shapes for the acetate wing.....	87
Figure 3.45 : Trailing edge amplitude ratios of different flexible wings.....	88
Figure 3.46 : Trailing edge amplitude ratios with respect to f/f_n	90
Figure 3.47 : Phase of the trailing edge with respect to the leading edge.....	91
Figure 3.48 : Trailing edge phases Φ_{TE} with respect to frequency ratio f/f_n	92
Figure 3.49 : Phase lag between F_y and the motion for different wings.	94
Figure 3.50 : Phase lag between F_y and the motion for the lexican wing.....	95
Figure 3.51 : Phase lag between F_y and the motion for the printed wing.	96
Figure 3.52 : Phase lag between F_y and the motion for the acetate wing.	96
Figure 3.53 : Trailing edge (Φ_{TE}) and vertical force (Φ_y) phases of the flexible wings.....	98
Figure 3.54 : Phase lag (Average of 1st and 2nd peaks) between F_x and the motion for different wings.	99
Figure 3.55 : Phase lag between F_x and the motion for the lexican wing.....	100
Figure 3.56 : Phase lag between F_x and the motion for the printed wing.	101
Figure 3.57 : Phase lag between F_x and the motion for the acetate wing.	101
Figure 3.58 : Thrust coefficients (C_T) for different wing types.	103
Figure 3.59 : Power input coefficients (C_P) for different wing types.	104
Figure 3.60 : Efficiencies (η) for different wing types.	106
Figure 3.61 : Thrust coefficients (C_T), power input coefficients (C_P) and efficiencies (η) for the lexican wing.....	107
Figure 3.62 : Thrust coefficients (C_T), power input coefficients (C_P) and efficiencies (η) for the printed wing.	108

Figure 3.63 : Thrust coefficients (C_T), power input coefficients (C_P) and efficiencies (η) for the acetate wing.	109
Figure 3.64 : Efficiencies (η) of four different wings with respect to Strouhal number.	110
Figure 3.65 : Efficiency vs. phase ratio Φ_{TE}/Φ_y	111
Figure 3.66 : Vortex shedding and positions in the motion cycle for the rigid wing.	113
Figure 3.67 : Vortex shedding and positions in the motion cycle for the lexan wing.	114
Figure 3.68 : Vortex shedding and positions in the motion cycle for the printed wing.	115
Figure 3.69 : Vortex shedding and positions in the motion cycle for the acetate wing.	116
Figure 3.70 : Similar TE vortex shedding observed in different positions (Left), similar LE vortex shedding observed in same positions (Right).	118
Figure 3.71 : Vortex shedding in natural frequency oscillations for flexible wings.	119
Figure 3.72 : Example of u velocity contours and extracted profiles line over the wing.	120
Figure 3.73 : Streamwise velocity ($u-U$) profiles in a period of motion for printed wing plunging at an amplitude of $a/c=0.05$	121
Figure 3.74 : Cross-stream velocity (v) profiles in a period for the printed wing plunging at an amplitude of $a/c=0.05$	123

EXPERIMENTAL INVESTIGATION OF FLEXIBILITY EFFECTS IN FLAPPING WING AERODYNAMICS

SUMMARY

In the present PhD thesis, flexibility effects in flapping wing aerodynamics are experimentally investigated. For that purpose, one rigid and three chordwise flexible wings are produced and their aerodynamic performances are compared in a water channel. Digital Particle Image Velocimetry (DPIV) system is used to determine instantaneous velocity fields and vortical structures around the wings in conjunction with simultaneous direct force/moment measurements. The imaging system also acquired the instantaneous deformation of the wing. Natural frequency effects and deformation of the flexible wings are linked to the force measurements and efficiencies. Since all natural flyers and swimmers have some degree of flexibility on their wings, it is important to understand the phenomena for a more effective aerial/nautical vehicle design. Main objective is to determine the aerodynamic performances of different flexible wings under harmonic plunging or rapid pitch-up motions.

The experiments are performed in the close-circuit, free-surface, large-scale water channel located in the Trisonic Laboratories at the Faculty of Aeronautics and Astronautics of Istanbul Technical University (Istanbul, Turkey).

Two distinct motions are executed in the experiments. Perching or pitch-up is one of these motions and based on sudden change in angle of attack and halting the wing at a constant degree of angle. The pitch-up motions of the airfoil were accomplished using a Kollmorgen/Danaher Motion AKM33E servo motor. The models were subjected to performing two types of pitch-up motion: fast and slow. The model started from 0° and attained its final angle of attack of 45° in 1 second for the fast motion and in 6 seconds for the slow motion, corresponding to 1 and 6 convective times, respectively. The motor motion profiles were generated by a signal generator Labview VI (Virtual Instrument) for the given amplitude and duration. Labview VI also triggers both the force data acquisition and the PIV system.

The other motion type is the purely plunging motion that is generated by harmonic cosine position function. Plunge motion of the model is accomplished with Kollmorgen/ Danaher Motion AKM54K servo motor. The motor motion profiles were generated by a Labview VI for various amplitudes and frequencies.

The experiments are performed on four different wing materials: a rigid wing produced of plexiglass, three flexible wings produced of homogeneous polycarbonate sheet (lexan), an acetate wing, and an elastic model produced in 3D printer. The rigid wing has a thickness of 5 mm, chord length of 100 mm and transparent to illuminate both sides of the wing. Flexible wings have 10 mm metal part on leading edge to avoid spanwise flexibility and the total chord length is 100 mm. The wing's rotation axis is the leading edge, which also coincides with the center of the force sensor.

Natural frequencies of the manufactured wings are one of the backbone parameters of the thesis. Motion parameters are determined based on these natural frequencies. The wings are exposed to sudden loading and given free chordwise oscillation to determine their natural frequencies while the wing is in its position, fully submerged in the water channel. Natural frequencies are determined as 7.40 Hz, 2.32 Hz, 1.25 Hz, 0.51 Hz for rigid, lexan, printed and acetate wings respectively.

Force data is collected by a six-component ATI NANO-17 IP68 Force/Torque sensor. The sensor was mounted on the rod between the model and the plunge servo motor, oriented with its cylindrical z-axis coincides with the leading edge of the wings.

For the perching rigid wings, whether the plate pitches up fast or slow, the flow remains mostly 2D along the span for plates with $AR = 4$ and above. During the motion, the effect of the AR is to shift the force variation in amplitude without changing its variation character. The effect of AR, hence, the three-dimensionality of the flow becomes pronounced after the motion ends. The formation of a local maximum in the force variations after the motion ends was evident for wings with $AR > 2$. There exist two peaks for wings with $AR \geq 6$. These secondary or even tertiary peaks occur because of the formation of a new LEV.

Even if the effective ARs of the wings are the same, the one with a symmetry plane did not yield exactly the same flow topology and hence the same force-time histories as the fully submerged wing. There were slight differences due to the three-dimensionality of the flow. Therefore, an endplate representing the symmetry plane should carefully be placed with special care to ensure that the gap between the wing root and the endplate is approximately 2 mm (i.e., 2% of the chord).

Perching motion in flexible wings primarily depend on the deflection of the wings caused by the oncoming freestream. The deflection is high for the most flexible acetate wing, which results in a lower angle of attack. As a result, low C_D is obtained for the acetate wing. When flow structures are examined, streamline topology of the acetate wing shows differences due to the reduced angle of attack both in fast and slow motion cases. Continuous LEV and TEV vortex shedding can be observed on the acetate wing.

For the plunging rigid wings, it is found that the phase lag between the motion and the cross-stream force component decreases as the reduced frequency increases, and for a given reduced frequency, the phase lag increases as the plunging amplitude increases. The variation of the horizontal spacing between vortex cores with the reduced frequency follows the same characteristics as those of the phase lag for the cross-stream force. On the other hand, the phase lag for the streamwise force component decreases as the plunging amplitude increases for low reduced frequencies. The decrease converges to a phase lag value of 90° , which coincides with the maximum velocity of the wing. After the minimum is reached, the phase lag for the streamwise force component starts to increase. The minimum phase lag coincides with the reduced frequency where the crossover from drag to thrust is observed and maximum flapping efficiency is obtained. When the thrust is produced, the phase lag for the streamwise force component increases. Moreover, according to the vortex structures, the crossover from drag to thrust is observed when the LEV starts to hold around the leading edge and does not convect downstream along the plate.

In flexible flapping wings, trailing edge amplitude makes a peak when the oscillations are performed near natural frequency of the wing ($f/f_n \sim 1$). For the acetate wing, frequencies beyond natural frequency can be tested and after $f/f_n = 2$, trailing edge amplitudes start to increase again. The values are in a continuous increase in the

measurement range up to $f/f_n = 4.4$. This finding suggests that, higher trailing edge amplitudes can be reached when the flapping frequencies are beyond the resonant frequency.

When Φ_y phases are considered, it is observed that the flexible wings have completely different phase variations compared to the rigid wings. Natural frequency appears to have an effect on Φ_y phase variations. Phase values increase up to the near natural frequency, and then exhibit a decreasing followed by an increasing trend at higher flapping frequencies (can be observed for acetate wing). Besides the natural frequency, flapping amplitude also has an effect on phases such as the peak near natural frequency diminishes for higher amplitudes in acetate wing. This implies that natural frequency and flapping amplitude should be interpreted together.

An interesting result is obtained from the combined $\Phi_y - \Phi_{TE}$ phases graph: trailing edge phases and Φ_y force phases are intersecting at different plunging frequencies for different wings. The intersecting frequencies coincide with the natural frequency of the wing. In other words, cross-stream force phases and trailing edge phases are equal when the wings are plunged near their natural frequencies. Flexible wings have peak efficiency around natural frequencies where their trailing edge phases and F_y force phases also coincide.

Unlike the rigid wing, distribution of the Φ_x phases have similar characteristics with the Φ_y phases in flexible wings. That similarity indicates that the flexibility effects are observed not only in cross-stream direction but also in streamwise direction. In flexible wings, elastic forces emerge in both streamwise and cross-stream directions coupled with the trailing edge deflection. The similarity between the streamwise and the cross-stream force phases is a result of these prevailing elastic forces over the other existing forces (circulatory and added mass).

The efficiency peaks shift towards high Strouhal numbers when the flapping amplitude increases. The peak efficiencies are obtained in a Strouhal number range of 0.1 – 0.6 for the flexible wings. High efficiency zone in the literature was expressed in a Strouhal number range of 0.2 – 0.4 and for the flexible wings, this range is generally valid. The boundaries of the range are slightly extended for the flexible wings in different flapping amplitudes.

Same vortical instances are attained at different stages of the motion cycle for the flexible wings. It is observed that the TE motion determines the vortex shedding timing. As the wing gets more flexible, vortex shedding from the TE delays and similar vortex structures on the TE are observed later in the flapping period. Chordwise flexibility under parameters presented herein, alters the TEV shedding timing and vortex strength but does not have a pronounced effect on LEV shedding.

For the rigid wing, the vortices burst after one chord length in the wake. As the wing gets more flexible, the vortices start to burst late. The vortices in the most flexible acetate wing's wake preserve their coherency and can be tracked in full measurement region. Also number of vortices observed in the wake increases when the wing is more flexible.

While the flexibility for the wing flapping around its natural frequency exploits and enhances the high velocity zones created around the wing with the TE timing, another low efficiency flapping frequency cases cannot perform that. It can be considered as “catching” the flow and transferring it to the wake through vortices, which is found to be crucial for high efficiency.



ÇIRPAN KANAT AERODİNAMİĞİNDE ESNEKLİK ETKİLERİNİN DENEYSEL OLARAK İNCELEMESİ

ÖZET

Bu doktora tezinde, esnek kanatların çirpan kanat aerodinamiğindeki etkileri deneysel olarak incelenmiştir. Bu amaçla bir tane rijit kanat ve üç tane veter doğrultusunda esnek kanat üretilmiş ve kanatların aerodinamik performansları su kanalı deneyleriyle karşılaştırılmıştır. Parçacık Görüntüleyerek Hız Ölçümü sistemi ile kanat etrafı anlık hız alanları ve girdap yapıları belirlenmiş, eş zamanlı olarak kuvvet ölçümleri alınmıştır. Görüntü alma sistemi aynı zamanda esnek kanatların anlık deformasyonlarını elde etmek için de kullanılmıştır. Doğal frekans etkileri ve kanat deformasyonları kuvvet verileri ve verimlilik ile ilişkilendirilmiştir. Doğada kanat çırpma hareketi yapan uçucu ya da yüzücü hayvanlara baktığımızda, kanatlarında ya da kuyruklarında esnek yapıya sahip olduğunu görebiliriz. Bu yüzden, doğayı örnek alınarak yapılacak olan hava/su aracı tasarımlarında bu esneklik etkilerinin incelenip anlaşılması önem taşımaktadır. Ana amaç olarak, harmonik çırpma hareketi ya da ani yunuslama hareketi yapan kanatların farklı esneklik dereceleri altında aerodinamik performanslarının incelenmesi hedeflenmiştir.

Deneysel çalışmalar İstanbul Teknik Üniversitesi, Uçak ve Uzay Bilimleri Fakültesi'ne bağlı Trisonik Laboratuvarı'nda bulunan kapalı devre, açık yüzey, geniş ölçekli su kanalında gerçekleştirilmiştir.

Deneysel çalışmada iki farklı hareket gerçekleştirilmiştir. Bunlardan birisi ani yunuslama hareketi olarak tanımlayacağımız, belirli bir sürede gerçekleşen hücum açısı değişimi ve sonrasında kanadın sabit hücum açısında kaldığı hareket tipidir. Kanatlara yunuslama hareketi Kollmorgen/Danaher Motion AKM33E servo motor kullanılarak verilmiştir. Kanat modellerine hızlı ve yavaş olmak üzere iki tip yunuslama hareketi verilmiştir. Kanatlar 0° hücum açısından 45° hücum açısına hızlı durumda 1 saniyede, yavaş durumda 6 saniyede getirilmiştir. Bunlar sırasıyla 1 ve 6 taşınım zamanına denk gelmektedir. Motor hareket profilleri belirli genlik ve süre için Labview programıyla oluşturulmuştur. Labview aynı zamanda kuvvet verisi alımını ve PIV sistemini senkronize çalışması için tetiklemektedir.

Diğer hareket türü ise harmonik kosinüs konum fonksiyonu ile oluşturulan ötelenme hareketidir. Modellerin ötelenme hareketi Kollmorgen/ Danaher Motion AKM54K servo motor ile sağlanmıştır. Farklı genlikler ve frekanslar için ötelenme hareketi profilleri yunuslama hareketinde olduğu gibi Labview programı ile oluşturulmuştur.

Deneysel çalışmalar dört farklı malzemeden üretilen kanatlar ile gerçekleştirilmiştir: pleksiglas malzemeden üretilen rijit kanat, esnek kanat olarak homojen polikarbon levha (lexan), asetat kanat ve üç boyutlu yazıcıda basılan kanat. Rijit kanat 5 mm kalınlığına, 100 mm veter uzunluğuna sahip olup her tarafının aydınlatılabilmesi için şeffaftir. Esnek kanatların hücum kenarında bulunan 10 mm metal parça ile kanatların veter boyunca esnekliğe sahip olmaları sağlanmış olup açıklık boyunca olan esneklik engellenmiştir.

Kanatların bağlantı ve dönme eksenini hücum kenarı olup bu eksen aynı zamanda kuvvet sensörünün merkezi ile çakışmaktadır.

Üretilen kanat modellerinin doğal frekansları bu tezin ana parametrelerinden birisidir. Hareket parametreleri bu doğal frekanslar göz önünde bulundurularak belirlenmiştir. Doğal frekans belirlenirken kanatlar su kanalının içerisinde, kendi deney pozisyonunda bulunurken ani yüklemeye ile veter doğrultusunda serbest salınımları sağlanmış ve sensör verileri hareket sönümleninceye kadar kaydedilmiştir. Bu verilerin analizi sonucunda rijit, lexan, baskı ve asetat kanatların doğal frekansları sırasıyla 7.40 Hz, 2.32 Hz, 1.25 Hz, 0.51 Hz olarak belirlenmiştir.

Kuvvet verisi altı bileşenli ATI NANO-17 IP68 Kuvvet/Tork sensörü ile alınmıştır. Sensör model çubuğu ile motordan gelen çubuk arasına, z-ekseni kanadın hücum kenarına denk gelecek şekilde yerleştirilmiştir.

Yunuslama hareketi yapan rijit kanatlar için, yavaş ya da hızlı harekette, akış genel olarak açıklık oranı $AR=4$ ve üzerinde iki boyutlu karakter göstermektedir. Hareket süresince, açıklık oranının etkisi kuvvet dağılımının karakterini değiştirmeden kuvvet genliğini ötelemek şeklinde olmaktadır. Açıklık oranının dolayısıyla akışın üç boyutluluğunun etkisi hareket bittikten sonra belirleyici olmaktadır. Kuvvet dağılımlarındaki lokal maksimumlar açıklık oranı $AR > 2$ için görülmektedir. $AR \geq 6$ durumunda iki tepe noktası oluşmaktadır. Bu ikincil hatta üçüncül tepe noktaları yeni oluşan hücum kenarı girdabı dolayısıyla meydana gelmektedir.

Kanatların efektif açıklık oranları aynı olsa bile, simetri eksenini kullanılanların, simetri eksenini kullanılmadan tamamen daldırılarak elde edilen açıklık oranlı kanatlar ile aynı akış topolojisine ve kuvvet-zaman dağılımlarına sahip olmadıkları görülmüştür. Akışın üç boyutluluğu sebebiyle bazı küçük farklılıklar oluşmaktadır. Bu yüzden, simetri eksenini vazifesi görece plaka dikkatli bir şekilde kullanılmalı ve kanat ile bu plaka arasındaki mesafe iyi ayarlanmalıdır. Bu çalışmada bu mesafe 2 mm (diğer bir deyişle veter uzunluğunun %2'si) kadardır.

Esnek kanatlarda yunuslama hareketi ana olarak gelen akışın kanatları deforme etmesi ile ilintilidir. Esnekliği en yüksek kanat olan asetat kanatta bu eğilme deformasyonu miktarı daha fazla olmakta bu da hücum açısını azaltmaktadır. Sonuç olarak da asetat kanatta düşük C_D elde edilmektedir. Akış yapıları incelendiğinde, asetat kanatta akım çizgileri hem yavaş hem hızlı hareket durumunda diğer kanatlardan farklılıklar göstermektedir. Sürekli bir hücum kenarı girdabı ve firar kenarı girdabı oluşumu asetat kanat için gözlenmektedir.

Ötelenme hareketi yapan rijit kanatlarda, hareket ile akışa dik kuvvet bileşeni arasında oluşan faz farkı, kanat çırpma frekansı arttıkça azalmaktadır. Belirli bir frekans için faz farkı, kanat çırpma genliği arttıkça artmaktadır. Kanadın iz bölgesinde oluşan girdaplar arasındaki yatay mesafenin dağılım grafiği ile akışa dik kuvvet bileşeninin fazlarının değişim grafiği benzer özellikler göstermektedir. Diğer taraftan, düşük kanat çırpma frekanslarında, akış doğrultusundaki kuvvet fazları çırpma genliği arttıkça azalmaktadır. Bu faz azalması, faz 90° değerine yakınsayacak şekilde devam etmekte, bu da kanadın maksimum hızına sahip olduğu duruma denk gelmektedir. Fazlar minimum değerine eriştikten sonra artış trendine girmektedir. Minimum faz gecikmesi, sürüklenme rejiminden itki rejimine geçildiği ve maksimum verim elde edildiği indirgenmiş frekans ile çakışmaktadır. İtki üretilmeye başlandığında akış doğrultusundaki kuvvet fazları artışa geçmektedir. Ayrıca, girdap yapılarına bakıldığında, sürüklenmeden itkiye geçiş, hücum kenarı girdabının hücum kenarı

civarında kalmaya başladığı ve kanat üzerinden iz bölgesine doğru ilerlemediği durumda görülmüştür.

Esnek çırpan kanatlarda, kanatlar doğal frekans civarında çırptırıldığında ($f/f_n \sim 1$), firar kenarı genliği dağılımı tepe noktası yapmaktadır. Asetat kanat için doğal frekanstan daha büyük çırpma frekansları test edilebilmektedir ve $f/f_n = 2$ 'den sonra firar kenarı genlikleri tekrar artışa geçmektedir. Genlik değerleri ölçüm aralığının maksimumu olan $f/f_n = 4.4$ 'e kadar sürekli artış göstermektedir. Bu gözlem, rezonans frekansının ötesindeki çırpma frekanslarında da yüksek firar kenarı genliği elde edildiğini göstermektedir.

Esnek kanatlar Φ_y fazlarında rijit kanatlara göre oldukça farklı dağılım göstermektedir. Doğal frekansın, Φ_y fazları üzerinde etkisi olduğu görülmektedir. Faz değerleri doğal frekans civarına kadar artmakta, daha sonra bir azalış ve sonrasında artış davranışı sergilemektedir (asetat kanat için gözlenebilir). Doğal frekansın yanında, çırpma genliğinin de fazlar üzerinde doğal frekans civarında görülen tepe noktasını yok edici şekilde etkisi vardır. Bu da doğal frekansın ve çırpma genliğinin birlikte yorumlanması gerektiğini göstermektedir.

Birleştirilmiş $\Phi_y - \Phi_{TE}$ faz grafiklerinde ise ilginç bir sonuç elde edilmiştir: firar kenarı fazları ve Φ_y kuvvet fazları farklı kanatlar için farklı çırpma frekanslarında kesişmektedirler. Kesiştikleri frekanslar kanadın doğal frekansına denk düşmektedir. Diğer bir deyişle, Φ_y ve Φ_{TE} fazları kanatlar doğal frekanslarında çırptırıldığında birbirine eşittir. Esnek kanatlar, firar kenarının ve F_y kuvveti fazlarının eşit olduğu doğal frekans salınımlarında yüksek verimliliğe sahiptirler.

Rijit kanatların aksine, Φ_x fazlarının değişimi esnek kanatlarda Φ_y fazları ile benzerlik göstermektedir. Bu benzerlik, esneklik etkilerinin sadece akıma dik doğrultudaki kuvvetlere değil akım doğrultusundaki kuvvetlere katkı sağladığını göstermektedir. Esnek kanatlarda firar kenarının eğilmesiyle beraber, elastik kuvvetler hem akıma dik doğrultuda hem de akım doğrultusunda ortaya çıkmaktadır. İki kuvvet bileşeni arasındaki bu benzerlik, özellikle akış doğrultusundaki kuvvetlerde elastik kuvvetlerin diğer kuvvetlere (sirkülasyon ve zahiri kütle) baskın olduğunu göstermektedir.

Verimlilik tepe noktaları kanat çırpma genliği arttırıldığında daha yüksek Strouhal sayılarına doğru kaymaktadır. Esnek kanatlarda maksimum verimlilik 0.1 – 0.6 Strouhal sayısı aralığında elde edilmiştir. Yüksek verim bölgesi literatürde 0.2 – 0.4 Strouhal sayısı aralığında belirtilmiştir ve esnek kanatlar için de bu aralık genellikle geçerlidir. Aralığın sınırları farklı genliklerde çırpan esnek kanatlar için biraz genişletilmiştir.

Aynı girdap yapıları esnek kanatlarda hareket döngüsünün farklı evrelerinde oluşmaktadır. Firar kenarı hareketinin girdap oluşum zamanını belirlediği gözlenmiştir. Kanatlar daha esnek hale geldikçe, firar kenarında oluşan girdaplar gecikmekte ve bunun sonucunda firar kenarı girdap yapıları bir kanat çırpma periyodunda daha geç oluşmaktadır. Veter boyunca olan esnekliğin burada sunulan parametreler ile firar kenarı girdap zamanlamasını ve girdap şiddetini değiştirdiği fakat hücum kenarı girdap yapılarına belirgin bir etkisinin olmadığı görülmüştür.

Rijit kanat için, girdaplar bir veter uzunluğu mesafeden sonra patlamaktadır. Kanatlar esnek hale geldikçe girdaplar daha geç patlamaya başlamaktadır. En esnek kanat olan asetat kanatta girdaplar ölçüm alanının tamamında bütünlüğünü korumakta ve takip edilebilmektedirler. Ayrıca, iz bölgesinde görülen girdap sayısı da kanat esnekliği arttıkça artmaktadır.

Dođal frekansý civarında ırpan esnek kanatların firar kenarı zamanlamasıyla beraber kanat etrafında oluşan yüksek hız alanlarını destekleyip bunlardan faydalandığı gözlenmiştir. Diđer düşük verimli durumlar ise bunu gerçekleştirmemektedir. Bunu bir çeşit akışı “yakalayıp” girdaplar vasıtasıyla iz bölgesine aktarma şeklinde düşünebiliriz. Bu durumun da yüksek verimlilik için anahtar noktalardan biri olduğu görülmüştür.



1. INTRODUCTION

Is it possible to overcome the nature? Is it possible to make designs, which are more efficient than the nature? Or is the nature an ultimate limit for all scientists, inventors and engineers could finally reach? Million years of evolution have shaped the earth and all the livings depending on revealed and unrevealed fundamental laws. We are the carriers of those extensive experience adapted and survived for ages. And so does the birds, insects, fish and other living creatures. All are perfectly attuned to their aquatic or aerial environment to perform different tasks like high maneuvering capability, traveling long distances, reaching high velocities, etc. Understanding the physics behind those natural phenomenons have been a voyage for human beings, taking many millennia and still currently an ongoing process.

Flying animals have always fascinated human beings in different ways. They have associated with freedom, since they have no boundaries on the sky. Human beings, as captives of gravity, admire them and “being in the sky” has been a dream since the ancient times. Once upon a time, there was an Athenian craftsman Daedalus who was imprisoned on the island of Crete. The only way to escape from the island was the airway. Therefore, Daedalus constructed wings from feather and wax both for himself and his young son named Icarus. Daedalus warned his son just before the take-off for not to fly too low because the feathers could get soaked, nor too high, because the sun would melt the wax. Icarus was ecstatic with the ability to fly. He ignored his father’s warning, soared upward towards the sun, which caused the heat to melt the wax. Icarus kept flapping his wings, but since no feathers left, he fell into the sea near the area, which today is known as the Icaria Island. Apart from mythical stories, the earliest example of the human-made flight is attributed to kite flying in China several hundred years BC. Kites were used for military purposes in those days, and some were so large in size that were powerful enough to carry men up in the air. After medieval ages, the renaissance was the rebirth of civilization and was also a milestone for aviation. Leonardo da Vinci had an interest in aviation besides his paintings and sculptures. In his detailed sketches, da Vinci had designs of ornithopters, which employed flapping

wings powered by human pilot that creates lift and propulsion. Also in *Codex on the Flight of Birds*, he had some observations and ideas on fundamental aerodynamics such as the center of gravity, the center of pressure and the wing sections. In the 17th century, legendary Ottoman aviator Hezarfen Ahmet Çelebi was purported to achieve unpowered flight from the top of the Galata Tower to Üsküdar. Montgolfier brothers in France raised the first hot air balloon into the sky in 1783. German engineer, Otto Lilienthal, was performing successful, repeated and well-documented gliding flights near Berlin. He published a book titled “*Bird Flight as the Basis of Aviation*” in 1889. His studies had a tremendous influence on Wright Brothers, who later developed their own theories and designs, and made the first controlled, sustained flight of a powered aircraft in 1903. In following decades, development in aviation technology was quite rapid, especially with the influence of increasing military use of the air vehicles and challenging World Wars’ boosting effects on technology race between countries. The sky was no longer a limit for manned flight in the 1960s when the first human send into space and then landing on the moon have expanded the horizons of humanity significantly.

Today, we can send spacecrafts to other planets, observe the stars and the galaxy, and even land a spacecraft on the comet’s nucleus. Meanwhile, aircrafts in the earth’s atmosphere progressed on eliminating the pilot, and remotely operated unmanned air vehicles (UAV) are take off to skies. The size of the UAVs are reduced, and Micro Air Vehicle (MAV) class has arisen with the aid of new manufacturing technology and advanced controlling techniques. Since MAVs dimensions have become comparable to birds and insects, inspiration from the nature phenomena or biomimetics has found a fresh and sophisticated area of implication. Its complexity arises from the wide range of wing motions and wing shapes, different structural properties and unsteady fluid interactions with these structures. Fundamental research is required to enlighten those areas separately. This thesis simplifies the parameters, and positions its topic on the intersection of engineering, biology and flow physics. When we recall the questions at the beginning of the chapter, we are not yet close to reach the efficiency of the nature’s working principles and still on the “understanding the nature” phase of human intellectual accumulation. The thesis endeavors to contribute this repository from an experimental perspective.

1.1 Purpose of Thesis

In the present PhD thesis, it is planned to experimentally investigate the flexibility effects in flapping wing aerodynamics. For that purpose, one rigid and three chordwise flexible wings are produced and their aerodynamic performances are compared in a water channel. A Digital Particle Image Velocimetry (DPIV) system is used to determine instantaneous velocity fields and therefore vortical structures around the body in conjunction with simultaneous direct force/moment measurements. The imaging system also acquired the instantaneous deformation of the wing. Since the phenomena is complicated and depend on various properties, these parameters of the study should be selected carefully to determine the optimum performance of the wings. Therefore, first objective was to reduce the parameters on possible wing types, wing motions and materials in the light of laboratory facility capabilities and previous experiences on our researches. Natural frequency effects and deformation of the wing models are linked to the force measurements. Since all natural flyers and swimmers have some degree of flexibility on their wings, it is important to understand the phenomena for a more effective aerial/nautical vehicle design. Flexibility has an effect on drag-thrust transition and efficiency of the motion. Main objective is to determine the aerodynamic performances of different flexible wings under harmonic plunging or rapid pitch-up motions.

The thesis is a combination of projects conducted during PhD studies. Experiments performed within the NATO STO AVT-202 task group titled “Extension of Fundamental Flow Physics to Practical MAV Aerodynamics” were one of these projects based on special cases including perching and flapping maneuvers. Impulsively pitching plates are examined; force and DPIV measurements are taken as a part of the project. The aim was to understand sudden maneuver mechanisms due to change in angle of attack and their applicability to aircraft design. Another project that was funded by the Scientific and Technological Research Council of Turkey (TUBITAK) Grant 112M682 titled “Investigation of Flow Structures and Unsteady Loading for a Wing in Periodic or Transient Flapping Motion”. In that TUBITAK funded project, a wide range of studies are conducted including pitch and plunge motion of a SD7003 airfoil, cross section effects on flapping airfoils, planform area and three-dimensionality effects on pitching wings, and flapping flexible wings. Other than these two projects, experiments are performed in the scope of a European Union

Seventh Framework Programme project titled “Non-Intrusive Optical Pressure and Loads Extraction for Aerodynamic Analysis” (NIOPLEX). Our duty in the project was to perform rigid and flexible flapping wing experiments and compare direct force measurements to force estimations that gained from the velocity fields of PIV data. The thesis has benefited from aforementioned projects and combined the outcomes within the framework of the focused thesis study.

1.2 Literature Review

Literature review section will be grouped under three main research topics including perching motion, plunging motion and flexibility.

1.2.1 Perching

Perching can be defined as a landing maneuver to a specific point where the cruising velocities in both vertical and horizontal directions are eventually reduced to zero. Birds rotate their bodies and wings in perching and gain high angles of attack, which causes high drag to exploit as a brake and reducing the horizontal speed. In addition, they aim a point lower than the landing location and as the high angle of attack increases the lift, the bird precisely finalize the landing process. Illustration of a perching maneuver is given in Figure 1.1 and Figure 1.2.

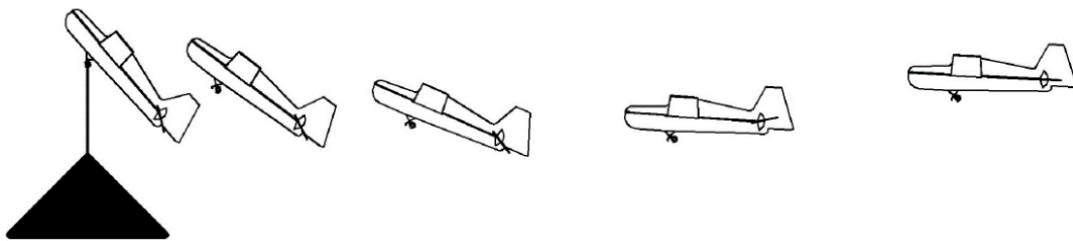


Figure 1.1 : Perching trajectory (Cory and Tedrake, 2008).

In literature, the maneuver of perching can be represented by an impulsive pitch-up and varying the angle of attack over a large amplitude (Reich et al., 2009), and an extensive number of studies have investigated force production in relation to the motion kinematics and flow structures either in translational (Ford and Babinsky, 2013; Garmann and Visbal, 2011; Baik et al., 2010; Jones and Babinsky, 2010; Mancini et al., 2015) or rotational (Carr et al., 2013; Venkata and Jones, 2013; Schlueter et al., 2014; Percin and Van Oudheusden, 2015) pitch-up motion.



Figure 1.2 : Perching maneuver of a bird (Url-1).

Lentink and Dickinson (2009) studied leading edge vortex (LEV) stability on revolving wings and showed that three terms, namely angular, centripetal and Coriolis accelerations govern LEV dynamics. They indicated that the LEV is stabilized by centripetal and Coriolis accelerations. Angular acceleration does not have an effect on LEV stability; however, it is important for LEV integrity. Pressure gradient and centrifugal forces are found to be responsible for outboard flow in the core of LEV in the study of Garmann et al. (2013). It is also pointed out that the Coriolis acceleration does not have an effect on LEV attachment. They compared the revolving wing with equivalent translating wing and observed similar features at the beginning of the motion, however, the evolution of the flow later shows differences. The differences between translating wings and revolving wings are discussed by Wang (2005) and one of the differences put forth is the absence of von Karman vortex shedding in revolving wings. Wang suggested that the conical shaped LEV in revolving motion is a result of zero velocity at the root and the pinned vortex line to the root prevents shedding. In translational case, the LEV is expected to have a cylindrical shape. It is also noted that 3D effects attributed to the spanwise flow in rotating wings are different from the 3D end effects in translating foils.

In the present study, the motion is translational, therefore particular focus is given to studies on translating wings. Three-dimensional flow simulations around low aspect ratio (AR) plates (from AR=1–4) and low Reynolds numbers ($Re=300$ and $Re=500$) were performed by Taira and Colonius (2009). These authors found that the stability of the wake and the forces were significantly affected by the AR and the angle of

attack. After the motion is completed, the wakes reach steady, periodic unsteady or aperiodic unsteady states depending on the interactions among the leading edge vortex (LEV), trailing edge vortex (TEV) and tip vortex (TV). The competition between LEV and TV has also been investigated by Hartloper et al. (2013) for a low-AR plate, and spanwise velocity induced by the TV was found to be responsible for inboard convection of LEV and vortex compression at the mid-span. Spanwise velocities in low-AR, pitching-up wings were also addressed by Yilmaz and Rockwell (2012); these spanwise velocities were shown to result in surface normal vorticity regions. Jantzen et al. (2014) examined the AR=2 and AR=4 pitching flat plates and concluded that the TV keeps the LEV near the wing in the AR=2 wing. However, for the AR=4 wing, the tip effect is reduced and LEV detach early and subsequently, second LEV formation is allowed. Leading edge vortex detachment mechanisms were explained in detail, and the influence of the chord length on formation and detachment of the LEV was investigated in a study by Widmann and Tropea (2015). Similar detachment mechanisms are observed in this study and will be addressed in the results section.

This investigation explores similar parameter values to those used by Stevens et al. (2013) and Granlund et al. (2013b). The current study focuses on the evolution of the LEV, its detachment, and its interactions with TEV and TV. In this perspective, the effect of AR has been studied in two different setups: An endplate is used to represent the symmetry plane, and the wing is submerged fully in the free-surface water channel. Even if the physical ARs are the same, our force measurement results reveal that the end conditions affect the flow physics, which leads to different variations, especially after the pitch-up is completed where the forces exhibit a local increase and decrease. Stevens and Babinsky (2014) also noted the existence of a secondary maximum on the lift coefficient time histories after the pitch-up ends for both fast and slow motions over the same chords of travel. The effect of AR becomes important to determine whether two-dimensional (sectional) properties of the wing are dictating the forces acting on the plate or not. The performance of the wing is evidently linked to vortex formation and evolution; in a two-dimensional perspective, low-order force models have been found to be capable of making reasonable predictions of force histories and magnitudes (Ford and Babinsky, 2013; NATO STO-TR-AVT-202, 2016). However, as indicated by Granlund et al. (2013a), three-dimensionality plays an important role in LEV stabilization, and spanwise pressure gradients due to tip vortices have a

significant effect on aerodynamic performance. Consequently, by studying the flow structures in the near-wake of an impulsively pitching flat plate at different rates and associated loading on, the current investigation seeks to better understand the effect of the AR on the three-dimensionality of the flow.

1.2.2 Harmonic motion

Due to the simplicity of the motion, the earliest theories concerning flapping wing flight are related to purely plunging airfoils. The theory of thrust generation using flapping foils was first proposed by Knoller (1909) and Betz (1912) and then experimentally confirmed by Katzmayr (1922). The Knoller-Betz theory states that a harmonically plunging wing in a freestream flow results in generation of an effective angle of attack and when the airfoil is oscillated at sufficiently high amplitude and frequency, the downstream velocity distribution becomes jet-like and thus is indicative of a net thrust on the airfoil. The schematic illustration of thrust production for a plunging foil is given in Figure 1.3.

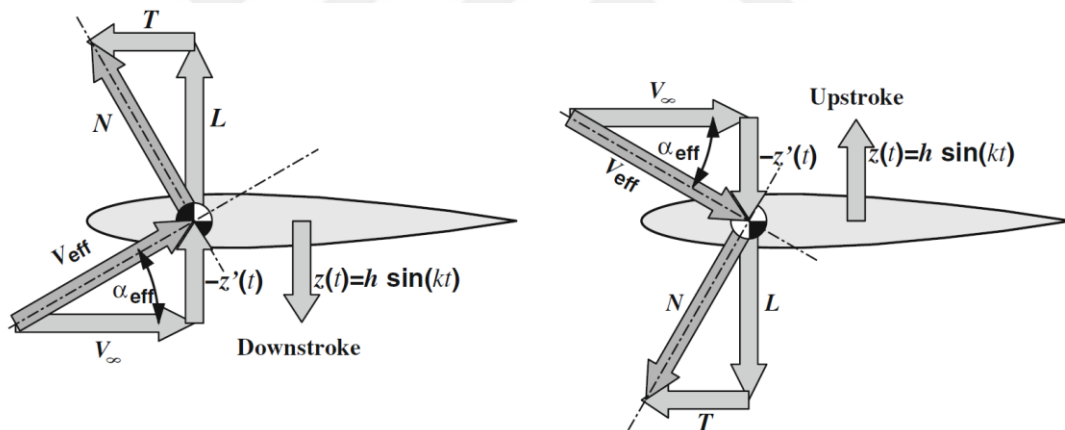


Figure 1.3 : Knoller-Betz effect for a plunging foil (Jones and Platzer, 2009).

Garrick (1936) applied the Theodorsen function (Theodorsen, 1935) with methods outlined by von Karman and Burgers (1935) to find the propulsion of an oscillating wing. Bratt (1953) experimentally obtained smoke patterns in the wake of an aerofoil performing oscillation in a wind stream and supported the aforementioned propulsion theories. Freymuth (1988) documented visualization results of propulsive vortical signatures for airfoils in pure plunging and pure pitching motions. Anderson et al. (1998) studied thrust producing harmonically oscillating foils with force and power measurement and DPIV data. Maximum efficiency is measured as 87% within the Strouhal number range of 0.3 to 0.4. High efficiency is accompanied with moderately

strong leading edge vorticity that is interacting with trailing edge vorticity, eventually leading to a reverse Karman street vortex formation. The Strouhal number range mentioned above coincides with that presented by Triantafyllou et al. (1991) for observed fish and cetaceans swimming at or near their maximum observed speed, which lies in the Strouhal number range of 0.25 – 0.35 as shown in Figure 1.4.

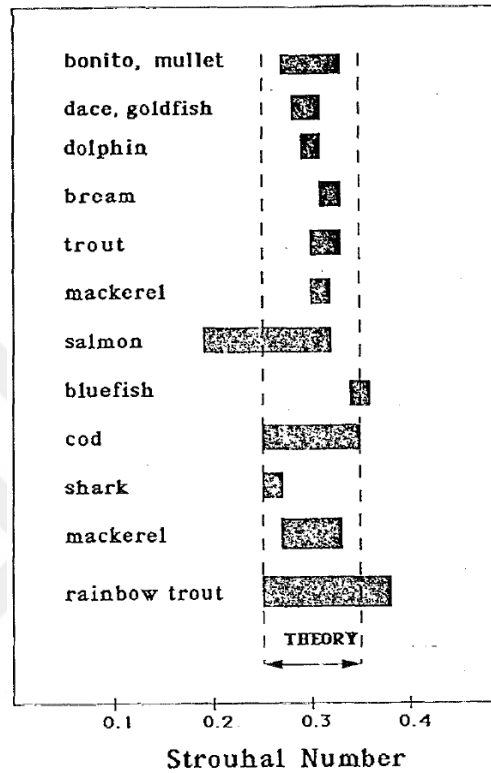


Figure 1.4 : Strouhal Number range of selected aquatic animals swimming at their maximum speed (Triantafyllou et al., 1991).

Koochesfahani (1989) studied the vortical flow patterns in the wake of a pitching NACA 0012 airfoil and showed that the vortical structures can be considerably modified by the control of amplitude, frequency, and the shape of oscillation waveform. Plunge frequency and amplitude effects on the wake characteristics are investigated by Jones et al. (1998) and presented in Figure 1.5 - Figure 1.8 for different wake types.

In Figure 1.5 upper image is representing the rotation of the eddies whereas lower image is taken from the water tunnel visualization experiment. Drag producing wake is represented in Figure 1.5, where the clockwise shedding vortices are positioned over the centerline and counter-clockwise vortices are positioned under the centerline. The result is a well-known Karman vortex street similar to the wake of a stationary cylinder.

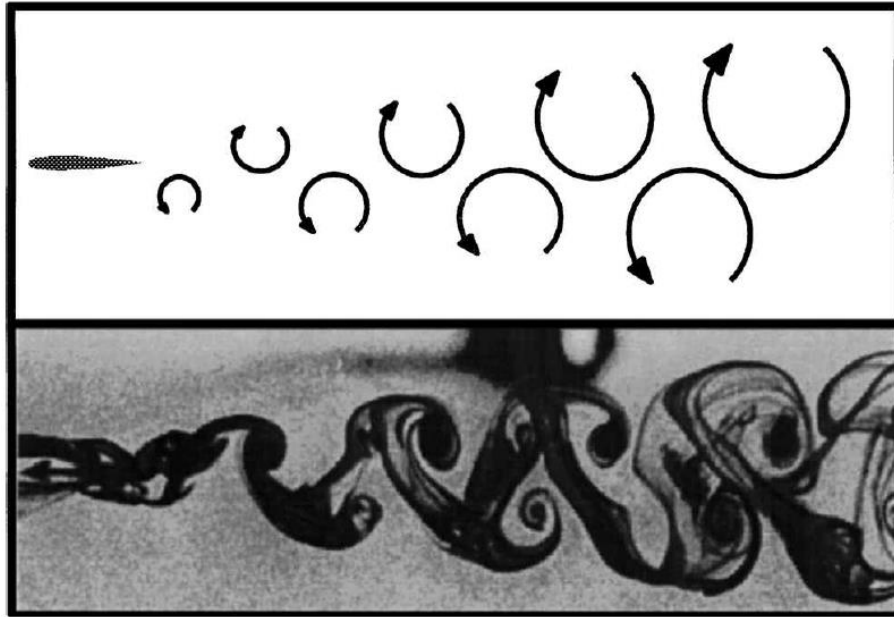


Figure 1.5 : Drag producing wake (Jones et al., 1998).

When the non-dimensional plunge velocity (ratio of maximum plunge velocity to freestream velocity) increased, vortical patterns starts to change and zero drag or neutral wake structure is observed (Figure 1.6). In this case, both clockwise and counterclockwise vortices are aligned at the centerline.

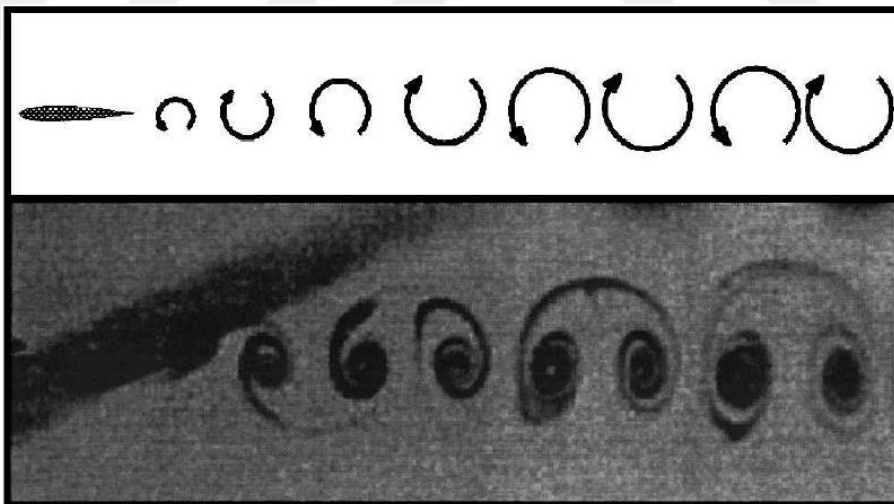


Figure 1.6 : Zero drag wake (Jones et al., 1998).

As the non-dimensional plunge velocity increased more, counter clockwise vortices are placed over the centerline and clockwise vortices are under the centerline, which is opposite of the drag producing wake, and called reverse Karman vortex street (Figure 1.7). That kind of vortex structure is indicative of thrust production.

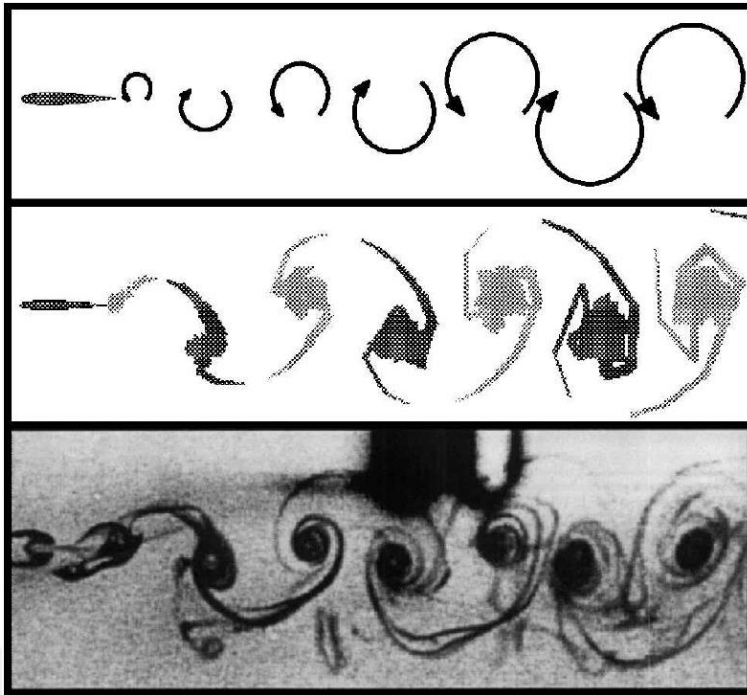


Figure 1.7 : Thrust producing wake (Jones et al., 1998).

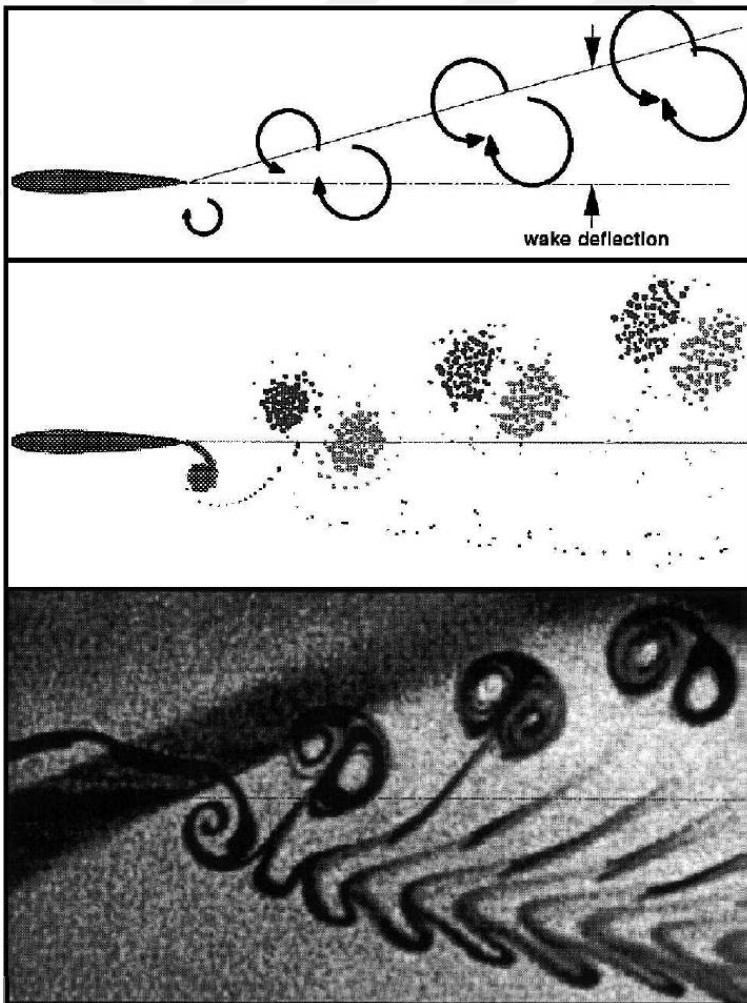


Figure 1.8 : Deflected wake (Jones et al., 1998).

Further increment in flapping frequency results in nonsymmetric deflected wake patterns for Strouhal numbers greater than 1.0, where both thrust and lift are being produced as shown in Figure 1.8. Flow structures in the wake of a sinusoidally plunging NACA 0012 airfoil is visualized in the study of Lai and Platzer (1999) for various amplitudes and frequencies. They found that the vortex patterns are changing from drag producing to thrust producing, when the ratio of maximum plunge velocity to freestream velocity (non-dimensional plunge velocity) exceeds 0.4. Furthermore, maximum mean streamwise velocity downstream of the plunging airfoil starts to exceed the freestream velocity, when the nondimensional plunge velocity is higher than 0.25.

The fundamental studies on natural flyers and swimmers and their relation to flapping wing aerodynamics were reported by Lighthill (1969), Ellington (1984), Ellington et al. (1996), Dickinson et al. (1999), Sane (2003), Sfakiotakis et al. (1999). Lighthill (1969) published a survey on different classes of aquatic animal's propulsion. Vortices cast off by the fish caudal fin trailing edge are presented in Figure 1.9 where a jet like streamline pattern is observed. They pointed out the analogy that the action of propulsive caudal fins of high aspect ratio can be analyzed by the same methods that have been used to analyze the flight of birds and insects.

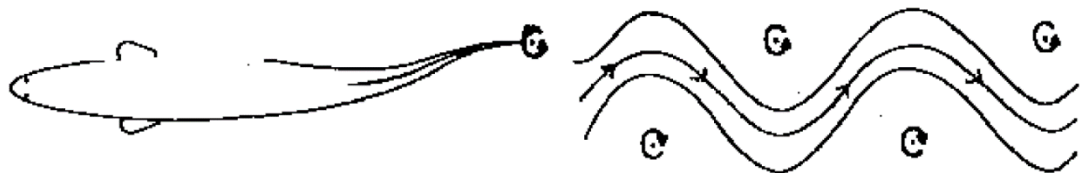


Figure 1.9 : Vortices in the wake of a fish (Lighthill, 1969).

An overview of the swimming mechanisms employed by fish is presented by Sfakiotakis et al. (1999) and specific swimming modes are identified based on the propulsor and the type of movements (oscillatory or undulatory) employed for thrust generation. It is noted that the aquatic animals are developed to perform different tasks like feeding, predator avoidance, energy conservation etc. and those tasks should be considered while mimicking them. The seahorse is given as an example, which has oscillating fins at a frequency around 40 Hz, higher than most of the other species utilizing fin undulations for propulsion (rarely exceeding 10 Hz). Around these oscillating frequencies, the swimming efficiency is noted as low. However, high fin beat frequency lies beyond the fusion frequency of the predators' eyes that makes the

seahorse indistinguishable from surrounding vegetation and gives them a chance to hide from potential predators. Therefore, when conceiving biomimetic designs, the significance of these nonlocomotor factors and the extent to which they have compromised performance should be considered.

Ellington (1984) examined the aerodynamics of hovering insect flight in a series of papers including quasi-steady analysis (Ellington, 1984), morphological parameters (Ellington, 1984b), kinematics (Ellington, 1984c), aerodynamic mechanisms (Ellington, 1984d), vortex theory (Ellington, 1984e) and lift and power requirements (Ellington, 1984f). He stated that the vast majority of insects hover with a horizontal stroke plane, and support their body mass with equal lift on the downstroke and upstroke and indicated that most of the hovering animals do not rely on quasi-steady aerodynamics, but use rotational lift mechanisms instead to operate. Airflow around the wings of hawkmoth *Manduca sexta* is visualized by Ellington et al. (1996) and an intense leading edge vortex is observed on the downstroke, which is sufficiently strong to explain the high lift forces. They noted that the vortex is created by dynamic stall not by rotational lift mechanisms as mentioned above. The vortex spirals towards the wingtip with a spanwise velocity in the order of the flapping velocity. In study of Dickinson et al. (1999) the enhanced aerodynamic performance of the insects are connected to three interactive mechanisms: delayed stall, rotational circulation and wake capture. Those translational and rotational mechanisms are explained for insect flight and a general theory is proposed to explain the force generating mechanisms of many species. The review of Sane (2003) also includes the basic physical principles underlying flapping flight in insects, experiments and different models to explain the phenomena.

Further works including modelling and numerical studies on flapping wings can be exemplified as DeLaurier (1993), Smith (1996), Vest and Katz (1996), Liu and Kawachi (1998), Tuncer and Platzer (2000).

Micro air vehicles are one of the main application areas of flapping wings. Ellington (1999) studied design characteristics of insect-based flying machines such as estimations of the supported mass, power requirements and maximum flight speeds. He stated that larger machines need less power to sustain the mass but small machines operating at higher frequencies will reach faster speeds. Jones and Platzer (2009) tried to use the flapping wing knowledge database to design and develop a micro air vehicle.

Their design resulted in a MAV that has a fixed wing for lift and two flapping wings for thrust generation. They argued that it would be quite difficult to use flapping wings to generate both lift and thrust and that is reflected in their designs. Willis et al. (2007) presented a computational framework to design and analyze flapping flight for MAVs and proposed methodology for computational savings and understanding the flapping flight design space. Main aerodynamic modelling approaches for MAVs are reviewed by Ansari et al. (2006) and unsteady aerodynamic model is found to be the most satisfactory method superior to steady state, quasi steady and semi empirical methods. Tarascio et al. (2005) conducted flow visualization experiments on insect-based flapping wings on MAV scale. Their images showed that the growth of the leading-edge vortex as a function of span and identified the presence of separated flow on the outboard regions of the wing. A collection of studies concerning the flapping wings and the MAVs can be found in Mueller (2001) and Floreano et al. (2010).

1.2.3 Flexible wings

Flexible flapping wings have drawn attention in recent years due to their possible high performance efficiencies compared to rigid ones. Since all natural flyers and swimmers have some degree of flexibility on their wings, it is important to understand the phenomena for a more effective aerial/nautical vehicle design. Birds for example have layers of feathers that are flexible and can slide over each other to maintain a smooth surface. On the other hand, bat wings consist of thin membrane surface, which passively adapt their shape to freestream conditions. Flow separation is prevented and lift to drag ratio is increased by the passive control of the wing surface. Insect wings also have a degree of flexibility both in spanwise and chordwise directions.

One of the early studies on oscillation of flexible airfoils is published by Katz and Weihs (1978). They found that the chordwise flexibility increase the propulsive efficiency up to 20% in expense of a small decrease of thrust. They also stated that as flexibility increased more, the efficiency gets even higher, but the thrust is reduced below practical levels.

A large number of recent studies, both experimental and numerical, have been focusing on the effects of flexibility to mimic the nature with the aim of not only producing energy from flapping but also increasing the efficiency of flapping using the storage and release of elastic energy appropriately. Combes and Daniel (2003a), Combes and

Daniel (2003b) investigated flexural stiffness of the insect wings. Their measurements indicate that spanwise flexural stiffness scales with cube of span length whereas chordwise flexural stiffness scales with square of the chord length. It is noted that spanwise flexural stiffness is 1-2 orders of magnitude larger than chordwise flexural stiffness. Combes and Daniel (2003b) stated that the insect wing deformations are largely passive and depends on the material properties and architecture of the wing. Flexural stiffness is found to be more close to the rigidity near the body while the edges are more flexible where the force production is sensitive to shape changes.

Flexible wings can be used for different designs and various demands. Membrane type fixed wings for example, can better adapt to the stall and has the potential for morphing to achieve enhanced agility and storage consideration compared to rigid fixed wings (Shyy et al., 2005) (Figure 1.10).

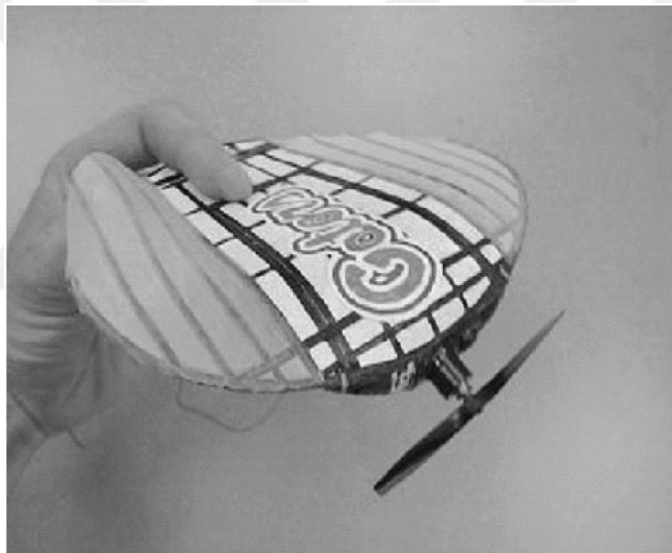


Figure 1.10 : MAV with membrane fixed wing (Ifju et al., 2002).

Control surfaces such as rudders, elevators, and ailerons can be manufactured from flexible materials. An example of such a morphing wing can be seen in Figure 1.11.

In the present thesis, wings will undergo flapping motions; therefore, detailed investigation is focused on flexible flapping wings. During the flapping motion, flexible wings deform due to forces acting on them. These forces could be aerodynamic or inertial-elastic forces. In what extent shape of the wing depends on these forces are investigated by Daniel and Combes (2002). They implied computational and analytic methods to compare the bending stresses arised from inertial-elastic mechanisms and fluid pressure forces. It is suggested that, fluid

pressure stresses play a relatively minor role in determining wing shape. It is later experimentally tested by the same authors (Combes and Daniel, 2003c) with fresh hawkmoth *Menduca sexta* wings attached to a motor. The wings are flapped at realistic wing beat frequencies and amplitudes in normal air and helium (%15 air density) medium. Experiments in lower density medium produced only slight changes in wing deformations and it is suggested that fluid dynamic forces have minimal effect on wing deformation.

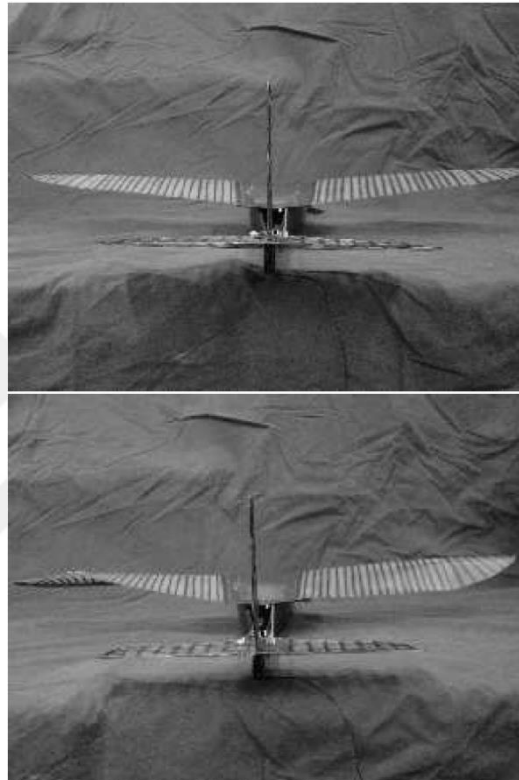


Figure 1.11 : Flexible wing application as a control surface for improved agility (Garcia et al., 2003).

Another experimental study on hawkmoth *Menduca sexta* wings are presented in Mountcastle and Daniel (2009) with special attention to the effect of wing compliance to induced flows. They found that flexible wings lead to high mean advective flows, beneficial to lift compared to rigid ones. Their results confirm that wing compliance plays critical role in production of flight forces.

Zhu (2007) employed a fluid–structure interaction model to numerically investigate the effect of structural deformation on the performance of the foil when it is immersed in two different density fluids. In a low-density fluid (e.g., air), where the deformation is determined mainly by the inertia of the foil, he found that the chordwise flexibility reduces both the thrust and the propulsion efficiency and the spanwise flexibility

increases the thrust without efficiency reduction. In a high-density fluid (e.g., water), where the fluid loading has a significant impact on deformation, he found that the chordwise flexibility increases the efficiency, however, spanwise flexibility reduces the performance of the foil by diminishing both the thrust and the efficiency. The performance augmentation in chordwise deformation is explained by two combined effects. One is the curvature-induced effect that an increment in hydrodynamic force component in thrust direction is observed as the foil bends. The other is the feathering effect that reduces the effective angle of attack, and therefore this results in low thrust but high efficiency.

Eberle et al. (2014) examined how the magnitude of tip displacement, coefficient of lift, and coefficient of thrust change for different actuation frequencies, phases of pitch-heave actuation, and wing stiffnesses via two-dimensional model that couples point vortex methods for fluid force computations with structural finite element methods to model the fluid–structure interaction of a wing in air. Their analysis shows that when the excitation frequency of an insect wing aligns with the resonant frequency of the elastic structure, then flight forces increase dramatically however, fluid loading is still relatively unimportant in resonant frequency regions. It is commented on different results observed for fins in water where the fluid forces are dominant that the ratio of fluid density to the wing density is three orders of magnitude greater in hydrodynamic cases. That causes the inertial effects dominate when the density of the solid is larger whereas the fluid forces dominate when the solid density is low. They showed that at the first and second structural resonant frequencies of the system the lift and thrust forces are maximized.

Hu et al. (2010) experimentally studied the performance of rigid and flexible wings in soaring and flapping flight. Their measurement results revealed that, the flexible membrane wings have better lift-to-drag ratio over the rigid wing for soaring flight, especially for high speed soaring flight or at relatively high angle of attack. The most flexible latex wing was found to have the best thrust generation performance for flapping flight. The less flexible nylon wing has the best overall aerodynamic performance for soaring flight, however it has the worst performance for flapping flight applications.

Wu et al. (2011) presented an experimental study on flexibility of flapping micro air vehicle's wing and thrust production with six different hummingbird-shaped

membrane wings. They showed that there is an effective frequency range in thrust production for different flexibilities. The more flexible wings are more effective at producing thrust at lower frequencies and as the flapping frequency increases, stiffer wings become superior when passive deformation is induced. Their deformation measurements contradicts with Combes and Daniel (2003) that wing deformations in vacuum and in air are substantially different showing that fluid structure interaction is significant and both aerodynamic and inertial effects are important.

Kang et al. (2011) numerically studied effect of chordwise, spanwise and isotropic flexibility on the force generation and propulsive efficiency of flapping wings. They obtained the maximum propulsive force when flapping near the resonance, whereas the optimal propulsive efficiency is reached when flapping at about 0.4 of the natural frequency.

Miao and Ho (2006) are numerically investigated the effect of chordwise flexure amplitude for flapping airfoil. When the flexure amplitude of the airfoil is less than 0.5 of the chord length, thrust-indicative wake structures are observed. At higher flexure amplitudes wake structure evolves into a drag-indicative form. Propulsive efficiency is optimized for flexure amplitude of 0.3 of the chord length with phase angle of 90° .

Vanella et al. (2009) numerically studied the influence of flexibility on the aerodynamic performance of a two dimensional hovering wing. They found that the best performance is achieved at a frequency ratio which is $1/3$ of the natural frequency. However it should be noted that driving frequencies near natural frequency were not examined in that study.

Heathcote et al. (2004) experimentally studied the thrust generation of rigid and flexible flapping airfoils at zero freestream velocity. PIV and force measurements are taken in a water tank for the wings having three different bending stiffness. Their results confirmed that the airfoil with intermediate stiffness has greatest thrust coefficient at high plunge frequencies. On the other hand, the least stiff airfoil can generate larger thrust at low frequencies. They suggested that there is an optimum airfoil stiffness for a given plunge frequency and amplitude.

Michelin and Smith (2009) investigated the flow around a two dimensional heaving flexible wing by using a reduced order model. The energy usage was increased with the introduction of flexibility, but the mean thrust gain is higher, resulting in a net

increase in the flapping efficiency with flexibility. They observed peaks in mean thrust, which correspond to maximum values in the trailing-edge amplitude. Maximum trailing edge amplitude is the result of the resonance between the forcing frequency of the heaving motion and the natural frequencies of the system.

Zhao et al. (2011) visualized the flow with 2D DPIV system and simultaneously measured the aerodynamic forces. They hypothesized that trailing edge flexion directly influences magnitude of LEV. The hypothesis was proposed by Zhao et al. (2010) and LEV and trailing edge shape can be seen in Figure 1.12. Another finding of Zhao et al. (2011) is that the LEV correlates well with the generated aerodynamic forces that is a good indicator of performance of the flapping wings during translational phase of flapping. That finding is also consistent with Ellington et al. (1996).

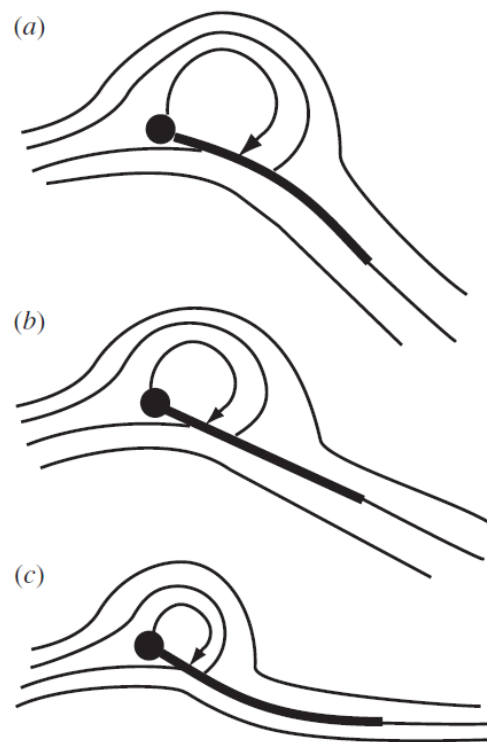


Figure 1.12 : LEV patterns in (a) positively cambered flexible wing, (b) rigid wing, (c) negatively cambered flexible wing (Zhao et al., 2010).

Fluid structure interaction simulations of unsteady viscous incompressible flows over an insect like flexible airfoil are carried out by Lee et al. (2011) to investigate the effects of wing flexibility under forward flight conditions. Linear and homogeneous type flexible airfoils are compared with the rigid airfoil and they found that the net lift is improved by about 13% in the homogeneous flexible airfoil, while the net thrust and

propulsive efficiency are enhanced by about 33% in the linear type flexible airfoil. Water tunnel experiments on chordwise flexible airfoils heaving with constant amplitude have been performed by Heathcote and Gursul (2007). In their high thrust cases the vortices are found to be stronger and farther apart in the cross-stream direction and time-averaged flow fields showed a stronger jet. Increment in the efficiency found around 15% for flexible wing compared to rigid one. Weaker leading edge vortices also observed in the cases of optimum efficiency. They made an analogy between heaving flexible foils and pitching and plunging rigid foils and found an efficiency peak at a pitch phase angle of 95-100 degrees and thrust peak at 110-120 degrees. Optimum efficiency is also observed in a Strouhal number of 0.29 within the observed range in nature of 0.2 - 0.4.

Paraz et al. (2016) studied the dynamic responses of a flexible foil heaving at its leading edge. They experimented on a forcing frequency range including the two first resonances of the foil+fluid system. They found that the forcing amplitude is an important parameter to predict the response. They proposed a model, and showed that the optimal propeller is achieved when the actuating frequency is set to a resonance of the system, and when the optimal forcing amplitude scales as the square root of the required thrust.

Park et al. (2016) performed experiments in zero freestream velocity for pitching panels with varying flexibility, planform shape and pitching frequency to explain the half- π phase delay condition (Park et al., 2012) which states $\pi/2$ phase lag between bending angle and pitching angle generates maximum thrust. They indicate that the wing has maximum camber when its angular velocity is maximum at $\pi/2$ delay and the region of strong streamwise momentum becomes wider along the streamwise direction. However, streamwise momentum is reduced significantly as the panel becomes stiffer (phase delay decreases). Furthermore, over-compliance (phase delay larger than $\pi/2$) weakens the TEV and the thrust generation, due to the increased energy waste in a fluid–structure interaction during the stroke reversal. They finally suggest that the delay mechanism may be different under freestream conditions where interaction between LEV is also crucial.

The review paper of Gursul et al. (2014) on the control of low Reynolds number flows by means of fluid-structure interactions gives an overall coverage of studies and findings focusing on lift and thrust enhancement of flexible wings. Prempraneerach et

al. (2003) also experimentally showed that chordwise flexibility can increase the propulsive efficiency up to 36% compared to rigid foils undergoing plunging and pitching motion. Timing of shed vortices is also an important issue affecting the performance of the flapping wing. Monnier et al. (2015) investigated harmonically pitching airfoils with a flexible tail and focused on circulation, the streamwise and cross-stream spacing of the vortices and the vortex core radius. They found out that flexibility has an effect of switching the wake vortex pattern to reverse von Karman street. Ramananarivo et al. (2011) suggest that the optimum performance is related to the temporal evolution of the wing shape rather than the resonance of the wing. Phase lag between the leading and trailing edges of the flapping wing up to some level is found to be useful for exploiting the elastic energy. A detailed review on the relation between performance and lower, near, and upper natural frequencies is given in Shyy et al. (2013).

Recently, Kancharala and Philen (2016) investigated the chordwise flexible fins with varying stiffness. First, they predicted the optimal chordwise stiffness profiles theoretically and then robotic fins are fabricated based on these stiffness profiles. They observed that the varying stiffness fins produce larger thrusts and efficiencies compared to constant stiffness fins due to their larger curvatures and trailing edge deflections that redirect the forces acting on the fin towards the swimming direction, thus increasing thrust.

Quinn et al. (2015) experimentally studied the efficiency optimization of heaving and pitching panels via direct force measurements and PIV. They stated that the optimum efficiency is achieved when the following criterias are met: Strouhal number between 0.40 and 0.53 for heave only and 0.26 and 0.33 for combined pitch and heave. The panel is flapped at a resonant frequency of the fluid panel system. Heaving amplitude is as high as possible while the flow along the body remains attached. High values of amplitude also reduces the contribution of the viscous drag. Phase lag between pitch and heave is 90° which also minimizes the effective angle of attack; reducing separation at leading edge. They also found out that optimized pitch and heave cases can produce up to double efficiency values of heave only cases.

Richards and Oshkai (2015) conducted an experimental study to investigate the effects of inertia, stiffness and oscillation kinematics on the thrust generation and efficiency of an oscillating foil. They achieved high efficiency in a band of frequency ratios 0.7-

0.9. Heavier and stiffer foils produce high thrust if they have the same resonant frequency. Frequency ratio providing the peak efficiency shifts to lower values when the heave amplitude increased. Pitch-heave combination is shown to increase efficiency at the expense of lower thrust.

Few studies are found in the literature concerning the phase relations between the motion and the generated forces, which is one of the concentrated topics of the thesis. Moryossef and Levy (2004) conducted numerical simulations to study oscillating airfoils in close proximity to the ground. They observed that in contrast to the classical case of oscillating airfoils in freestream where the reduced frequency approaches zero ($k=0$), the phase lag approaches 90° , oscillating in ground effect conditions which suggest that as the k approaches zero, the phase lag also approaches to zero with inviscid flow concept. Molina and Zhang (2011) also numerically investigated a heaving airfoil in ground effect. They classified three different features based on the phase lag between aerodynamic coefficients and the airfoil motion: ground effect, incidence effect caused by the effective angle of attack, and added mass effect related to the acceleration of the airfoil which is important at higher frequencies and can be accounted as an inviscid condition.

Rival et al. (2009) observed phase lags on lift variation as high as 90° in a fully stalled flow in which the history effects (boundary-layer separation and reattachment) from the previous cycles are also effective. They stated that with the attached flow assumption, Theodorsen's circulatory approach is not suitable for estimation of lift variation on fully stalled conditions. On the other hand, Ol et al. (2009) studied experimentally, computationally, and theoretically, shallow and deep dynamic stall conditions for flapping airfoils. Theodorsen's formula is found useful to capture general trends in lift coefficient even for the deep-stall cases. They observed that the lift response is more quasi-steady than the flow field response and flow separation does not have a dominant effect on the integrated lift.

The importance of the phase between the motion and the force becomes more crucial when the flapping foils are flexible. In chordwise flexible wings, e.g., the work of Son and Cetiner (2016), trailing edge motion will also have a lag with respect to the leading edge, and that will affect the force timing entirely. The phase can be treated as how and when the motion is "felt" by the flapping animal. From the control point of view, the feedback and response to the changes during flight, e.g., gust encounter or

environmental changes that require rapid maneuvering can be designed more accurately if we have a better knowledge about phase variations. A basic understanding should be developed on rigid wings' motion–force relations to approach those more complex physical problems. In this perspective, experiments are performed on a purely plunging plate that is fully submerged in the water channel and then the study extended to flexible flapping wings.

1.3 Definition of Major Parameters

Motion of the wing is considered as a pure plunging harmonic motion with the following equation:

$$h(t) = a \cos(2\pi ft) \quad (1.1)$$

Where $h(t)$ is the plunge position of the wing as a function of time, a is the plunge amplitude and f is the plunge frequency. In early stages of the thesis, the motion is considered as a sine function, however when the function is sine, the velocity is maximum at $t=0$ which causes the rapid acceleration of the wing, and eventually bias errors on the force measurements. Therefore, cosine function is selected where the initial velocity is zero on a given plunge amplitude.

Reduced frequency is defined as;

$$k = \frac{\pi f c}{U} \quad (1.2)$$

Where f is plunging frequency, c is the chord length, and U is the freestream velocity. Plunge amplitude is non-dimensionalized by the chord length (a/c) in most of the graphs.

Strouhal number is presented based on flapping frequency and amplitude:

$$St = \frac{2f a_{amp}}{U} \quad (1.3)$$

Reynolds number is defined as;

$$Re = \frac{\rho U c}{\mu} \quad (1.4)$$

Where the ρ is density of the fluid, μ is the dynamic viscosity. In the present thesis the Reynolds number is constant at 10000, which is in the range of the operation Reynolds number of MAVs 10^4 — 10^5 (Shyy et al., 2013).

Force coefficients are calculated based on the formulas given in Heathcote and Gursul (2007). Time averaged thrust coefficient C_T is calculated as:

$$C_T = \frac{T}{\frac{1}{2}\rho U^2 c} \quad (1.5)$$

Where T is time averaged thrust per unit span, U is freestream velocity and c is the chord length. Time averaged power input coefficient C_P is calculated from the formula:

$$C_P = \frac{\overline{F_y v}}{\frac{1}{2}\rho U^3 c} \quad (1.6)$$

F_y is the measured force in motion direction, v is the velocity of the leading edge of the wing given by the servo motor system. Efficiency (η) is determined by taking into account the thrust and the power input coefficients:

$$\eta = \frac{C_T}{C_P} \quad (1.7)$$

1.4 Outline of the Thesis

In Chapter 1, general introduction to the flapping wing is presented with the historic background. Different projects composing the thesis are mentioned and detailed literature review is given under subdivisions of perching, plunging and flexible wings. Major parameters are defined and an outline of the dissertation is introduced.

In Chapter 2, experimental setup including flow system, motion system, force measurements and PIV measurements are explained. Model manufacturing is given in detail.

In Chapter 3, results of the performed experiments are presented starting with the rigid wings. Force and PIV measurements results for different motion types are given and the effect of introducing various degrees of flexibility is investigated.

Finally in Chapter 4, major contributions and findings along with recommendations for further studies are provided.



2. EXPERIMENTAL SETUP

2.1 Flow System

The experiments are performed in the close-circuit, free-surface, large-scale water channel located in the Trisonic Laboratories at the Faculty of Aeronautics and Astronautics of Istanbul Technical University (Istanbul, Turkey). The cross-sectional dimensions of the main test section is 1010×790 mm. Test section is produced of plexiglass which allows optical access from two side and bottom walls. Water is filled in the channel from the tap water after a filtering process. A centrifugal pump recirculates water in the channel through settling chamber, a set of honeycombs and screens to reduce the turbulence, contraction section to accelerate the flow, test section where the experiments are performed, and finally downstream reservoir where water is sent back to settling chamber via a pipe system. An image of the water channel can be seen in Figure 2.1.



Figure 2.1 : Water Channel at Trisonic Laboratory.

The water channel is a replica of the one in Fluid Mechanics Laboratories of Lehigh University, which has a 4.5 m test section that is increased to 6 m in our system. Honeycomb and screen locations, numbers and sizes are determined according to the Reshotko et al. (1997) to reduce the turbulence level of the flow. Turbulence intensity of the channel is below 1% and anticipated to be about 0.2%. The coefficient of variation equivalent to turbulence intensity is measured to be 0.029 for $U_{\infty}=0.0058$ m/s (Aydin et al., 2010). Flow velocity is controlled by the ABB AC drive (ABB-ACS800-01) adjusting the rpm of the centrifugal pump. Calibration of the velocities are performed on a non-flowing water height of 713 mm. Reynolds Number is constant in the present study, therefore, the velocity of the water channel is fixed to 0.1 m/s at 1080 rpm.

2.2 Motion System

Two distinct motions are executed in the experiments as mentioned in the introduction section. Perching or pitch-up is one of these motions and based on sudden change in angle of attack and halting the wing at a constant degree of angle. The pitch-up motions of the airfoil were accomplished using a Kollmorgen/Danaher Motion AKM33E servo motor with an accuracy of 0.15° . The models were subjected to performing two types of motion: fast and slow. The model started from 0° and attained its final angle of attack of 45° in 1 second for the fast motion and in 6 seconds for the slow motion, corresponding to 1 and 6 convective times, respectively (Figure 2.2). The motor motion profiles were generated by a signal generator Labview VI (Virtual Instrument) for the given amplitude and duration. The servo motors are connected to computer via ServoSTAR S300 servo driver. Generated position signal is transmitted to servo driver's control unit and transformed into velocity signal. The following error between the position command and the actual motion is less than 1° for pitch motions.

Labview VI also triggers both the force data acquisition and the PIV system. The force measurement started 5 seconds prior to the beginning of the pitch motion; the synchronization with the PIV system was achieved using a National Instruments PCI-6601 timer device.

The other motion is the purely plunging motion that is generated by harmonic cosine position function (Figure 2.3). In preliminary experiments a sine function was executed as position signal, however, at $t=0$ the wing has maximum velocity on a sine

function that causes rapid acceleration and following errors at the motion start-up. Therefore, cosine function is preferred on subsequent experiments, in which the velocity is zero at the beginning of motion. It is observed that the force bias errors are reduced by choosing a cosine function.

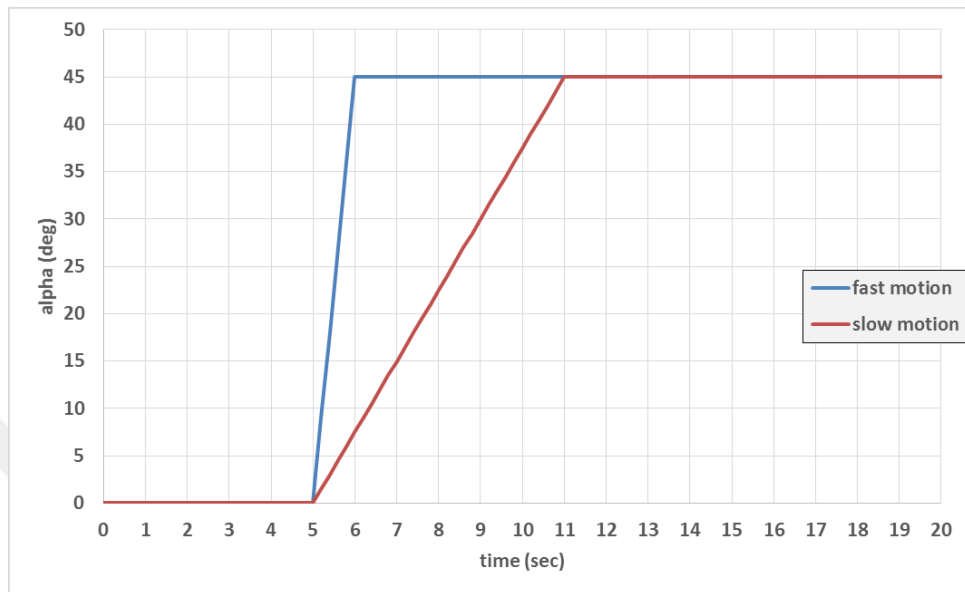


Figure 2.2 : Position signal for the fast and the slow pitch-up motions.

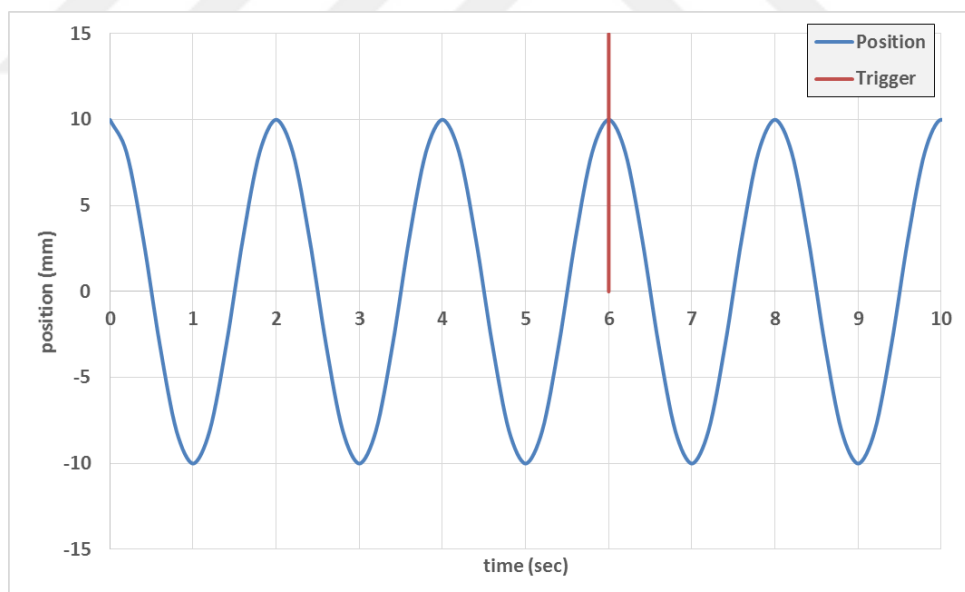


Figure 2.3 : Position and trigger signal for plunging motion ($a=10$ mm, $f=0.5$ Hz).

Plunge motion of the model is accomplished with Kollmorgen/Danaher Motion AKM54K servo motor, which was connected to a computer via ServoSTAR S700 digital servo amplifier. The accuracy of the plunge motion is 0.0104 mm. The motor motion profiles were generated by a signal generator Labview VI for the given amplitude and frequency. The following error between the position command and the

actual motion is less than 1 mm for plunge motions. Labview VI also triggers both the force data acquisition and the PIV system. The force and PIV measurements are started at the 3rd period of the motion and the synchronization was achieved using a National Instruments PCI-6601 timer device.

2.3 Models

The experiments are performed on four different wing materials: a rigid wing produced of plexiglass, three flexible wings produced of homogeneous polycarbonate sheet (lexan), an acetate wing, and an elastic model produced in 3D Printer. The rigid wing has a thickness of 5 mm, chord length of 100 mm and transparent to illuminate both sides of the wing. Flexible wings have 10 mm metal part on leading edge to avoid spanwise flexibility and the total chord length is 100 mm (Figure 2.4). The wing's rotation axis is leading edge, which also coincides with the center of the force sensor.



Figure 2.4 : Flexible wing mounting.

Natural frequencies of the manufactured wings are one of the backbone parameters of the thesis. Motion parameters are determined based on these natural frequencies. It should be noted that the natural frequencies mentioned in the thesis are first mode of natural frequencies that are also equal to the resonant frequency of the wings. The wings are exposed to sudden loading and given free chordwise oscillation to determine their natural frequencies while the wing is in its position, fully submerged in the water channel. Then, force and moment data are recorded until the oscillation is totally damped (Figure 2.5).

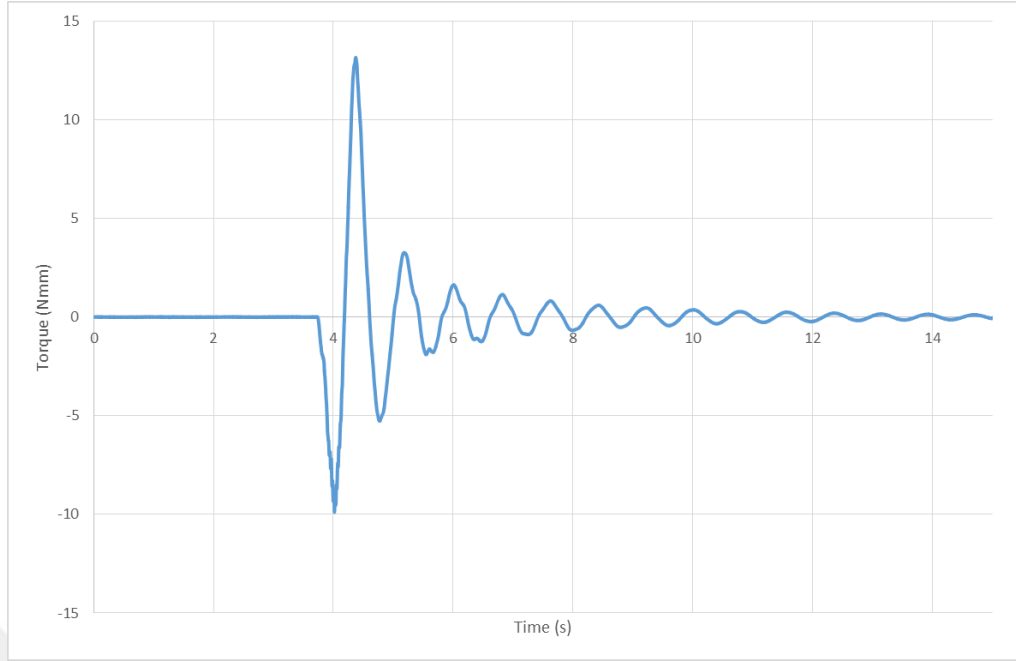


Figure 2.5 : Free oscillation and damping of the 3D Printed wing.

Logarithmic decrement and damping ratio are used to estimate the natural frequency from the recorded force-torque data. Logarithmic decrement can be expressed as:

$$\delta = \frac{1}{n} \ln \frac{x(t)}{x(t + nT)} \quad (2.1)$$

Where $x(t)$ is the amplitude at time instant t and $x(t + nT)$ is the amplitude of the peak n periods away. Damping ratio is expressed as:

$$\zeta = \frac{1}{\sqrt{1 + \left(\frac{2\pi}{\delta}\right)^2}} \quad (2.2)$$

Damped natural frequency ω_d and natural frequency ω_n determined as;

$$\omega_d = \frac{2\pi}{T} \quad (2.3)$$

$$\omega_n = \frac{\omega_d}{\sqrt{1 - \zeta^2}} \quad (2.4)$$

Five successive peaks are selected on the free oscillation graph and the experiment is repeated five times. Implying this method, natural frequencies are determined as 7.40 Hz, 2.32 Hz, 1.25 Hz, 0.51 Hz for rigid, lexan, printed and acetate wings respectively as presented in Table 2.1, along with the thicknesses measured by a caliper and flexural stiffnesses determined by the weight deflection method explained later in detail.

Table 2.1 : Wing material properties.

Material	Thickness (mm)	Natural frequency in water (Hz)	Flexural stiffness (EI)
Rigid	5	7.40	-
Lexan	0.76	2.32	150×10^{-4}
Printed	0.60	1.25	61.12×10^{-4}
Acetate	0.15	0.51	3.21×10^{-4}

2.3.1 3D printed model

A new wing is produced on the 3D Ultimaker Printer with a polymer based material (colorfabb_xt transparent) (Figure 2.6). Layer thickness, plate and nozzle temperatures and print speed are main parameters on the 3D printer to produce the wing model. These parameters are decided after several tryouts on small scale models. Final parameters were; layer height: 0.1 mm (6 layers total), plate temperature: 75° C, nozzle temperature: 260° C, print speed: 60 mm/s. Glue stick is applied on the glass plate surface for easy removal of the model after production and to stick the model on the surface during the production process.

The production of a new wing model enabled us to adjust the required natural frequencies. It is seen that a natural frequency between 0.51 Hz - 2.32 Hz is required for further examination. New 3D printed wing model's natural frequency in water is measured as 1.25 Hz, which is nearly in the middle of our frequency range.

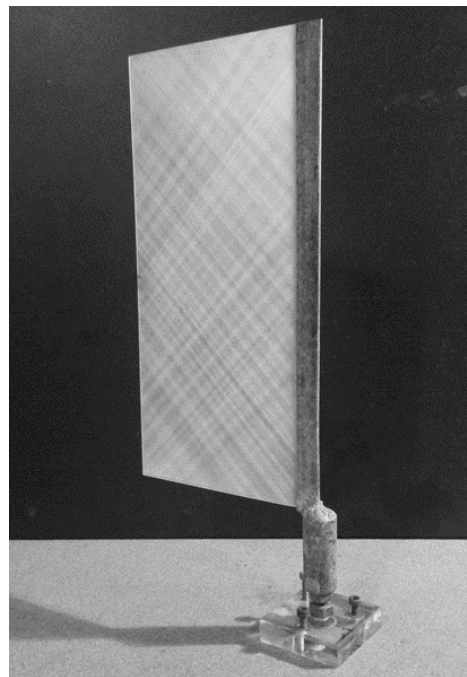


Figure 2.6 : 3D Printed model.

2.3.2 Material properties determination

Material properties are required to provide the input for numerical studies and further experimental studies for consistency. Young modulus or elastic modulus (E), second moment of area (I), density of material (ρ_{wing}) are some basic material properties of the wing model. In the present study, natural frequency (f_n) is also accounted as a material property and determined in water medium.

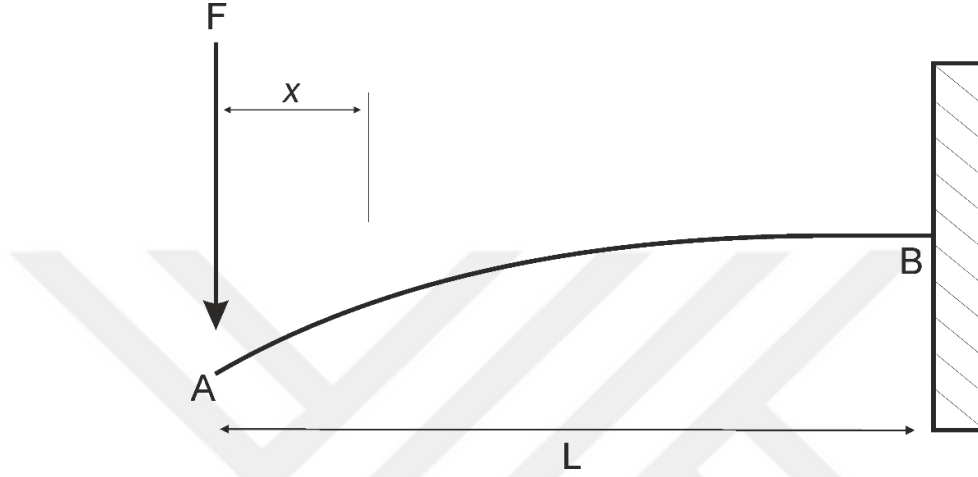


Figure 2.7 : Deflection of the beam.

The point load at the end of the beam and the deflection can be seen in Figure 2.7. Deflection at x can be defined as (Gordon, 1978);

$$y = \frac{1}{6} \frac{F}{EI} (x^3 - 3L^2x + 2L^3) \quad (2.5)$$

Maximum deflection will be at point A, where $x=0$;

$$y_{max} = \frac{1}{3} \frac{FL^3}{EI} \quad (2.6)$$

Flexural stiffness or flexural rigidity (EI) than can be defined as;

$$EI = \frac{1}{3} \frac{FL^3}{y_{max}} \quad (2.7)$$

The formula above enables to determine the flexural stiffness (EI) experimentally by applying forces to the wing trailing edge and measuring the displacements. A simple experimental procedure is followed to have the relation between load and the deformation therefore the EI . The wing is attached and known masses are placed to the trailing edge of the wing as in Figure 2.8.

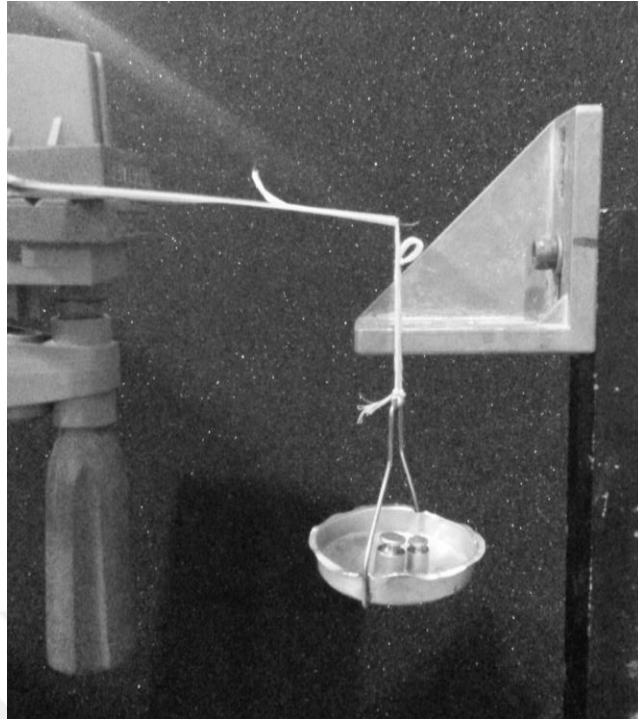


Figure 2.8 : Wing and the mass attached to trailing edge.

Deflection of the wing is measured by a caliper and applied force vs displacement graph is plotted in Figure 2.9.

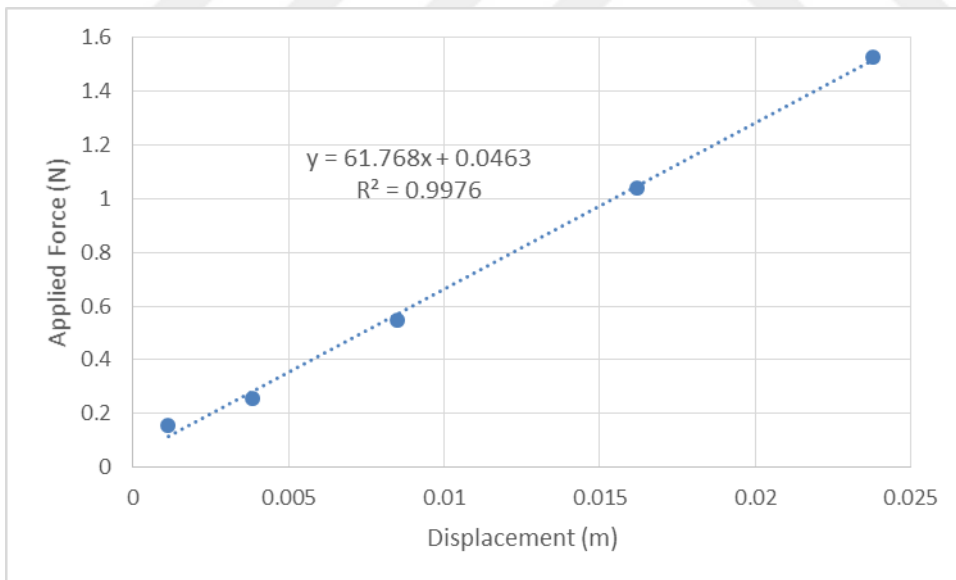


Figure 2.9 : Displacement vs applied force for the lexan wing.

F/y_{max} can be determined from the slope of the trendline and replaced into the above formula which finally lets us to calculate EI . For the lexan plate, EI is determined as $150 \times 10^{-4} \text{ Nm}^2$. If the Young modulus (E) of the material is known, then flexural stiffness EI can directly be calculated multiplying Young modulus (E) with second moment of area (I). For our wing types, I is depend on span (s) and thickness (b);

$$I = \frac{sb^3}{12} \quad (2.8)$$

The lexan wing has a span $s=20$ mm, thickness $b=0.75$ mm and Young modulus is given by the lexan manufacturer company as $E=2300$ MPa which gives us the $EI=161.72 \times 10^{-4}$ Nm². As it can be seen from the results, experimental weight method also works well to determine the flexural stiffness of the wing. If the young modulus is not given or cannot be known after production of the 3D wing model, weight experiment makes a good approximation. Therefore, this method is applied to 3D printed model and applied force vs displacement graph is presented in Figure 2.10.

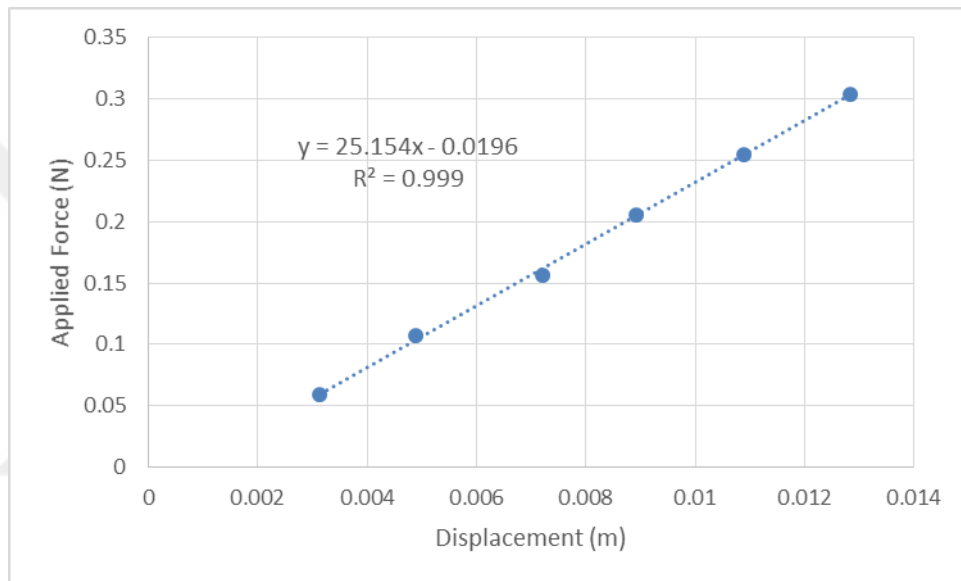


Figure 2.10 : Displacement vs applied force for 3D printed wing.

EI of the 3D printed wing is determined as $EI=61.12 \times 10^{-4}$ Nm² from the information gained from Figure 2.10. Same method is applied to the acetate wing and the EI of the acetate wing is determined as $EI=3.21 \times 10^{-4}$ Nm².

2.4 Force Measurements

Force data is collected by a six-component ATI NANO-17 IP68 Force/Torque (F/T) sensor (ATI Industrial Automation, Inc., NC, USA) as shown in Figure 2.11. The sensor was mounted on the rod between the model and the plunge servomotor, oriented with its cylindrical z-axis coinciding with the leading edge of the wings. The sensor is submersible up to 4 m and suitable for underwater applications. Different calibrations, therefore different measurement ranges can be obtained for a single sensor. SI-25-0.25 calibration is selected, which has the following specifications presented in Table 2.2.

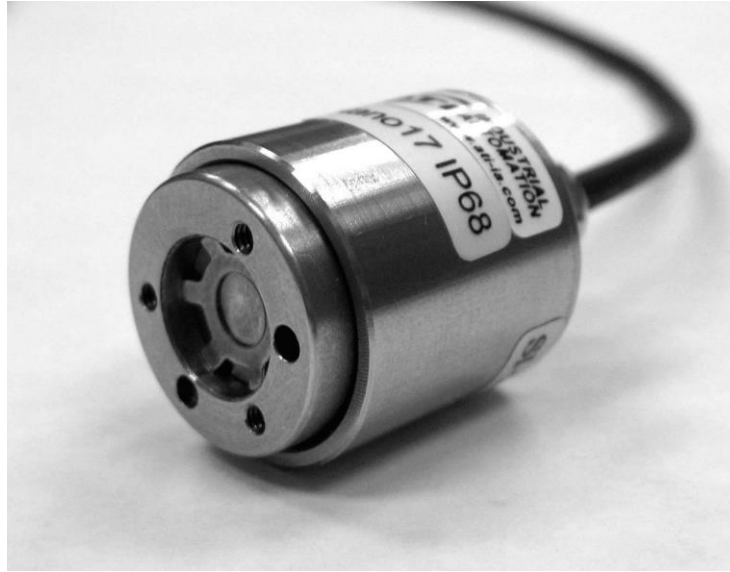


Figure 2.11 : ATI NANO-17 IP68 Force/Torque (F/T) sensor.

For the plunge motion, data is collected at 1000 Hz starting by a trigger signal sent after the 3rd period of motion. 50 periods of plunge motion force data is collected for each case. The data is then averaged to obtain thrust and drag values and filtered by an ideal low pass filter that eliminates the fluctuations four times higher than the driving frequencies and above to represent variations in one period.

Table 2.2 : Sensor ranges and resolution.

Sensing Ranges				Resolution			
F_x, F_y	F_z	T_x, T_y	T_z	F_x, F_y	F_z	T_x, T_y	T_z
25 N	35 N	250 Nmm	250 Nmm	1/160 N	1/160 N	1/32 Nmm	1/32 Nmm

For the impulsive pitch-up motion, force data is collected at 1000 Hz. The data were averaged over five runs and then filtered with a 5-Hz low-pass filter to avoid the natural frequency effects of the system.

2.5 DPIV Measurements and Post Processing

Quantitative flow field information is gained by Digital Particle Image Velocimetry (DPIV) system. DPIV is a non-intrusive, optical flow measurement technique that provides flow field data on the illuminated section of the flow. Vector fields are obtained by the correlation between two images in which the particles are travelled during two light pulses. A schematic of a PIV system is presented in Figure 2.12.

Water is seeded with 10 μ m silver coated hollow glass spheres and water channel is run at high rpm to ensure that the particles are distributed homogeneously in the channel.

Particles' density are about 1.1g/cm^3 that is close to the water density, ensuring the particles to follow the fluid motion without sinking or floating on the surface.

Seeded flow is illuminated by a dual cavity New Wave Solo-PIV Nd:Yag laser which has a maximum energy output of 120 mJ per pulse at 532 nm wavelength with pulse duration of 3-5 ns. Time between the pulses of two laser cavities is set to $2000\mu\text{s}$ and since our freestream velocity is fixed, same value is used for all experiments.

The images are acquired by two 10-bit Dantec Dynamics FlowSense 2M CCD cameras with Nikkor 60mm/f 2.8D lenses, which are positioned beneath the water channel on a tandem arrangement that allows to visualize more distance on the flapping wing's wake. The image acquisition frequency is adjusted so that one period of flapping motion is represented by 8 images which are acquired throughout 25 periods for the plunging motion cases.

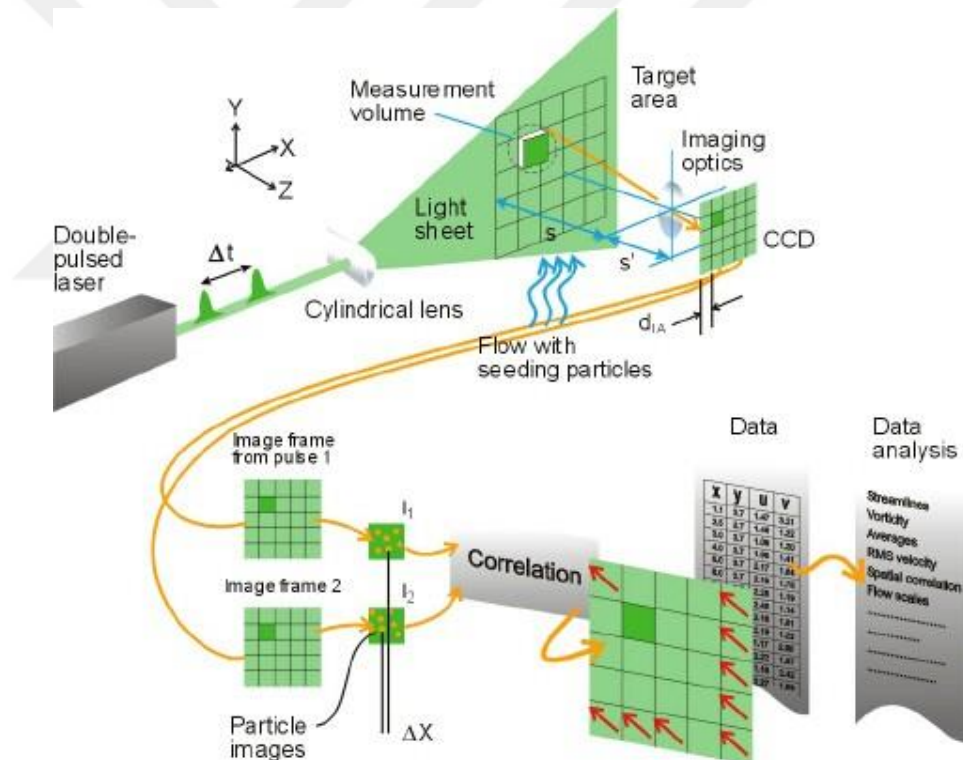


Figure 2.12 : PIV system overview (Url-2).

Two images are stitched before correlation by an in-house script on MATLAB (The MathWorks Inc., 1984) link of Dynamic Studio software. The script takes coordinates of two identical points on two cameras and the scale factor of those images as input variables and stitches the images using this information. Stitched images are interrogated using an average correlation with a window size of 32×32 pixels for 25

images in plunging motion. The final grid resolution of velocity vectors is $1.75 \text{ mm} \times 1.75 \text{ mm}$ and measurement plane is represented by approximately 14,250 velocity vectors. For the ramp type motion, double frame, cross-correlation technique is applied to interrogate the stitched DPIV images with a 64×64 pixels window size and 50% overlapping in each direction. The resulting measurement plane was represented by approximately 3,240 velocity vectors with a spatial resolution of $3.5 \times 3.5 \text{ mm}$.

After interrogation, the data is exported from Dynamic Studio and further post processing steps are employed on MATLAB environment. Masking, bad vector removing, filtering and vorticity field calculations are performed sequentially. Vorticity contours and other flow field information are plotted on Tecplot software (Amtec Engineering Inc.).

Error analysis in PIV imaging is performed according to Adrian (1991) and Raffel et al. (2007). The random measurement uncertainty remains below 2% in total, including uncertainty due to particle slip, uncertainty of magnification, and uncertainty in locating the particle centroid.

3. RESULTS

Results section is divided into four main subtitles: Perching motion of the rigid wings, perching motion of the flexible wings, plunging motion of the rigid wings, and plunging motion of the flexible wings.

3.1 Perching of a Rigid Wing

Perching, as described in the introduction section, is a sudden pitch up motion in which the wing has a final angle of attack and the motion is not harmonic. Two motion types are investigated in Son and Cetiner (2017): duration of the motion is 1 second (fast) and duration of the motion is 6 seconds (slow), corresponding to 1 and 6 convective times respectively, where convective time is defined as chords traveled by freestream ($t^*=tU/c$). Since all experiments are performed in a constant freestream of $U=0.1$ m/s and a chord length of $c=0.1$ m, convective times are equal to actual times. In this study, actual times are preferred.

3.1.1 Effect of aspect ratio

A series of experiments was performed for AR variation using either an endplate to represent the symmetry plane or submerging the wing deep in water (Figure 3.1).

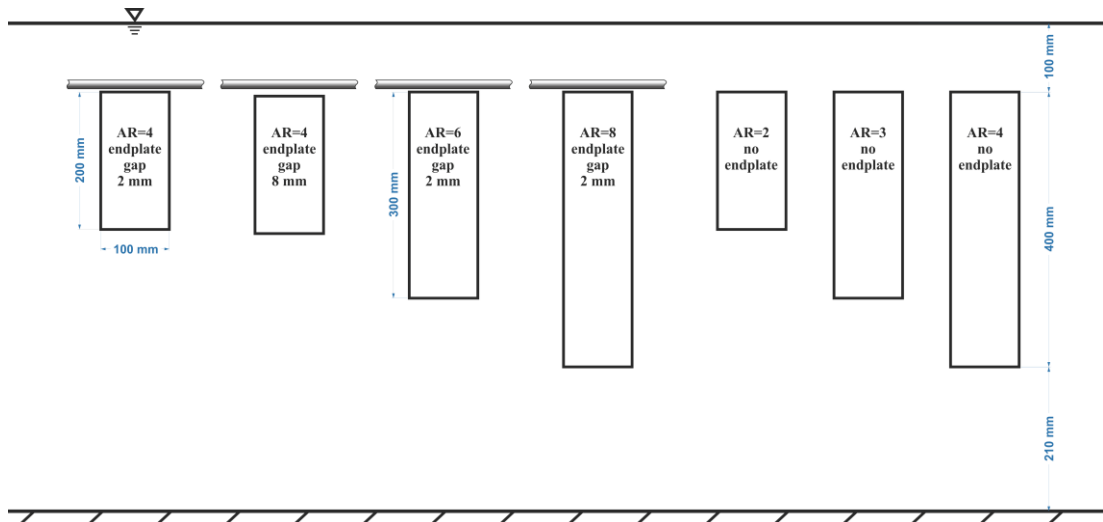


Figure 3.1 : Different aspect ratio wings.

The chord length of the models was $c=10$ cm, and models had a span of $s=20, 30$ or 40 cm to obtain different ARs. Intentionally, the gap between the root of the wing and the endplate was increased to 8 mm instead of 2 mm to determine the three-dimensionality at the wing root and its consequences on the force variations.

3.1.1.1 Force measurement results

Force-time histories for lift and drag are given in Figure 3.2 and Figure 3.3 for fast and slow motions, respectively. The observations are as follows:

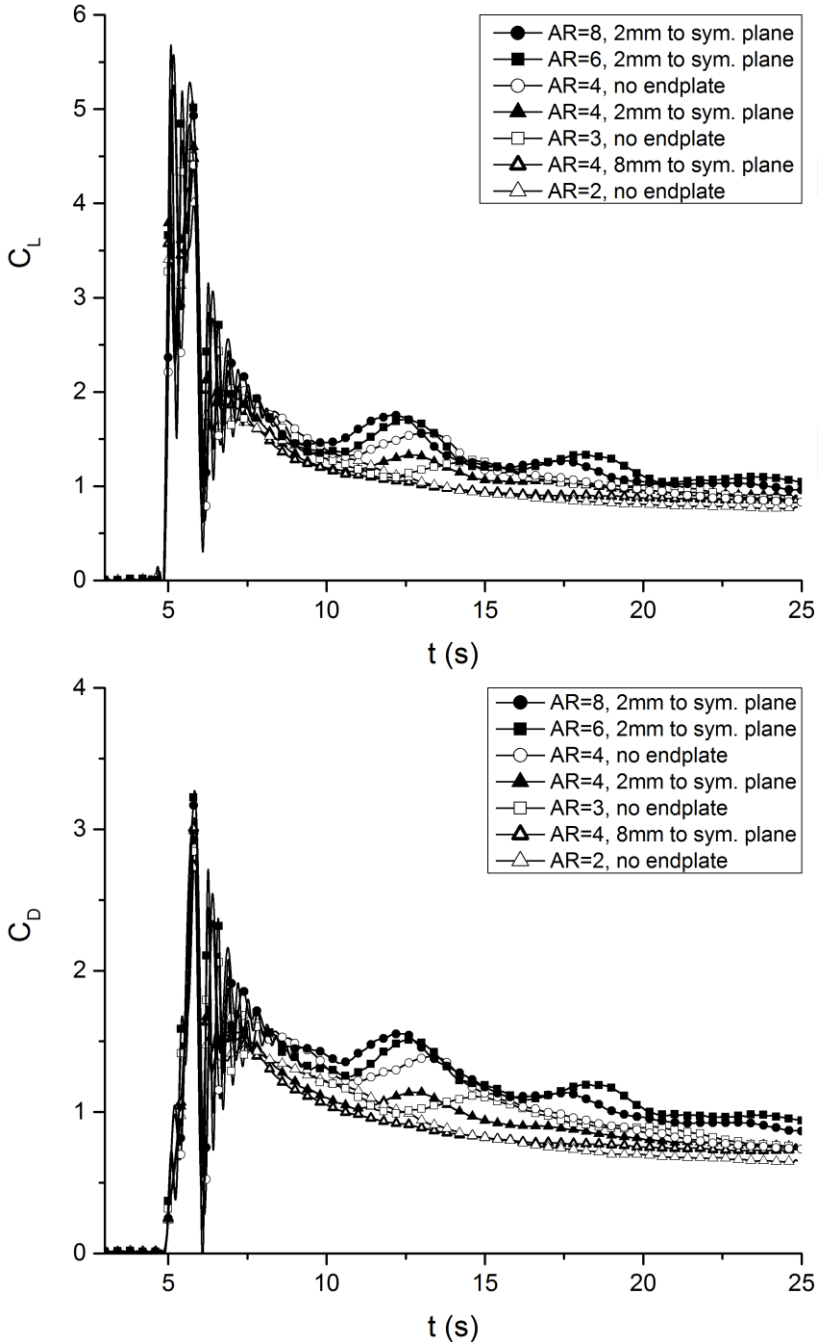


Figure 3.2 : C_L and C_D variation as a function of time in fast motion.

When there was a large gap between the endplate representing the symmetry plane and the root of the wing, the force time histories during the pitch-up and long time later are identical to those of the case with small gap. This does not depend on neither the force in consideration, lift or drag, nor the motion speed, slow or fast. However, when there is a small gap between the root and the symmetry plane, for plates of $AR > 2$, there is a secondary maximum in the force variations after the motion ceases. This local increase and decrease, which will hereafter be named shortly as "bump" is related to the consecutive shedding of LEV and TEV as will be shown with DPIV results.

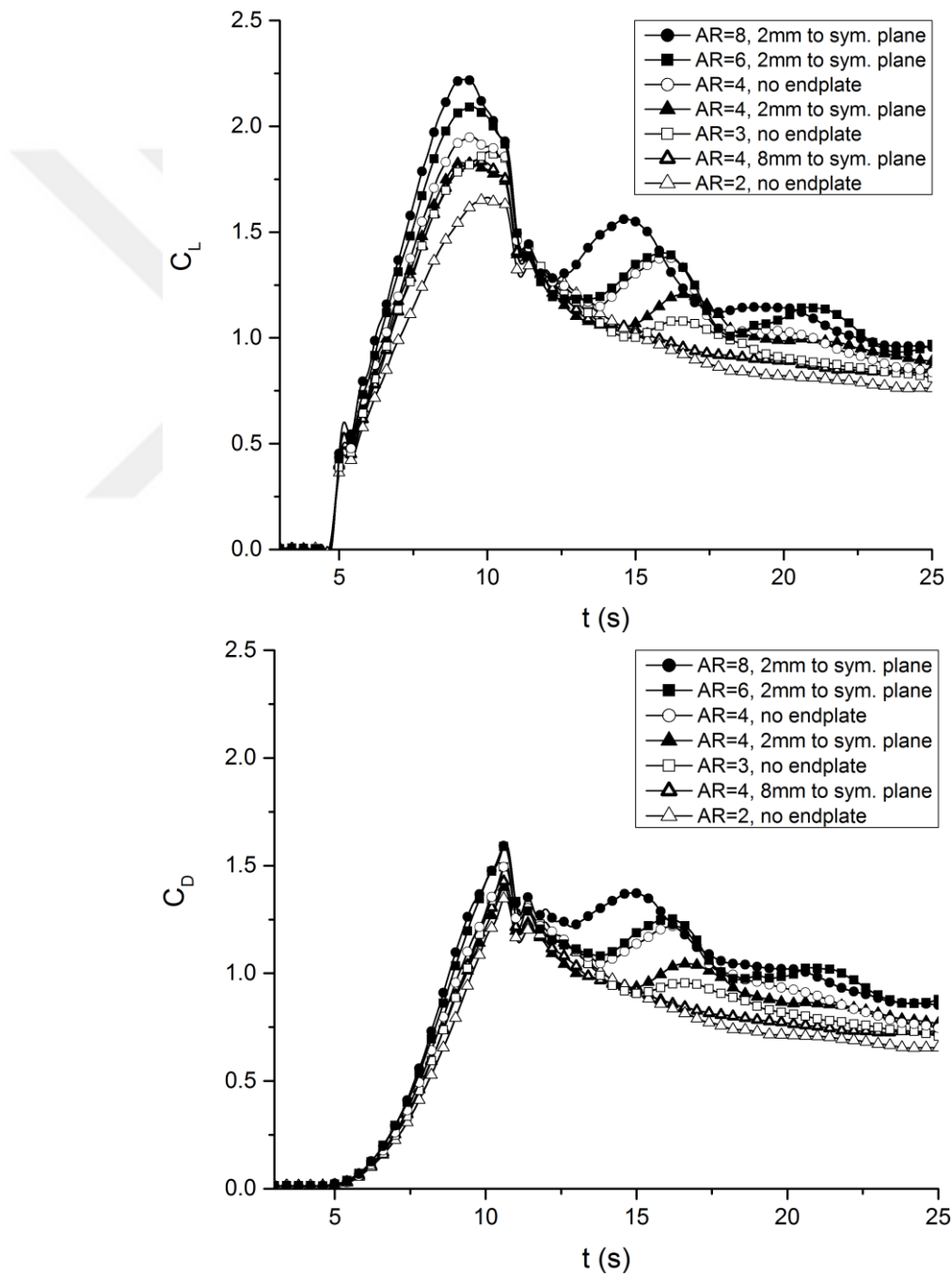


Figure 3.3 : C_L and C_D variation as a function of time in slow motion.

When there is a large gap between the root and the symmetry plane, the plate of $AR=4$ does not exhibit a bump in the force traces similar to its counterpart without the symmetry plane which has an AR of 2. Therefore, when the gap between the wing root and the endplate is 8 mm instead of 2 mm, the endplate no longer represents the symmetry plane and the wing behaves as if its effective AR is equal to its geometric AR .

Considering that the span of the plates is different for the same AR if a symmetry plane is used or not, differences in force variations are not pronounced during the motion, irrespective of the pitch-up speed. On the other hand, the bump in the force-time histories is larger for cases in which the geometric and effective AR s are the same (cases of no symmetry plane). When a symmetry plane is not used, on both force-time histories, the occurrence of the bump is slightly later in time for fast pitch-up and distinctively earlier in time for slow pitch-up.

When the AR is increased to 6 or higher, a second bump and even a third bump are evident in the force-time histories. As the AR increases, the bump occurs at an earlier time with a larger peak value. The increase in the peak value of the force coefficients during the motion is only evident in the slow pitch-up lift traces.

3.1.1.2 DPIV results

Apparently, all of the observations are related to the three-dimensionality of the flow, which will also be revealed within the differences in flow structures (Son and Cetiner, 2015). Vorticity contours and streamlines are shown in Figure 3.4.a for the wing with $AR=4$ (with end-plate/symmetry plane; the gap is 2 mm) in fast pitch-up at some critical instances selected from the force coefficient variations. The cross-section at which the DPIV images were taken was at half of the geometric span. Comparison between same spanwise locations in terms of the effective span is intentionally not preferred because the effective midplane is the root-plane for cases with the endplate. Also the aim, besides studying the use of an endplate with the proper gap, is to assess and show how much the flow is two-dimensional along the midplane and 0.75 span positions. The baseline case is the $AR=4$ wing, which is studied with and without the endplate. The quantitatively visualized plane is at 0.75 span position for the case of $AR=4$ wing with the endplate and for the larger aspect ratio wing studied with the endplate, namely $AR=6$. However, it is at 0.5 position for the case of $AR=4$ wing

without the endplate and for lower aspect ratio wing studied without the endplate, namely $AR=2$. The first picture on the left in Figure 3.4.a shows the flow topology at the end of the pitch-up, the second shows the valley before the bump occurs in the lift coefficient, the third shows the peak of this bump, and the fourth shows just when the bump ends. The dividing streamline is observed on the second picture, approximately at half of the chord, and then, evident in the third image, the streamlines close over the wing when the local maximum is attained. Figure 3.4.b shows vorticity contours and streamlines for the wing with $AR=4$ (without end-plate/symmetry plane). The preceding observations are very similar for this case, with some slight differences:

- When a symmetry plane is not used, the streamlines close over the plate before the trailing edge implying a pseudo-reattachment (NATO STO-TR-AVT-202, 2016). However, when there is a symmetry plane, the streamlines close over the plate at the trailing edge, and the outer streamline is highly curved. As will be noticed in the following for other cases, lower lift coefficient values are attained for streamlines with greater curvature.
- When there is a symmetry plane, the streamlines exhibit a limit cycle formation.
- The occurrence of the local maximum is, in general, earlier in time for wings of high AR . It should be noted that the same results cannot be exactly obtained when there is a symmetry plane and the variations indicate as if the wing has a slightly lower AR than its effective AR . On the other hand, as will be shown later for other cases, this generalization does not hold for the wings with $AR=4$ in fast pitch-up; the occurrence of the local maximum for the wing with $AR=4$ (with endplate/symmetry plane; the gap is 2 mm) is observed approximately half a second earlier than that of the wing with $AR=4$ (without endplate/symmetry plane).

Figure 3.4.c shows the results when there exists a large gap between the endplate representing the symmetry plane and the wing root for the case of $AR=4$. As it has been pointed out previously, the force coefficient variations do not exhibit any bump for this case. In comparison with other cases with same aspect ratio, except the picture visualizing the end of the motion, correlation regarding vorticity contours and streamlines cannot be found, e.g., the dividing streamline at the local minimum of force variations or closing streamlines at the local maximum cannot be detected. After

all, when the force variations reach a static value a long time later, the flow structures resemble those of other cases of $AR=4$, notably the case with a symmetry plane.

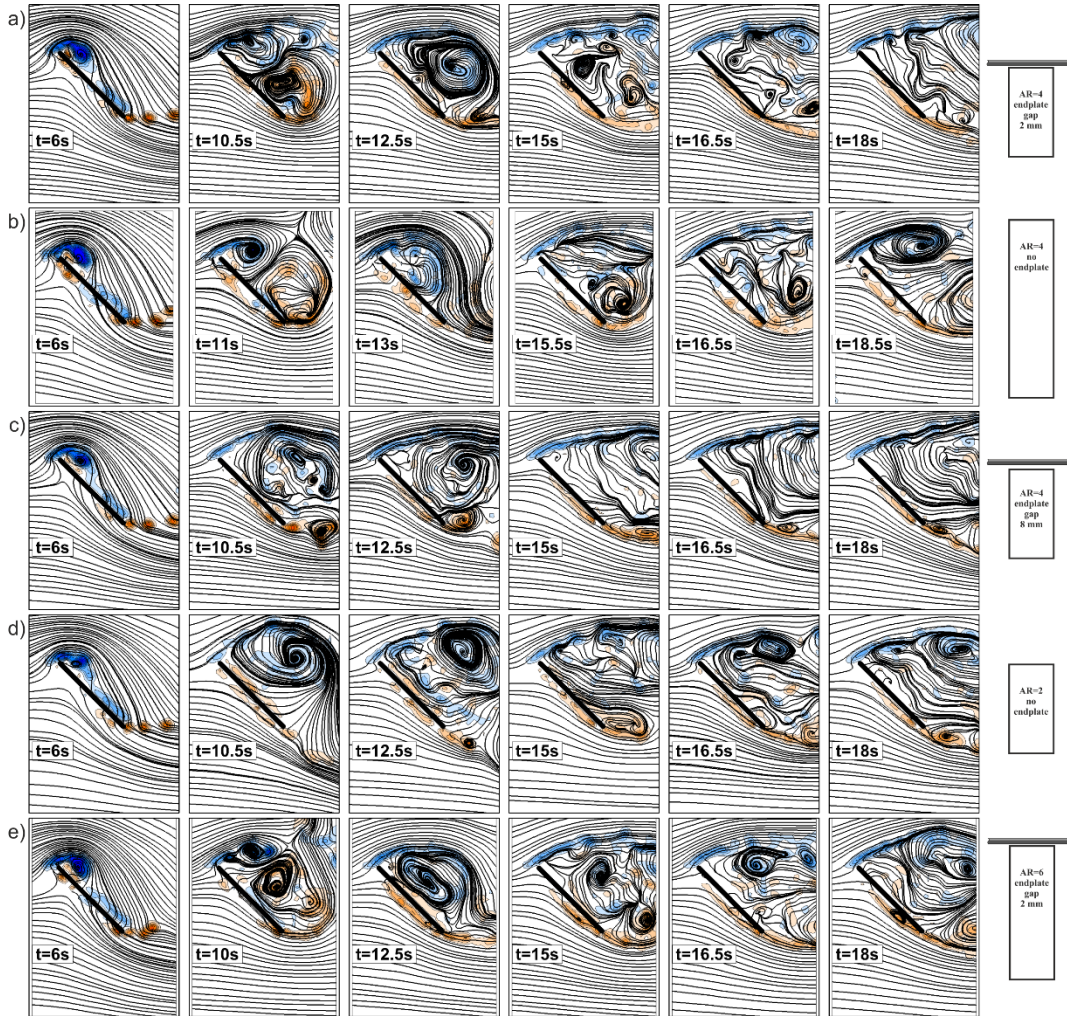


Figure 3.4 : Vortex formations together with the streamlines in fast motion, (a) $AR=4$ (with endplate/symmetry plane; the gap is 2 mm), (b) $AR=4$ (without endplate/symmetry plane), (c) $AR=4$ (with endplate/symmetry plane; the gap is 8 mm), (d) $AR=2$ (without endplate/symmetry plane), (e) $AR=6$ (with endplate/symmetry plane; the gap is 2 mm).

Vortex formations and streamline topology for the wing with $AR=2$ (without endplate/symmetry plane) are presented in Figure 3.4.d. After the end of the pitch-up motion, based on the observations made on the second and third images, the LEV appears to remain close to the plate surface for a longer period and does not shed, which is also in agreement with the findings of Jantzen et al. (2014). When the motion ends, the streamlines appear to close over the wing. However, this is not enough to indicate the existence of a bump on the force variations. According to the scenario, the formation of a dividing streamline is expected between the nearly symmetric leading and trailing edge vortices covering each half of the wing chord.

The effectiveness of the endplate to represent the symmetry plane will be discussed revisiting the results and comparing the wings having either the same effective or geometric aspect ratio. Wings of AR=4 with endplate have actually the same geometric aspect ratio as the wing of AR=2 without endplate, i.e., the wings of cases shown in Figure 3.4.a, Figure 3.4.c, Figure 3.4.d. There are clear distinctions for the wing of AR=4 when there is a large gap between the endplate representing the symmetry plane and the root of the wing in comparison with other wings of AR=4. However, the flow topology around that wing of AR=4 exhibits similarities with that of the AR=2 wing, especially evident in the second, third, and fourth images of Figure 3.4, e.g., the lack of dividing streamline, the timing of the pseudo-reattachment, etc. On the other hand, despite the aforementioned slight differences, the flow topology around the wing of AR=4 with a small gap between its root and the endplate shows the same features as the wing of AR=4 without endplate. Therefore, also in agreement with the results of force measurements related to the lack of the bump, it is concluded that the endplate does not represent the symmetry plane for a gap of 8 mm.

Figure 3.4.e shows the streamline topology and vortex formations for the wing of AR=6 (with endplate/symmetry plane; the gap is 2 mm). It should be noted that the force variations exhibit two bumps in this case. The third picture from the right ($t=15s$) corresponds to the instant in time when the first bump in lift coefficient time trace is over, the second ($t=16.5s$) corresponds to the instant when the local minimum occurs between the first and the second bumps, and the first ($t=18s$) corresponds to the instant when the maximum is reached for the second bump. Similar to what is observed for the wing with AR=4 (without endplate/symmetry plane), the outer streamline forms a flat arc at the first bump, and a high lift coefficient is attained. However, the outer streamline at the second bump exhibits greater curvature, and a lower lift coefficient is observed. Even if the field of view is limited to visualize the extent of LEV and TEV, and the outer limit of the dividing streamline cannot be seen, all major elements of flow topology are present in pictures for a scenario when a bump occurs in force variations.

Similar specific instants in force coefficient variations as in Figure 3.4 have been selected for slow pitch-up and are presented in Figure 3.5.

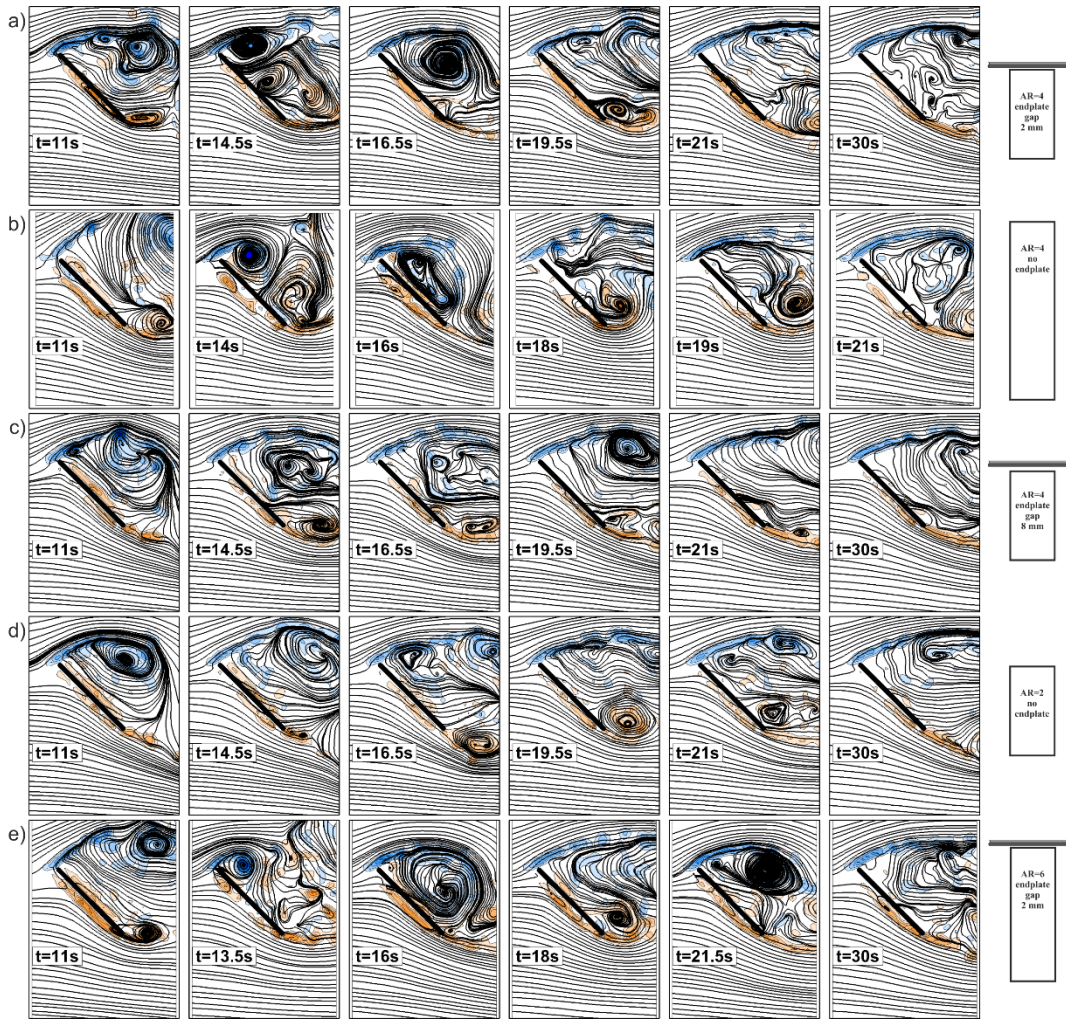


Figure 3.5 : Vortex formations together with the streamlines in slow motion, (a) AR=4 (with endplate/symmetry plane; the gap is 2 mm), (b) AR=4 (without endplate/symmetry plane), (c) AR=4 (with endplate/symmetry plane; the gap is 8 mm), (d) AR=2 (without endplate/symmetry plane), (e) AR=6 (with endplate/symmetry plane; the gap is 2 mm).

The streamline topology and vortex formations for the wing of AR=4 are given in Figure 3.5.a, Figure 3.5.b, Figure 3.5.c and show that observations made previously for the same AR wings undergoing fast pitch-up are similar to those undergoing slow pitch-up. Taking into account that the ARs of the plates with a symmetry plane are slightly lower than their effective value, the observations for the slow pitch-up case exhibit the general trend, i.e., the occurrence of the local maximum is earlier in time for wings with a larger AR. When there is a large gap between the endplate representing symmetry plane and the root of the wing, i.e., 8 mm for this investigation, the effective AR should be considered to be more likely equal to the geometric AR because the local increase in lift variation does not occur for the wing with AR=4 (with

endplate/symmetry plane; the gap is 8 mm), and the flow topology is more like that of the wing with AR=2 in the selected instants presented in Figure 3.5.d.

Streamline topology and vortex formations are shown in Figure 3.5.e for the wing with AR=6 (with endplate/symmetry plane; the gap is 2 mm) undergoing slow pitch up. This case also exhibits two bumps on the force variations. The third picture from the left ($t=16s$) corresponds to the instant when the local maximum is attained for the first bump, and the second picture from the right ($t=21.5s$) corresponds to when the local maximum is attained for the second bump. If the outer streamlines are compared for the first and second bumps, the second is highly curved, and as a consequence, a lower lift coefficient value is attained at this local minimum. Despite the fact that a dividing streamline is not observed at the local minimum before the second bump, which corresponds to the third image from the right ($t=18s$), a TEV formation is evident and a counter-rotating LEV formation is out of sight.

The occurrence and the number of bumps on the force-time traces after the pitch-up is completed are of interest for 3D analysis because they are sensitive to AR. Therefore, DPIV images are acquired at different cross-sections on the flat plate (i.e., the tip, mid, and root sections). It should be noted that an endplate was used as a symmetry plane and the root section represented the midspan of the wing.

In Figure 3.6, those DPIV results are given for the AR=4 plate undergoing fast motion at selected time instances. At $t=9s$, just before the start of the increase in force coefficients, a TEV is formed along the wing from root to tip; based on streamlines of the midsection, a new LEV is about to develop. At $t=10.5s$, this TEV rolls over the wing and meets the developed LEV. A stagnation point occurs between the leading and trailing edge vortices, and forces increase to form the aforementioned bump. At later times, the LEV grows and covers the entire chord of the wing, which is evident in both mid and root section views at $t=12.5s$. This growth coincides with the timing of the peak value on the bump. When the LEV is shed, a new TEV starts to form again; however, this time the roll-up radius of the TEV is large, and therefore it is not capable of rolling over the wing ($t=15.5s$). Furthermore, a vortex emanating from the leading edge, which is observed on the tip section plane, represents a projection of the three-dimensionality of the flow and affects the flow topology at inboard spanwise locations. It also seems to prevent the formation of the LEV along the span and the roll-up of the TEV afterwards. Later on, coherent LEV and TEV formations are not evident, and

shear layer separations are observed in accordance with the force coefficients converging to their static values.

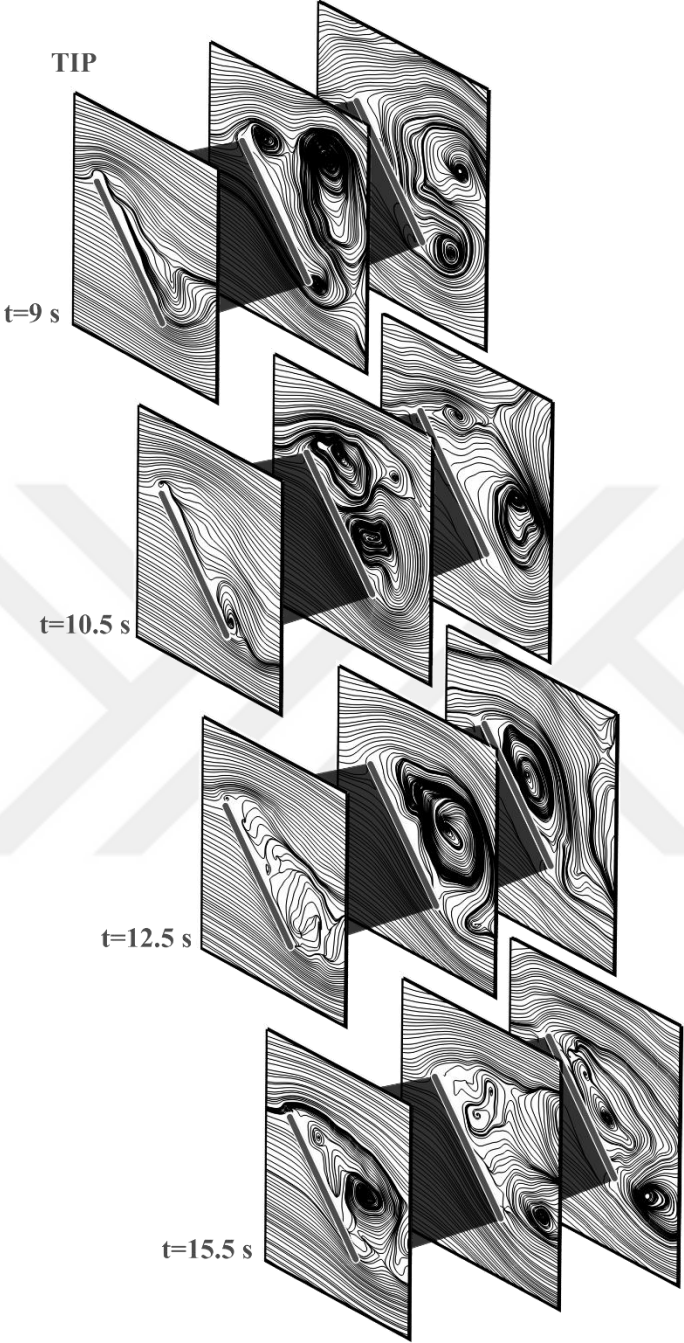


Figure 3.6 : Streamlines at the tip, mid, and root sections of the AR=4 plate (with endplate/symmetry plane; the gap is 2 mm) in fast motion.

The mid and root section flow topologies were similar at all instants, particularly considering that the flow field images were instantaneous and that the slight differences were associated with the existence of an endplate representing the symmetry plane. Therefore, the flow was mostly two-dimensional for more than half of the span, and the three-dimensionality was revealed only on the tip section flow

topologies. Irrespective of whether the plate pitches up fast or slow, the observations for both flow topologies along the span and the evolution of vortices related to the occurrence of the bump are the same as those observed in Figure 3.7, which shows the DPIV results for the AR=4 plate undergoing slow motion.

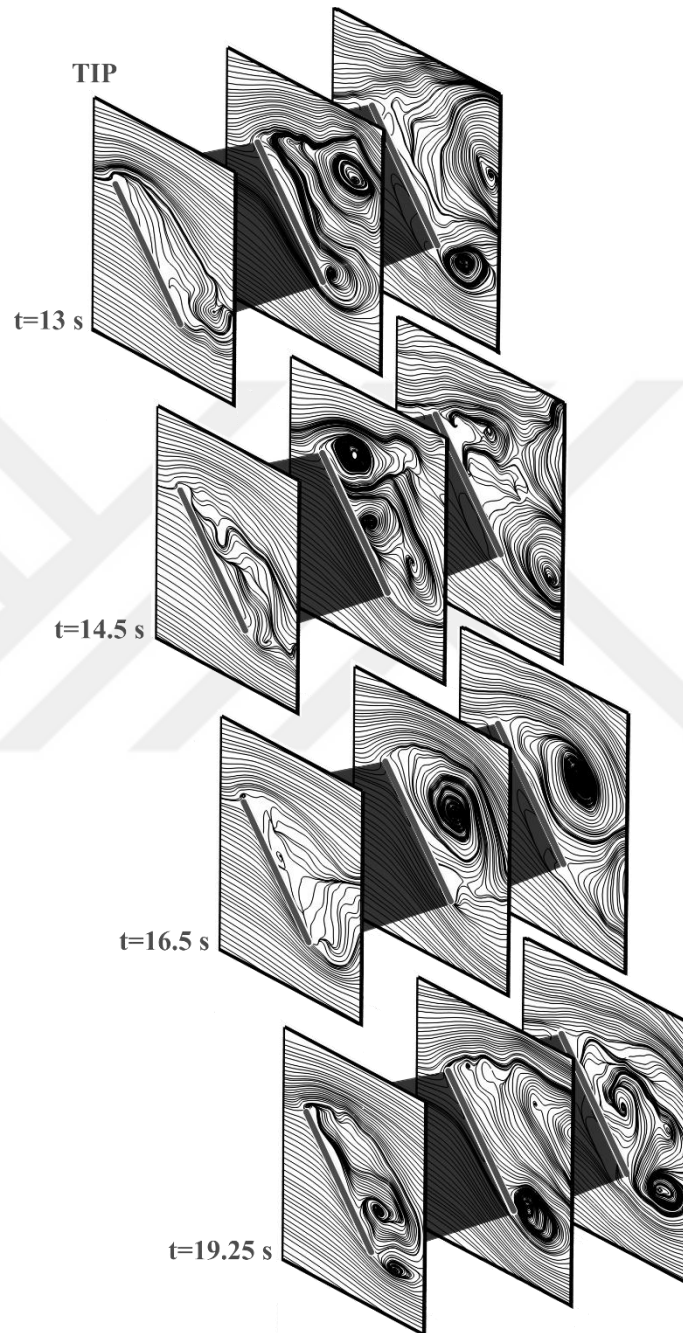


Figure 3.7 : Streamlines at the tip, mid, and root sections of the AR=4 plate (with endplate/symmetry plane; the gap is 2 mm) in slow motion.

Until the formation of the second bump, the AR=6 plate exhibited similar 3D flow features (Figure 3.8) as those of the AR=4 plate, e.g., a TEV along the span ($t=8.75\text{s}$) and meeting leading and trailing edge vortices ($t=10\text{s}$) and LEV covering the entire

upper surface ($t=12.5s$). The differences observed later on support to explain the occurrence of multiple bumps after the motion ends. The formation of another TEV is observed on the wing, and it has a smaller roll-up radius compared with the AR=4 plate. On the other hand, the vortex emanating from the leading edge, observed on the tip section plane, is absent in this case. As a consequence of those two facts, the TEV rolls up again on the plate surface, the LEV is coherent along the span, and they meet again to form a stagnation point, evident especially on the root section plane at $t=16s$. In accordance with the vortex formations, the forces start to increase again and attain their second maximum at $t=18s$. The flow topology observed on the tip section plane at $t=19.5s$ for the AR=6 plate and at $t=15.5s$ for the AR=4 plate are very similar, indicating the end of periodic vortex shedding and consequently the occurrence of bumps on the force traces.

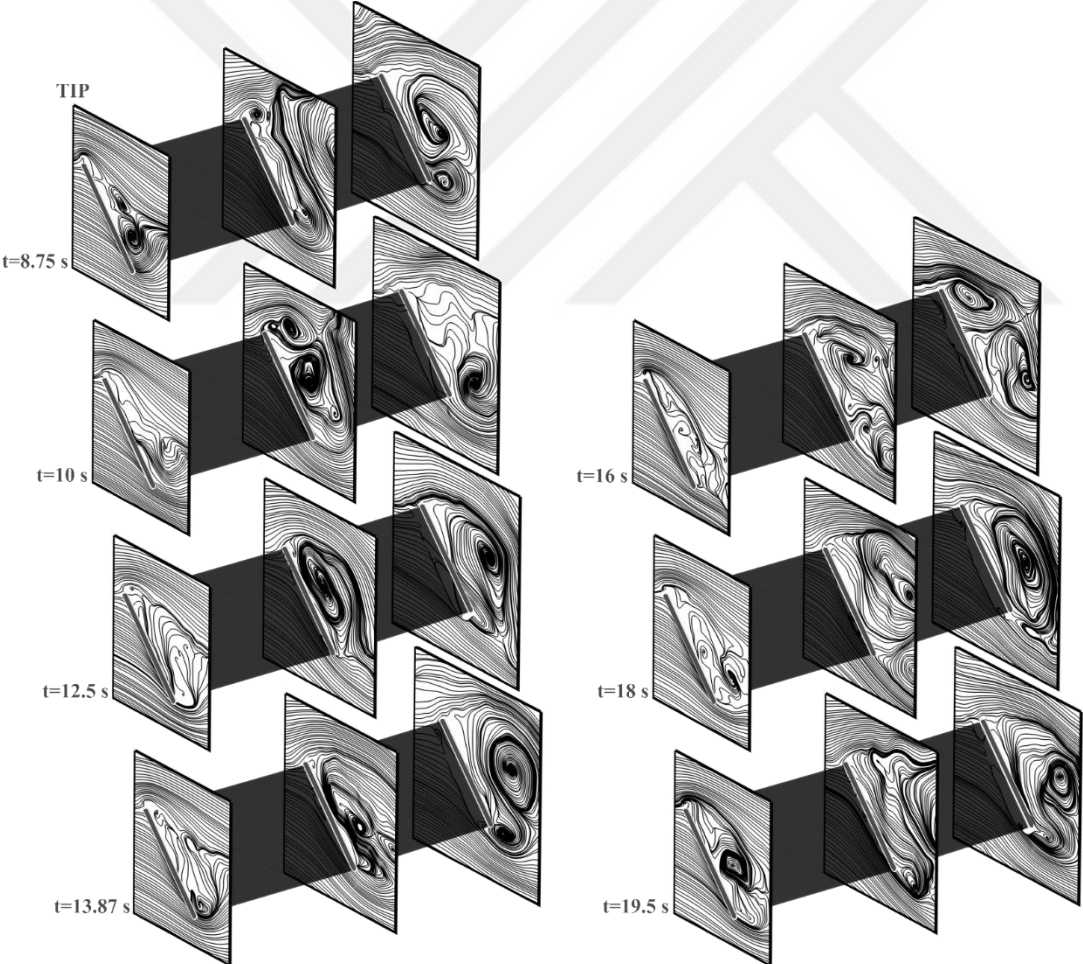


Figure 3.8 : Streamlines at the tip, mid, and root sections of the AR=6 plate (with endplate/symmetry plane; the gap is 2 mm) in fast motion.

The LEV detachment mechanisms are described in Widmann and Tropea (2015) as “bluff body detachment mechanism” and “boundary layer eruption.” Flow reversal at

the trailing edge and an upstream boundary layer flow over the entire plate are evident on the midsection planes for both ARs in Figure 3.6 ($t=9s$) and Figure 3.8 ($t=8.75s$); the LEV formed during the motion is considered to be detached at this instant. This upstream flow on the plate initiates the formation of the next LEV, leading to a LEV and TEV system that resembles the flow around bluff bodies. After the motion is completed, when the tip effects are not strong, the plate acts as a bluff body and the “bluff body detachment mechanism” prevails for the vortex behaviors. When the tip effects become pronounced, that mechanism breaks down, and a fully separated flow is observed. For higher-AR plates, the LEV and TEV system along the span lasts longer, and the communication of TV with the mostly two-dimensional flow is delayed. It can be foreseen that if the flow is two-dimensional, i.e., the AR is infinite, the alternating vortex shedding and consequently the bumps on the force time traces will be observed continuously, which is, in fact, consistent with the findings of Taira and Colonius (2009).

3.1.2 Effect of leading edge and trailing edge shape

The shape of the leading and trailing edge and their effect on vortex structures and force measurements are investigated in this chapter. In Figure 3.9 investigated shapes are illustrated.

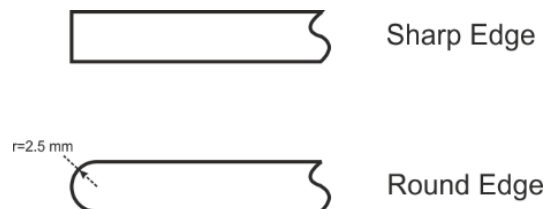


Figure 3.9 : Round and sharp edge plates.

The effect of using different leading and trailing edge geometries in fast and slow rectilinear pitch motion are studied based on force measurements and DPIV experiments. Figure 3.10 and Figure 3.11 show lift coefficient variation and vorticity contours together with streamlines for slow and fast motions respectively.

The occurrence of peaks and valleys during the motion and after are very similar for both edge shapes. In accordance with that, the general characteristics of flow topology for some critical instants selected from the force-time history are also parallel between the two cases. The DPIV results presented herein are for plates with aspect ratio of 4 and with an endplate being used to represent the symmetry plane.

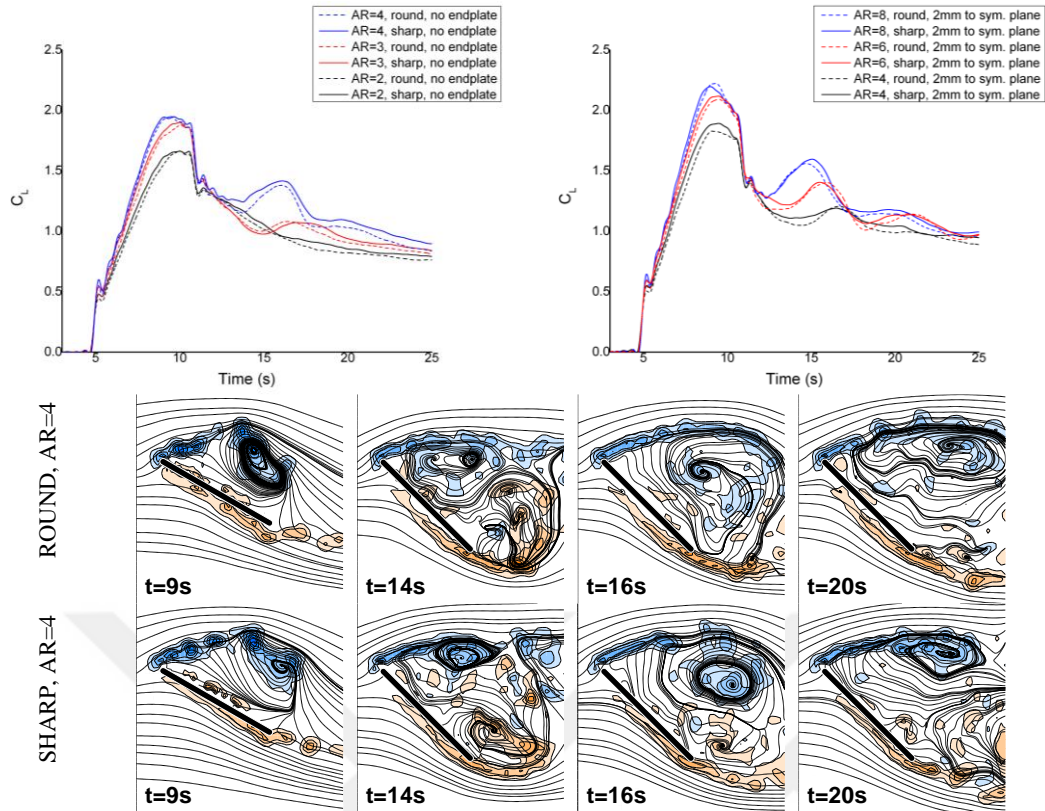


Figure 3.10 : C_L variation with respect to time and vorticity contours together with streamlines for the flat plate with round and sharp edges in slow motion.

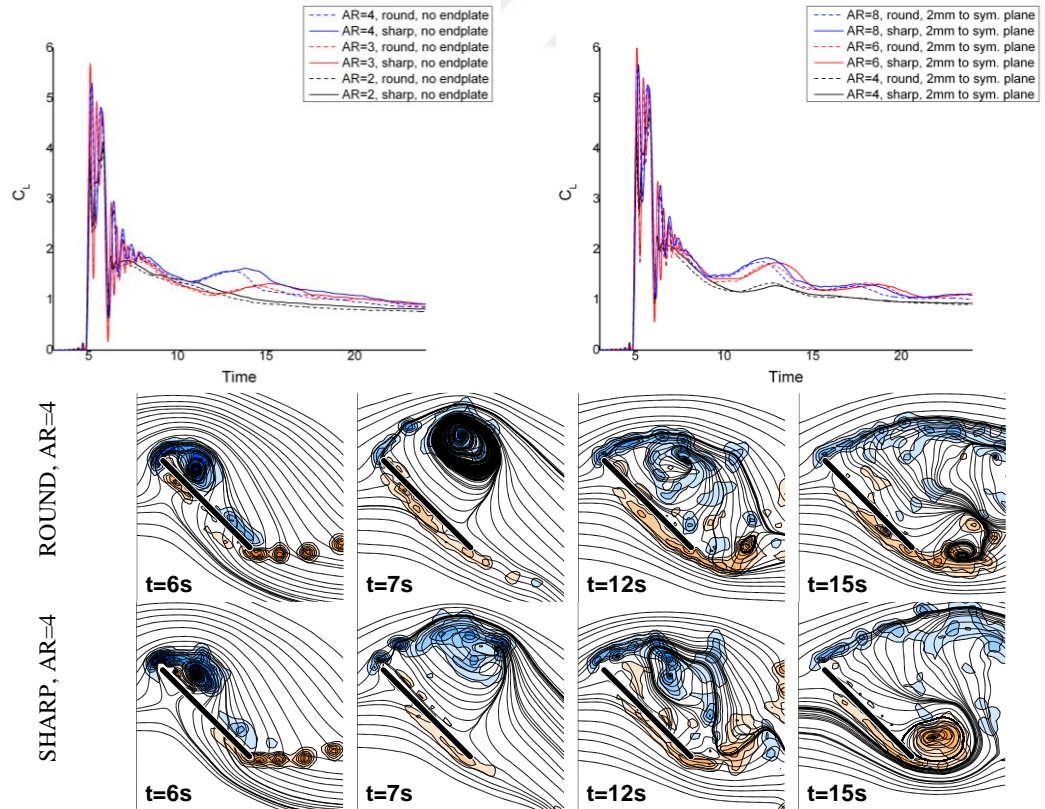


Figure 3.11 : C_L variation with respect to time and vorticity contours together with streamlines for the flat plate with round and sharp edges in fast motion.

3.1.3 Effect of planform shape

The effect of planform shape is investigated on the models, which are thin triangular, trapezoidal, rectangular, elliptic and Zimmerman profile plates as shown in Figure 3.12.

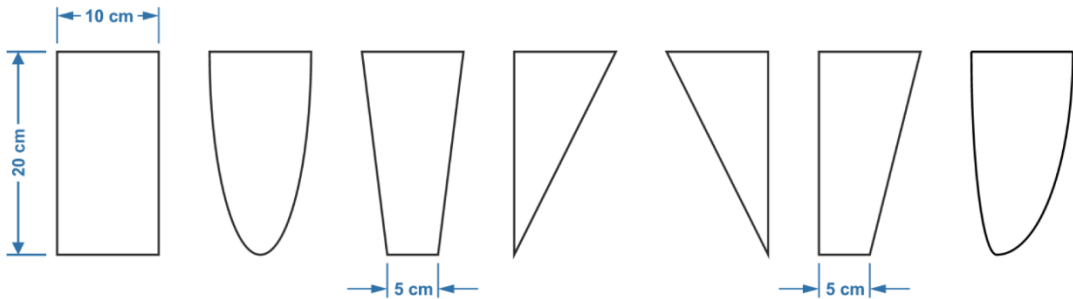


Figure 3.12 : Sketch of different planform wings: (from left to right) rectangular, elliptic, trapezoidal (isosceles), two triangular wings (angled from trailing edge and leading edge), trapezoidal (right) and Zimmerman.

Figure 3.13 shows the lift and drag coefficient variation with respect to time for all the investigated planform geometries, in fast and slow motions respectively. In fast motion, only triangular shapes differ from the others. Although the characteristic variations are very similar, the flat plate with triangular planform and angled from the leading edge experiences higher lift and drag while the flat plate with triangular planform and angled from the trailing edge experiences lower lift and drag with respect to the other flat plates with different planform geometries. In a detailed observation, the characteristic bump in the force traces of the rectangular plate is present for some of the cases, such as the flat plates having triangular leading edge, Zimmerman and trapezoidal planforms.

The slow motion reveals better the difference and similarities between the planform geometries. The lift and drag variations of flat plates with Zimmerman and elliptic planforms are very similar especially during the motion, the only major difference is that the flat plate having elliptic planform exhibits bump(s) in the force traces. The same similarity exists for the trapezoidal planforms during the motion phase. The rectangular flat plate experiences always the largest lift and drag coefficient values for the slow motion. The flat plate with triangular planform and angled from the trailing edge, in general, experiences smallest lift and drag coefficient for slow motion as it is also the case for the fast motion.

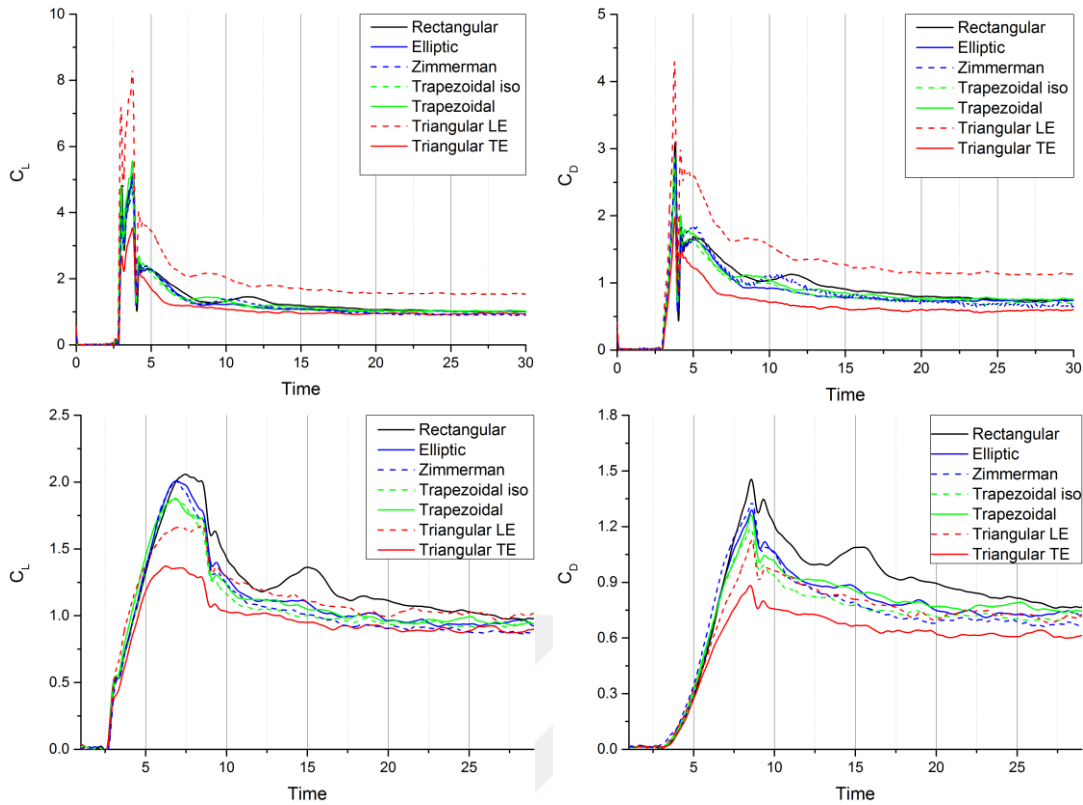


Figure 3.13 : Force Coefficient comparisons for fast (top) and slow motions (bottom).

The differences in force traces are obviously related to the three-dimensionality of the flow and are expected to be explained with the differences in vortex formations. Figure 3.14 shows the vorticity contours together with streamlines for the rectangular flat plate in fast motion at some critical instances selected from the force-time history. The cross-section where the DPIV images are taken is at the half of the geometric span. The first image on the left visualizes the vortex formations and the flow topology at the end of the motion, the third at the valley before the bump occurs in lift coefficient, the fourth at the peak of this bump and the fifth just when the bump ceases. The dividing streamline on the third image is approximately at the half of the chord and the streamlines close over the wing when the local maximum is reached.

Based on the rectangular flat plate results, Figure 3.14 show the vortex formations together with the streamlines at the same instances in time for the other planform shapes in fast motion. The flow structures are in accordance with the force measurement results. During the development phase of the leading edge vortex (LEV), the flow topology is not sensitive to the planform shape or the local chord length of the wing for all investigated cases except the flat plates with a triangular planform.

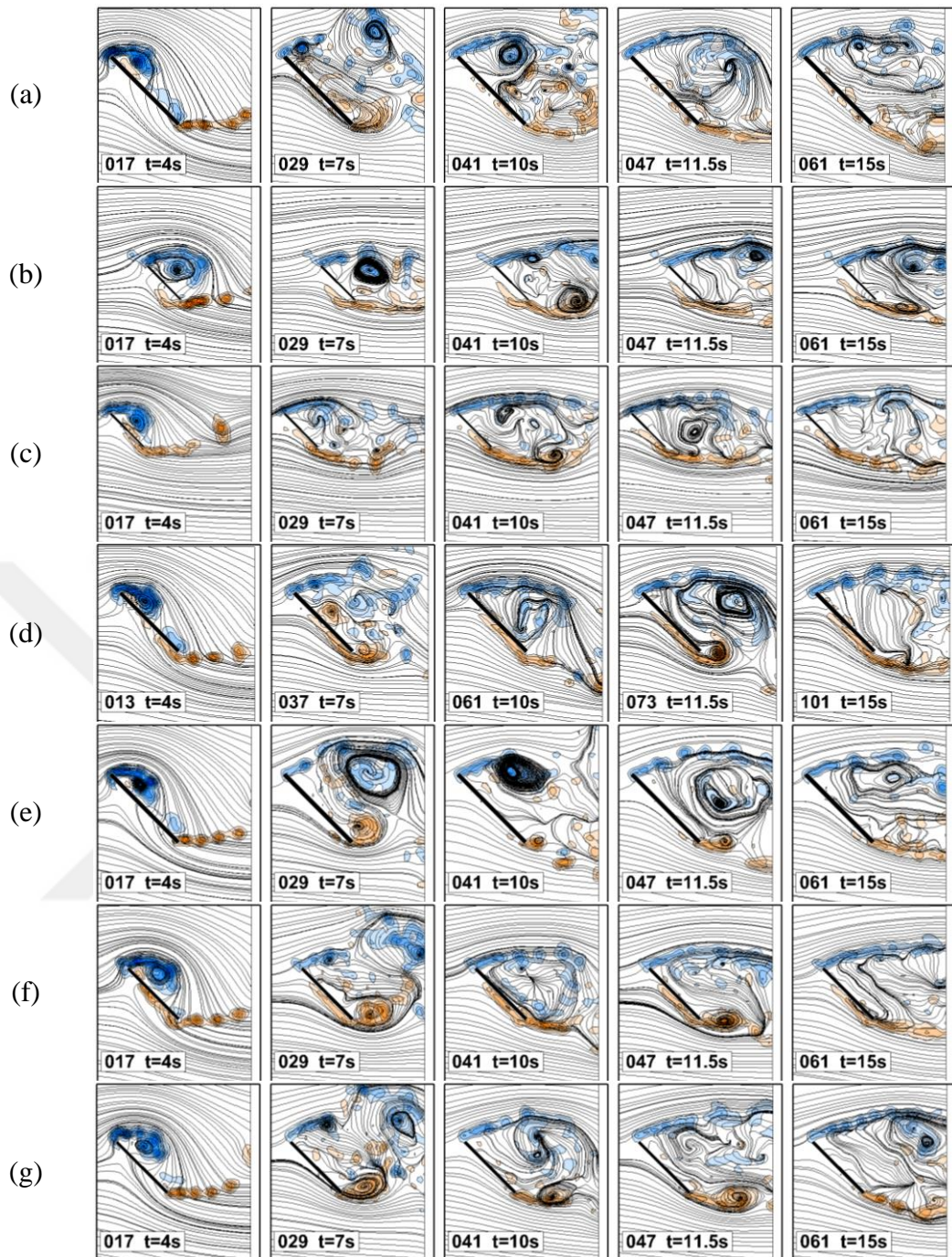


Figure 3.14 : Vortex formations together with the streamlines in fast motion (a) rectangular wing, (b) triangular (angled from leading edge), (c) triangular (angled from trailing edge), (d) Zimmerman, (e) elliptic, (f) trapezoidal, (g) trapezoidal isosceles.

Focusing on the first image representing the end of the motion, the flat plate with triangular planform and angled from the leading edge exhibits nearly a fully developed LEV. On the contrary, the flat plate with triangular planform and angled from the trailing edge has weaker leading and trailing edge vortices and exhibits separating shear layers just after the motion ends. The streamlines closing over the wing when

the local maximum of the bump in force traces is reached are found in the third images (approximately $t=10s$) instead of the fourth image as in the rectangular flat plate case for Zimmerman and trapezoidal planforms. A close look in the lift coefficient variation indicates an early occurrence of the bump in time, in accordance with the flow topology.

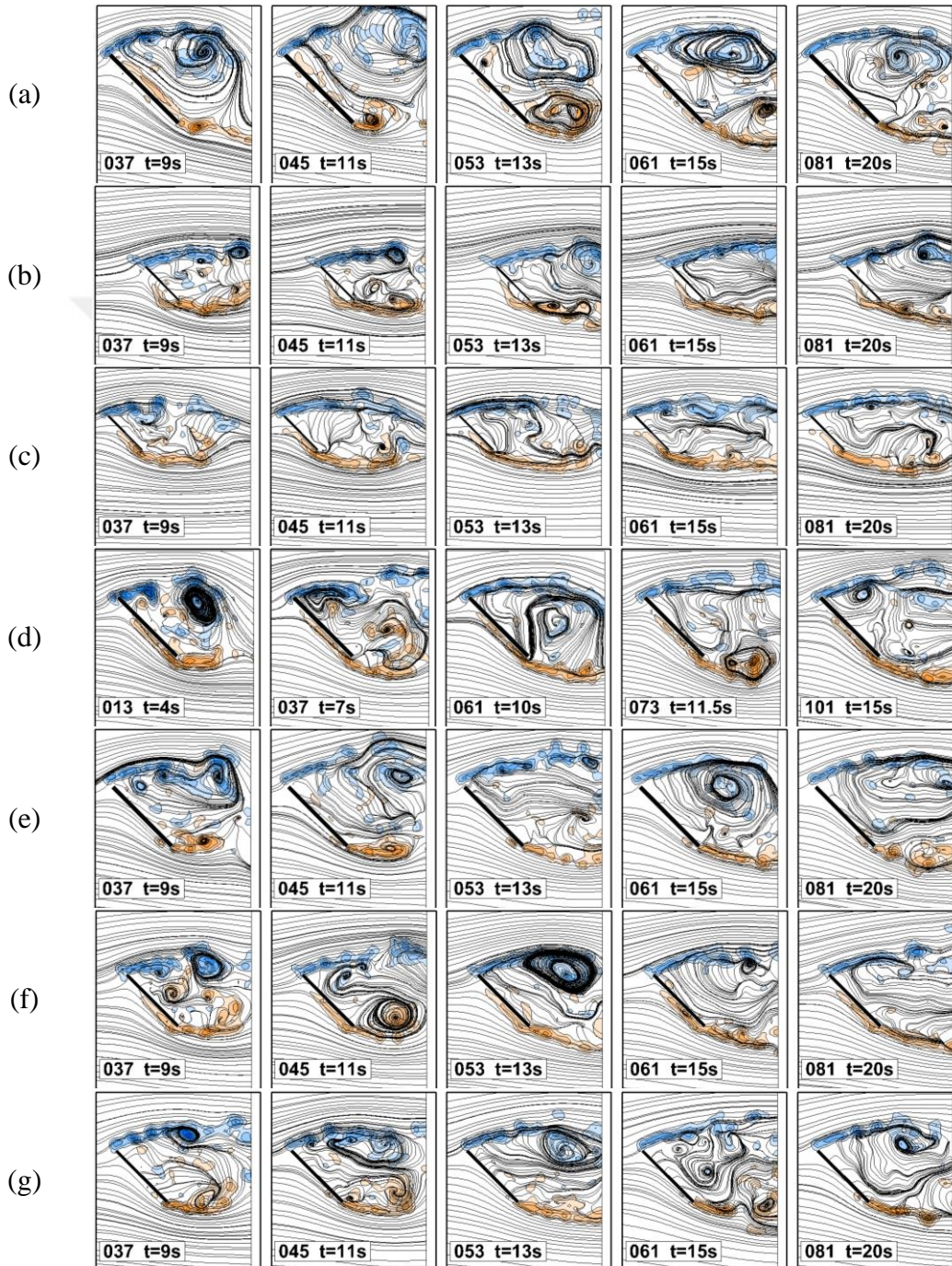


Figure 3.15 : Vortex formations together with the streamlines in slow motion, (a) rectangular wing, (b) triangular (angled from leading edge), (c) triangular (angled from trailing edge), (d) Zimmerman, (e) elliptic, (f) trapezoidal, (g) trapezoidal isosceles.

Figure 3.15 show the vortex formations together with the streamlines for the flat plates having different planform geometries in slow motion at some critical instances selected from the force-time history. The previous observations made for the same wings at fast motion are similar for slow motion. Based on the rectangular flat plate, the valley before the bump is again characterized by the dividing streamline being approximately at the half of the chord (on the third image) and the peak of the bump by the streamlines closing over the wing (fourth image). The first image on the left visualizes again the vortex formations and the flow topology at the end of the motion. In accordance with the force-time histories and compared with other planforms, triangular flat plates have weaker leading and trailing edge vortices and exhibit separating shear layers when the motion ends. Among those two cases, the flat plate with triangular planform and angled from the trailing edge has lowest lift and drag in parallel with weakest vortical structures. The flow topologies at the end of the motion for Zimmerman and elliptic planforms have similar features. The difference in the existence of the bump is also revealed in the flow topology since the flat plate with elliptic planform exhibits streamlines closing over the wing on the forth image while the Zimmerman has no sign of it. The flow topologies at the end of the motion and at the valley before the bump (third image) have similar features for the flat plates with trapezoidal planforms, in agreement with their force-time histories.

In order to reveal the differences in terms of the three-dimensionality of the flow, the DPIV results obtained for three different illumination planes have been reconstructed in a perspective view, the image on the left most represents the tip plane of the wing. Figure 3.16 shows the reference case of rectangular flat plate together with the triangular flat plates as they exhibit predominant differences. Figure 3.16 (top row) indicates the instant just before the flat plates stop in fast motion ($t=3.75s$). However, Figure 3.16 (bottom row) shows the vortex formations together with the streamlines long time after the motion ends. The two cross-sections except the tip plane exhibit very similar vortex formations for the rectangular flat plate. Although LEV interacts with the tip vortex and therefore the extent of LEV on the upper surface of the plate diminishes towards the tip plane, it is possible to conclude that LEV covers a considerable part of the plate's upper surface. LEV is stronger for the two cross-sections except the tip plane for the case of the flat plate with triangular planform and angled from the leading edge. Effectively the chord length is zero for the flat plates

with triangular planform and this is also clearly seen in the images with no distinguishable vortices on the tip plane. Although the triangular flat plates have half the planform area compared to rectangular flat plate, the LEV occupies approximately all the chord length in both illumination planes except the tip plane for the flat plate with triangular planform and angled from the leading edge. The vortical structures and flow topology for the flat plate with triangular planform and angled from the trailing edge is mostly similar to those of the rectangular flat plate, however the deficiency in the lift and drag comes from the reduction of the chord length towards tip plane. Similar observations can be made based on Figure 3.16 (bottom row), showing similarity of the flow topology between the rectangular flat plate and the flat plate with triangular planform and angled from the trailing edge.

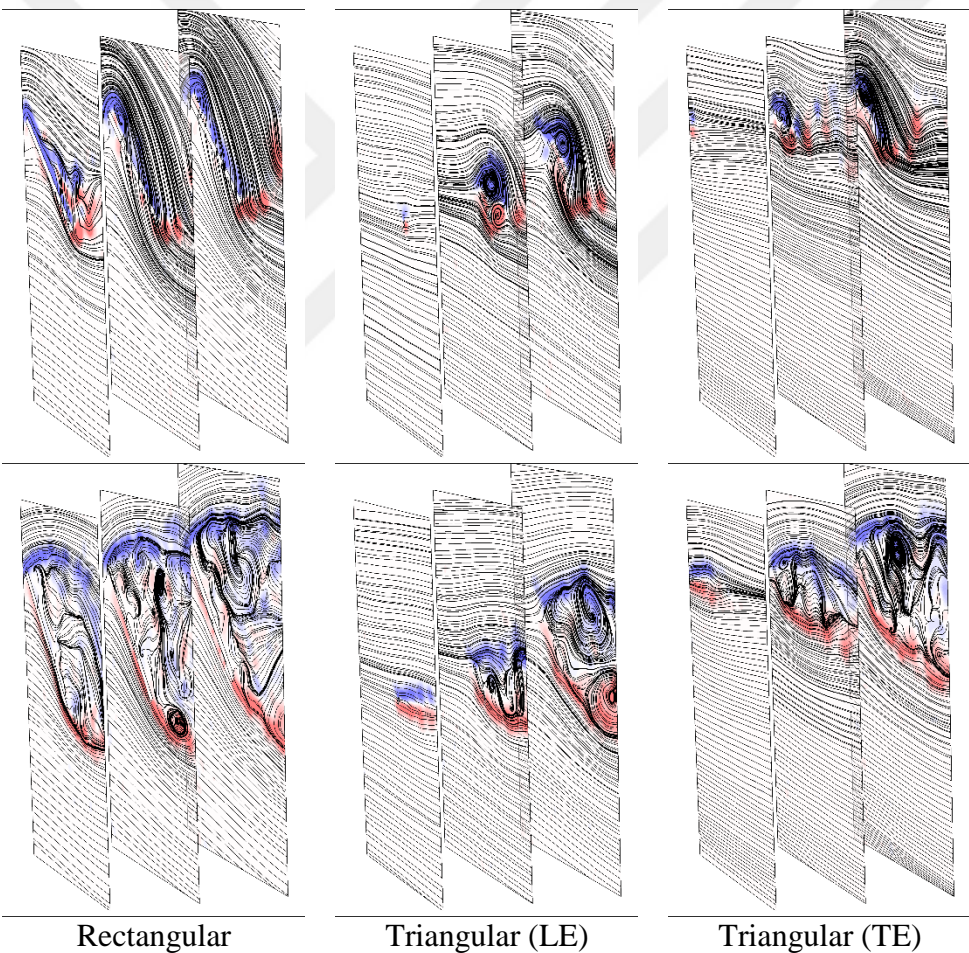


Figure 3.16 : Vortex formations together with the streamlines in fast motion for three cross-sections along the span. Top row $t=3.75s$, bottom row $t=20s$.

As the motion lasts longer in slow motion cases, two instances during the motion have been selected and the perspective view of three illumination planes are shown in Figure 3.17 to reveal the differences in terms of the three-dimensionality of the flow. The

evolution of the LEV and its interaction with the tip vortex are better understood in those figures especially for the rectangular plate. Although the LEV is attached to the upper surface at $t=7s$ as observed on the two cross-sections except the tip plane, interacting with the tip vortex it lifts off at the later instant as observed on the mid cross-section view. The perspective views also show that the difference in the flow topology for the flat plate with triangular planform and angled from the leading edge is not pronounced in the slow motion, in accordance with the force-time history.

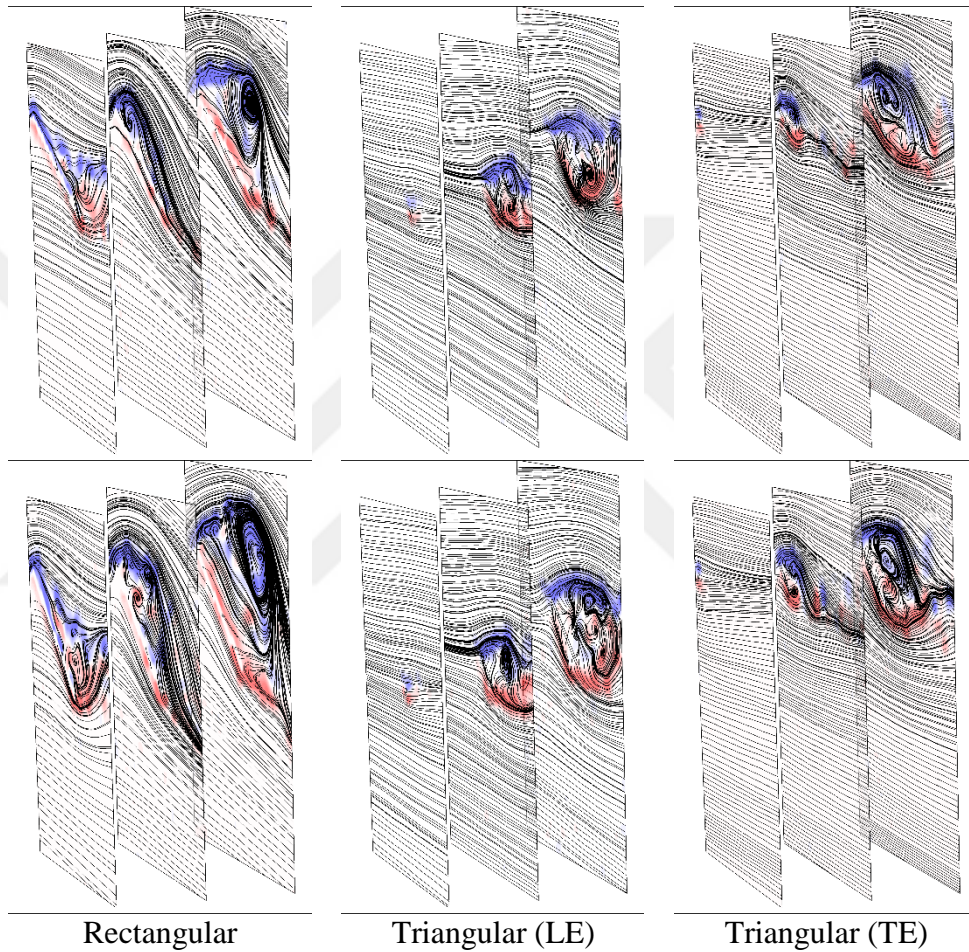


Figure 3.17 : Vortex formations together with the streamlines in slow motion for three cross-sections along the span. Top row $t=7s$, bottom row $t=8.5s$.

3.2 Effect of Flexibility for Perching

Effect of flexibility for the wings performing impulsive pitch up motion is investigated in this section. The tested wings have chord length of $c=10$ cm and span of $s=20$ cm which corresponds to $AR=4$ with endplate cases aforementioned in previous sections. One rigid and three flexible wings are performed fast and slow pitch up motions. Force measurements and DPIV images are obtained and the results are compared.

3.2.1 Force measurement results

Force measurements are performed on four different wings pitching about their leading edge at two pitching rates. The data is averaged over five runs and then filtered by a low pass filter of 4 Hz for fast motion and 2 Hz for slow motion.

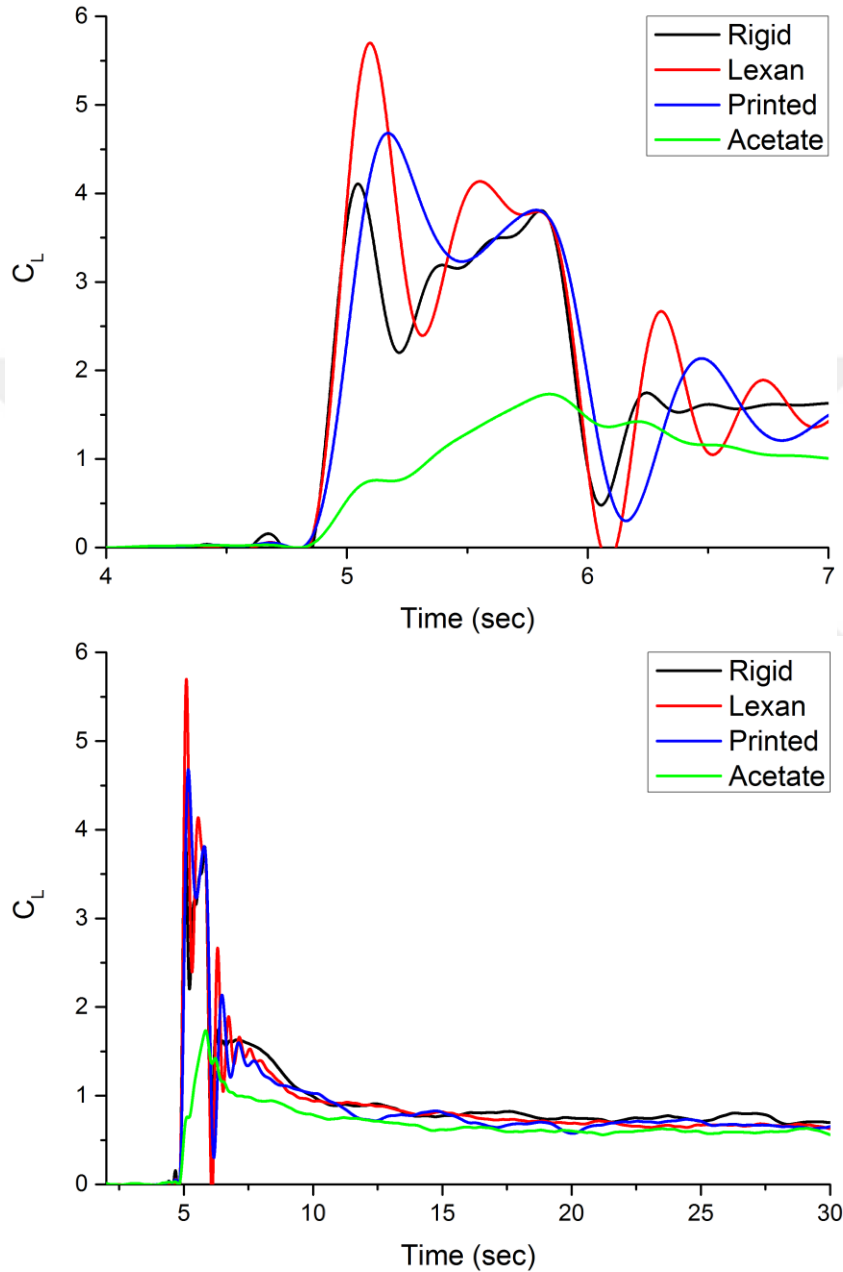


Figure 3.18 : Lift coefficient variation for the fast pitch-up motion (Upper graph: time axis focused on the motion phase).

In Figure 3.18 motion starts at $t=5$ s and ends at $t=6$ s. On the upper graph, lift coefficient variation can be observed during the motion phase. Peaks on the C_L at the beginning and the end of the motion are higher for the lexan wing. Printed wing has slightly higher peaks than the rigid wing. On the other hand, the peaks are disappeared

on the acetate wing and C_L is low compared to the other wings during the motion. When the bottom graph is examined in Figure 3.18 it can be seen that the C_L values converge to a value around $C_L=1$ for all the wing types. Therefore, it can be said that flexibility do not have an effect on the static lift values after the motion is completed.

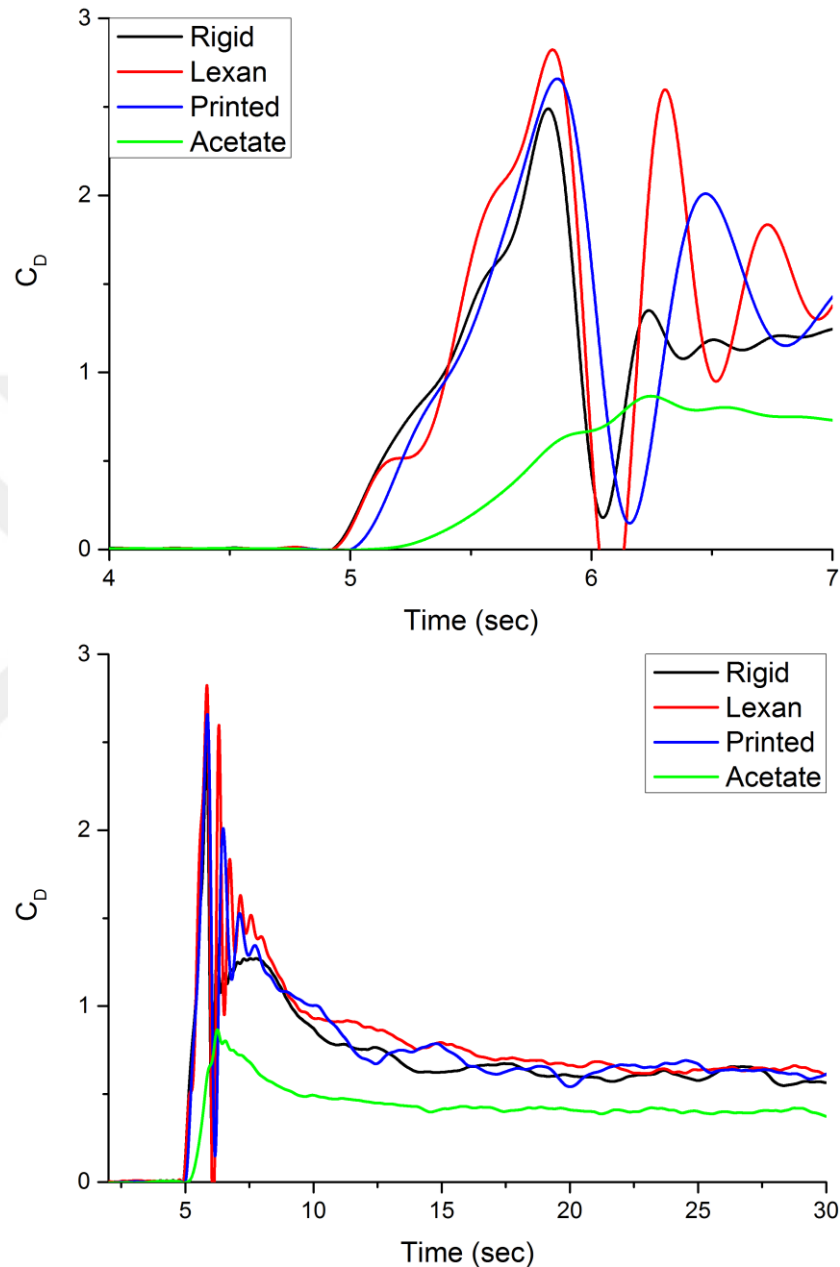


Figure 3.19 : Drag coefficient variation for the fast pitch-up motion (Upper graph: time axis focused on the motion phase).

In Figure 3.19 drag coefficients of the same wings are presented. Distribution of the C_D is similar for the rigid, lexan and printed wings during the motion. The peak values are slightly different: lexan has the highest value, and then printed and rigid wings are sorted respectively. Acetate wing has lower C_D values during the motion and its peak

value is also lower than the other three wings. After the motion is completed, C_D converges to static values, in that case acetate wing has the lowest C_D . The reason can be attributed to the bending of the wing at 45 degrees by the effect of freestream flow. That bending results in decreasing the effective angle of attack and as a consequence, low C_D values are obtained for the acetate wing.

In Figure 3.20 lift coefficient variation of different wings for slow pitch-up motion is presented. Motion starts at $t=5s$ and lexan and printed wings have higher C_L values till $t=7s$. After that instant, rigid wing has the highest C_L . Acetate wing has the lowest C_L during the motion among the other wings.

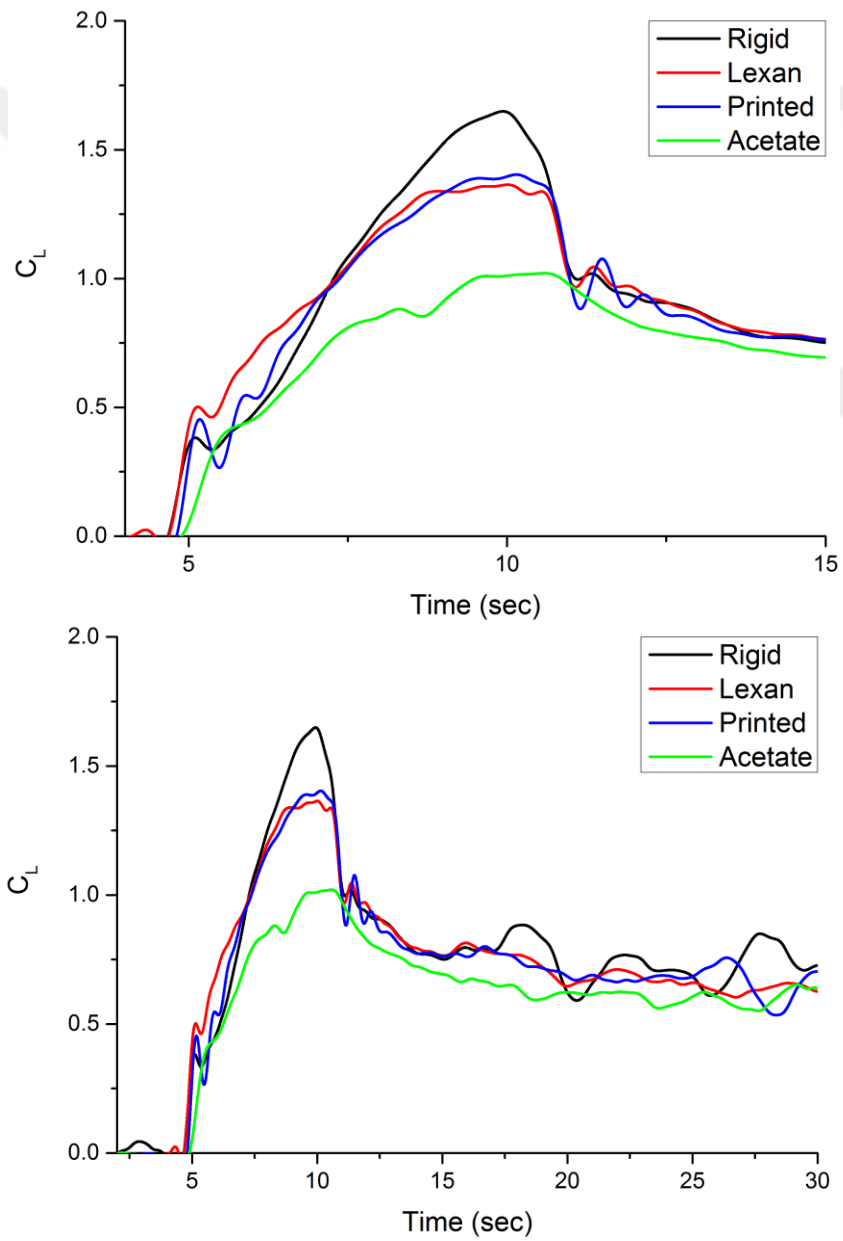


Figure 3.20 : Lift coefficient variation for the slow pitch-up motion (Upper graph: time axis focused on the motion phase).

For the drag coefficient of the slow pitch-up motion (Figure 3.21) not a significant difference is observed for rigid, lexan and printed wings during the motion. On the other hand, acetate wing has the lowest C_D values during the motion and after the motion is completed. The deflection of the acetate wing due to freestream caused that low C_D as in the fast ramp motion.

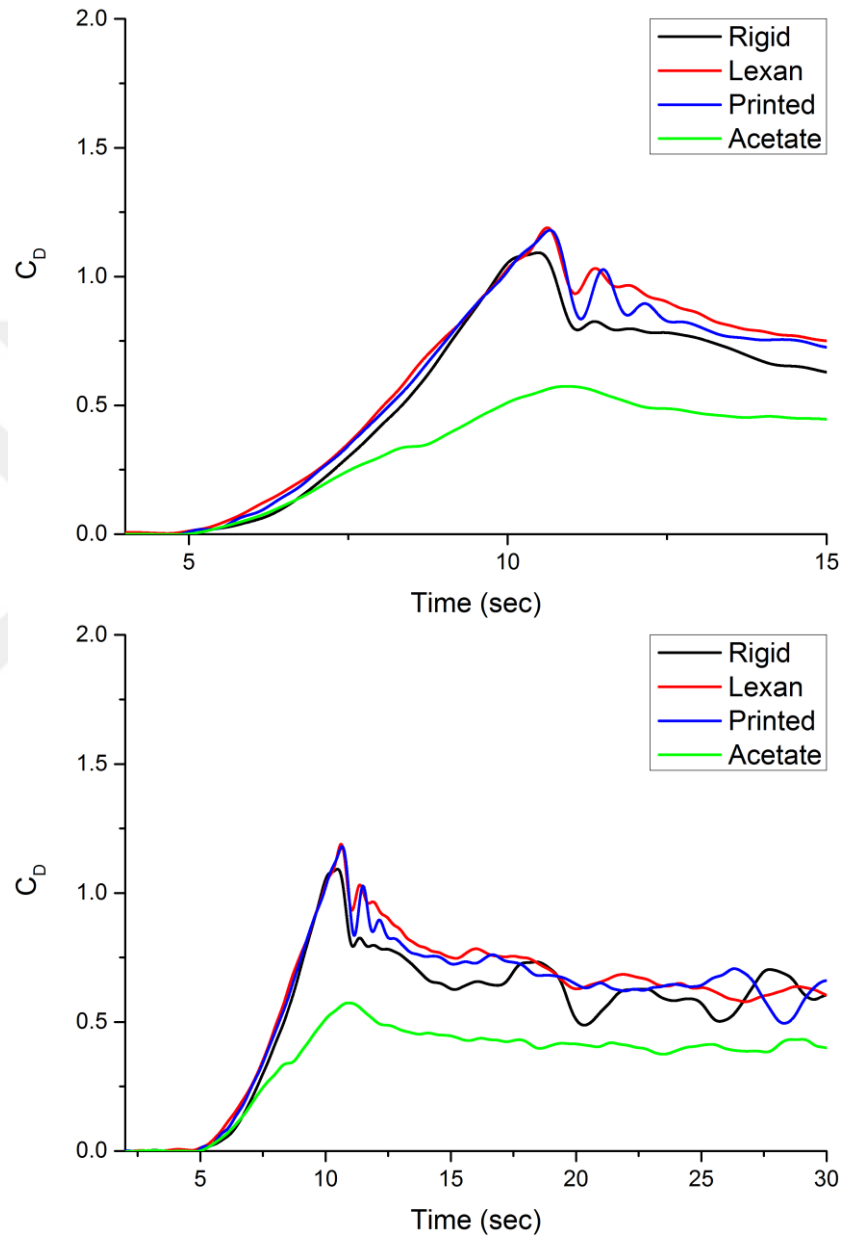


Figure 3.21 : Drag coefficient variation for the slow pitch-up motion (Upper graph: time axis focused on the motion phase).

3.2.2 DPIV results

PIV measurement results for four different pitching-up wings are presented in this chapter. Selected snapshots from PIV time history including instants before, during and after the motion are shown in the following figures.

In Figure 3.22 vorticity contours and streamlines are presented for the rigid wing performing fast pitch-up motion. At $t=5$ s, the wing is just about to start its motion, at $t=5.5$ s the wing is in the middle of the pitching motion and at $t=6$ s the motion stops and the wing remains stationary at that angle. A leading edge vortex formation can be observed starting from $t=6$ s until its lift-off from the surface of the wing at $t=9$ s. After that instant, a LEV-TEV system develops as investigated in the previous chapters in detail. After $t=15$ s shear layer separation is observed and the force coefficients converge to the static values. The fast motion is repeated for three different flexible wings and the PIV results are presented in the Figure 3.23-25.

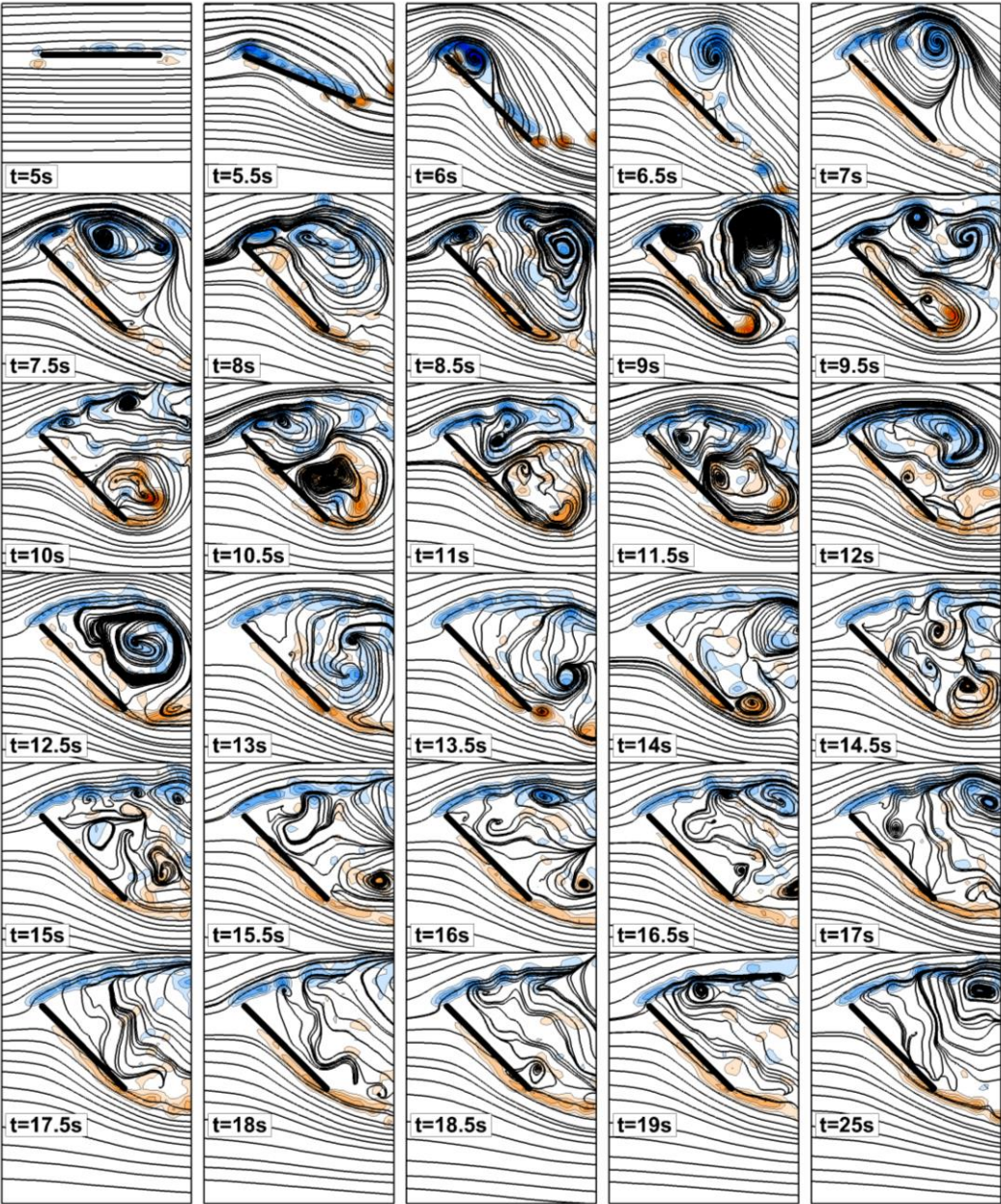


Figure 3.22 : Vorticity contours and streamlines for rigid wing in fast pitch-up motion.

In Figure 3.23, the lexan wing is pitching-up between time interval 5-6s. After that instant, similar vortical structures and streamline topology are observed compared to the rigid wing. LEV lift-off for the rigid wing at $t=9s$ is occurring around $t=10s$ for the lexan wing. LEV and TEV meeting on the surface of the wing is observed at $t=10.5s$ for rigid wing whereas in the lexan wing it is at $t=11.5s$. LEV over the wing surface is observed at $t=12.5s$ for rigid wing and $t=13.5s$ for the lexan wing. Moreover, the arc over the LEV can be observed at time instants up to $t=13.5s$ for rigid wing, on the other hand, it can be observed until $t=15.5s$. for the lexan wing. After that time, separated flow structures are similar on rigid and lexan wings.

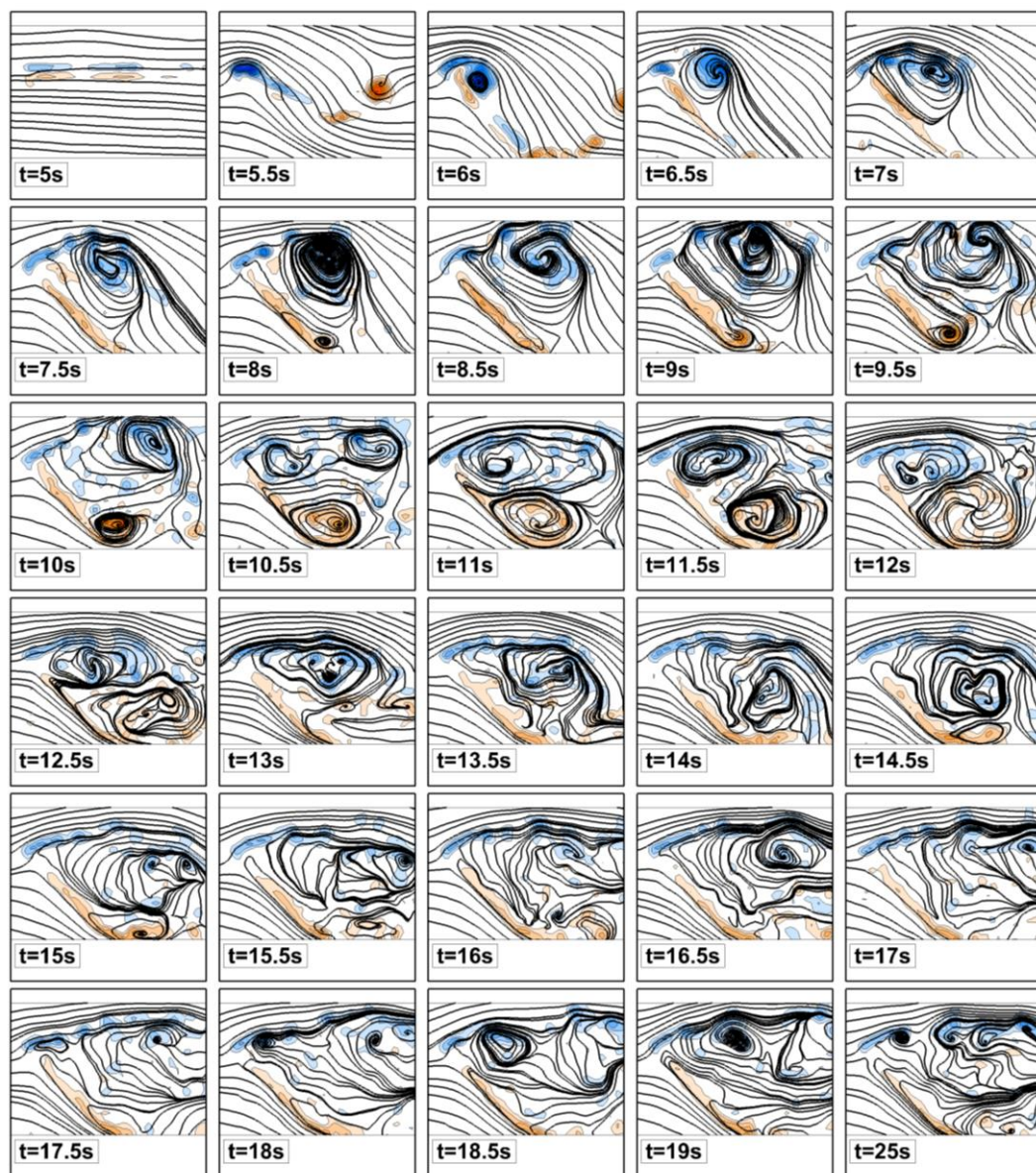


Figure 3.23 : Vorticity contours and streamlines for lexan wing in fast pitch-up motion.

In Figure 3.24 printed wing's fast pitch up motion is investigated. Vortical structures and streamlines are similar with the lexan wing as also observed in force coefficients. Main difference can be seen long after the motion is completed. A large vortex formation can be observed on the bottom row in Figure 3.24 starting from $t=17.5s$. This situation cannot be seen on lexan and rigid wing's vortex formations. However, this vortex structure is not attached on the wing surface and it does not have a significant effect on force coefficients.

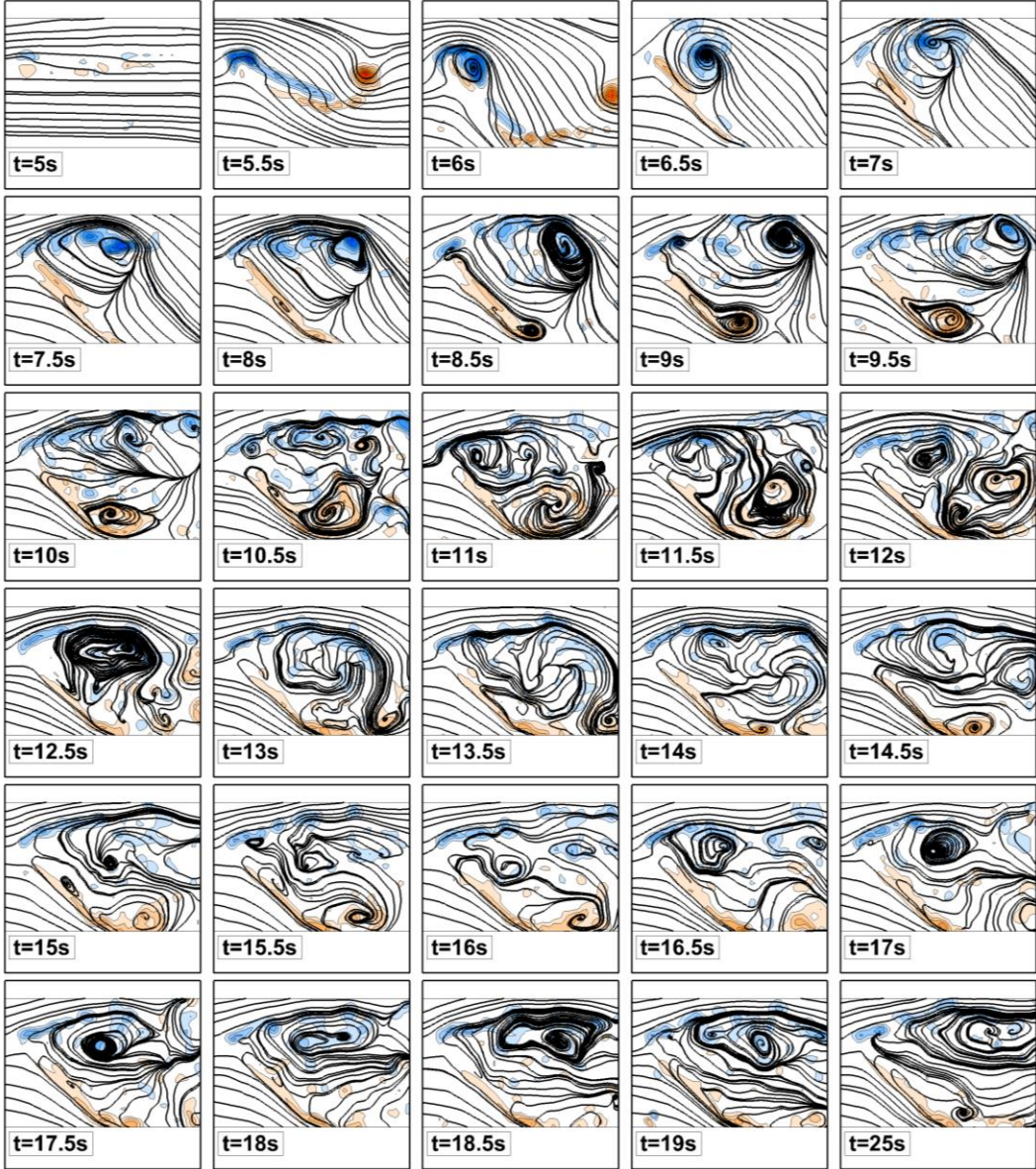


Figure 3.24 : Vorticity contours and streamlines for printed wing in fast pitch-up motion.

The acetate wing as the most flexible wing amongst the wing types, undergoing fast pitch up motion is presented in Figure 3.25. There are significant differences in vortex structures and streamlines in that case starting from the beginning of the motion. At

$t=6.5s$ when the motion is completed, the LEV observed on the upper surface of the wing is weaker than the ones observed on the other three wings. Also the final angle of attack of 45 degrees is more smaller for the acetate wing due to bending of the flexible wing with the effect of freestream. That bending effect is smaller for the lexan and the printed wings. The final angle of attack of the wings are determined as 45° , 44.78° , 43.97° , 31.14° for rigid, lexan, printed and acetate wings respectively. As a result of decreased angle of attack, streamline curvature around the wing is smaller. Force coefficients are also smaller compared to other wing types.

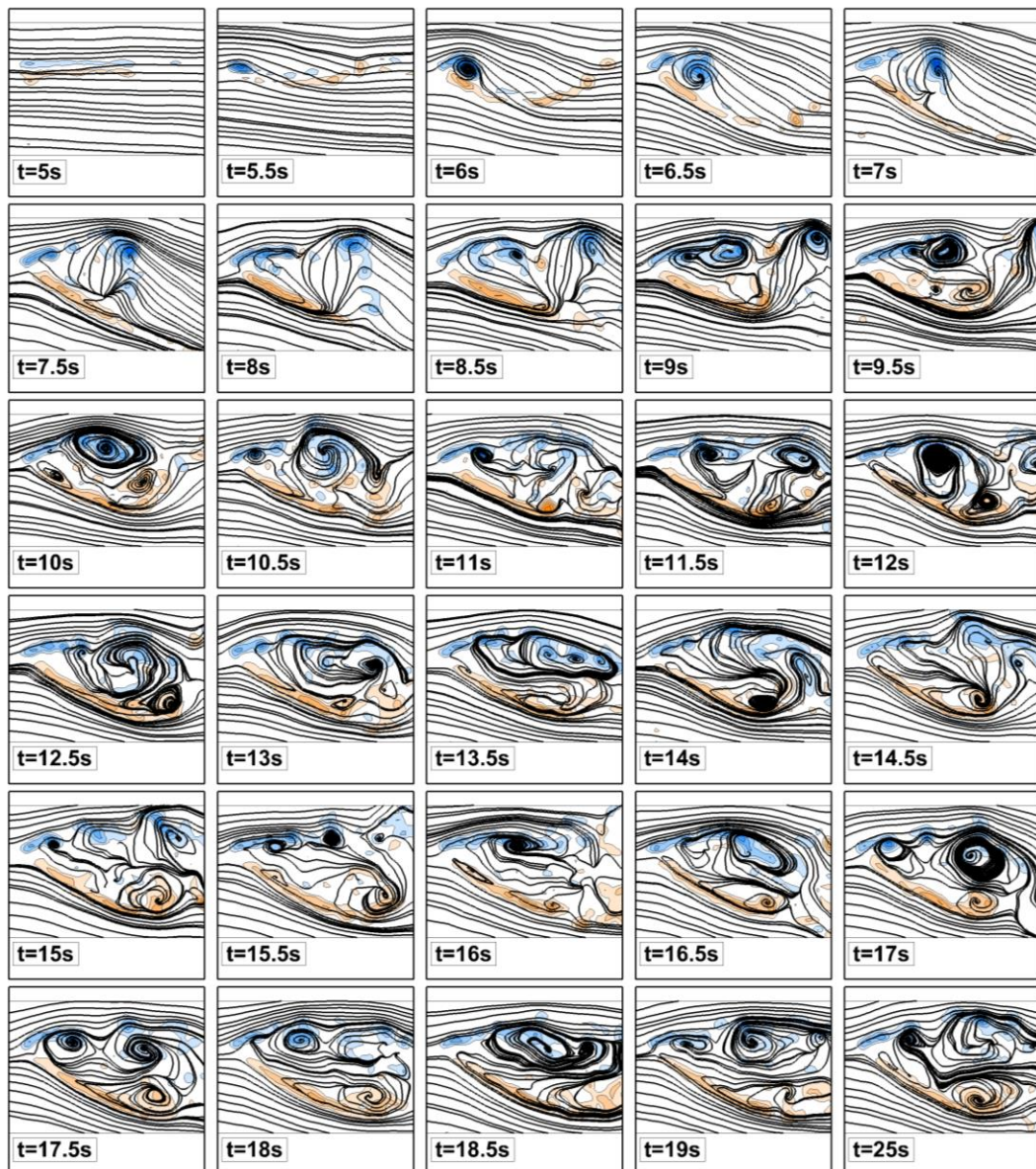


Figure 3.25 : Vorticity contours and streamlines for acetate wing in fast pitch-up motion.

Another characteristic that should be emphasized is that the continuous vortex shedding from the acetate wing. Vortex shedding from the leading and trailing edge of the wing can be observed in all time instants.

Slow pitch-up motion for the rigid wing is presented in Figure 3.26. In that case the motion starts at $t=5s$ and ends at $t=11s$. A large LEV formation after the motion can be observed which is then followed by TEV formation, meeting of the TEV and the second LEV at $t=15s$, LEV covering the upper surface of the wing ($t=17s$) and finally the shear layer separations.

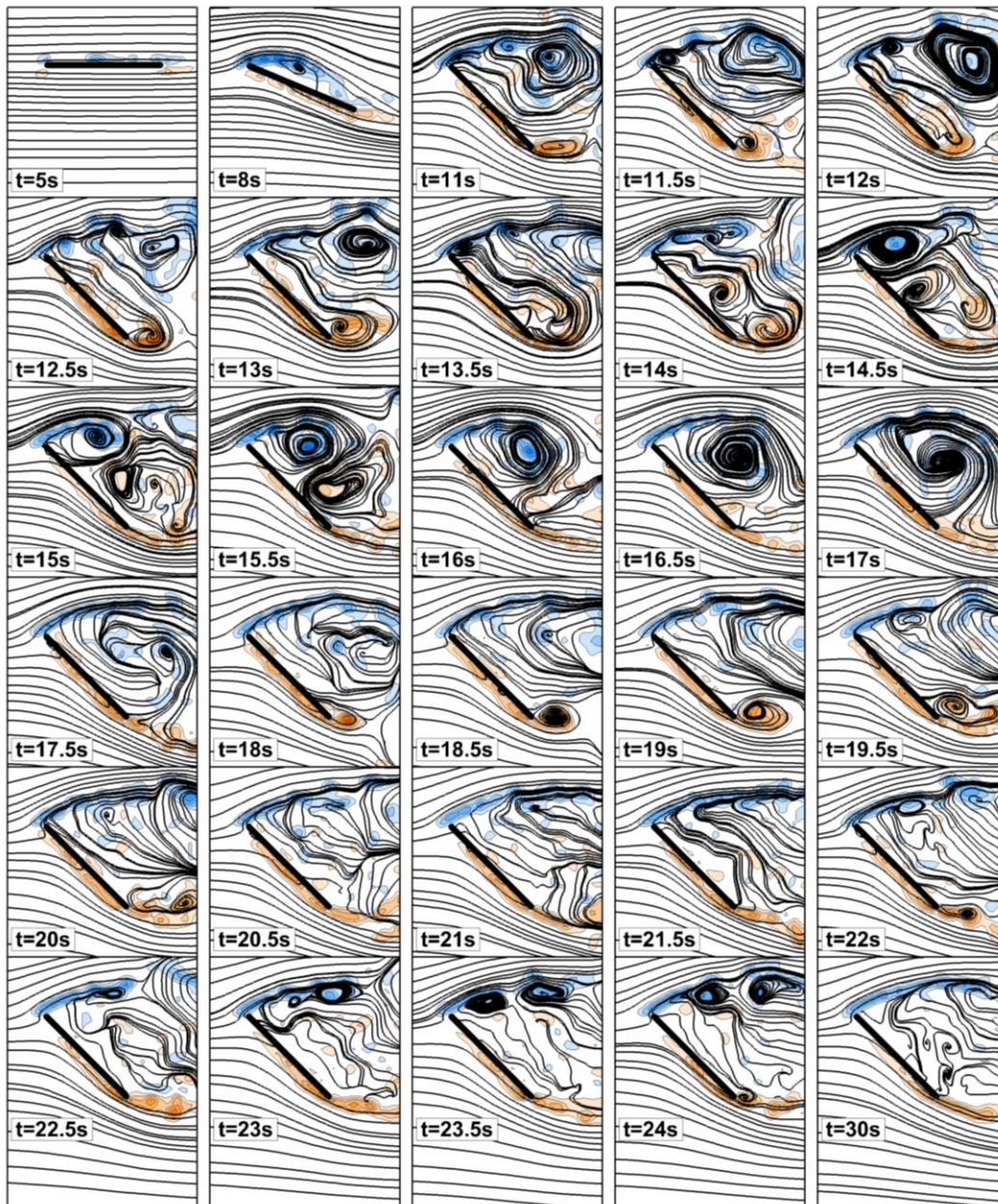


Figure 3.26 : Vorticity contours and streamlines for rigid wing in slow pitch-up motion.

When the flexible cases are considered, lexan and printed wings have similar vortical structures as shown on Figure 3.27 and Figure 3.28. LEV and TEV formation starting from $t=16s$ is more evident in these flexible cases compared to the rigid one.

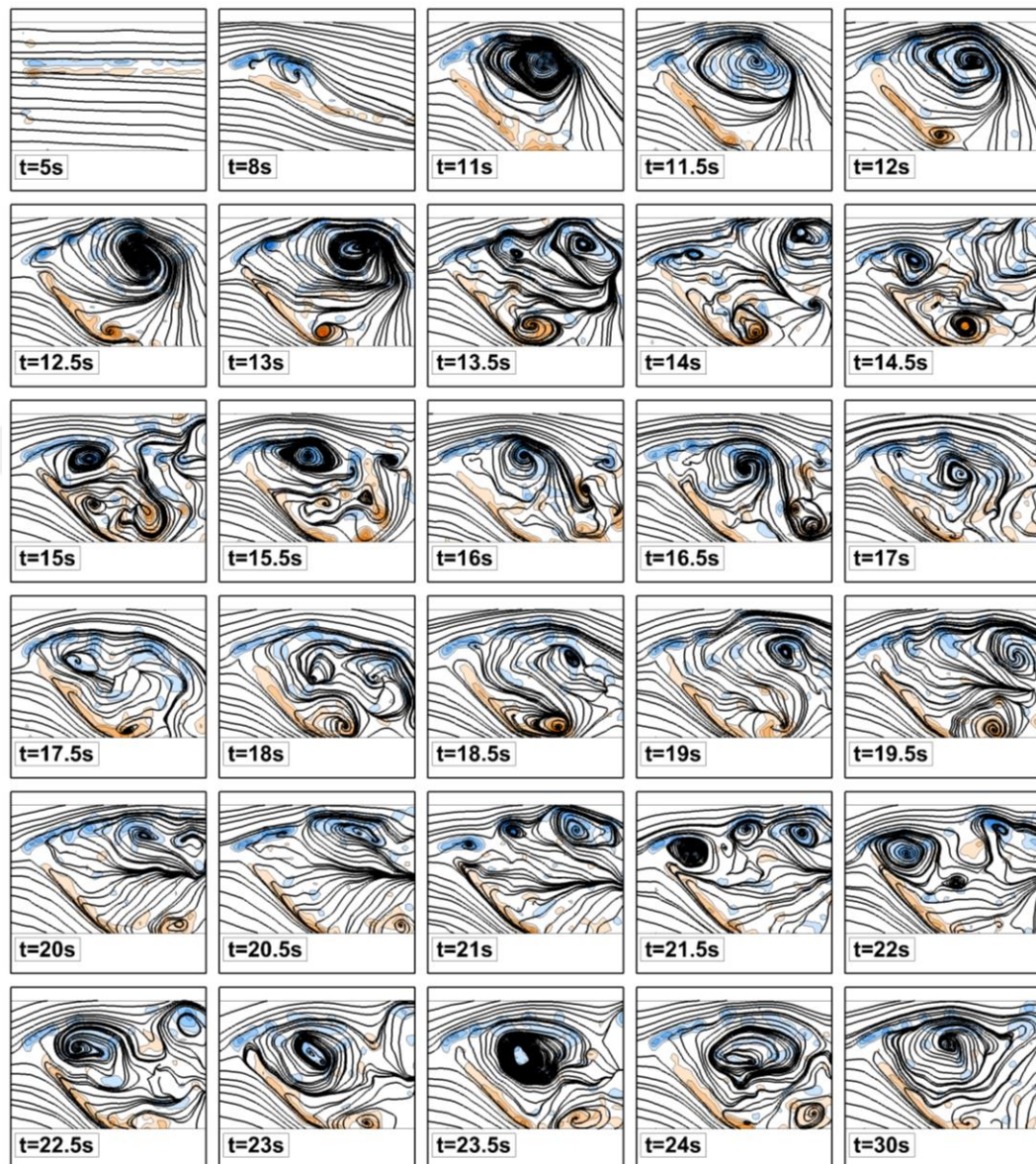


Figure 3.27 : Vorticity contours and streamlines for lexan wing in slow pitch-up motion.

Acetate wing undergoing slow pitch up motion is presented in Figure 3.29. Streamline topology shows differences due to the reduced angle of attack as in the fast motion case. Continuous LEV and TEV vortex shedding can be also observed in that case. During the slow pitch-up motion, emanated LEV is smaller and weaker compared to other three wings.

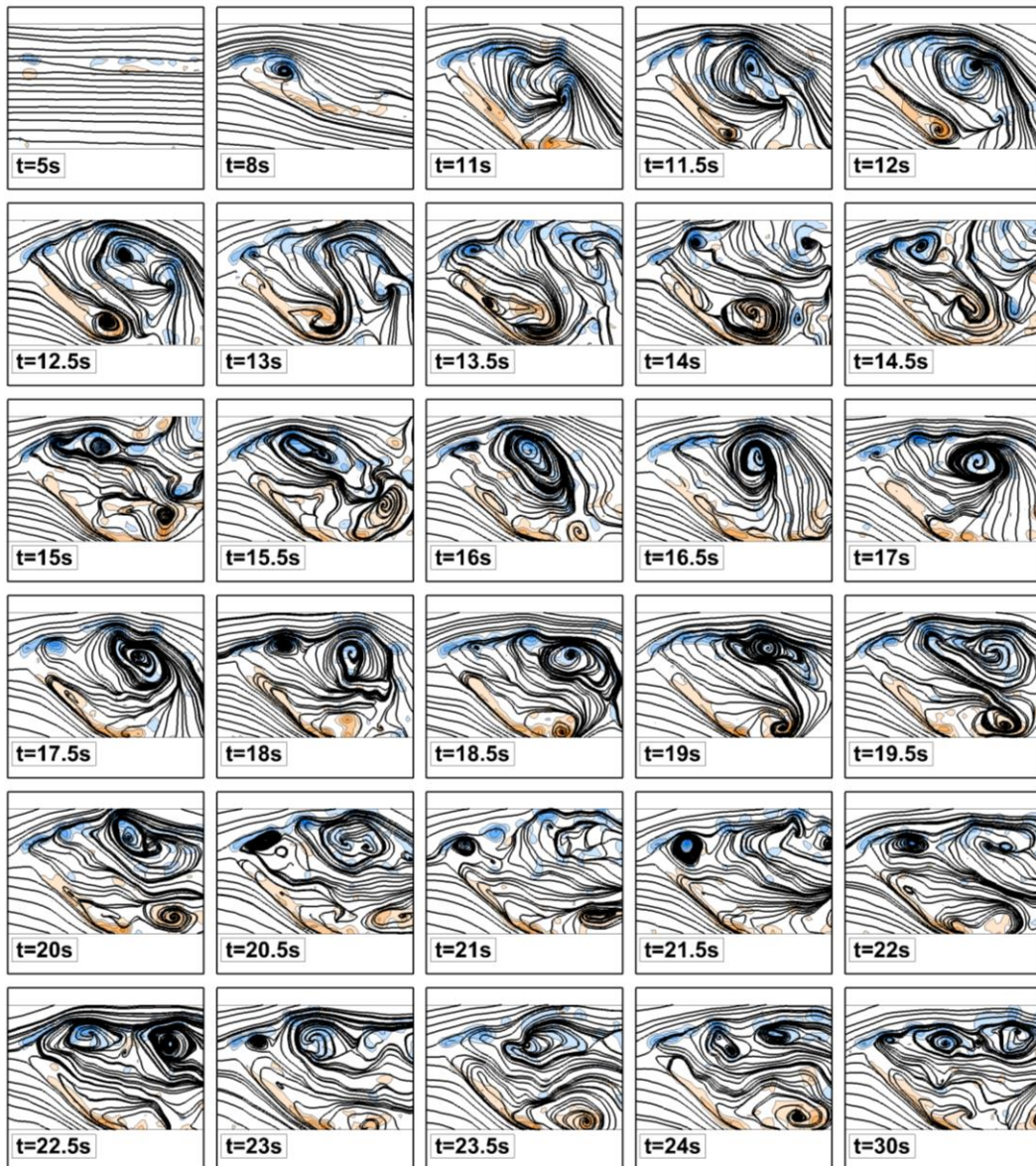


Figure 3.28 : Vorticity contours and streamlines for printed wing in slow pitch-up motion.



Figure 3.29 : Vorticity contours and streamlines for acetate wing in slow pitch-up motion.

3.3 Plunging of a Rigid Wing

Second motion type in the experiments (Son and Cetiner, 2018) is the purely plunging motion with zero degree angle of attack. The motion is harmonic and main parameters are amplitude and frequency of the motion. These parameters are determined by considering the limitations of the force measurement system, motion system and the range of natural frequencies of different flexible materials. Motion parameters are given in Table 3.1.

Table 3.1 : Motion parameters of the plunging wing.

f (Hz)	k ($\pi fc/U$)	a (mm)	(a/c)
0.25	0.785	5	0.05
0.50	1.570	5	0.05
0.75	2.356	5	0.05
1.00	3.141	5	0.05
1.25	3.926	5	0.05
1.50	4.712	5	0.05
1.75	5.497	5	0.05
2.00	6.283	5	0.05
2.25	7.068	5	0.05
0.25	0.785	10	0.10
0.50	1.570	10	0.10
0.75	2.356	10	0.10
1.00	3.141	10	0.10
1.25	3.926	10	0.10
1.50	4.712	10	0.10
1.75	5.497	10	0.10
0.25	0.785	20	0.20
0.50	1.570	20	0.20
0.75	2.356	20	0.20
1.00	3.141	20	0.20
1.25	3.926	20	0.20
0.25	0.785	40	0.40
0.50	1.570	40	0.40
0.75	2.356	40	0.40
0.25	0.785	60	0.60

3.3.1 Force measurement results

Freestream velocity and measured force directions according to the wing cross-section are defined in Figure 3.30, where F_x is the force component in the freestream direction, and F_y is perpendicular to the freestream direction.

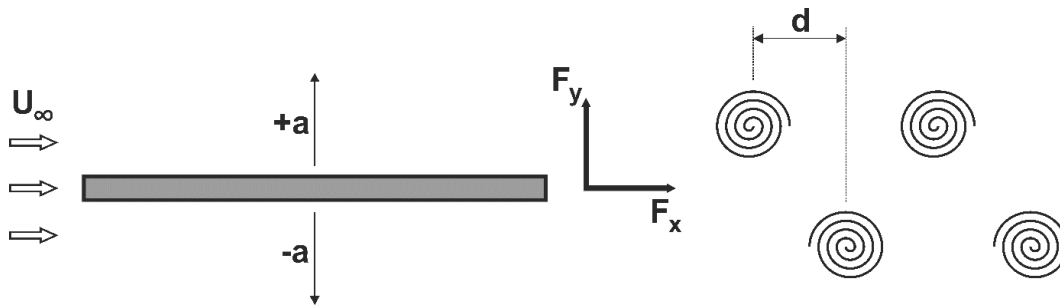


Figure 3.30 : Freestream and force directions.

Forces are measured simultaneously while the plate is undergoing a purely plunging motion. In Figure 3.31, measured F_y force for the plate plunging with a reduced frequency of $k=1.57$ and amplitude of $a/c=0.2$ is presented together with the position

of the plate and Theodorsen solution for the same case. When the plate is at its maximum amplitude, the force is still in an increasing state. The F_y force reaches its maximum during the downstroke of the plate which creates a phase lag between motion and the force. The phase lag between the motion and the F_y is shown on the same graph as Φ_y . Theodorsen solution is quite consistent with the measured force in terms of the phase difference, and the amplitude is slightly lower than the measurement. Considering Theodorsen's theory, the evolution of flow structures yields the circulatory force component, and therefore, a phase lag relative to the kinematics of the plate motion, as also stated in Ol et al. (2009).

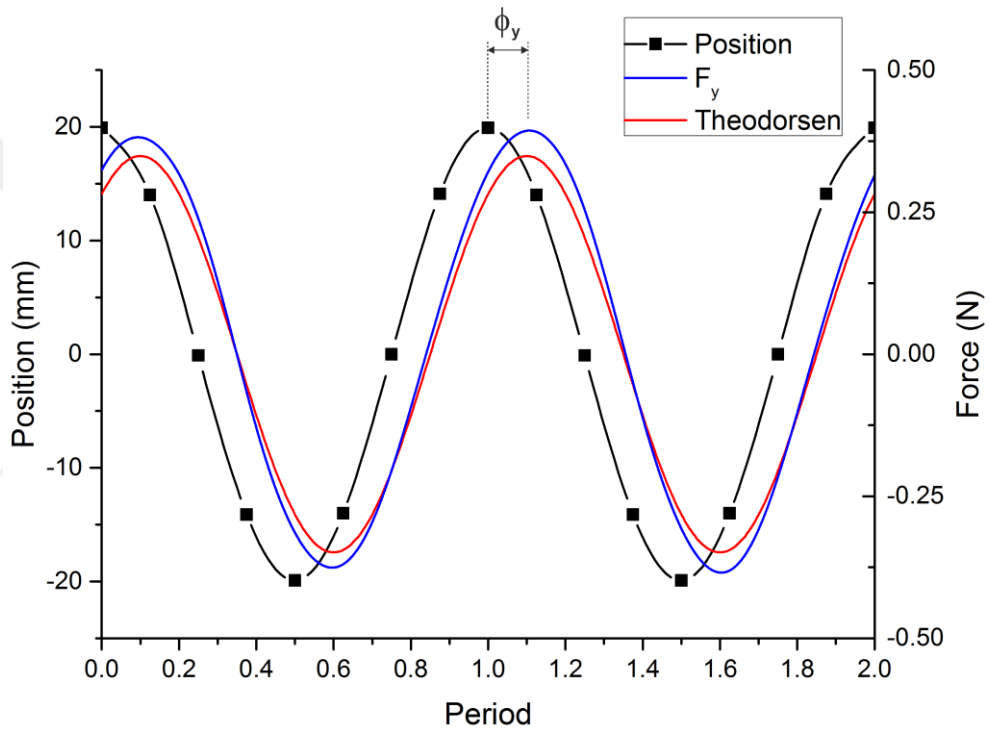


Figure 3.31 : Position of the plate, measured F_y force and Theodorsen solution for $k=1.57$ and $a/c=0.2$.

In unsteady aerodynamics, as the wing position changes by time, the aerodynamic response of the body will have a phase lag with regard to the motion (Gülçat, 2016; Leishmann, 2006). The lift component of the force and the phase lag can be predicted using Theodorsen's theory (Theodorsen, 1935). Garrick (1936) applied the Theodorsen's theory with methods outlined by von Kármán and Burgers (1935) to find the propulsion of an oscillating wing. Evolution of flow structures yields a phase lag in both force components relative to the kinematics of the plate motion. Although the lift force is also a function of the motion's amplitude, the phase lag determined by the Theodorsen's theory is only a function of the reduced frequency. Besides frequency

dependency, variations of the phase lag with amplitude are also investigated in the present experiments.

A pure plunging oscillation can be expressed as follows;

$$h(t) = a \cos(2\pi ft) \quad (3.1)$$

and the lift coefficient for pure plunging oscillation can be given as from Theodorsen's theory;

$$C_L = -\frac{\pi c}{2} \frac{\ddot{h}}{U^2} - 2\pi C(k) \frac{\dot{h}}{U} \quad (3.2)$$

$C(k)$ is Theodorsen function which consists of real and imaginary parts as $C(k)=F(k)+iG(k)$. The function attenuates the lift amplitude and introduces a phase lag in lift response from its real and imaginary parts. The first term in the lift coefficient is the non-circulatory term or the added mass, and the second term includes circulatory effects due to vortex shedding. Circulatory effects are more important at lower reduced frequencies, whereas added mass effects become dominant as the reduced frequency increases. At $k=0$, Theodorsen function becomes $C(k)=1$, and the quasi-steady solution is obtained. It should be noted that the Theodorsen model is based on linear potential flow theory that assumes inviscid flow, small disturbances (attached flow) and a planar wake.

Theodorsen function gives the lift forces and the phase differences as a function of frequency. To visualize the increasing effect of the non-circulatory forces in the total lift with increasing reduced frequency, the circulatory and non-circulatory lift components are plotted in Figure 3.32, separately for four reduced frequencies ranging from minimum to maximum used in the study. As only one amplitude of motion could be tested for the largest reduced frequency ($k = 7.06$), that amplitude ($a/c = 0.05$) is used for the plots given in Figure 3.32. At lower reduced frequencies, the circulatory forces have a dominant effect in total force variation. As the plunging frequency increases, the non-circulatory forces, proportional to the acceleration term in Theodorsen function grow by the square of the plunging frequency and become dominant to the circulatory forces which grow by the plunging frequency as a consequence of being proportional to the velocity term in the function. When the noncirculatory forces become dominant compared to the circulatory forces, the total

force variation becomes more in phase with the variation of the wing position, because the acceleration values are the highest as the wing is close to its peak positions.

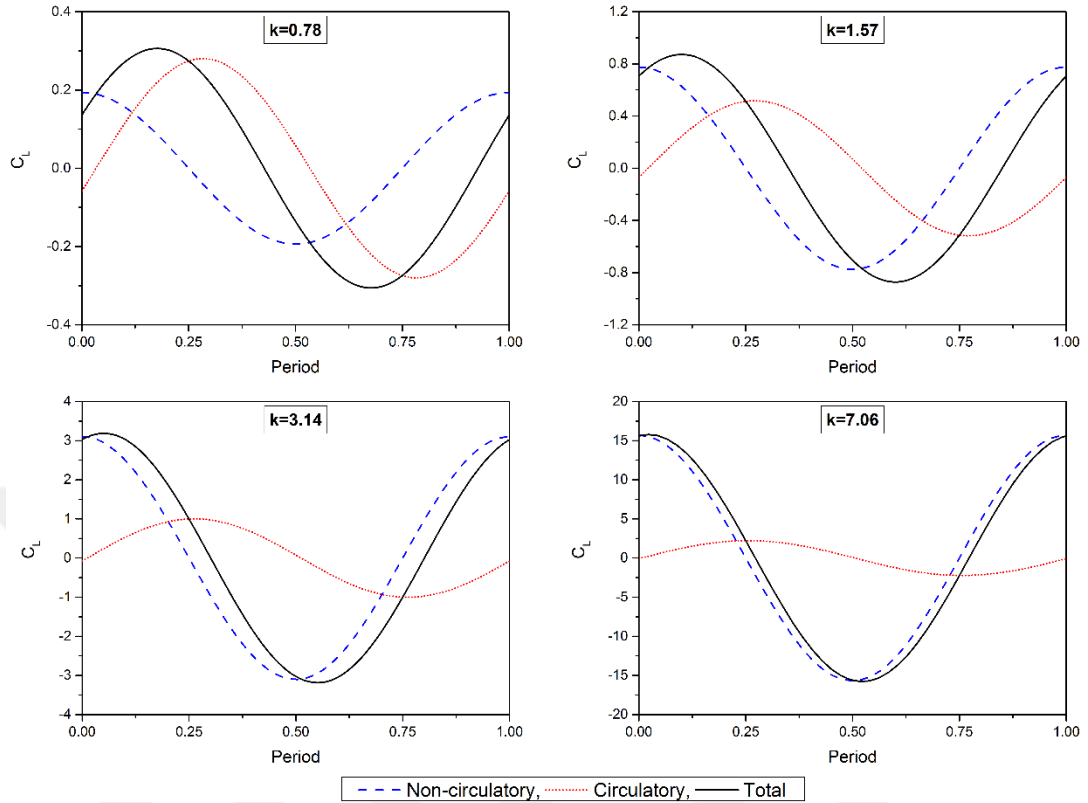


Figure 3.32 : Contribution of non-circulatory and circulatory force components to the total lift force for four different reduced frequencies.

In the experiments, amplitude dependence of the phase lag is also investigated and presented in Figure 3.33 for the F_y force. As it can be seen from the figure and in accordance with the Theodorsen's function, the phase lag is higher at lower reduced frequencies, and the lag decreases when the reduced frequency is increased. The increase in the amplitude has an effect of increasing the lag for the same plunging frequency. It should be noted that the Theodorsen's theory considers attached flow; therefore, a deviation is expected for motions at higher reduced frequencies with high motion amplitudes. On the other hand, at higher reduced frequencies, the non-circulatory term becomes dominant and forces the lift response to be in phase with the motion kinematics. Therefore, as long as the motion amplitude is small, the Theodorsen solution holds reasonably well for higher reduced frequencies in the present experiments. However, for large motion amplitudes, the deviation from the Theodorsen solution occurs at lower reduced frequencies; the deviation is larger when the amplitude of motion is increased for the same reduced frequency. Phases

determined by Theodorsen function are also presented in the same graph, which has a compatible variation with the experimental results.

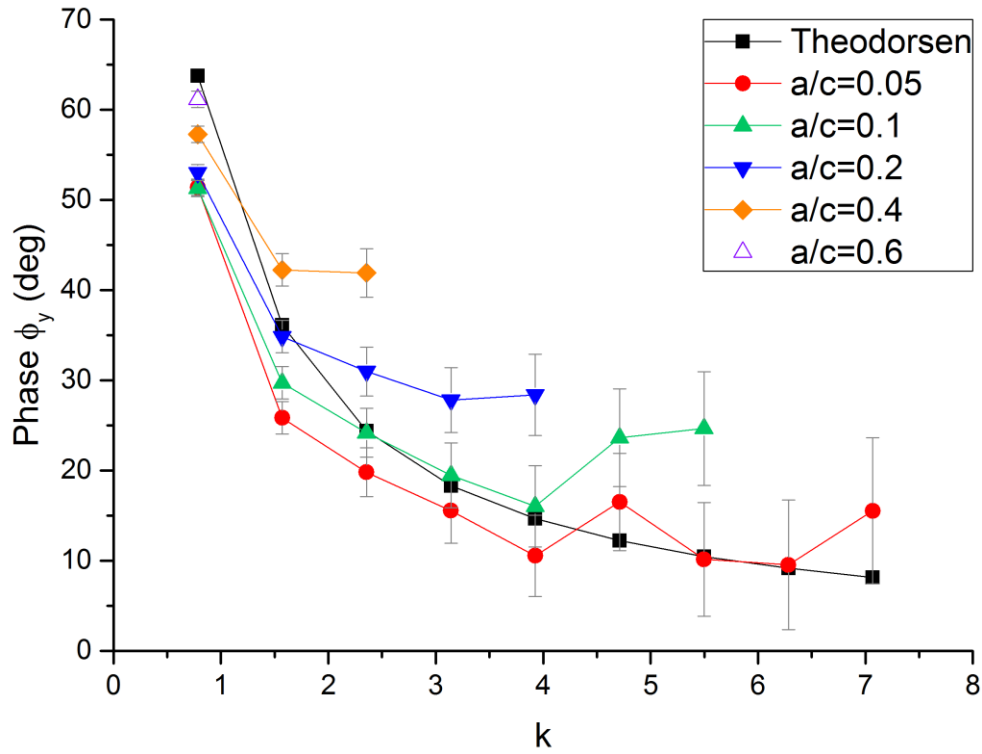


Figure 3.33 : Phase lag between F_y and the motion.

Phase lag on the streamwise force component F_x is determined in the same manner as F_y ; however, there are some differences on the force distribution over one period. For the plunging motion at 0° angle of attack, thrust is produced twice in one period of motion. Both downstroke and upstroke motions create thrust (or drag) in freestream direction that results in double peaks on force distribution in a period, as shown in Figure 3.34. In that case, two phase values are determined: the first one is the difference between the maximum position of the plate and the first thrust peak (Φ_{x1}), and the second one is the difference between the minimum position of the plate and the second thrust peak (Φ_{x2}). Average of these two-phase differences is calculated, and then, the final streamwise force phases are determined as $\Phi_x = (\Phi_{x1} + \Phi_{x2})/2$. Results obtained from Garrick's theory for the reduced frequency of $k = 1.57$ and flapping amplitude of $a/c = 0.2$ are also presented in Figure 3.34. As aforementioned, Garrick's theory is an extension of Theodorsen's theory for the propulsion of a flapping airfoil. In purely plunging motion, the formula for sectional propulsive force coefficient based on Garrick's theory is presented in Gulcat (2016) as follows:

$$C_s = -2\pi k^2 [G(k) \cos(2\pi ft) + F(k) \sin(2\pi ft)]^2 \left(\frac{2a}{c}\right)^2 \quad (3.3)$$

The mean value of streamwise force component F_x and Garrick's solution are biased to zero to observe the phase and amplitude differences. The amplitude of the measured force is slightly higher compared to theoretical solution, and the phase of two distributions is quite close.

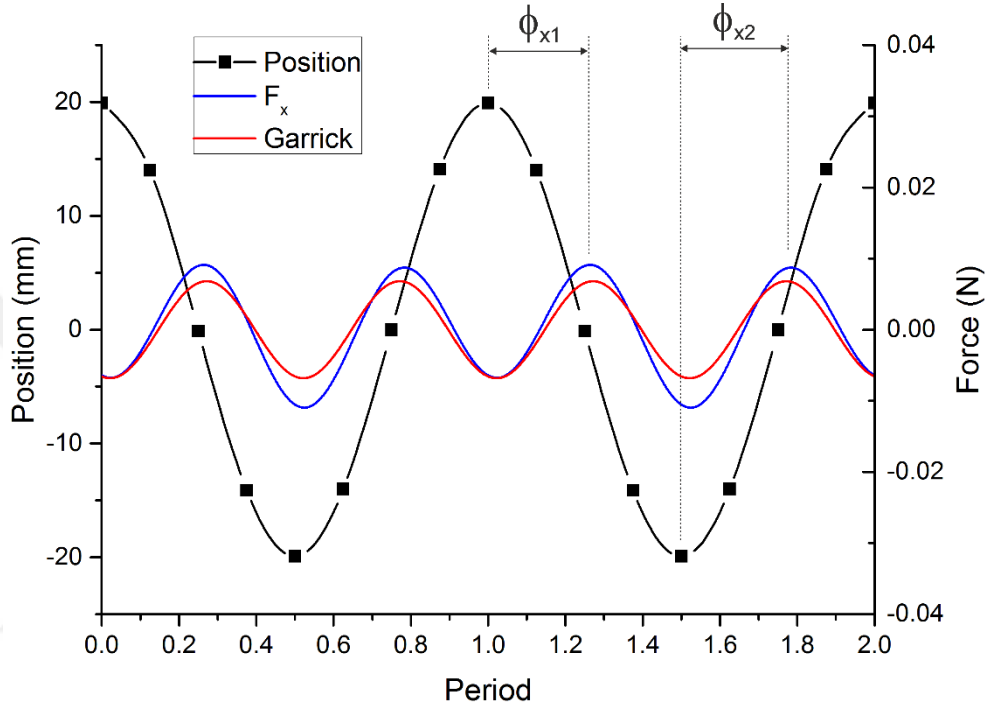


Figure 3.34 : Position of the plate and measured F_x force for $k = 1.57$ and $a/c = 0.2$.

Phase lag variations of F_x are presented in Figure 3.35 as a function of reduced frequencies and amplitudes. For amplitudes of $a/c = 0.05$ and $a/c = 0.1$, the phase lag is higher at lower frequencies and phase lag values decrease as the frequency increases. At lower frequencies, phase lag decreases towards the value of 90° when the amplitude is increased. For amplitudes of $a/c = 0.2$ and $a/c = 0.4$, a minimum phase lag around $\Phi_x = 90^\circ$ is determined, and then, the values start to increase. 90° phase lag means that the thrust is maximized at the mid-point of the full range of the flapping amplitude (position = 0 mm), where the wing has its maximum velocity. Increases in the phase lags can be clearly observed for the two large amplitude cases after the minimum is reached at $\Phi_x = 90^\circ$. When $a/c = 0.4$, this minimum is obtained for $k = 1.57$, and when $a/c = 0.2$, it is at $k = 2.35$. A slight increase can also be observed after $k = 3.92$ when $a/c = 0.1$. These points coincide with the drag/thrust transition of the wing as given in Figure 3.36. After the thrust is being produced, the phases tend to increase. Increased

phase lag means that the force in the stream direction is maximized later than the wing reaches its maximum velocity. Phase lags on the streamwise force component obtained from Garrick's theory are also presented in Figure 3.35. At low reduced frequencies, the phase is higher and when the reduced frequency increases, the values are converging to 90°.

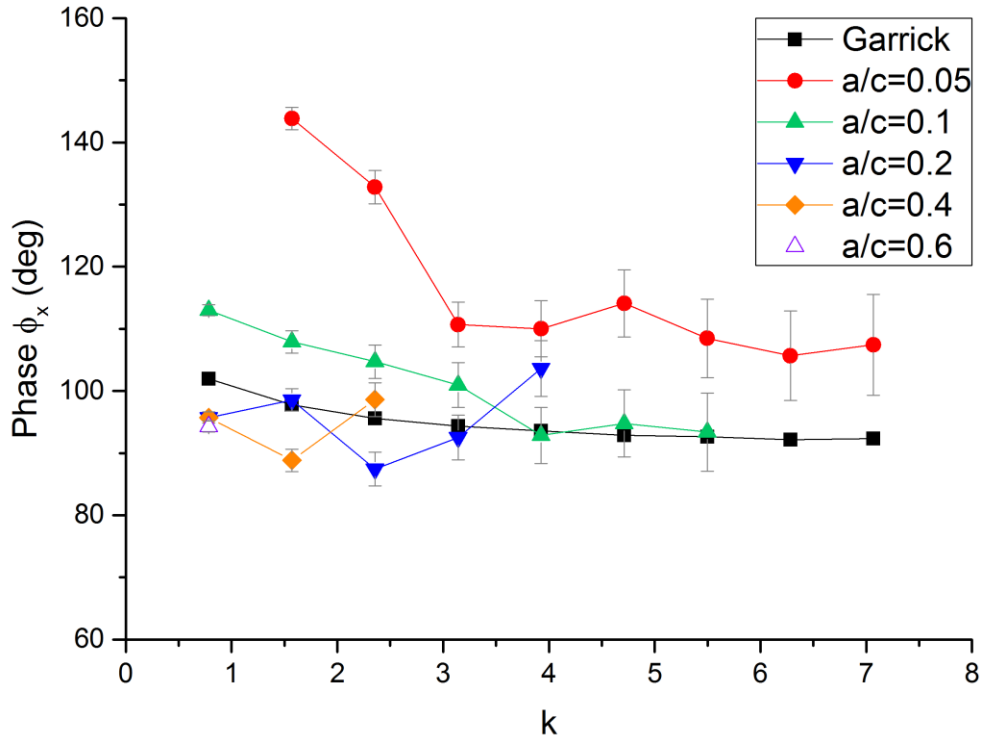


Figure 3.35 : Phase lag between F_x and the motion.

Thrust coefficients (C_T), power input coefficients (C_P) and efficiencies (η) are calculated (Figure 3.36) based on the formulas presented in Heathcote and Gursul (2007).

$$C_T = \frac{\overline{F_x}}{\frac{1}{2}\rho U^2 c s} \quad (3.4)$$

$$C_P = \frac{\overline{F_y v}}{\frac{1}{2}\rho U^3 c s} \quad (3.5)$$

$$\eta = \frac{C_T}{C_P} \quad (3.6)$$

Where $\overline{F_x}$ is the time-averaged streamwise force component, s is the span length, and $\overline{F_y v}$ is the time average of cross-stream force component multiplied by the

instantaneous velocity of the plate. Efficiency is defined as the resultant C_T is divided by the C_P .

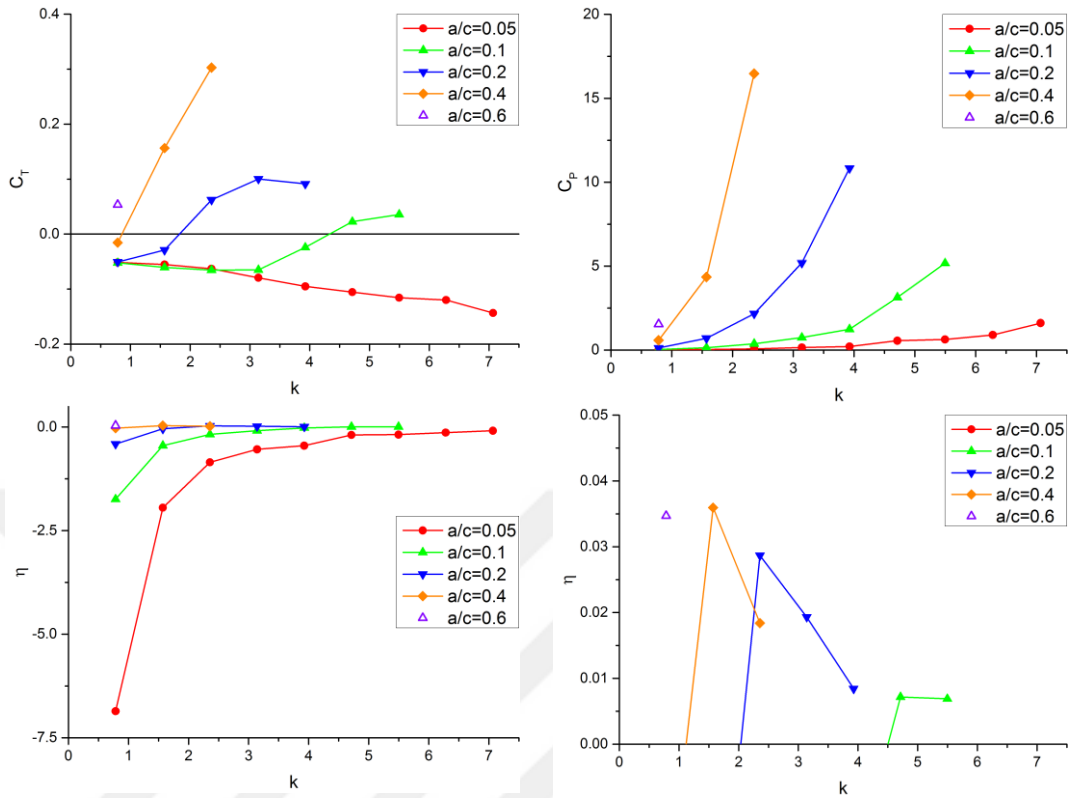


Figure 3.36 : Thrust coefficients (C_T), power input coefficients (C_P) and efficiencies (η) (lower left: full scale, lower right: thrust producing cases only).

When Figure 3.36 is considered, it can be seen that thrust coefficients are increasing as the flapping frequency increases. In addition, higher thrust is obtained when the amplitude increased. Zero line on the y-axis indicates the drag/thrust transition; values below the line imply drag and above the line are indicating thrust production. The variation of C_T with respect to the reduced frequency is examined together with Figure 3.35 to reveal the thrust force and the phase relations. As aforementioned, when C_T values change from negative to positive, phase lag starts to increase. As a particular case, if $a/c = 0.2$ is considered, $k = 2.35$ is the frequency where phase lag is at the onset of a rise. This point on the C_T graph is right above the zero line, and a frequency rise to $k = 3.14$ leads to an increase in thrust coefficient and also in phase lag. Similar observations can be made for amplitudes of $a/c = 0.4$ and $a/c = 0.1$. Although a similar and distinct increase in the phase angle of the streamwise force is present and beyond the uncertainty range for $a/c = 0.4$, the onset of a rise for $a/c = 0.1$ should be reworded as the end of decrease due to the fact that the uncertainty increases with increasing

reduced frequency which is a consequence of using a constant data sampling rate for all cases.

Power input coefficients (C_P) have the same variation character with C_T , both amplitude and frequency increases lead to a rise in C_P values. Since both C_T and C_P follow the same trend, the analysis will be made on the efficiency which combines the two. Drag producing cases have a negative sign for C_T values; therefore, negative efficiency values are indicating drag in Figure 3.36. On the lower right, the efficiency plot is zoomed in above zero in Figure 3.36 to focus on the thrust producing cases. The case of $a/c = 0.4$ and $k = 1.57$ exhibits the highest efficiency among all thrust producing cases. Although this case does not exhibit the highest thrust, its low power input coefficient leads to a greater efficiency.

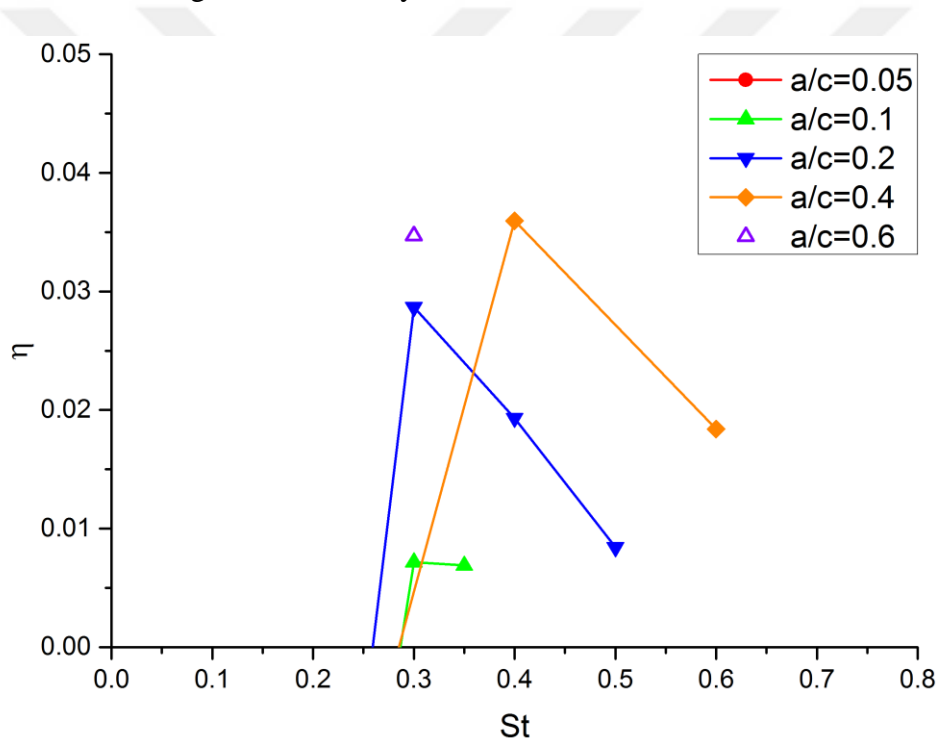


Figure 3.37 : Efficiencies (η) with respect to Strouhal number.

The efficiencies on Figure 3.36 are presented with respect to the reduced frequency of the flapping wing. If the efficiencies are plotted with respect to the Strouhal number, peak points gather into a Strouhal number range of 0.25 – 0.4, as shown in Figure 3.37. This Strouhal number range coincides with the ranges where optimum propulsive efficiency is found and reported in the previous studies (Triantafyllou et al., 1991; Anderson et al., 1998). Another observation that should be added is that the same Strouhal numbers obtained for different plunge amplitudes do not yield the same efficiencies. Higher amplitude cases are observed to yield higher efficiencies in the

thrust producing regime. It should also be noted that the reduced frequencies at which the maximum efficiencies are obtained coincide with those where the phase lag in streamwise force is minimum and close to a value of 90° .

3.3.2 DPIV results

DPIV measurements of the plunging rigid wing are performed and the relation between vortical structures and the force measurements are revealed. In the previous chapter, the focus was directed into the phase lag between the plunging motion and force measurements, which is not studied in the literature thoroughly.

As aforementioned, evolution of flow structures is responsible for the phase lag in both force components relative to the kinematics of the plate motion. Although the force component in the cross-stream direction also includes a non-circulatory term, the force component in the freestream direction is only governed by circulatory effects. Therefore, to put forward the flow physics in the variation of loading with respect to the motion kinematics, namely the phase lag in forces, in addition to the force and phase measurements, vortical structures around the plate are visualized via a DPIV system. In Figure 3.38, selected vorticity contours are presented at an instant corresponding to the maximum position of the plate for the case with a plunge amplitude of $a/c = 0.1$. At low frequencies ($k = 0.78$), the wake has a wavy character, and the wavelength of the oscillating wake is high. As the frequency increases, vortical structures become coherent, and counter-rotating vortices on the wake can be tracked easily. Reverse Karman-street type vortex structures are observed starting from $k = 3.14$. At higher frequencies, the horizontal distance between counter-rotating vortices decreases and vortices start to burst early. The horizontal distance between vortex cores indicates one of the important wake characteristics, and as shown in the study of Monnier et al. (2015), mean thrust is inversely proportional to horizontal spacing of the vortices. In the present study, the horizontal distance between vortex cores is denoted as d , as shown in Figure 3.30, and non-dimensionalized with the chord length (d/c). When d/c is plotted with respect to the reduced frequency as can be seen in Figure 3.39, it is evident that the horizontal distance variation shows a similar character as that of the cross-stream force phase variation presented in Figure 3.33. The maximum uncertainty in the detection of horizontal distance between vortices is the same as the vector resolution. At lower frequencies, the phase lag is high, and the

distance between vortices is large. As the plunging frequency increases, vortex cores are getting closer, and phase lag reduces. An increase in plunge amplitude for a given reduced frequency generally results in a rise in the horizontal distance between vortices and in the phase lag.

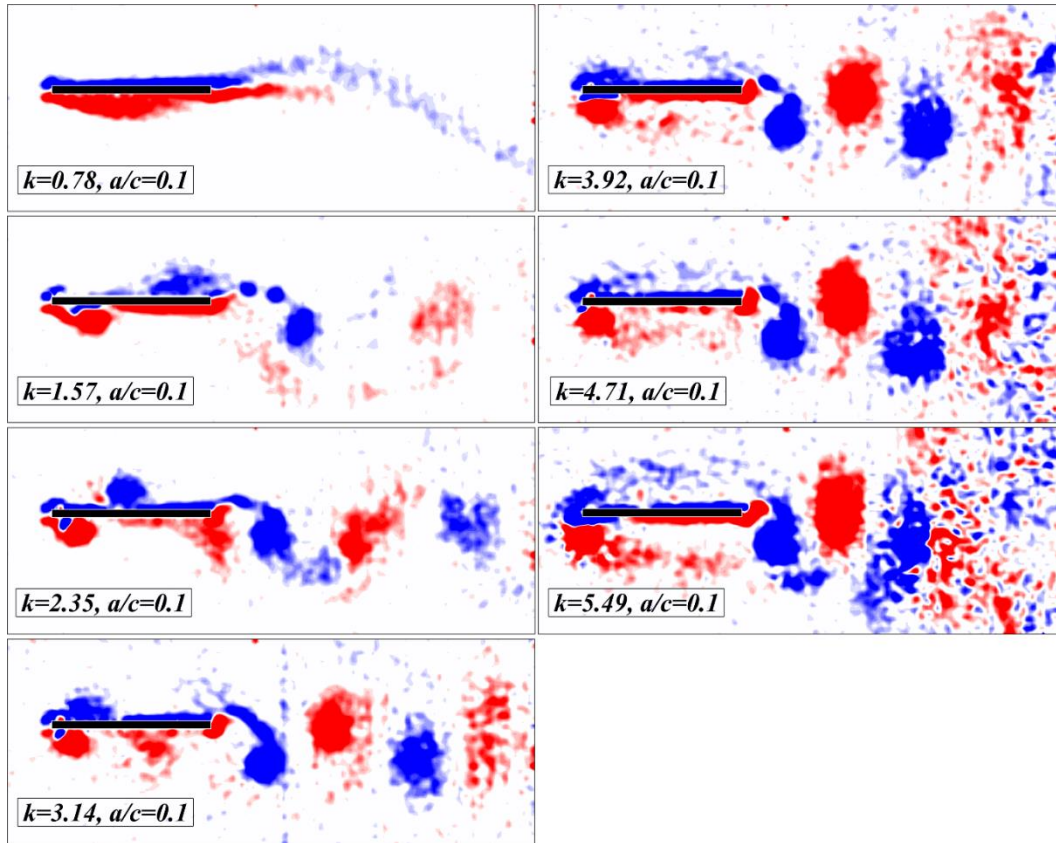


Figure 3.38 : Vortical structures around the plate plunging at an amplitude of $a/c = 0.1$.

Vortex array orientation in the wake is investigated in the experimental study of Bohl and Koochesfahani (2009) for a sinusoidally pitching NACA-0012 airfoil. They indicated that, as the reduced frequency increases, the transverse alignment of the vortex array changes from an orientation corresponding to a wake profile to one corresponding to a jet-like profile. However, the switch in the vortex array orientation is not found to match with the crossover from drag to thrust. The similar observation can be made in the present experiments. In Figure 3.38, a reverse Karman street is observed starting from the reduced frequency of $k = 3.14$; however, the crossover from drag to thrust is observed at higher reduced frequencies between $k = 3.92$ and $k = 4.71$ for the plunge amplitude of $a/c = 0.1$. Therefore, the thrust production is not started at the exact reduced frequency when the wake turns to a reverse Karman vortex street but at a slightly higher frequency after the reverse Karman street is observed.

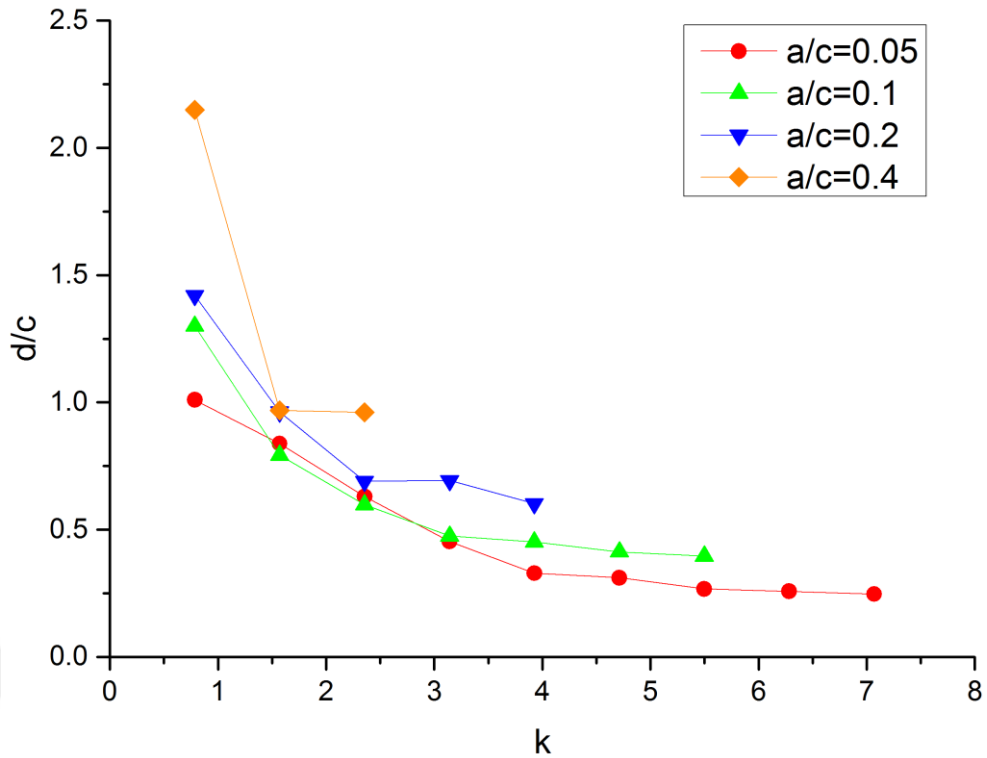


Figure 3.39 : Horizontal distance between vortex cores.

Apart from the observations related to the orientation of trailing edge vortices shed to the wake, the formation of the leading edge vortex can be observed starting from the reduced frequency of $k = 1.57$, also evident in Figure 3.38. LEV emanates and sheds moving along the plate surface, and this behavior can be observed for plunging frequencies up to $k = 3.92$. Above that frequency, LEV is not swept with the freestream and stays around the leading edge until the plate moves on and breaks it. The plunging frequency where the LEV is observed to start holding around the leading edge coincides with the plunging frequency where the increase in the phase of streamwise force begins (Figure 3.35). As aforementioned, this frequency and beyond is also indicative of the beginning of thrust production. In summary, three observations are combined yielding that there exists a threshold reduced frequency, different for each a/c , where, at the same time, emanated LEV stays on the leading edge, phase lag increases and thrust production starts. The threshold reduced frequency is low for large amplitudes of motion and high for small amplitudes in agreement with the observations of Triantafyllou et al. (1993) and Jones et al. (1996) where the crossover from drag to thrust depends on the plunge velocity which is a product of reduced frequency and a/c . The time-averaged wakes for the cases presented in Figure 3.38 are given in Figure 3.40. The velocity profile in the wake presented in the figure is obtained by subtracting

the freestream velocity from the streamwise velocity component. The time-averaged wake of the case that gives a reverse von Kármán street presents a jet-like flow close to the centerline of the motion; however, a reverse flow is present above and below this core region. Considering the integration of momentum to obtain the loading, the result of obtaining drag or thrust depends on the extent and the strength of the two regions. Although a jet-like flow is present for $k = 3.14$, it is obvious that reverse flow region is dominant and, as a result, drag is obtained. For $k = 3.92$, it would not be wise to comment on drag or thrust production just with the observation of a jet-like flow. As stated in Bohl and Koochesfahani (2009), the switch in the vortex array orientation is not found to match with the crossover from drag to thrust. Actually, a qualitative flow observation will fall short to estimate the net force in this crossover region, since, in such an unsteady flow case, the calculation of the force also needs to incorporate the velocity fluctuations into the control volume analysis around the plate.

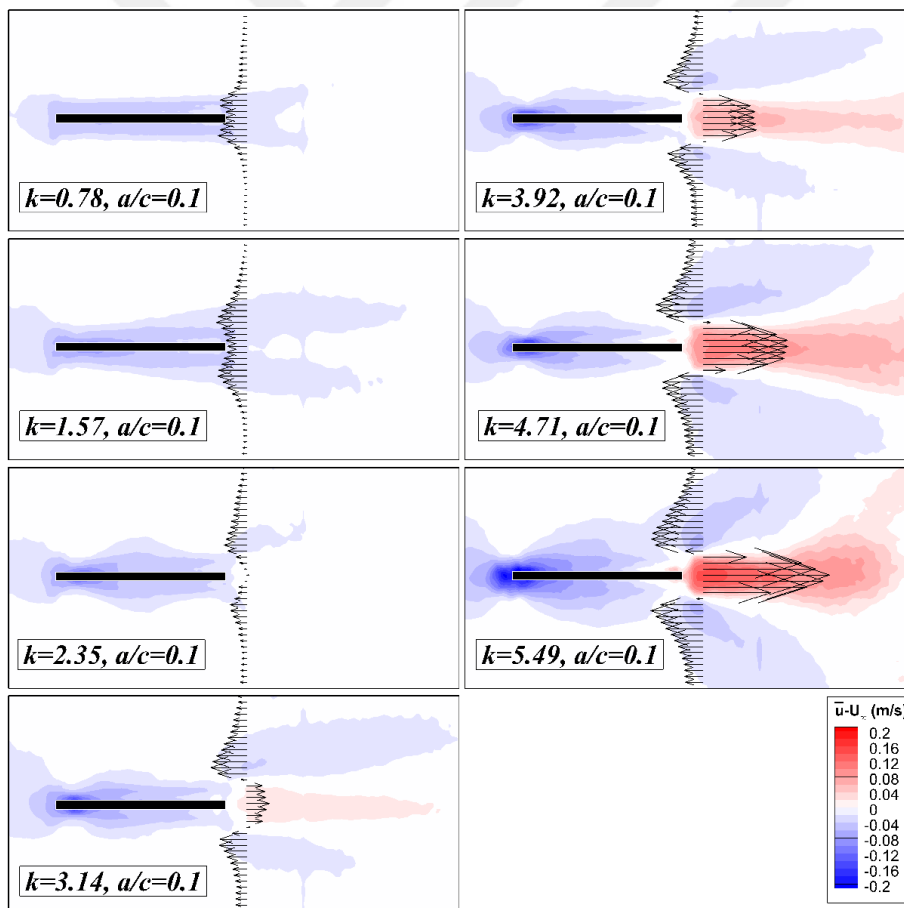


Figure 3.40 : Time-averaged velocity profile in the near-wake and distribution of $u - U_\infty$ for the plate plunging at an amplitude of $a/c = 0.1$.

DPIV vorticity contours detailed in time within one plunge cycle are presented in Figure 3.41 for the plunge motion. Alternate shedding of leading edge vortices can be

seen in the left column of images given for the case of $k = 2.35$ with an amplitude of $a/c = 0.1$. LEVs are convecting towards the trailing edge of the plate and interacting with the trailing edge vortices. This is a drag producing case, which can also be confirmed by the vortex array orientation in the near-wake. In the right column of images, results are presented for the case of $k = 4.71$, with an amplitude of $a/c = 0.1$. LEVs are also emanating for that case; however, they hold around the leading edge until they encounter the plate on its way back and do not shed into the wake. As a result, the wake exhibits a reverse Karman vortex street, and a thrust producing case is obtained.

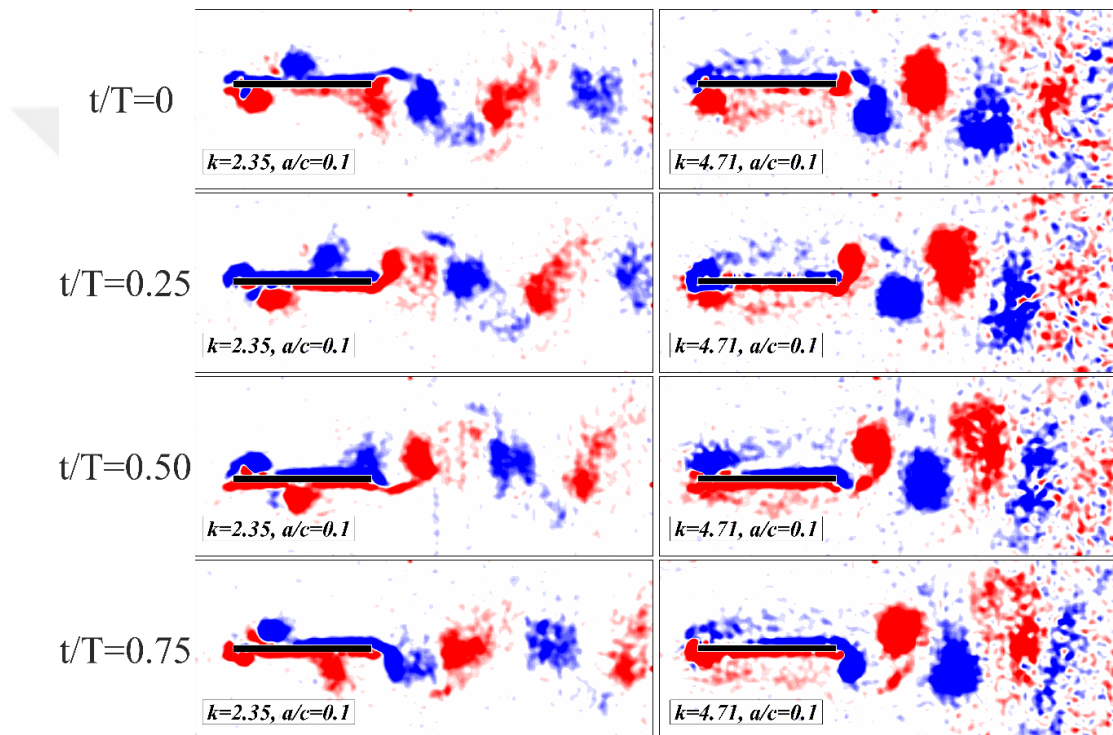


Figure 3.41 : Comparison of two different LEV shedding mechanisms in a motion cycle.

This LEV and wing interaction is previously observed and mentioned in the study of Cleaver et al. (2011) for an NACA-0012 profile performing sinusoidal plunging motion with a fixed geometric angle of attack of 15° . Their resultant flow field is characterized by low lift and high thrust. They suggested that both stronger trailing edge vorticity and absence of the destructive interference from the leading edge vortex facilitate the thrust production. In the present study, similar observations are made for a flat plate sinusoidally plunging with 0° angle of attack and thrust production is started when the leading edge vortex is not anymore convected downstream and remained near the leading edge. Although this conclusion is exemplified only for $a/c = 0.1$ in

Figure 3.38 and Figure 3.41, it should be noted that all cases are reviewed in this perspective, and no exceptions are identified.

The onset of thrust production linked above to the evolution of flow structures coincides with the minimum of the streamwise force phase with respect to the motion kinematics which is close to a value of 90° . At this reduced frequency, the efficiency of flapping is also maximized. Although thrust increases up to a certain reduced frequency for thrust producing cases, power input continuously increases with the reduced frequency with a much higher gradient, mainly due to the non-circulatory effects. As a consequence, the maximum flapping efficiency is achieved when a net thrust is first obtained with its instantaneous maximum at the maximum flapping speed.

3.4 Effect of Flexibility for Plunging

In previous section, pure plunging motion of the rigid wings was investigated by mainly focusing on the phase relations between motion and force measurements. In this section, these phase relations are examined when different degrees of flexibilities are introduced to the wings. Wing shapes for different cases of flapping frequencies and amplitudes are reported. Force measurements and PIV results are presented by comparing the wings with different flexibilities.

3.4.1 Airfoil shape characteristics

As distinct from previous section on rigid flapping wings, flexible flapping wings have shape deformations depending on the loading and the degree of flexibility of the wings. In the present study, the flexibility is only allowed on the chordwise direction. Images acquired from the PIV system are used to determine the shape of the wings in a flapping cycle. Characteristics of the wing shapes are revealed before commenting on the force measurements and the vortical structures around the flexible wings. The epitome of the wing shapes in the present flapping frequency-amplitude measurement range are presented in Figure 3.42 - Figure 3.44 for different flexible wings. The horizontal axis in Figure 3.42 - Figure 3.44 corresponds to flapping frequency and the vertical axis corresponds to flapping amplitude.

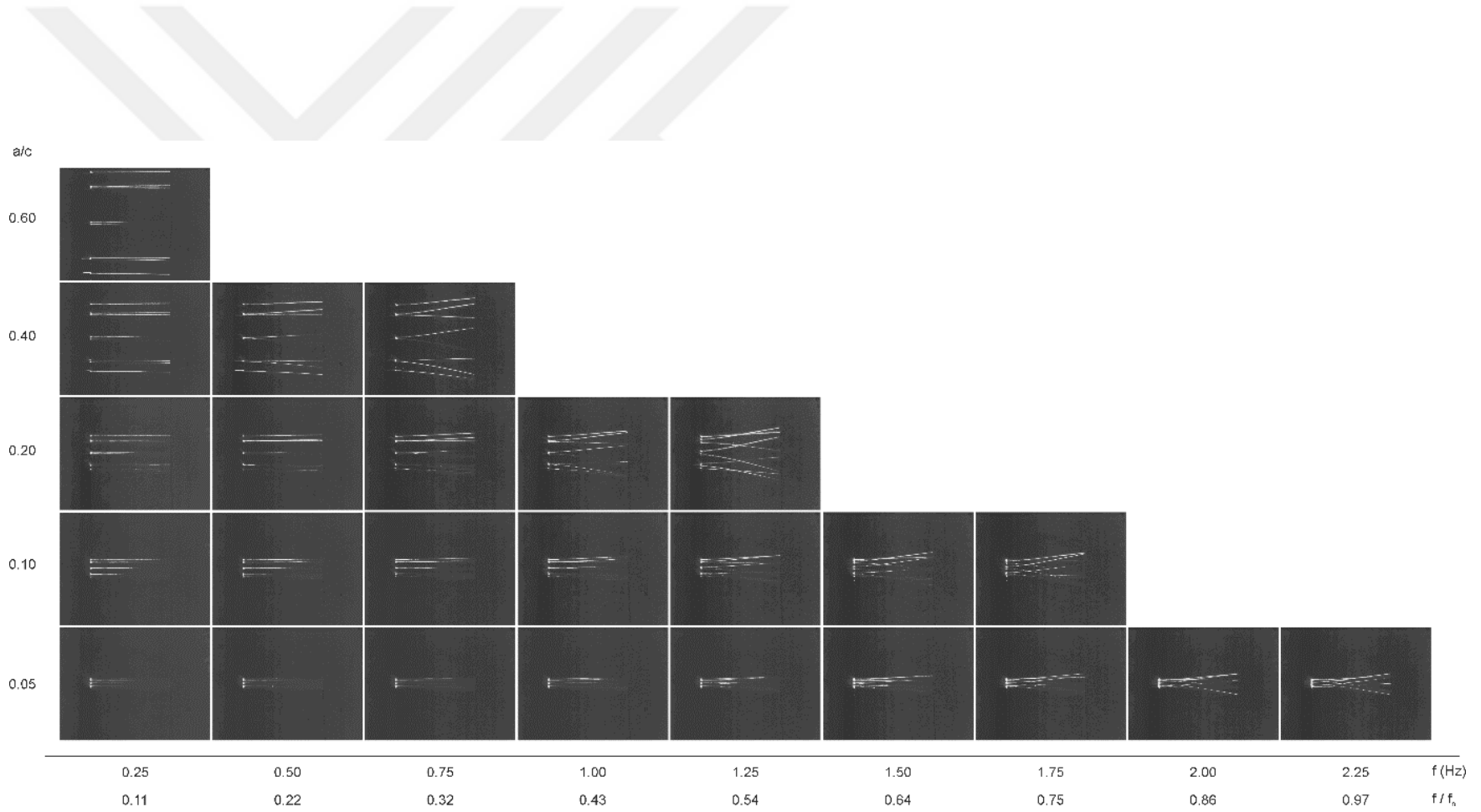


Figure 3.42 : Airfoil shapes for the lexan wing.

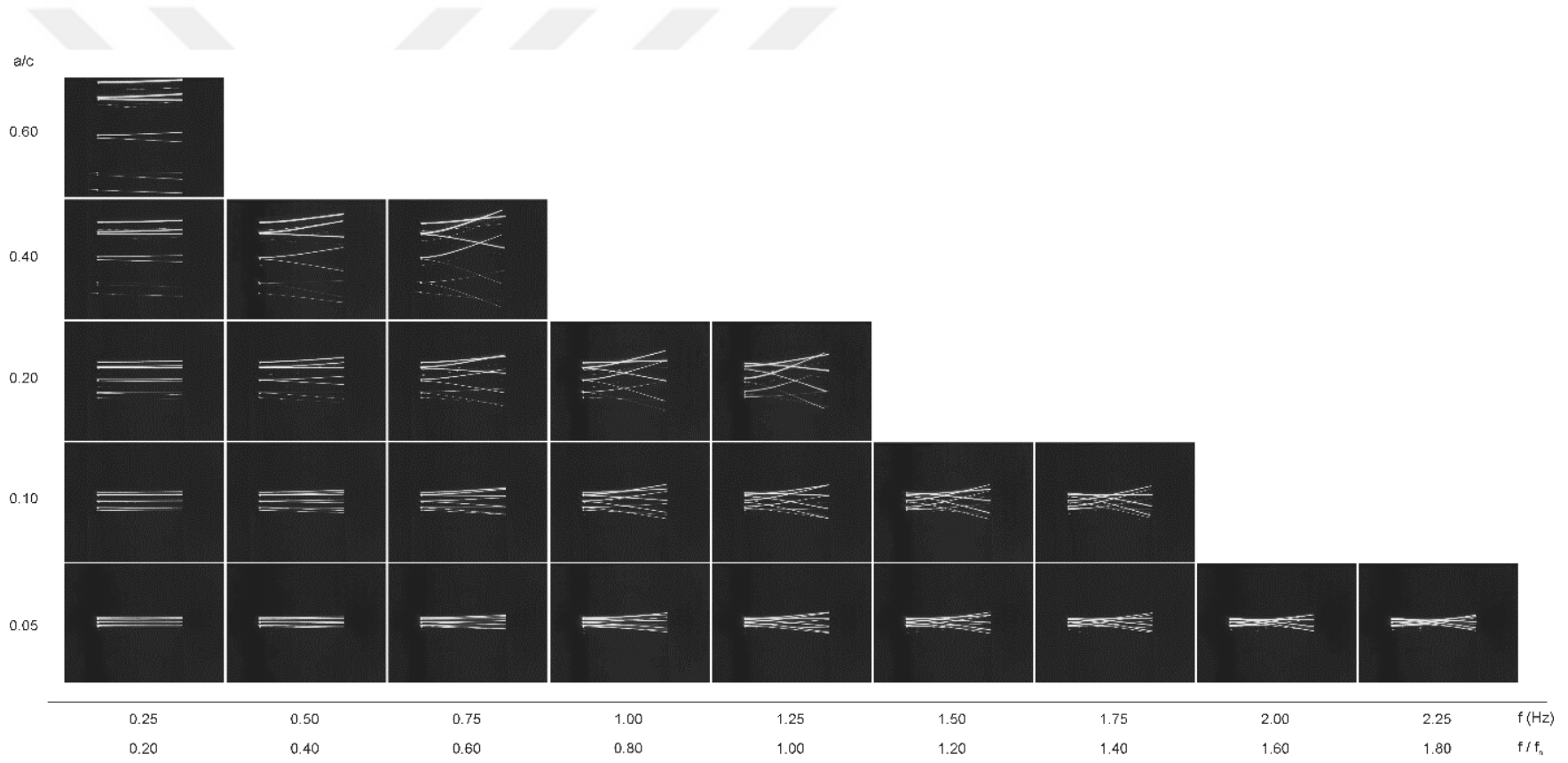


Figure 3.43 : Airfoil shapes for the printed wing.

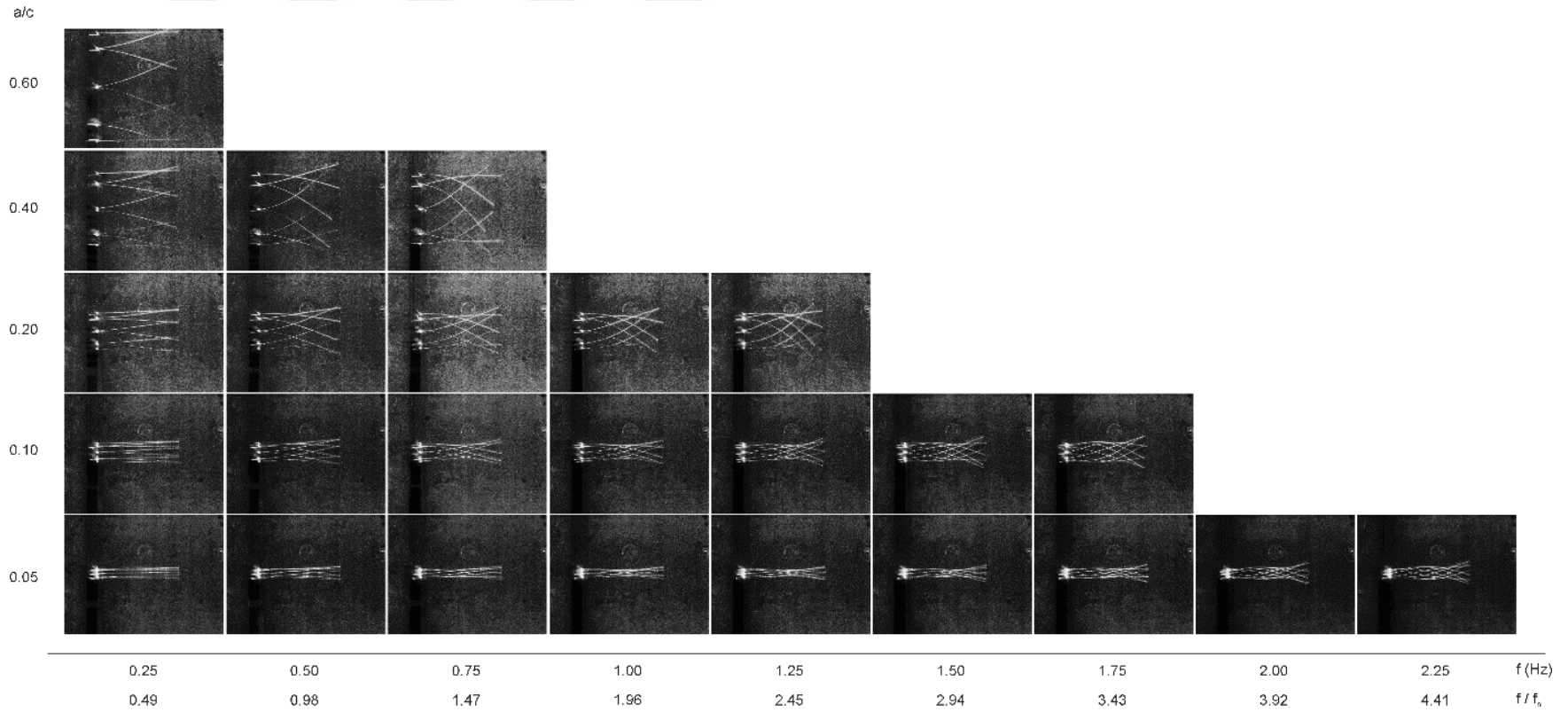


Figure 3.44 : Airfoil shapes for the acetate wing.

Horizontal axis also contains flapping frequencies normalized by the natural frequency of the flexible wing. By doing so, natural frequency effects are aimed to be demonstrated and the universality of the shape deformations near natural frequency is investigated.

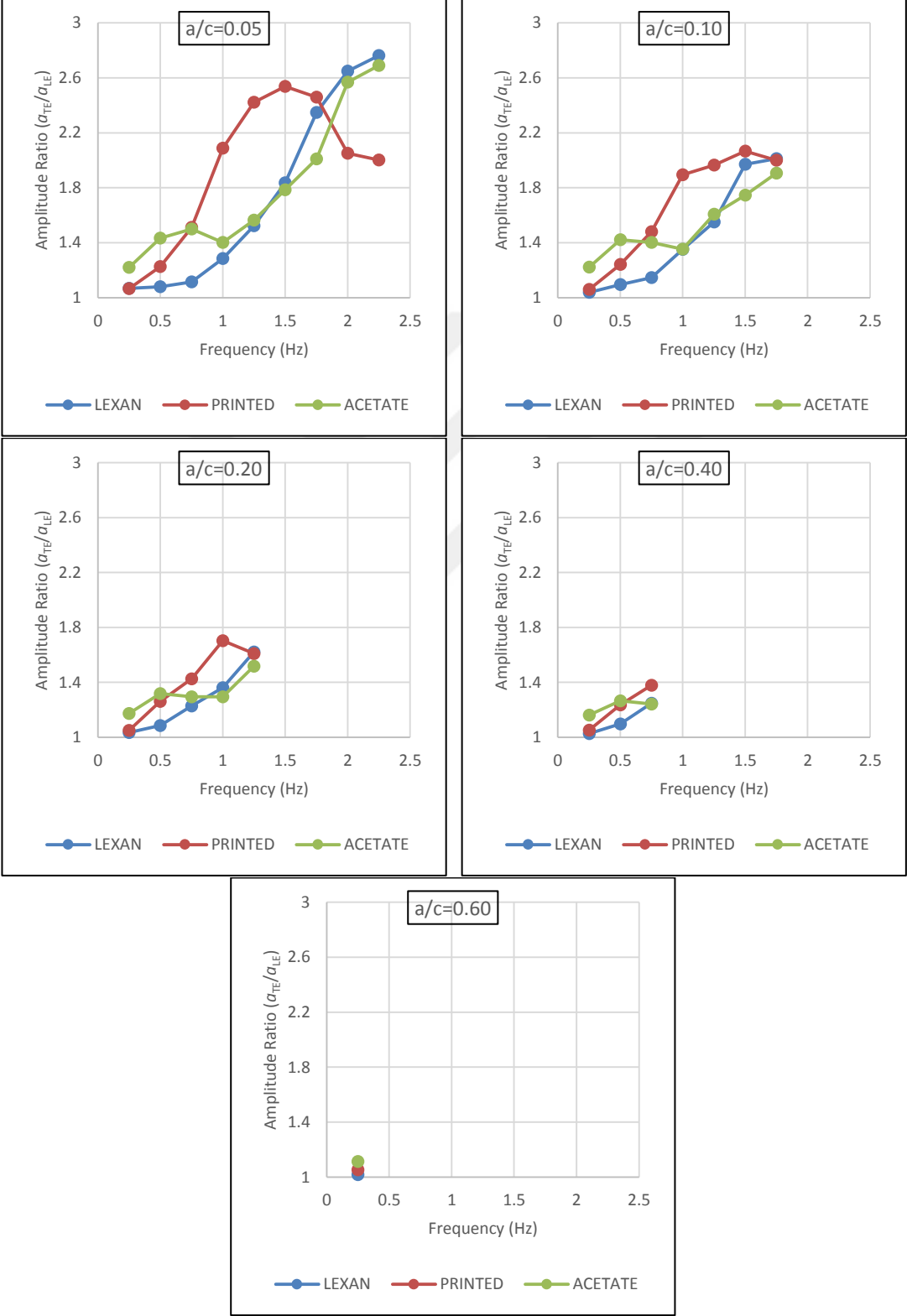


Figure 3.45 : Trailing edge amplitude ratios of different flexible wings.

At lower flapping frequencies and low flapping amplitudes, flexible wings do not change their shape and behave as thin rigid foils. As the frequency or the amplitude of the motion increased, trailing edge amplitude starts to increase and follows the leading edge with a lag. Trailing edge amplitude variations for different flapping amplitudes and frequencies are given in Figure 3.45. When we consider the amplitude of $a/c=0.05$, for the lexan wing, as the flapping frequency increases, the trailing edge amplitude also increases. For the printed wing, the behavior is similar up to flapping frequency of 1.5 Hz then amplitude starts to decrease. For the acetate wing, a small peak is observed between frequencies 0.5 – 1 Hz then the values start to increase again. Similar observations can be made for other flapping amplitudes.

Different variations of the trailing edge amplitude for different wings can be attributed to the flexibility, and therefore interrelated to the natural frequency of the wings. When the same amplitude ratio graphs are plotted with respect to the non-dimensionalized frequency ratio (f/f_n), natural frequency effects can be clearly observed (Figure 3.46). As it can be seen from the Figure 3.46 that, trailing edge amplitude makes a peak when the oscillations are performed near natural frequency of the wing ($f/f_n \sim 1$). Actually the peak point is observed at a slightly higher frequency than the natural frequency, nonetheless, the comments will be made as “near the natural frequency” deliberately. For the acetate wing, frequencies beyond natural frequency can be observed and after $f/f_n = 2$ the trailing edge amplitudes start to increase again. The values are in a continuous increase in the measurement range up to $f/f_n = 4.4$. This finding suggests that, higher trailing edge amplitudes can be reached when the flapping frequencies are beyond the resonant frequency.

At that point, we have to recall the properties of the resonance. There are two main characteristics of the resonance: maximum amplitude response and 90° phase difference between input and output (Rao, 2011). When these properties are applied to the present flapping flexible wing problem, amplitude response of the system will correspond to the trailing edge amplitude and the phase difference will be the phases between leading edge (input) and the trailing edge (output). Above, the maximum amplitude response near the natural frequency is presented and the other property, phases, are given in the following Figure 3.47.

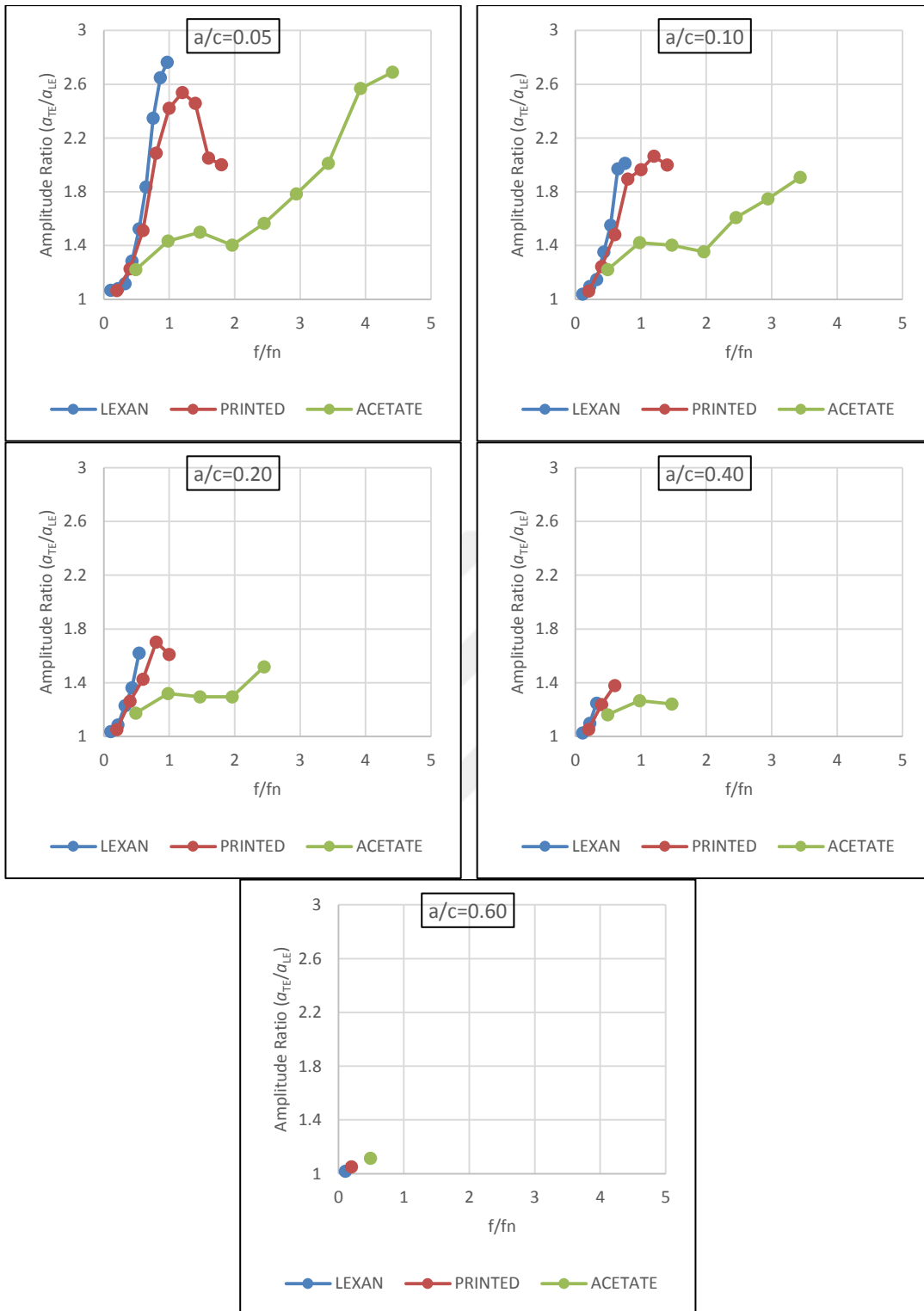


Figure 3.46 : Trailing edge amplitude ratios with respect to f/f_n .

At low flapping frequencies, the leading edge and the trailing edge has no or very small phase difference. As the flapping frequency or the flapping amplitude increases, trailing edge starts to lag behind the leading edge. For highly flexible acetate wing, even in small flapping frequencies, a phase lag exists and the lag increases with increasing flapping frequency.

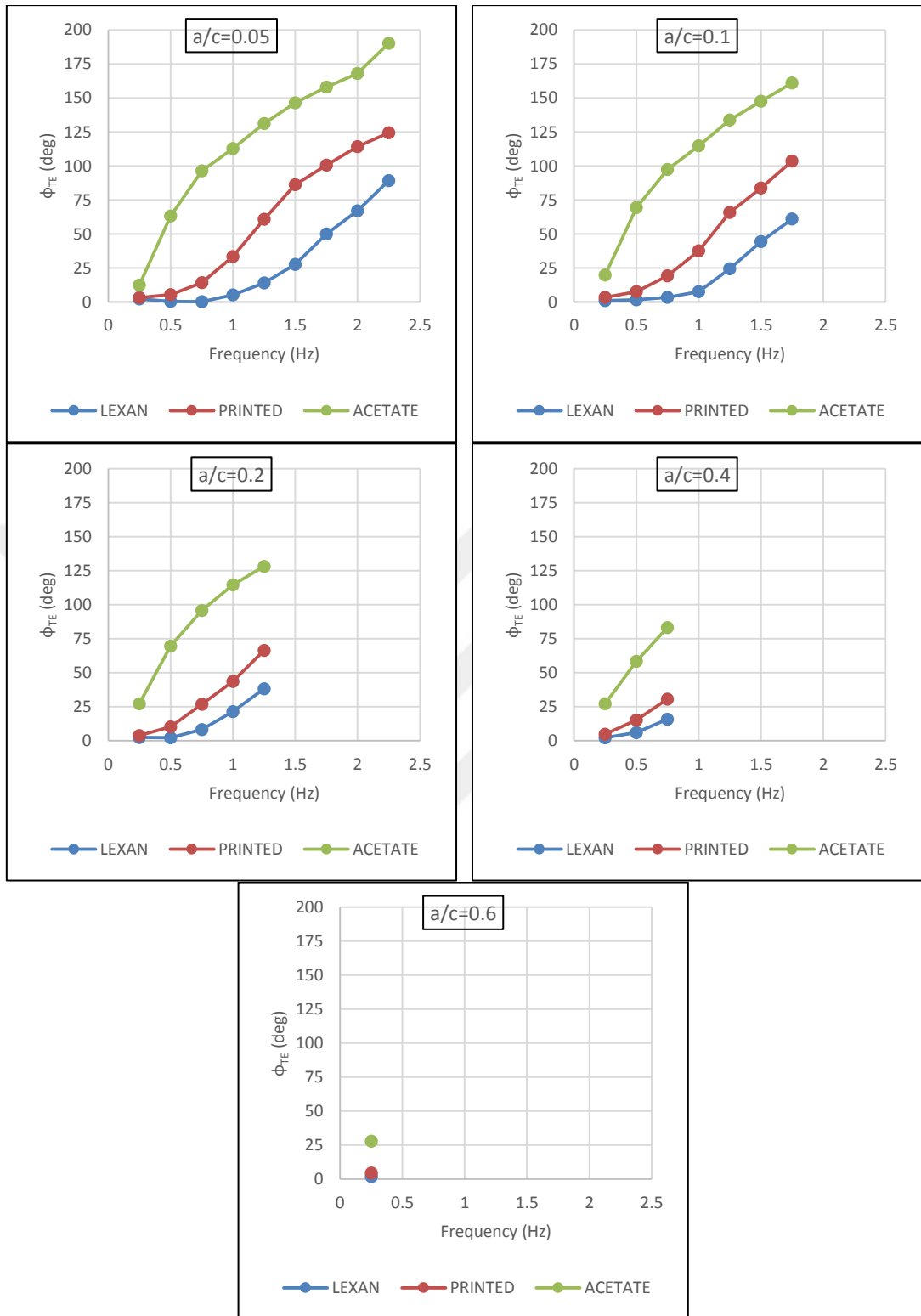


Figure 3.47 : Phase of the trailing edge with respect to the leading edge.

To see the natural frequency effects on phases, horizontal axis is normalized with natural frequency in following Figure 3.48. It is expected that a phase difference of 90° will occur between leading edge and the trailing edge at resonance conditions. This phase lag value is obtained for some of the cases such as lexan wing with a plunging

amplitude of $a/c=0.05$. However, in most of the cases at resonance conditions, the phase lag obtained is less than 90° .

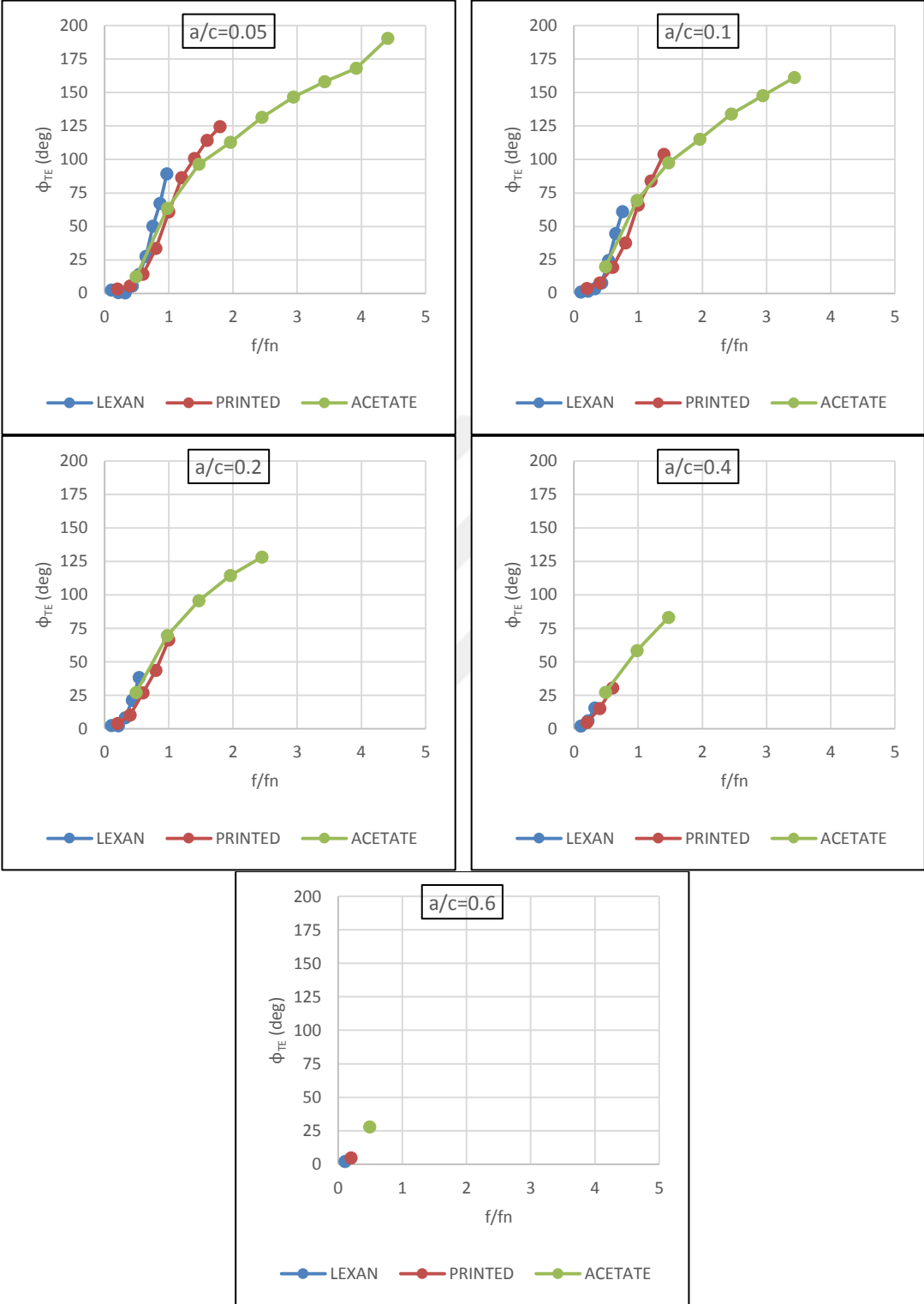


Figure 3.48 : Trailing edge phases Φ_{TE} with respect to frequency ratio f/f_n .

Another parameter that can be attained from the shape deformation is the pitch phase angle (Heathcote and Gursul, 2007). This parameter is obtained by connecting leading

and trailing edges and measuring the instantaneous pitch angle. The phase between leading edge and the pitch angle is then named as the pitch phase angle. In this approach, the actual input is a purely plunging motion, however the output is a combination of pitch and plunge motion. The efficiencies and related properties then can be evaluated considering pitching and plunging wing and the values in the literature are found to be consistent with this approach (Heathcote and Gursul, 2007). In the present study, phases between leading and trailing edges are selected as the main parameters. The reason was to eliminate the weaknesses of the pitch phase angle approach, which does not take into account the continuous change in actual angle of attack in chordwise direction. Also, the mode shape starts to change at higher flapping frequencies which cannot be represented in pitch phase angle but can be observed in trailing edge phase. Actually all those parameters are related to each other and the details can be found in the study of Heathcote and Gursul (2007). In the thesis, the trailing edge amplitude and the trailing edge phase are thought to be good representatives of the current flapping wing problem and the results are obtained using these parameters.

3.4.2 Force measurement results

Force measurements are performed on three different flexible wings and the results will be presented in this section. A phase-based approach is adopted as it is done for the rigid wing results. Firstly, phases between motion and the forces in streamwise and cross-stream direction are examined and presented. In Figure 3.49, phases obtained from Theodorsen solution and the rigid wing's phases in cross-stream direction are presented together with the phases of flexible wings. As explained earlier, when the plunging frequency increases, Φ_y phase lags decrease in rigid wings. The decrement is related to the inertial forces, which become in phase with the motion and dominant at higher plunging frequencies. As a result, motion and the measured forces become in-phase. When the flexible wings are examined, the behavior of the phase distribution is similar to those of rigid wings at lower flapping frequencies. This is an expected result since the trailing edge deflection will not occur at low flapping frequencies and the wings will behave as thin rigid foils. However, as the flapping frequency increases, trailing edge start to deflect and the flexibility effects are perceived on the flow field. Φ_y phase lag starts to increase as a result of increased frequency for lexan and printed wings. For the acetate wing, in plunging amplitudes of $a/c=0.05$ and $a/c=0.1$, Φ_y values

peak at the flapping frequency of 0.5 Hz and then start to decrease. The decrement turns out to an increase at higher frequencies such as 1.5 Hz for $a/c=0.05$ and 1.25 Hz for $a/c=0.1$. At higher plunging amplitudes for the acetate wing, peak at the flapping frequency of $f=0.5$ Hz disappears.

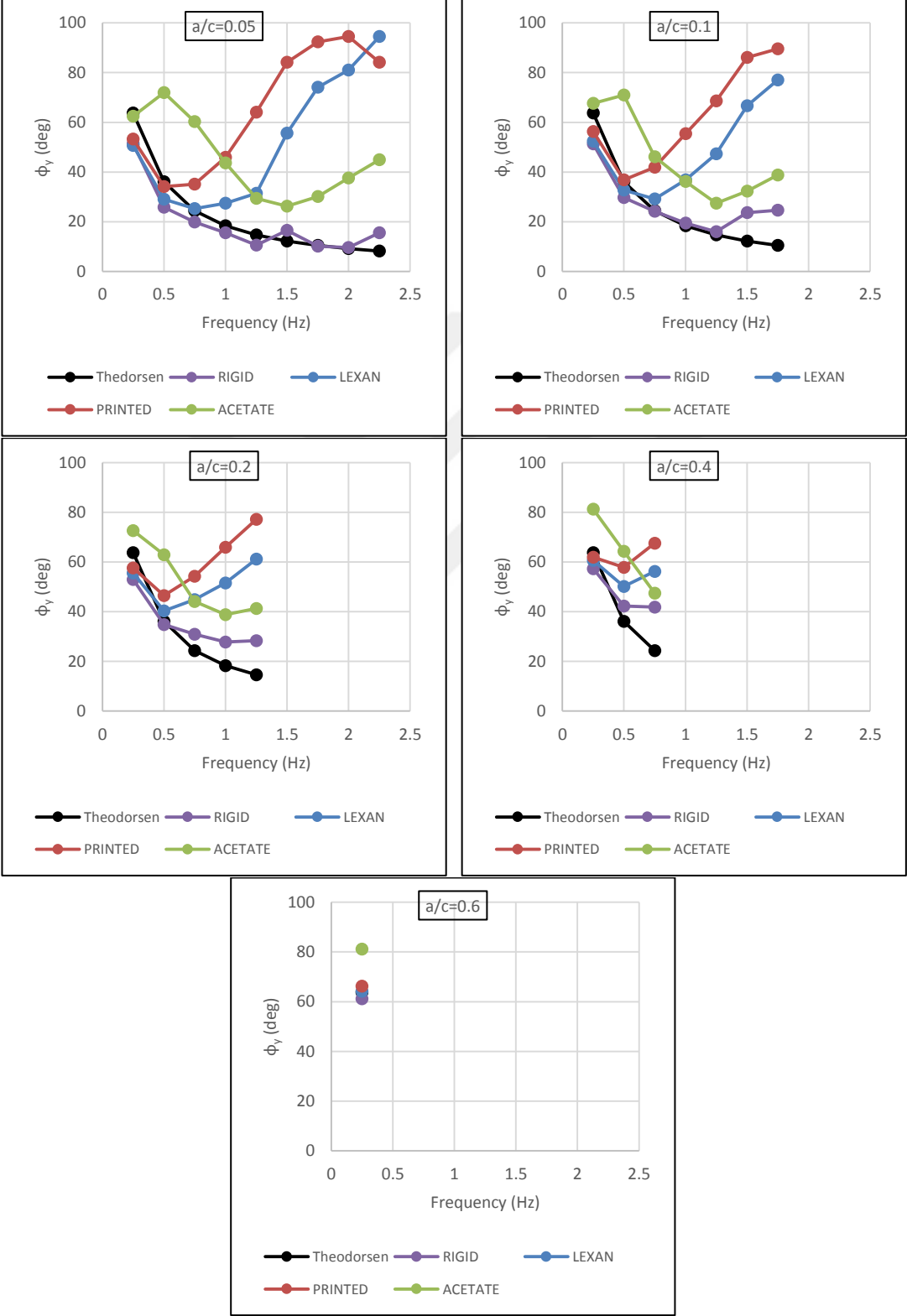


Figure 3.49 : Phase lag between F_y and the motion for different wings.

When all the phase graphs in Figure 3.49 are considered, it is evident that flexible wings have completely different phase variations compared to rigid wings. Natural frequency appears to have an effect on Φ_y phase variations. Phase values increase up to the natural frequency (observed in the plunging amplitude of $a/c=0.05$) and then a decrease followed by an increase behavior is observed at higher flapping frequencies (observed for the acetate wing). Besides the natural frequency, flapping amplitude also has an effect on phases such as the peak near the natural frequency diminishes for higher amplitudes in acetate wing. This implies that natural frequency and the flapping amplitude should be interpreted together.

The same graphs are plotted by grouping different materials in Figure 3.50 - Figure 3.52. For the lexan wing (see Figure 3.50), phase values have a similar trend with Theodorsen solution at lower flapping frequencies. Phases decrease as the plunging frequency increases, and phases increase when the plunging amplitude is increased for a constant frequency. This observation was also made for the rigid wing's phases. As the flapping frequency increases, flexibility effects start to be observed and the phase values diverge from Theodorsen solution. Increasing phase lag with increased plunging amplitude is conserved in whole measurement space for the lexan wing.

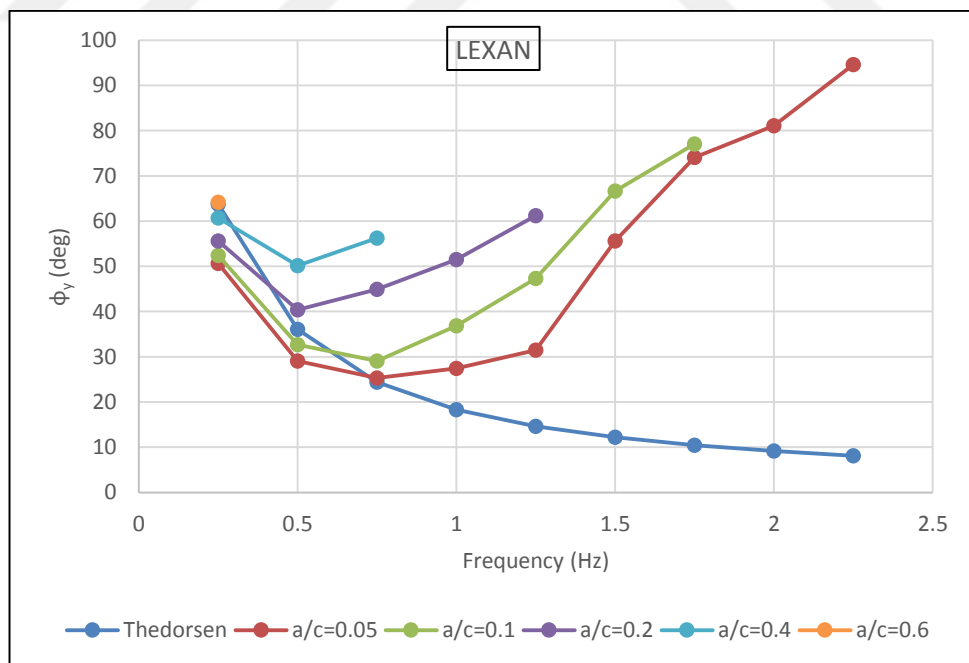


Figure 3.50 : Phase lag between F_y and the motion for the lexan wing.

Similar observations can be made for the printed wing's phase variations shown in Figure 3.51. The main distinction from the lexan wing is that phase variations peak around $f=2$ Hz.

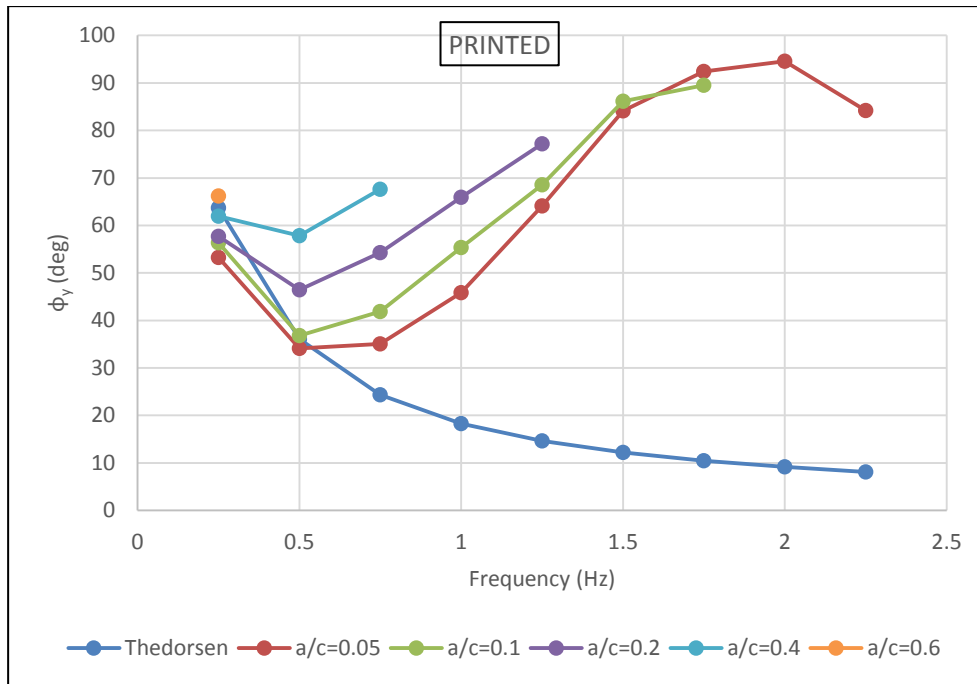


Figure 3.51 : Phase lag between F_y and the motion for the printed wing.

For the acetate wing, the phase lag between F_y and the motion has a quite different variation than those of the lexan and the printed wings (Figure 3.52). For the plunging frequency of $f=0.25$ Hz, the sorting of the Φ_y values is same as that of the two other flexible wings, however beyond this frequency the variation is different. While a peak point is observed at two low flapping amplitudes of $a/c=0.05$ and $a/c=0.1$, for the other high amplitude cases of $a/c=0.2$ and $a/c=0.4$, Φ_y decreases without exhibiting a peak.

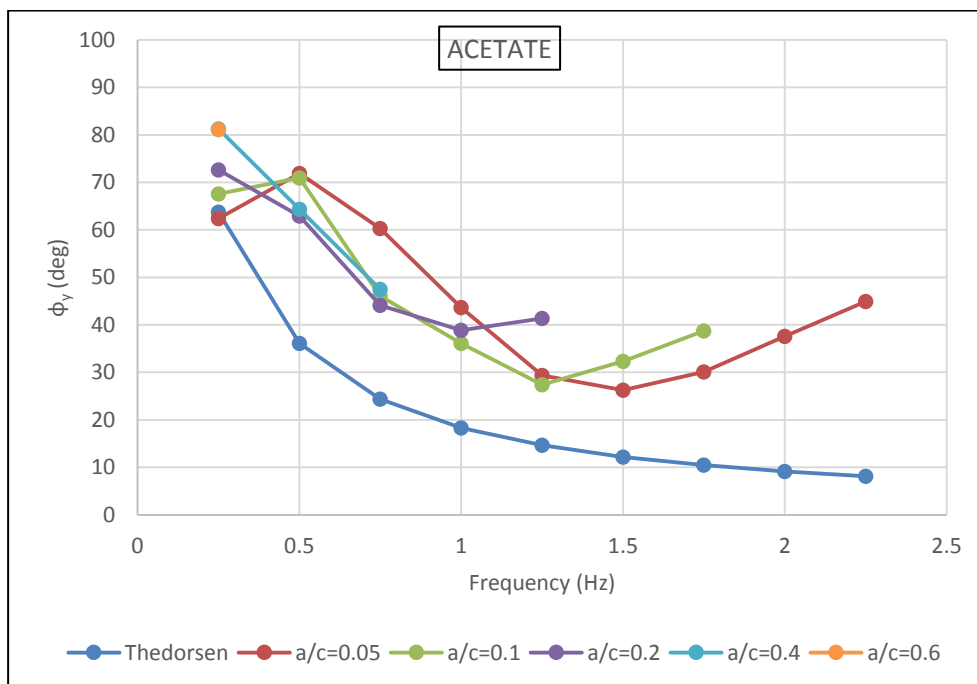


Figure 3.52 : Phase lag between F_y and the motion for the acetate wing.

One can presume that these amplitudes reach their peak values earlier and we observe them in their decline phase after the peak. This suggestion can be supported by the alignment of the local minimum points followed by the increasing values at higher flapping frequencies. The local minimum point is $f=1.5$ Hz for $a/c=0.05$, $f=1.25$ Hz for $a/c=0.1$ and $f=1$ Hz for $a/c=0.2$. The conclusion from this observation is that the flapping amplitude increments lead the peaks and similar variations to occur at lower flapping frequencies. This fact also supports the idea to examine the natural frequency and the flapping amplitude together.

Up to now, we have examined the shape deformations, trailing edge amplitude and trailing edge phase with respect to the leading edge, and force phases with respect to the leading edge. Combinations of these parameters are thought to include valuable information on the flexible flapping wing problem. For that purpose, two graphs obtained from force phase Φ_y and trailing edge phase Φ_{TE} are combined and plotted together in Figure 3.53. An interesting result is obtained from the combined phase graph: trailing edge phases and force phases are intersecting at different plunging frequencies for different wings. The intersecting frequencies coincide with the natural frequency of the wing. In other words, cross-stream force phases and trailing edge phases are equal when the wings are plunged near their natural frequencies. When the flapping flexible wing problem is physically considered, firstly, the leading edge reaches its maximum amplitude, then the trailing edge reaches its maximum with a lag and then the lift force reaches its peak following the trailing edge in the flapping frequencies below natural frequency. At resonant frequency, trailing edge and lift forces reach their maximum at the same time. After the resonant frequency, sequence of the peaks changes and in the order of appearance, the peaks belong to leading edge, lift force, and trailing edge respectively.

Streamwise force component's phases (Φ_x) are determined by the same method described in the rigid wing's force measurement results. Firstly, in Figure 3.54, Φ_x phases are grouped under flapping amplitudes and presented for different wing types. If we recall the results gained from the rigid wings, the phases were higher at low flapping amplitudes and decreasing toward 90° as the flapping amplitude was increased. Also, phases were in a trend of increase when the thrust was started to be produced.

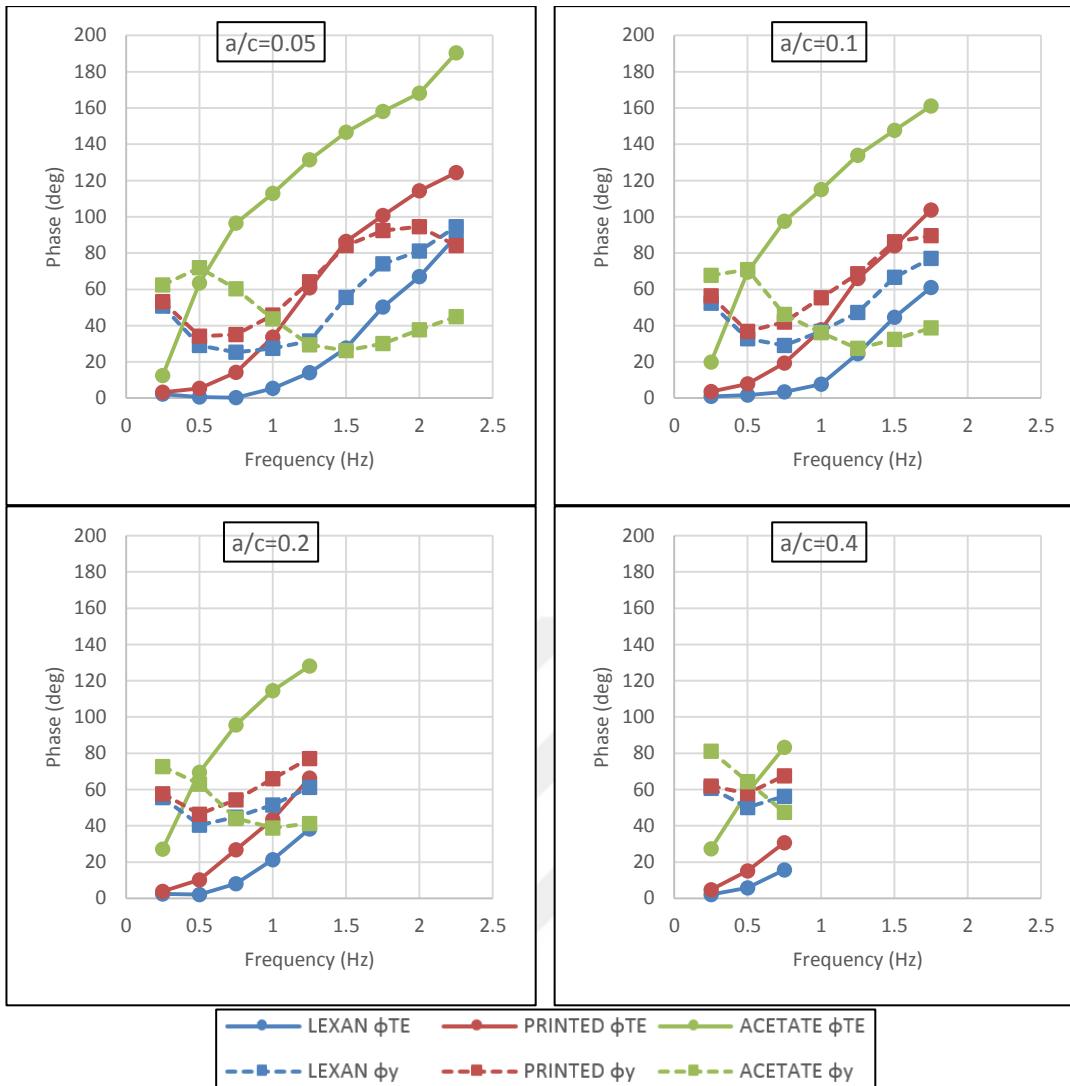


Figure 3.53 : Trailing edge (Φ_{TE}) and vertical force (Φ_y) phases of the flexible wings.

In Figure 3.54, for low frequencies, flexible wings excluding acetate have lower phases compared to those of the rigid wing. Actually, it is expected to have similar Φ_x values for the rigid and the flexible wings especially when the flexible wings are not deforming. This expectation is not met possibly due to the differences in wing thickness. The association of the phases with drag/thrust transition will be investigated after the force coefficients are presented in the forthcoming sections.

The phase angles Φ_x are presented for each flexible wing separately in Figure 3.55 to Figure 3.57. For the lexan wing, Φ_x values increase when the plunging amplitude increases. Phase angles first drop then start to increase when the flapping frequency increases. The onset of increase in phase angles is different for every flapping amplitude. Unlike the rigid wing, distribution of Φ_x values has similar characteristics with that of Φ_y in flexible wings. This similarity indicates that the flexibility effects

are not only observed in cross-stream direction but also for forces in streamwise direction.

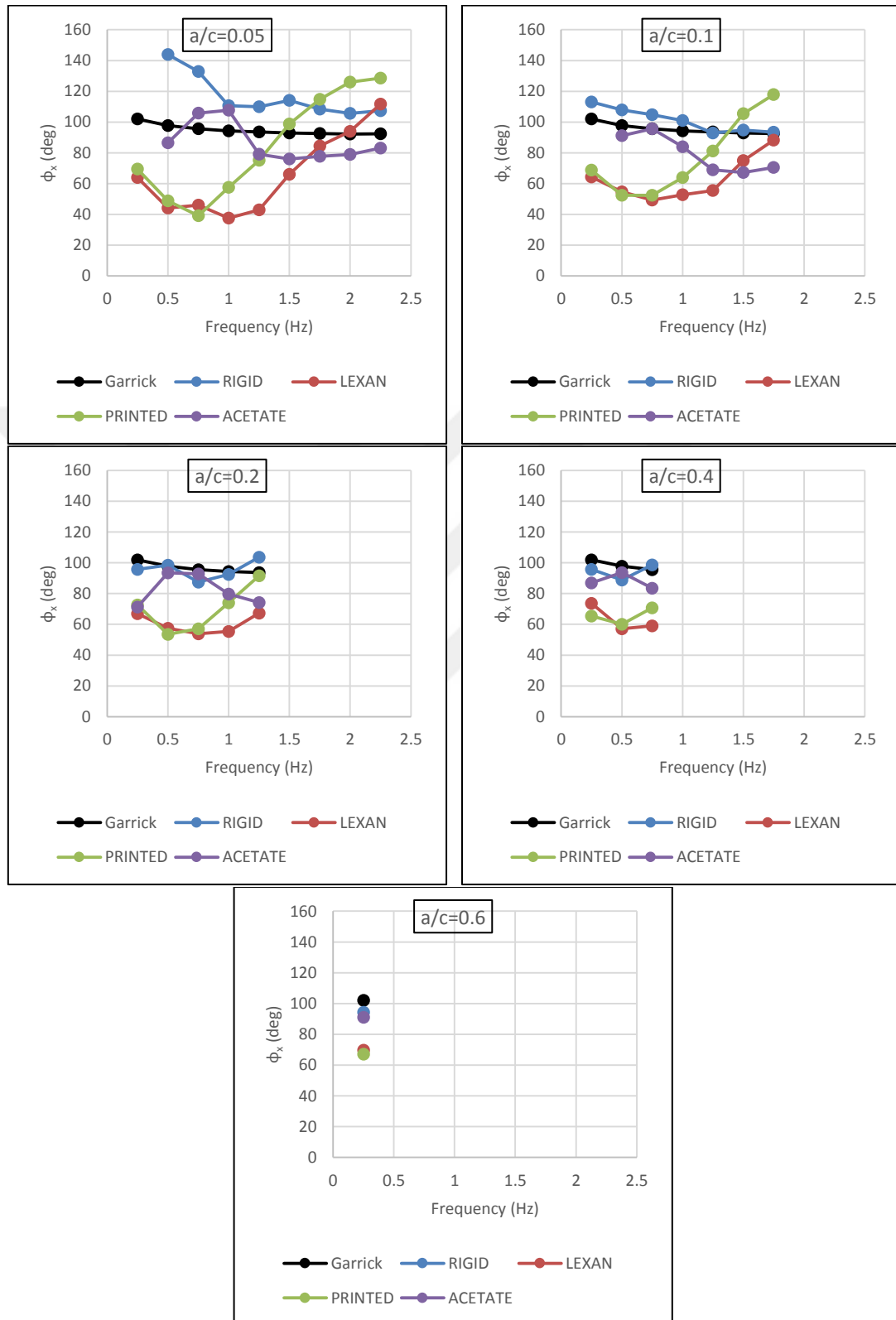


Figure 3.54 : Phase lag (Average of 1st and 2nd peaks) between F_x and the motion for different wings.

As mentioned earlier, in cross-stream direction, forces acting on the wing are circulatory and non-circulatory (added mass) forces. In the flexible wings, another force, to be named as the elastic force, arises from the deformation of the wing. This elastic force is stored and released continuously by the flexible wing due to its flapping motion. Elastic force, expectedly, has an effect on the crosstream forces both in phases and in amplitudes. On the other hand, streamwise force components are only created by the circulation effects, which also can be deduced from the Garrick's formulation. As it is a pure plunge motion for rigid wings, added mass effect does not exist in streamwise direction. However, in flexible wings, elastic forces also emerge in streamwise direction coupled with the trailing edge deflection of the flexible wing. The similarity between the streamwise and the cross-stream force phases is a result of these prevailing elastic forces over the other existing forces (circulatory and added mass). Since the measured circulatory forces are quite small in streamwise direction, the elastic forces are dominant in streamwise direction.

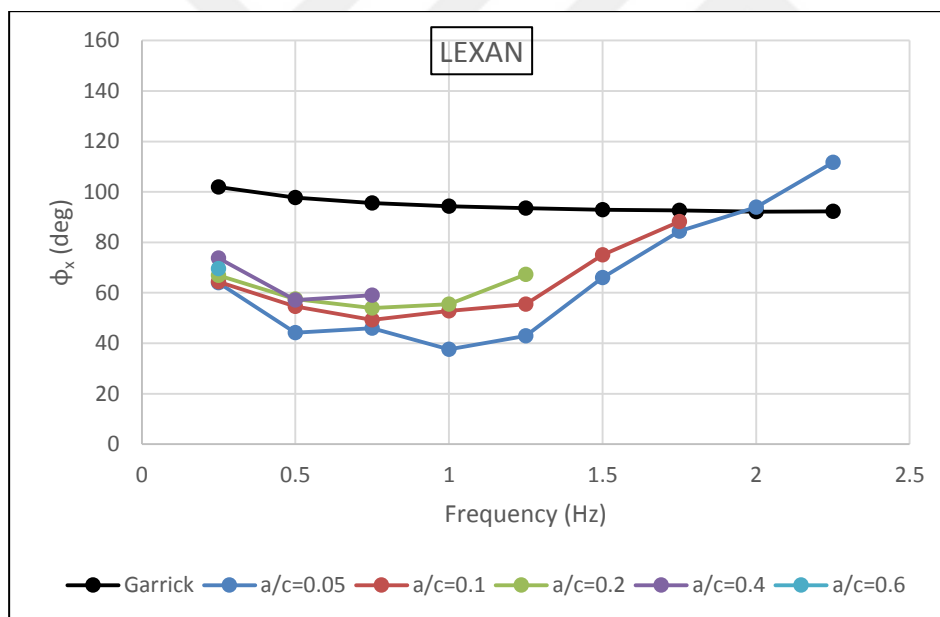


Figure 3.55 : Phase lag between F_x and the motion for the lexan wing.

For the printed wing, variation of the Φ_x angles is similar to that of the lexan wing (Figure 3.56). The onset of increase in phase values is smaller for the printed wing compared to that of the lexan wing. The increase in phases is started at $f=1$ Hz for the lexan wing and $f=0.75$ Hz for the printed wing at a flapping amplitude of $a/c=0.05$. Also the phase value reaches its maximum after $f=2$ Hz. Similarities between Φ_x and Φ_y variations are also evident for the printed wing, which confirm the role of elastic forces in flexible flapping wings.

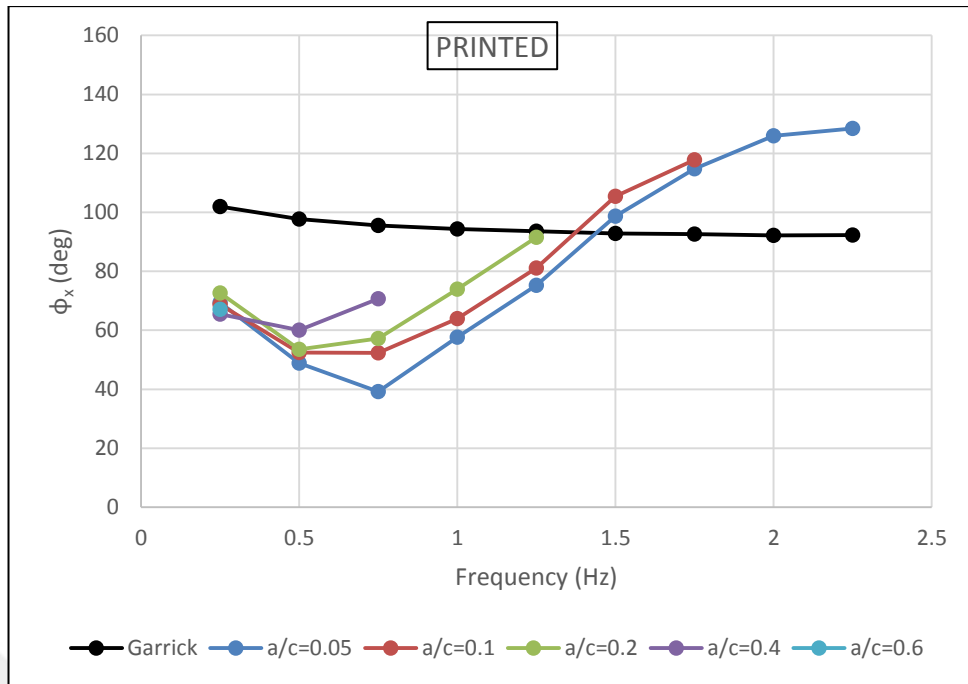


Figure 3.56 : Phase lag between F_x and the motion for the printed wing.

For the acetate wing, the distribution of Φ_x shows differences from those of the other two flexible wings (Figure 3.57). The sorting of the phases changes at flapping frequencies higher than $f=0.5$ Hz. Smaller flapping amplitudes have higher phase values as in the rigid wings. The peak point observed in Φ_y variations near the natural frequency (for acetate wing, $f\sim 0.5$ Hz) is also observed in Φ_x variations. However, the peaks occur at slightly higher flapping frequencies.

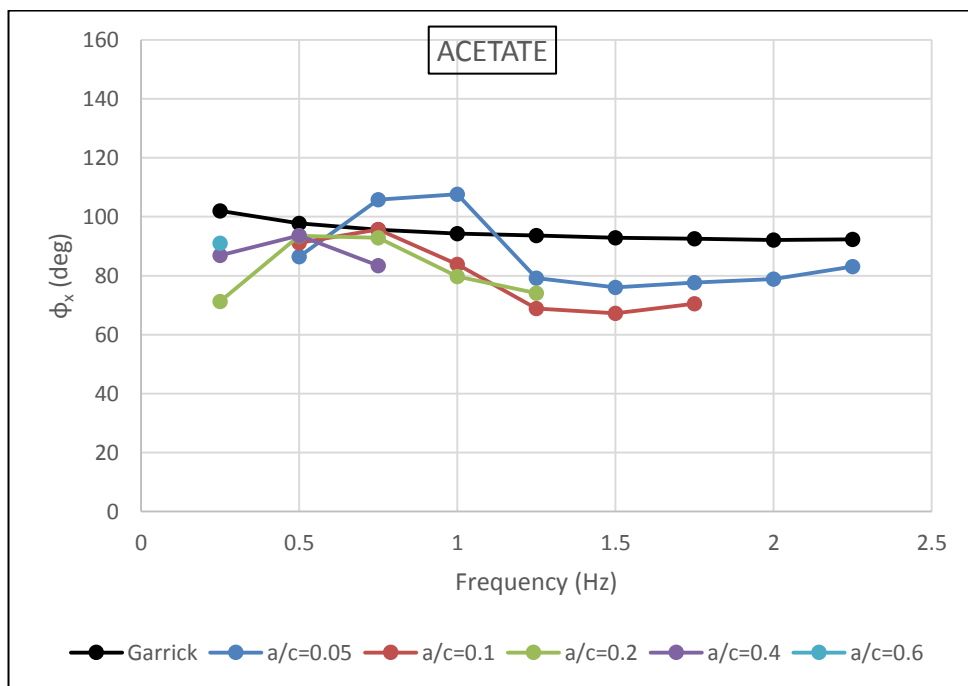


Figure 3.57 : Phase lag between F_x and the motion for the acetate wing.

The region where the flapping frequencies are higher than the natural frequency is interesting to study for further studies. High lags and out of phase behavior in trailing edge motion, further change the mode shapes of the wing and alter the forces and the flow structures. Future investigations in this region are worthwhile referring to the results studied so far.

After the investigations on the phase relations, thrust coefficients (C_T), power input coefficients (C_P), and efficiencies (η) are calculated from the time averaged force measurements for different flexible wings. In Figure 3.58, thrust coefficients are presented for four different type of wings. When the amplitude of $a/c=0.05$ is investigated, the rigid wing does not exhibit any results in the thrust zone. On the other hand, for flexible wings there is a switch from drag to thrust after a certain flapping frequency. Firstly, the printed wing exhibits a switch from drag to thrust around the flapping frequency of 0.75 Hz, then the lexan wing around 0.9 Hz and finally the acetate wing around 1.1 Hz. Although the acetate wing deforms more than the lexan and the printed wings at lower flapping frequencies, these deformations are not sufficient for producing thrust. The acetate wing starts to produce thrust at frequencies about two times higher than its natural frequency and thrust values increase exponentially beyond that frequency. Between frequencies $f=0.75$ and 1.5 Hz, the printed wing has the highest thrust values among other wings. On the other hand, the lexan wing has the highest thrust values for frequencies higher than $f=1.5$ Hz. When the flapping amplitude is increased to $a/c=0.1$ some cases of the rigid wing exhibit thrust and flexible wing's threshold frequency for drag to thrust switch is reduced. The order of the switch from drag to thrust changes for this amplitude; first the acetate wing then the printed and the lexan wing switch drag to thrust respectively. The acetate wing has the highest thrust up to the flapping frequency of $f=0.5$ Hz, the printed wing has the highest thrust values between frequencies $f=0.5$ and 1.25 Hz, and beyond this frequency, lexan wing has the highest thrust values.

For higher flapping amplitudes the scenario prevails and the threshold frequency for drag to thrust transition decreases and finally at a flapping amplitude of $a/c=0.6$ all wings reside in thrust producing regime.

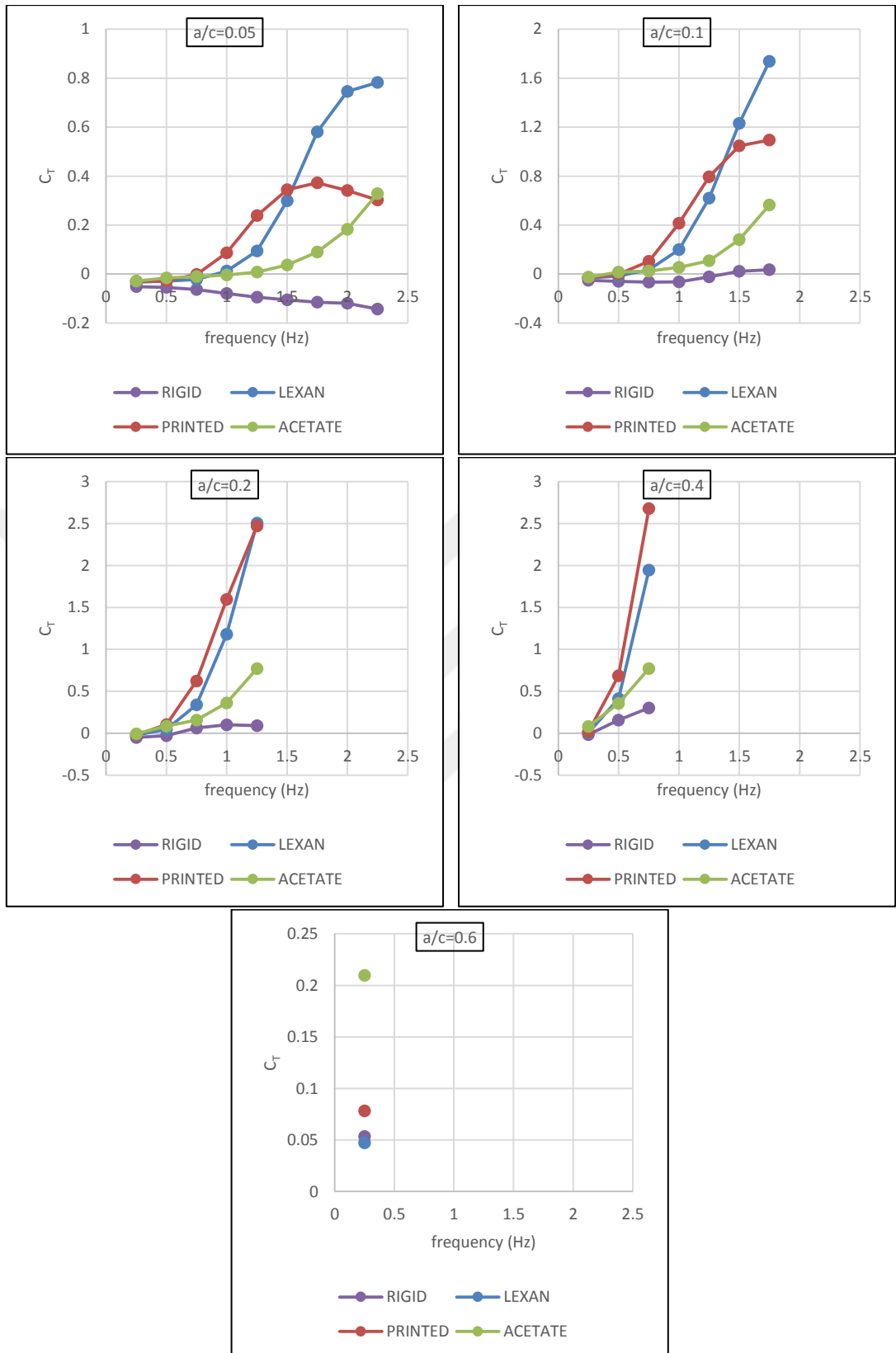


Figure 3.58 : Thrust coefficients (C_T) for different wing types.

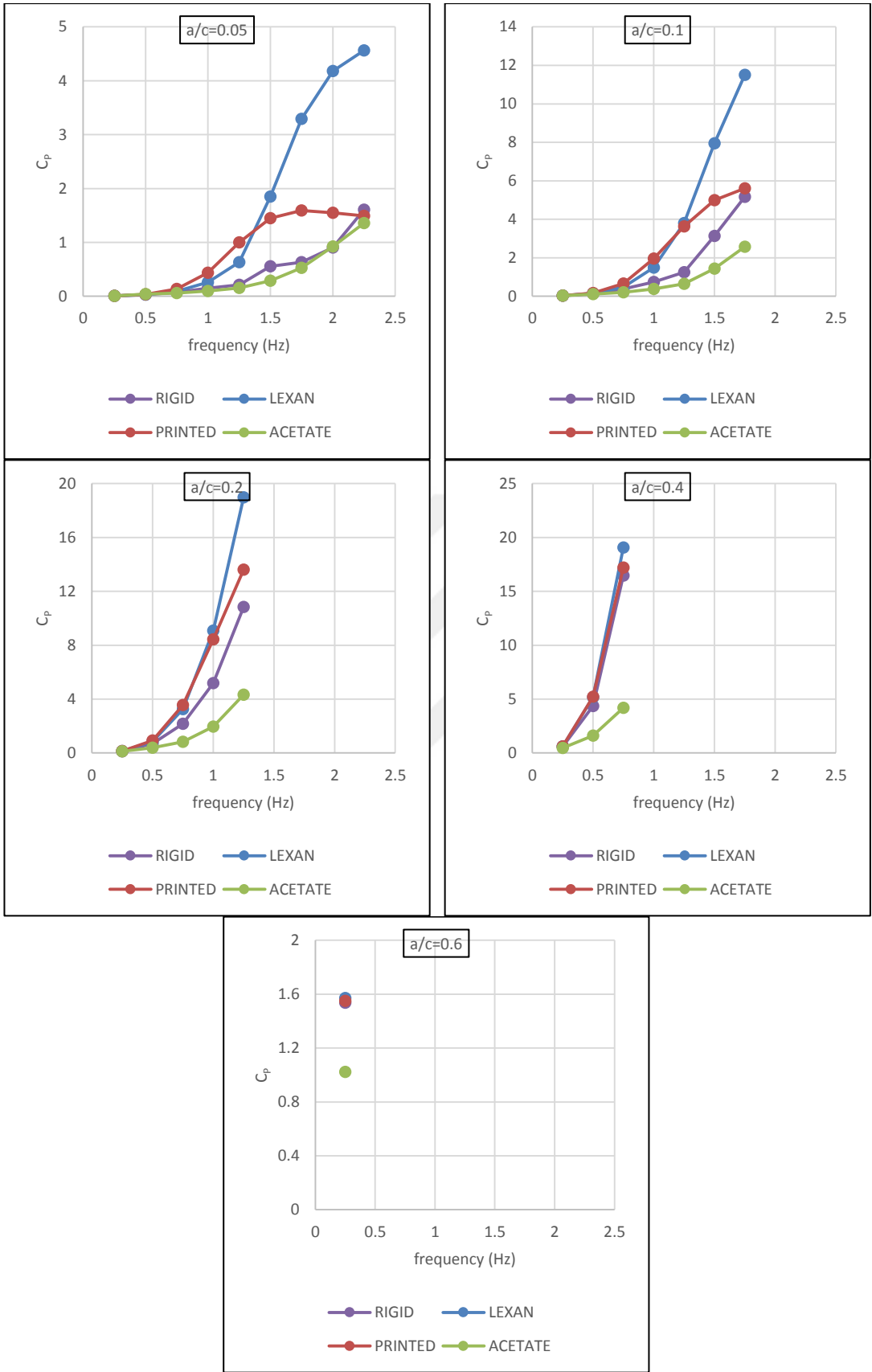


Figure 3.59 : Power input coefficients (C_p) for different wing types.

Power input coefficients are presented in Figure 3.59 for all wing types. The distribution of C_P is similar to C_T in most of the cases and similar comments can be made. At a flapping amplitude of $a/c=0.05$, rigid and acetate wings have similar C_P distribution. For higher amplitudes, acetate wing has the lowest power input coefficients among other wings. Especially at an amplitude of $a/c=0.4$ the distinction between acetate wing and other wings is clear.

Combination of the thrust and the power input coefficients will lead to the efficiency of the wings, which is presented in Figure 3.60. For the amplitude of $a/c=0.05$, the printed wing has the highest efficiency except the flapping frequency of $f=2.25$ Hz. The rigid wing is not on the graph since only the positive value (thrust producing) cases are plotted. When the amplitude is increased to $a/c=0.01$, the acetate wing starts to produce thrust at low flapping frequencies and exhibits a peak value at $f=0.5$ Hz, which coincides with natural frequency of the acetate wing. The efficiencies decrease and then increase continuously for the acetate wing at higher flapping frequencies. Rigid wing has two thrust producing cases, which can be seen at the bottom of the graph. As the amplitude increases to $a/c=0.2$ and $a/c=0.4$, in terms of being efficient the wings sort from the most flexible one to the rigid one. The acetate wing has the best efficiency in these flapping amplitudes. The natural frequency of the acetate wing is $f_n=0.51$ Hz and around this frequency the acetate wing has the best efficiency. The amplitude of the motion also seems to be an important parameter and should be considered together with the natural frequency. The printed wing, having a natural frequency of $f_n=1.25$ Hz has the best efficiency at around this frequency for the plunging amplitudes of $a/c=0.05$ and $a/c=0.1$. The lexan wing has a natural frequency of $f_n=2.32$ Hz and its efficiency increases towards this frequency, however printed and acetate wing have higher efficiencies around. Natural frequency and its multiples have an effect on efficiency, and should be considered with the amplitude of the motion, shape of the wings and phases as mentioned earlier. It should also be noted that the best thrust performance and the best efficiency could be attained in different flexibilities and should be examined separately. A wing can have the best efficiency with a low thrust or a high thrust with a low efficiency. Therefore, based on the expectations and performance requirements, the flexibility of the wings should be carefully selected and the wing should be operated to meet those demands.

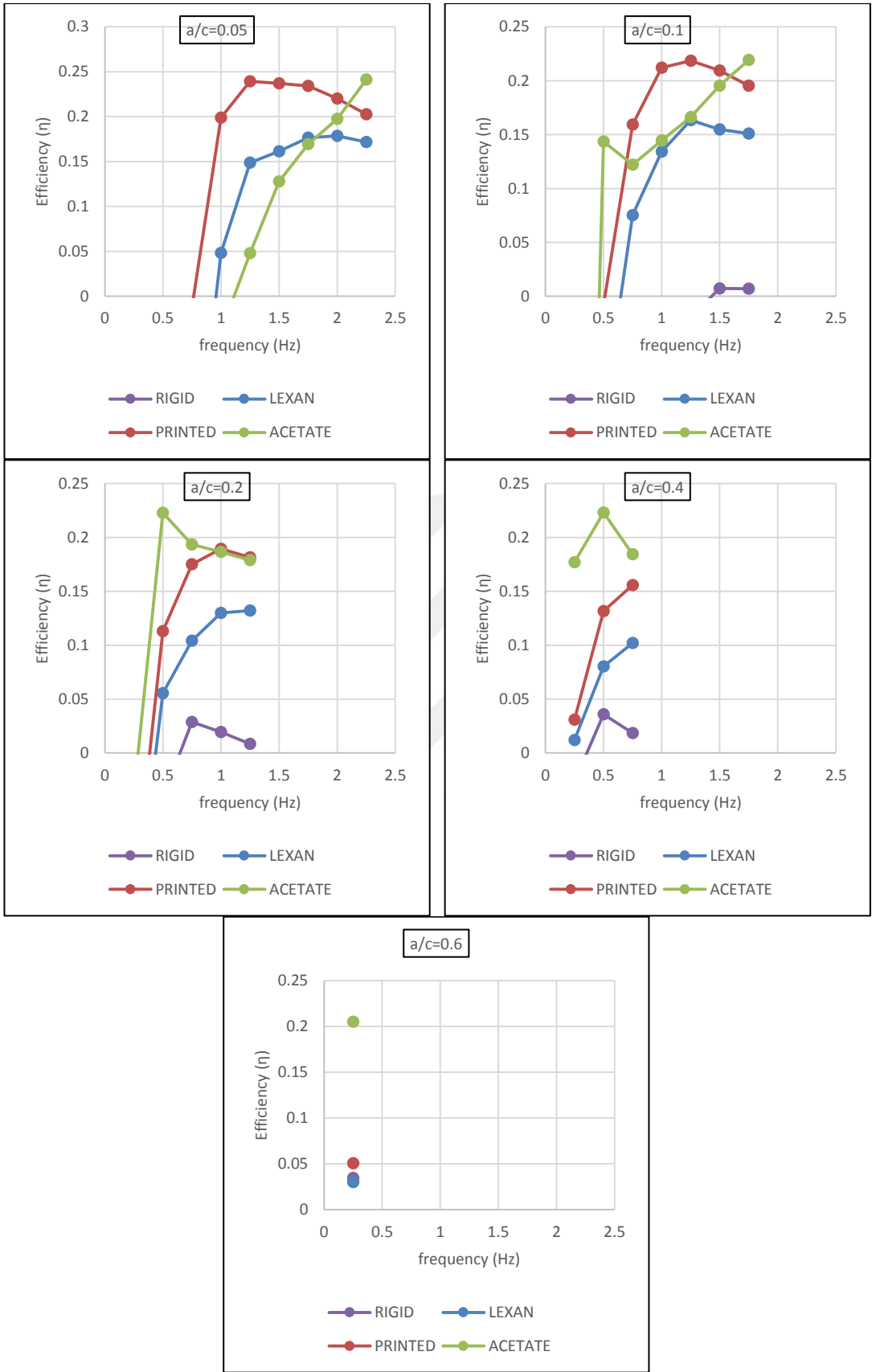


Figure 3.60 : Efficiencies (η) for different wing types.

After comparing different wings, these variations are plotted for each wing for different amplitude and frequency parameters in the Figure 3.61 to Figure 3.63. For the lexican wing presented in Figure 3.61, C_T and C_P graphs have similar distributions. As the flapping amplitude increases, both C_T and C_P increase for the same flapping frequency. When the efficiencies are examined, the maximum among peak values is attained at the lowest flapping amplitude ($a/c=0.05$).

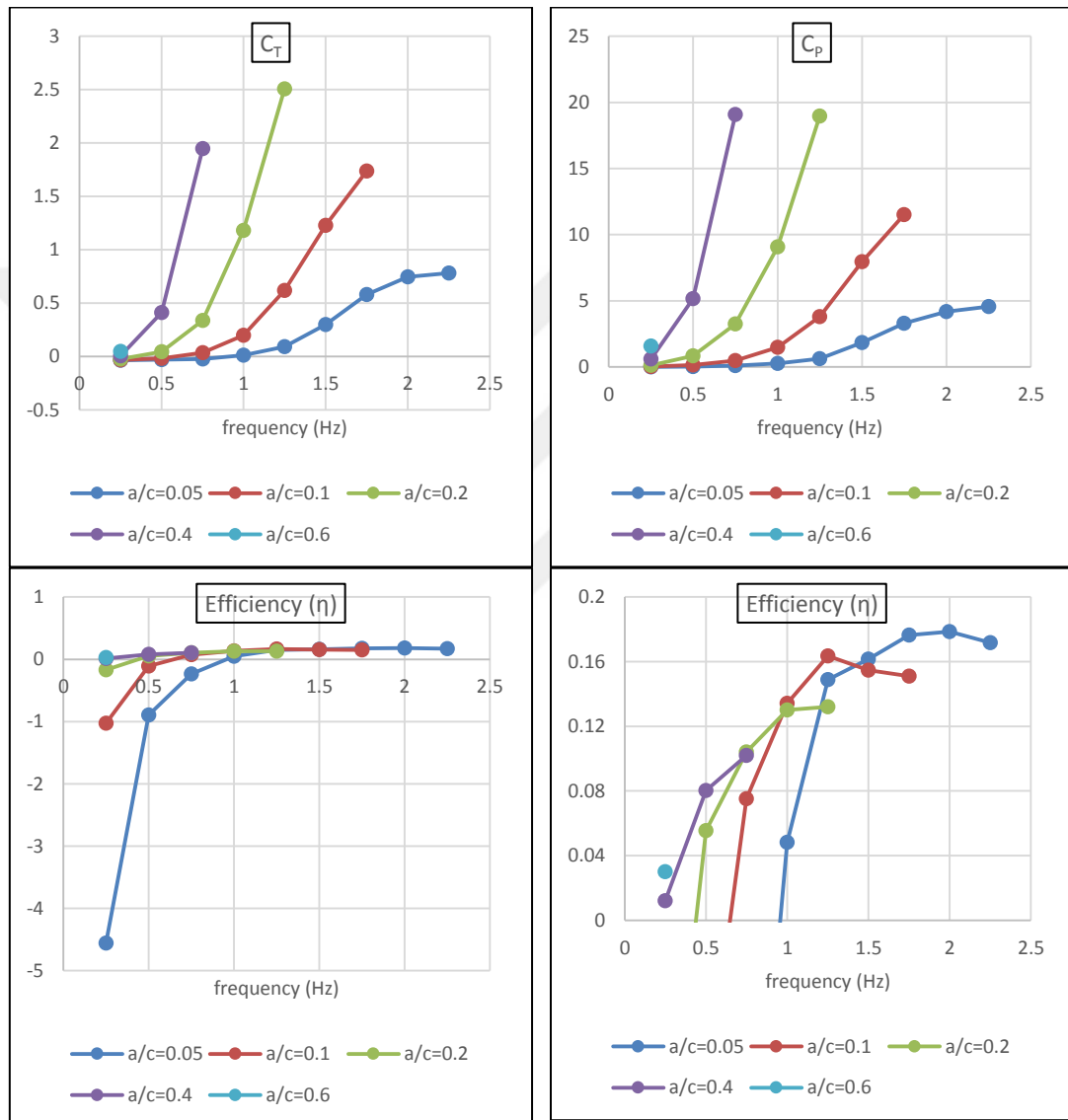


Figure 3.61 : Thrust coefficients (C_T), power input coefficients (C_P) and efficiencies (η) for the lexican wing.

When the printed wing is examined in Figure 3.62 for C_T and C_P , similar comments can be made as those of the lexican wing. The maximum efficiency peak is attained again at the lowest flapping amplitude and at a flapping frequency of $f=1.25$ Hz, which is equal to the natural frequency of the printed wing.

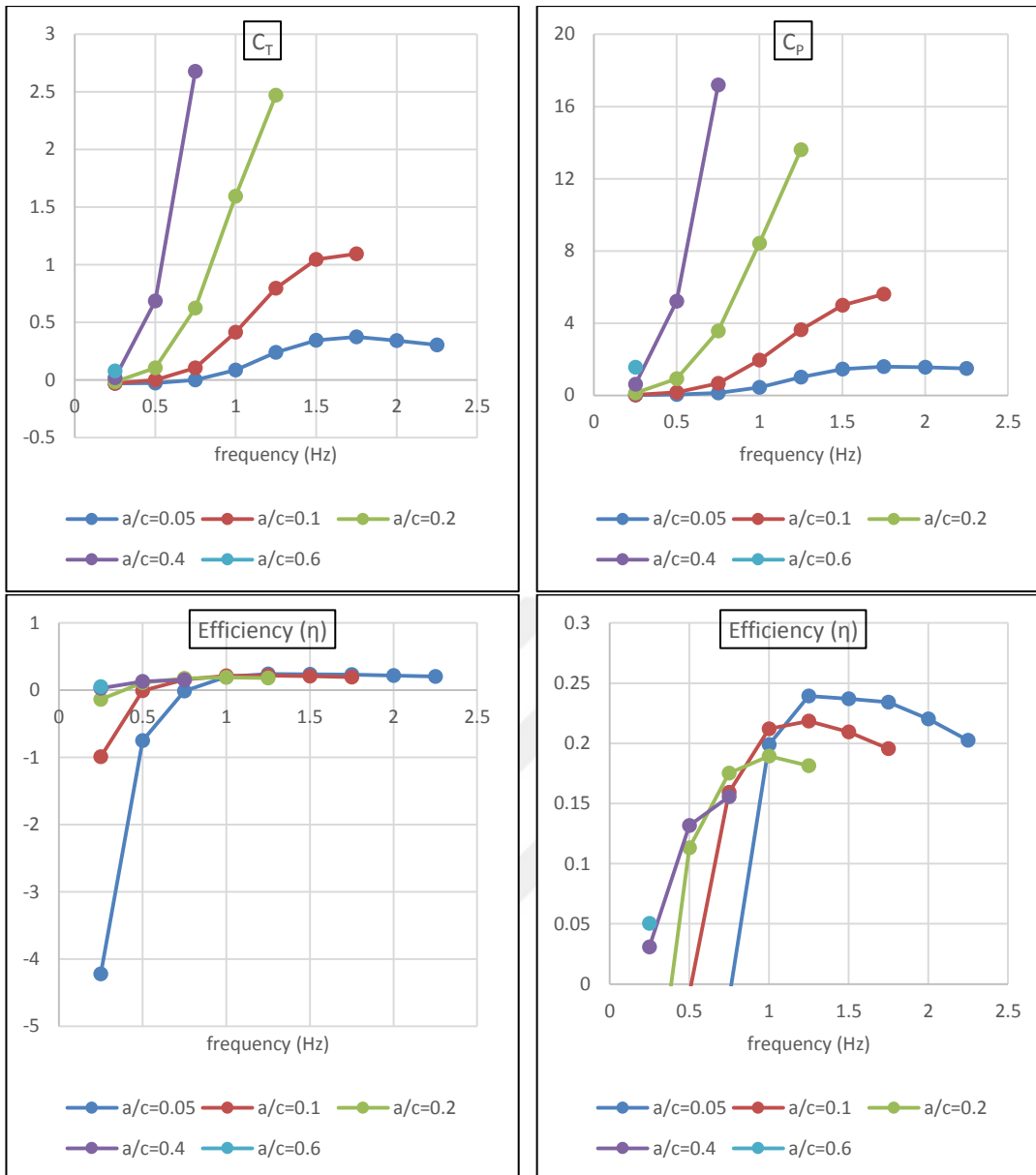


Figure 3.62 : Thrust coefficients (C_T), power input coefficients (C_P) and efficiencies (η) for the printed wing.

The acetate wing has similar distributions with the other two flexible wings in terms of C_T and C_P graphs (Figure 3.63). However, on the efficiency graph there are some differences. The maximum peak efficiency value is obtained at a high amplitude ($a/c=0.4$) and at the flapping frequency of $f=0.5$ Hz, which coincides with the natural frequency of acetate wing. At lower flapping amplitudes, the peak efficiency is attained around flapping frequency of $f=2.25$ Hz. This suggests that flapping frequencies considerably higher than the natural frequency can also yield high efficiency. The region of flapping frequencies that are higher than the natural frequency are deserve for further investigations.

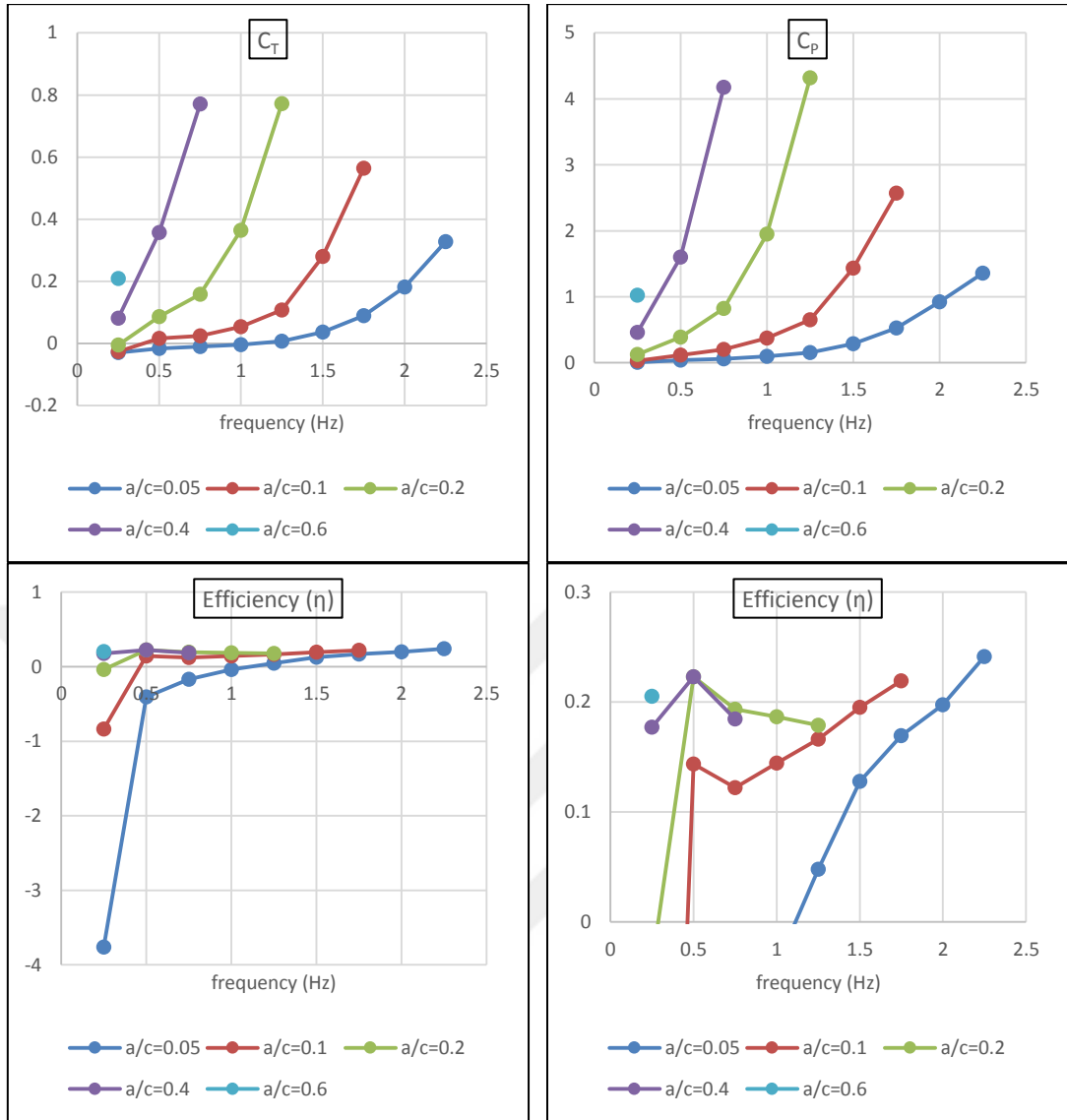


Figure 3.63 : Thrust coefficients (C_T), power input coefficients (C_P) and efficiencies (η) for the acetate wing.

As explained in the rigid wing's force measurement results, efficiency vs. Strouhal number graph is sometimes preferred to interpret the results of flapping motion. Strouhal number is calculated based on the leading edge flapping frequency and amplitude and presented for four wings in Figure 3.64. For the lexan and the printed wing, the efficiency decreases as the flapping amplitude increased. The efficiency peaks shift towards high Strouhal numbers when the flapping amplitude is increased. The peak efficiencies are obtained in a Strouhal number range of 0.2 – 0.6 for the lexan wing and 0.125 – 0.6 for the printed wing. For the acetate wing, the peaks are observed in a range of 0.1 – 0.4. For the rigid wing, the peaks are between Strouhal numbers of 0.2 and 0.4. The high efficiency zone in the literature is expressed in a Strouhal number range of 0.2 – 0.4 and for the flexible wings this range is found to be generally valid.

The boundaries of the range are slightly extended for the flexible wings in different flapping amplitudes. It should be noted that Strouhal number calculation is done with the leading edge amplitude.

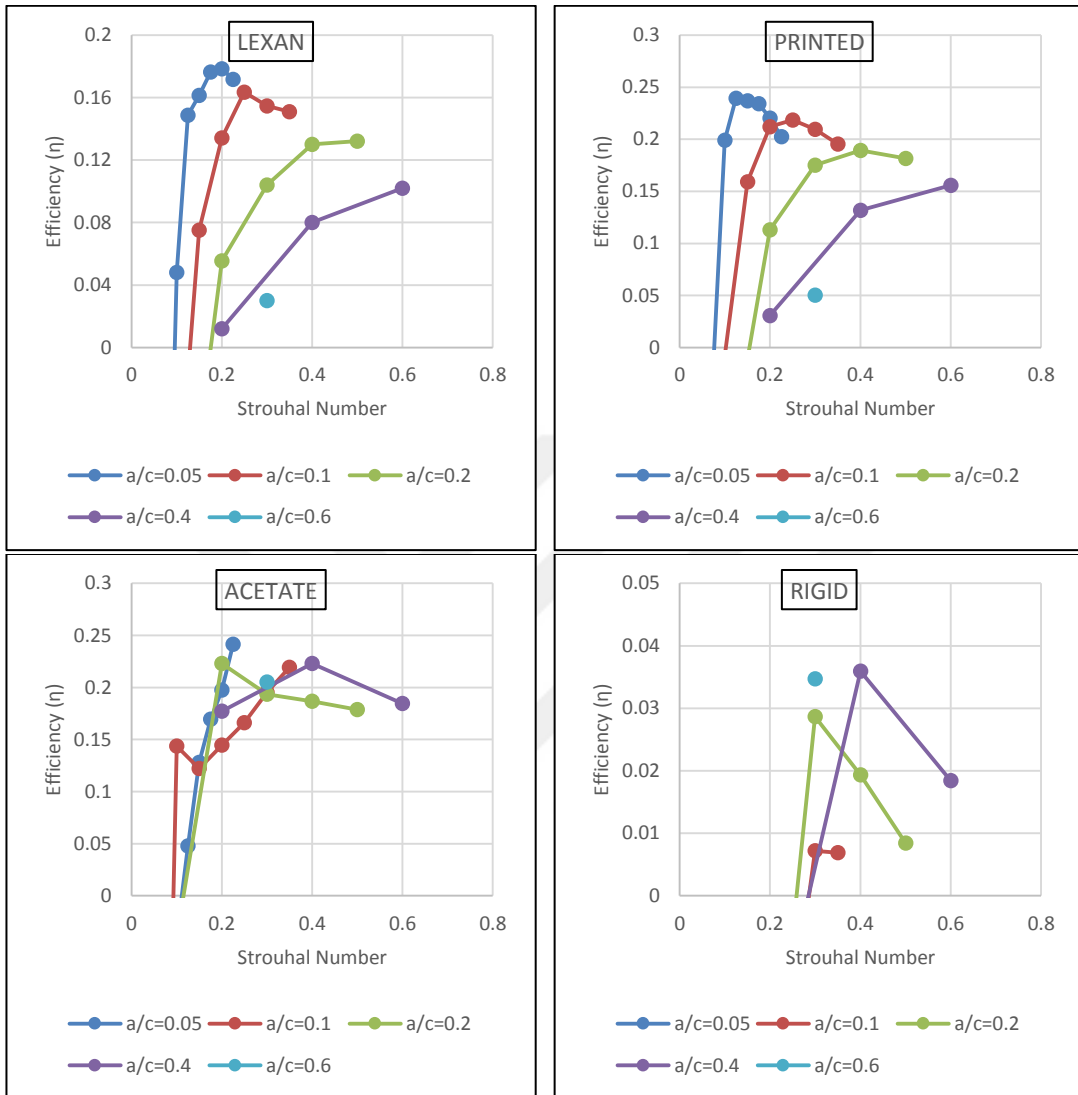


Figure 3.64 : Efficiencies (η) of four different wings with respect to Strouhal number.

To sum up all the force measurements and link various data, a similar graph to the one previously plotted in Son and Cetiner (2016) will be presented for the actual measurements (Figure 3.65). In this graph, y-axis is the efficiency (an indicator of power input and output) and x-axis is the ratio of the phases of trailing edge to leading edge (shape deformation) and F_y to the leading edge (force lag). By combining those features, a clear insight into the flow physics will be gained. In the study of Son and Cetiner (2016), it was stated that the efficiencies are peaking around the phase ratio of 1, however more data was required to reveal the general trend.

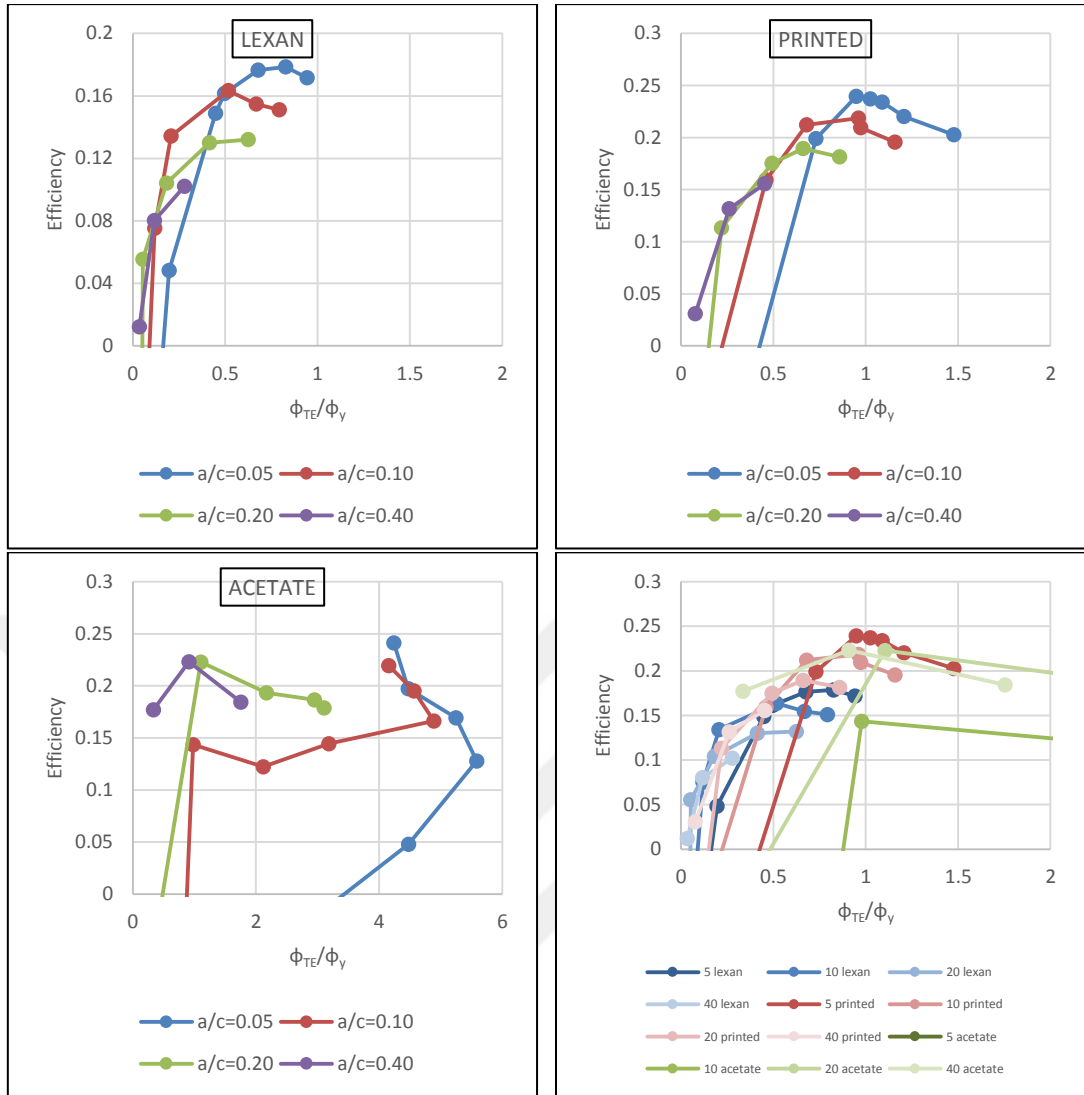


Figure 3.65 : Efficiency vs. phase ratio Φ_{TE}/Φ_y .

In Figure 3.65, efficiency with respect to the phase ratio is plotted for three different flexible wings. For the lexan wing, the efficiency peaks are observed in phase ratios between 0.5 and 1 for different flapping amplitudes. For the printed wing, the peaks are observed around phase ratio of 1. For the acetate wing, again there are peaks around phase ratio of 1, and at higher ratios where forces and trailing edge are totally out of phase, a different behavior is observed. Despite that, high efficiency values are attained at high phase ratios.

As aforementioned, trailing edge phases Φ_{TE} coincide with the cross-stream force phases Φ_y at natural frequency oscillations. The phase ratio of 1 on the graphs above corresponds to this situation, therefore it also includes natural frequency information. To sum up, flexible wings have peak efficiency values around natural frequencies where their trailing edge phases and F_y force phases also coincide.

3.4.3 DPIV results

Following the shape deformation and the force measurement results, DPIV data are presented herein to examine the vortical structures around flexible wings. Inheriting from shape deformations and force measurement results, one of the main features of chordwise flexible wings is explained aforementioned as the phase differences between leading and trailing edges and their impact on forces acting on the body with different time lags. Main focus of the study is proceeded on this phase lag and extended to the phase relations in vortex shedding. For that purpose, selected cases are presented in Figure 3.66 - Figure 3.69 at an instant when the clockwise vortex (blue) is just shed and a counter-clockwise vortex (red) is about to grow out at the trailing edge. That instant is noted on the upper right corner of each image as a number ranging from 1 to 9 indicating the position of the wing in a full motion cycle.

At lower frequency and amplitude cases (e.g. $f=0.5$ Hz, $a/c=0.05$ for the rigid wing) the wake has a long wavelength, low amplitude shape and is represented by a sketch, which implies that the coherent vortical structures and shedding cannot be observed. For the rigid wing, the shedding occurs at position #2 where the wing accelerates downwards. As the plunging frequency increases to $a/c=0.2$ and $a/c=0.4$, this instant is shifted to position #1 which indicates the shedding occurred in earlier stages of the motion cycle. When the flexible wings are considered, the most significant observation is that the position number is increasing systematically for the same cases. Therefore, it is evident that same vortex formations are attained at different stages of the motion cycle for the flexible wings. Leading and trailing edges in flexible wings have different temporal behaviors and vortex structures are affected by them accordingly. It is observed that the trailing edge motion determines the vortex shedding timing. As the wing gets more flexible, vortex shedding from the trailing edge is delayed and same vortex structures around the trailing edge are observed later in the flapping period.

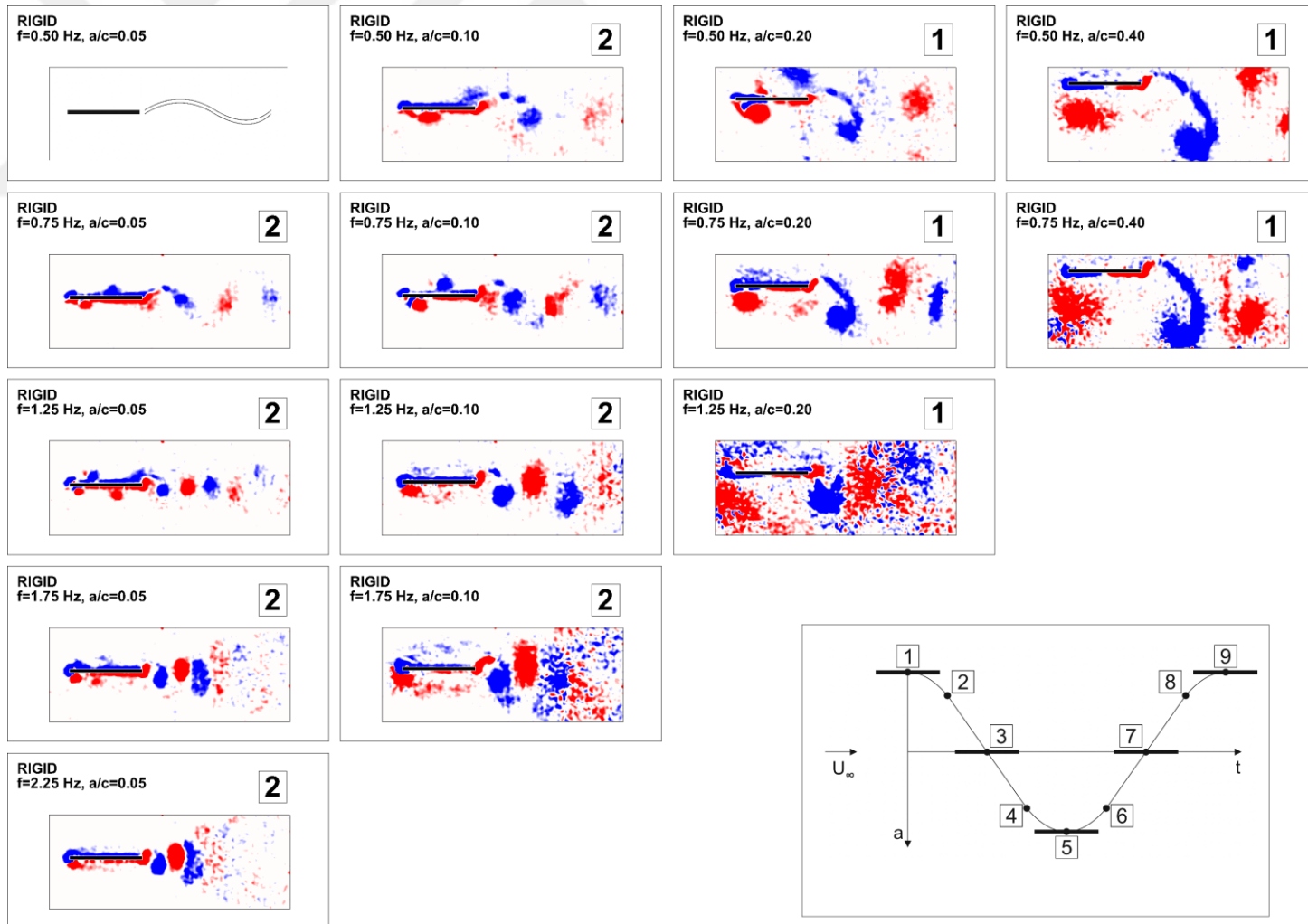


Figure 3.66 : Vortex shedding and positions in the motion cycle for the rigid wing.

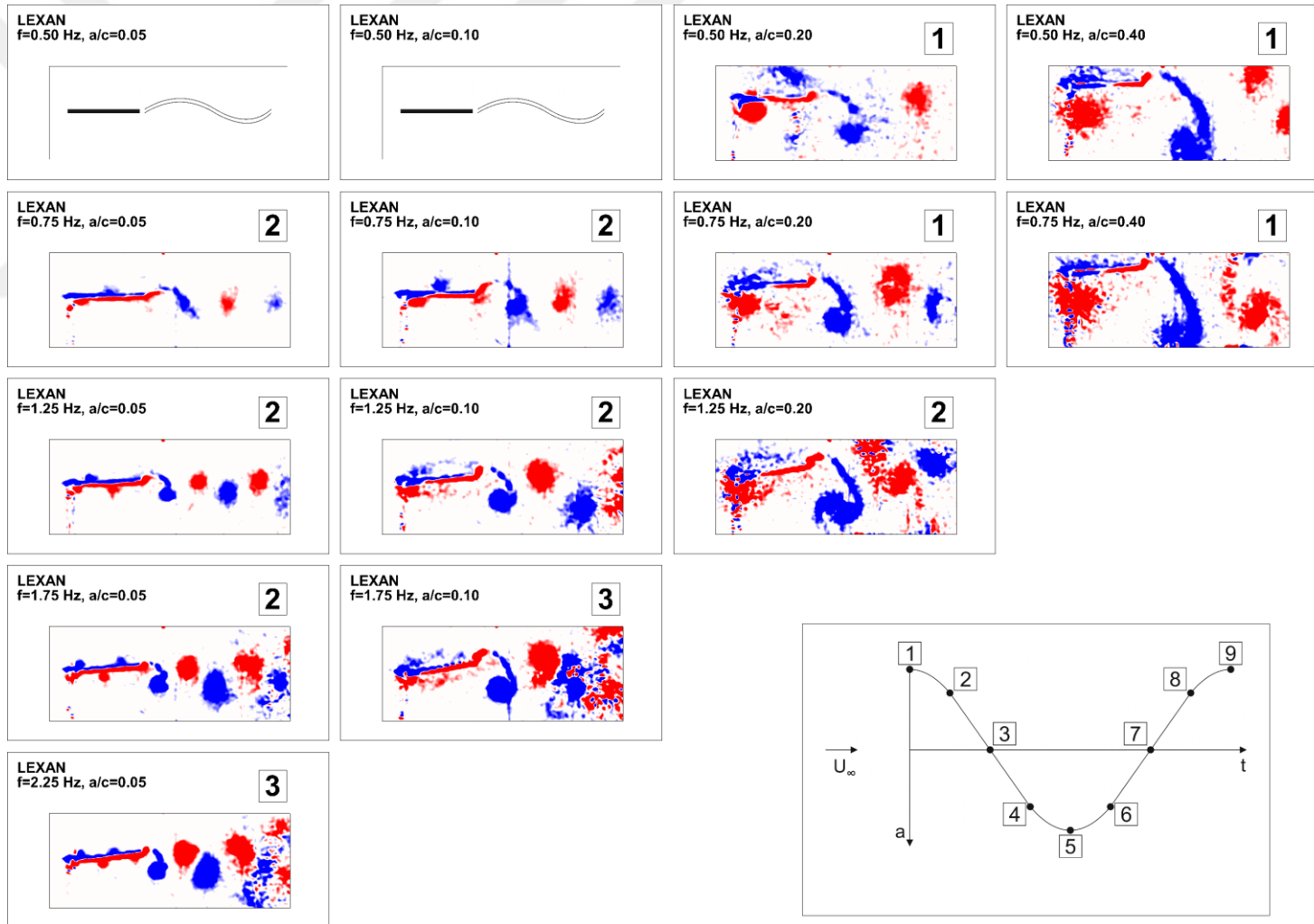


Figure 3.67 : Vortex shedding and positions in the motion cycle for the lexican wing.

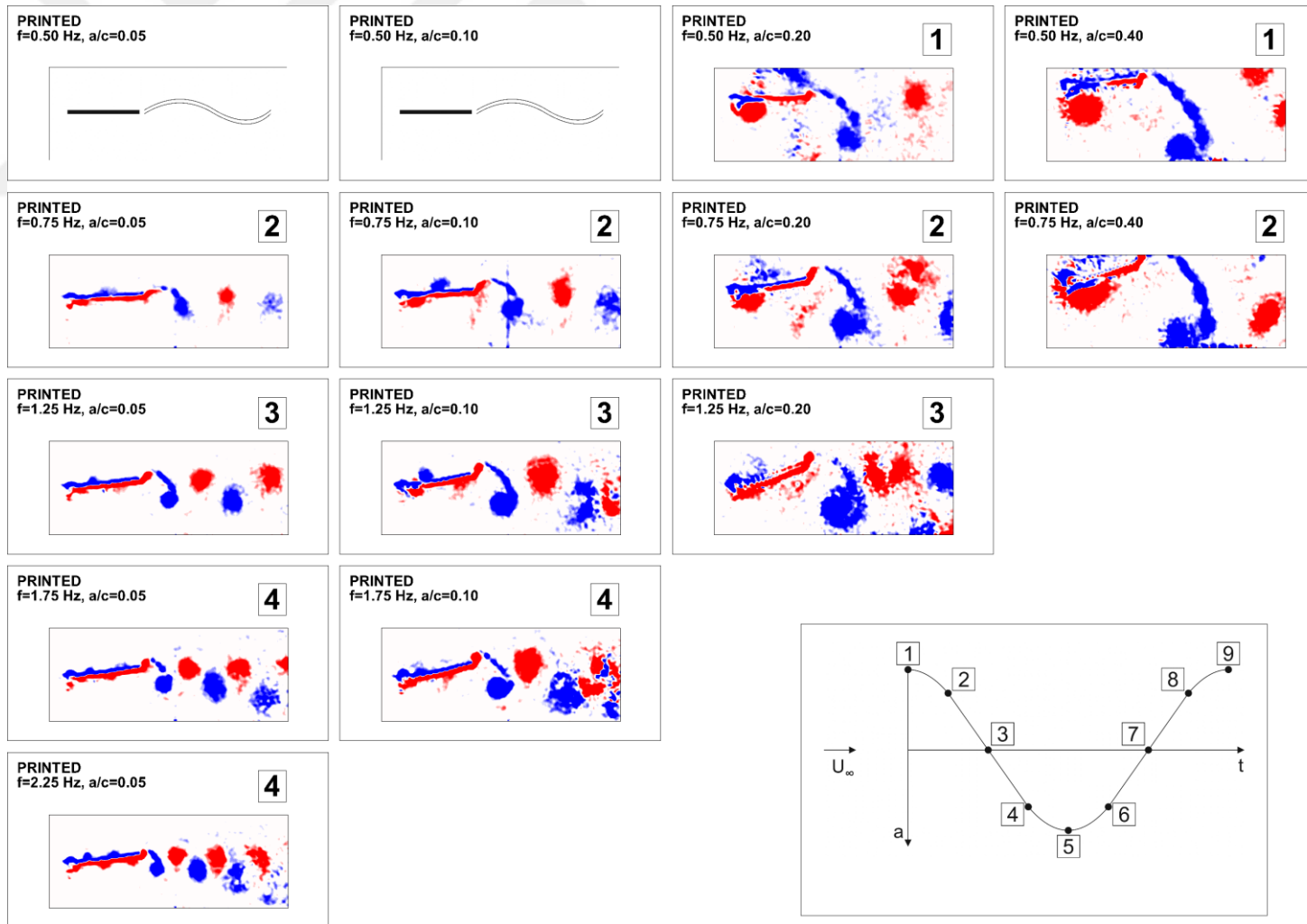


Figure 3.68 : Vortex shedding and positions in the motion cycle for the printed wing.

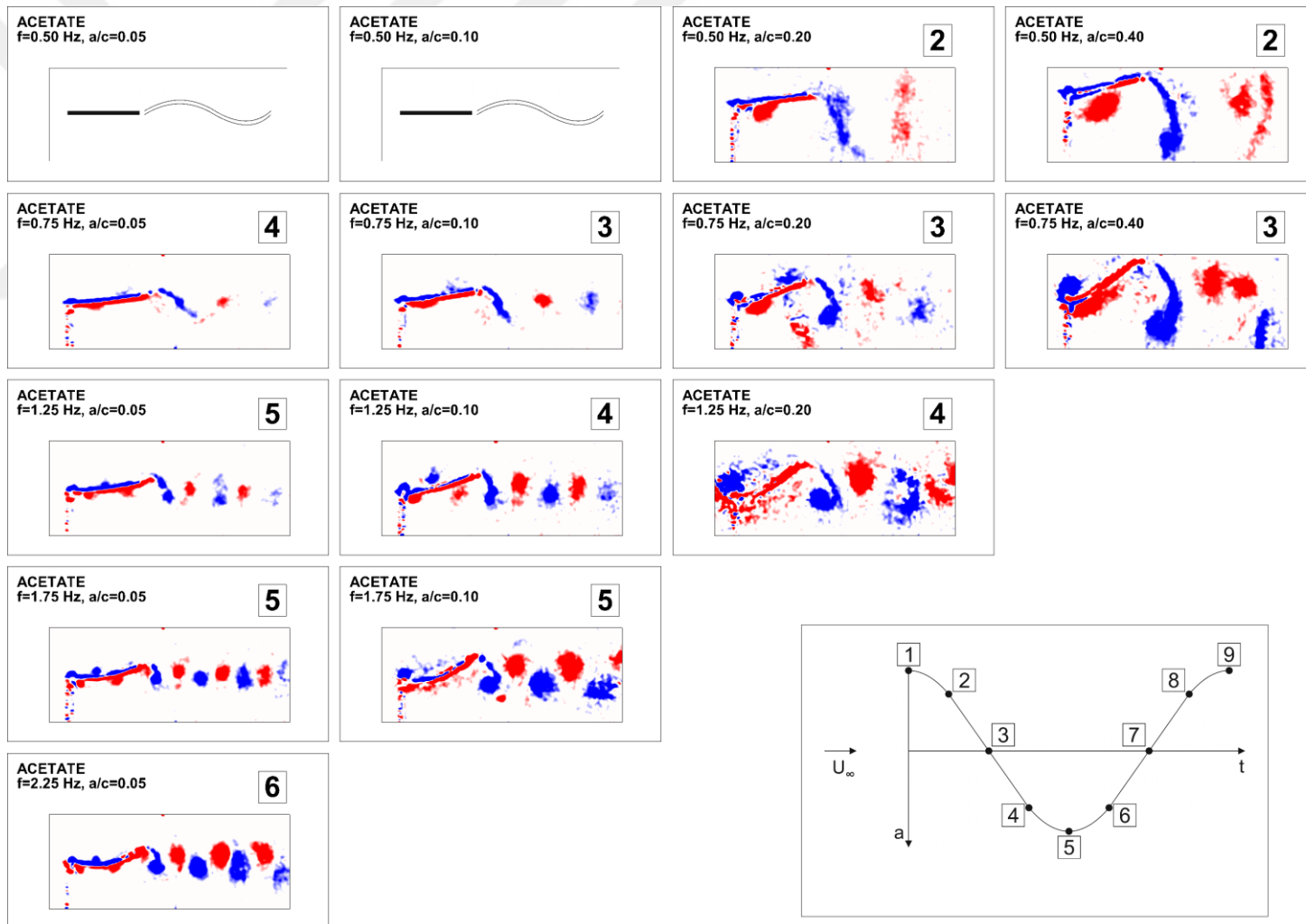


Figure 3.69 : Vortex shedding and positions in the motion cycle for the acetate wing.

In Figure 3.70 the case of $f=1.75$ Hz and $a/c=0.05$ is presented for all wing types in two columns. On the left, same flow structure pattern around the trailing edge is captured for four different wings. For the rigid and the lexan wings, similar vortex formation and shedding is observed around TE at position #2, whereas for the printed wing it is observed at position-4 and for the acetate wing at position #5. This also shows that increased TE vortex shedding delays when the flexibility is increased. On the right column, all wings are captured at the same LE position, namely at position #4. At this instant, TE vortex shedding is different for all wings. On the other hand, LE vortex shedding is similar for all wings. Clockwise vortex (blue) is on the upper surface at around quarter chord and the counter-clockwise (red) vortex is on the lower surface at around half chord. The position and the structure of the vortices shed from leading edge is similar for all flexible wings. Therefore, it is evident that the chordwise flexibility under parameters presented herein, alters the TEV shedding timing and strength, however it does not have a pronounced effect on LEV shedding.

In the Figure 3.70 the sketch representing position of the LE considers one period of motion made of 8 equidistant time snapshots. Therefore, each position number with respect to the next corresponds to 45 degrees of phase difference. For example, the acetate wing has a position number of 5 while the rigid wing has a position number of 2, which roughly corresponds to 135 degrees of phase difference between rigid and acetate wing in terms of vortex formation. Phase difference between LE and TE, calculated based on the wing shape from raw PIV images, is about 158 degrees as given in Figure 3.47. Position numbers differs by two between printed and the rigid wings, which corresponds to 90 degrees of phase difference. From the same graph (Figure 3.47), the actual value is measured to be about 100 degrees. It concluded that the LE-TE phases are the main factor responsible for the lag in vortex shedding from the TE. More time resolved PIV data in one period of motion can be more descriptive for vortex shedding timing and therefore for phase relations.

Another observation on the vortices shed into the wake is the coherency of the vortices at downstream of the wing. For the rigid wing, the vortices burst after one chord length in the wake as can be seen in Figure 3.70. As the wing gets more flexible, the vortices start to burst later. The vortices in the wake of the most flexible acetate wing preserve their coherency and can be tracked in full field of view. Early burst of the vortices can be attributed to the three-dimensionality effects. Therefore, it can be suggested that the

chordwise flexibility reduces the three-dimensionality effects that leads to a more two-dimensional flow. Also number of vortices observed in the wake increases when the wing gets more flexible.

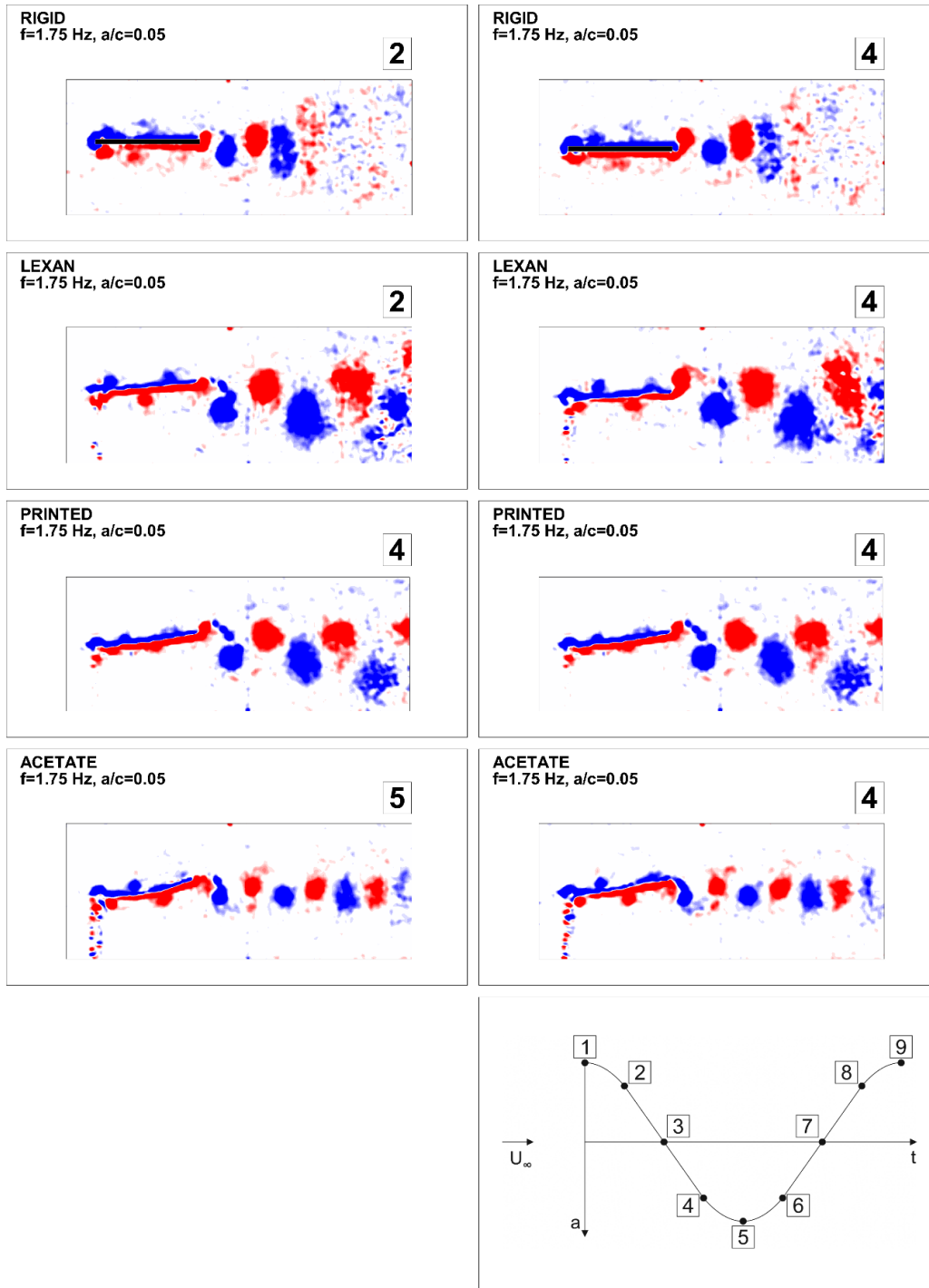


Figure 3.70 : Similar TE vortex shedding observed in different positions (Left), similar LE vortex shedding observed in same positions (Right).

Finally, vortical structures and velocity fields are presented in Figure 3.71 to investigate the natural frequency effects (e.g. intersecting phases, efficiency peaks) on

the flow field. Cases are selected to include the efficiency peaks and the wing also oscillates at its natural frequency. The images are selected such that the TE of the wing is at its maximum amplitude. Position number in all images are 3, which indicates that the LE is at the mid position of the motion amplitude and have the maximum velocity. At that instant, TE reaches its maximum, yielding a phase difference around 90 degrees between LE and TE. Vortex shedding in terms of timing is similar in the presented images. Clockwise (blue) vortex just detaches from the TE when the TE reaches its maximum and counter-clockwise (red) vortex is about to form at that instant. This is also an indication of the TE dominance on the flow structures. Although the vortex shedding from TE is similar, whole vortex map in the wake has different characteristics. Distance between vortices, vortex strengths, vortex burst etc. are different for all wings. Therefore, the assessment on the efficiency should be made individually for each wing among its own cases. At this point, the freestream velocity, horizontal and vertical flow velocities around the wing, LE and TE velocities and phases will be decisive parameters for efficiency.

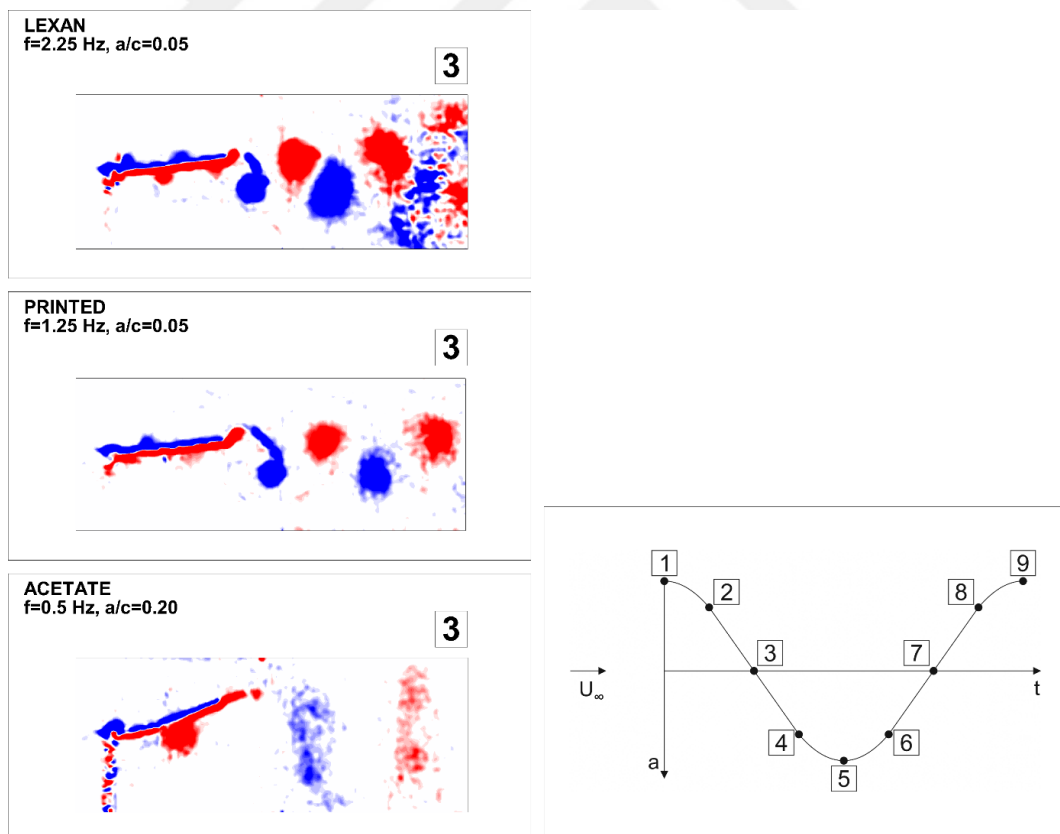


Figure 3.71 : Vortex shedding in natural frequency oscillations for flexible wings.

Horizontal (u) and vertical (v) components of velocity near the top surface of the wing are extracted on a line (Figure 3.72) for each time step and presented in Figure 3.73

and Figure 3.74. This representation aims to reveal how the flow field is affected by the flexibility of the flapping wing. It shows in detail where the high and the low velocity zones occur around the wing and how these velocity zones are transferred to the wake.

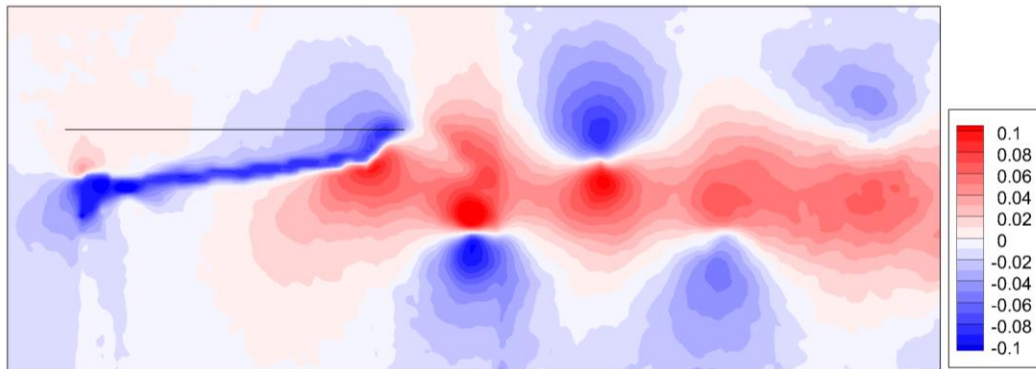


Figure 3.72 : Example of u velocity contours and extracted profiles line over the wing.

In Figure 3.73, profiles for streamwise velocity component, obtained in a reference frame moving with the freestream, ($u-U$), extracted from the line defined in Figure 3.72, are plotted for four different plunging frequencies. The wing is the printed one, and the cases are selected considering the efficiencies presented in Figure 3.62. For the amplitude of $a/c=0.05$, the efficiencies are positive (thrust is produced) starting from $f=1.00$ Hz, peaking at $f=1.25$ Hz, and decreasing after this frequency. Therefore, these cases are selected to investigate the peaking efficiency, and velocity profiles are plotted in a period of motion. The position numbers are taken from the sketch in Figure 3.71, and placed on the left column.

The red lines indicate the instance when the clockwise trailing edge vortex is shed and the counter clockwise vortex is just emerged. For the $f=1.00$ Hz case, red line falls in between 2nd and 3rd images, therefore color marking is not used. A delayed vortex shedding with increasing flapping frequency can be observed in this representation as previously shown on PIV images. Red lines gradually shift from position #3 to position #5 when the flapping frequency is increased from $f=1.25$ Hz to $f=2.25$ Hz. The shape of velocity profiles colored in red is similar for different frequencies. However, before and after this instant, velocity distributions are different, which is key to understand how the aerodynamic performance of the wings are also different.

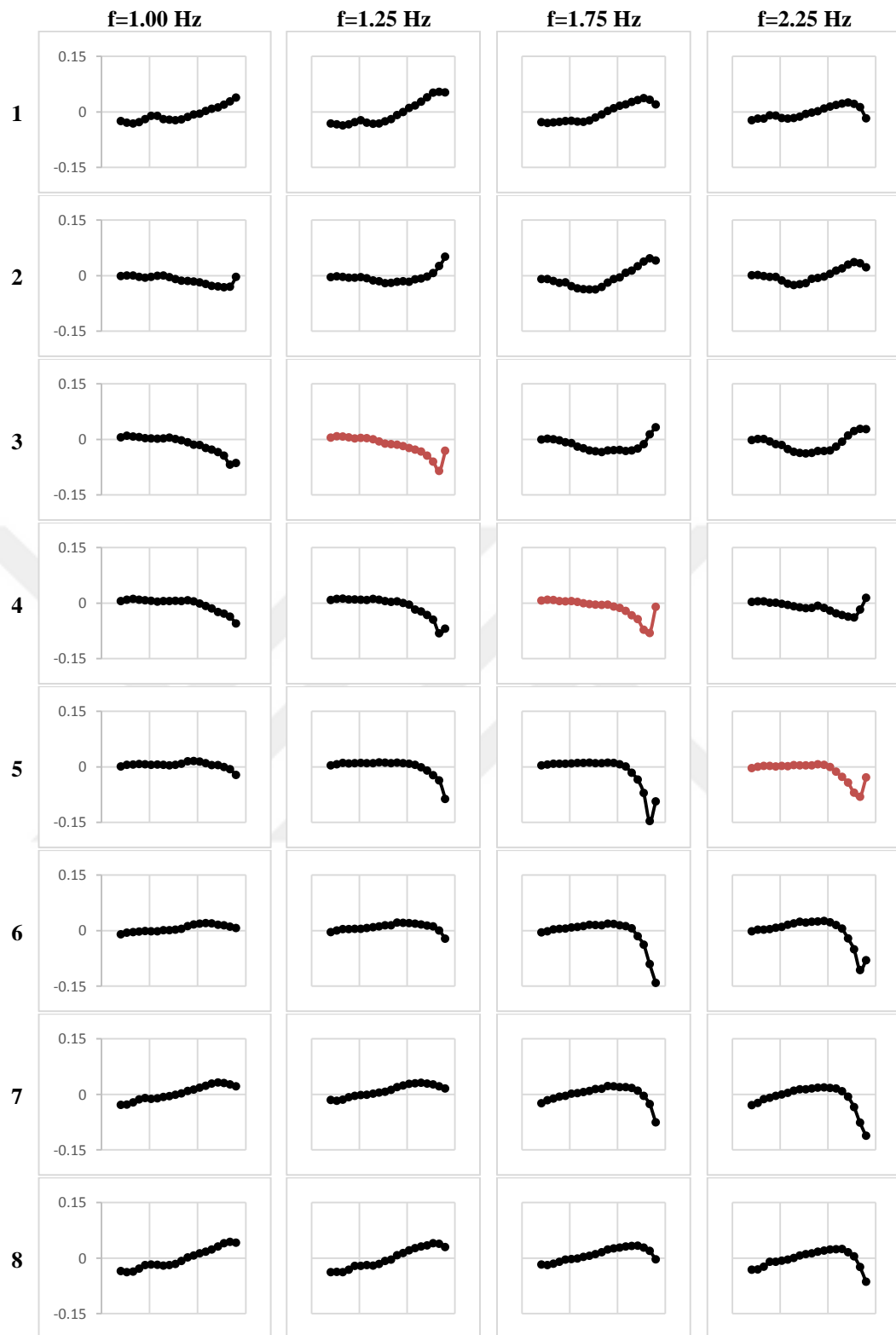


Figure 3.73 : Streamwise velocity ($u-U$) profiles in a period of motion for printed wing plunging at an amplitude of $a/c=0.05$

To start with, the lowest position of the plunge amplitude (position #5) is considered. At position #5, the velocity distribution is mainly around zero, meaning that the velocities are around freestream velocity. Around the trailing edge, the velocities are

negative indicating a flow zone slower than the freestream. A local minimum peak and then an increase is observed for $f=1.75$ Hz and $f=2.25$ Hz at position #5 implying the occurrence of the trailing edge vortex, which is also evident in the early stages for $f=1.00$ Hz and $f=1.25$ Hz. When the leading edge of the wing moves upwards, position numbers of 6 to 8 should be considered. Therefore, during the upward motion of the LE for flapping frequencies of $f=1.00$ Hz and $f=1.25$ Hz, a low velocity zone is observed in the first half of the chord. On the other hand, in the second half there is a gradual increase creating a peak around the trailing edge at position #8. For frequencies of $f=1.75$ Hz and $f=2.25$ Hz, velocity also increases towards the TE, however this increase is accompanied by a sharp decrease at the TE indicating the effect of the TEV with a lag. This negative velocity values are recovered and positive velocities are obtained at position #8 for $f=1.75$ and at position #2 for $f=2.25$. When this is compared to the case of $f=1.25$ Hz, the positive velocity values at the TE are obtained in earlier stages (position #7). And this increase is continuously enlarged in accordance with the wing motion and TE lag due to flexibility, until the high velocity zone is transferred to the freshly emerged TEV. When the case of $f=2.25$ Hz is considered, velocities at the trailing edge can barely reach positive values at positions #2 and #3, having a peak value smaller than those of the cases $f=1.25$ Hz and $f=1.75$ Hz. One of the reasons for not reaching high peak values for the case of $f=2.25$ Hz is the strong vortex created at the TE, which decreases the velocity values significantly as can be seen in positions #6 and #7. The flow cannot properly recover from these extreme negative values. Therefore, a stronger vortex is not always preferable for efficiency.

Another reason is that, while the flexibility for the wing flapping at $f=1.25$ Hz exploits and enhances the high velocity zone created on the upper surface of the wing with the correct trailing edge timing, the case of $f=2.25$ Hz cannot achieve this. We can describe this phenomenon as “catching” the flow and transferring the kinetic energy of the flow to the wake in the form of shed vortices. The case of $f=1.25$ Hz properly exemplifies this phenomenon and performs the motion with the highest efficiency as shown in Figure 3.73. When all cases are compared in Figure 3.73, the case of $f=1.25$ Hz has the highest peak velocity at trailing edge just before the occurrence of the TEV at position #1. This peak is both shifted to later positions in time and decreased in amplitude as the frequency increases to $f=1.75$ Hz and then to $f=2.25$ Hz, leading to a decrease in the efficiency.

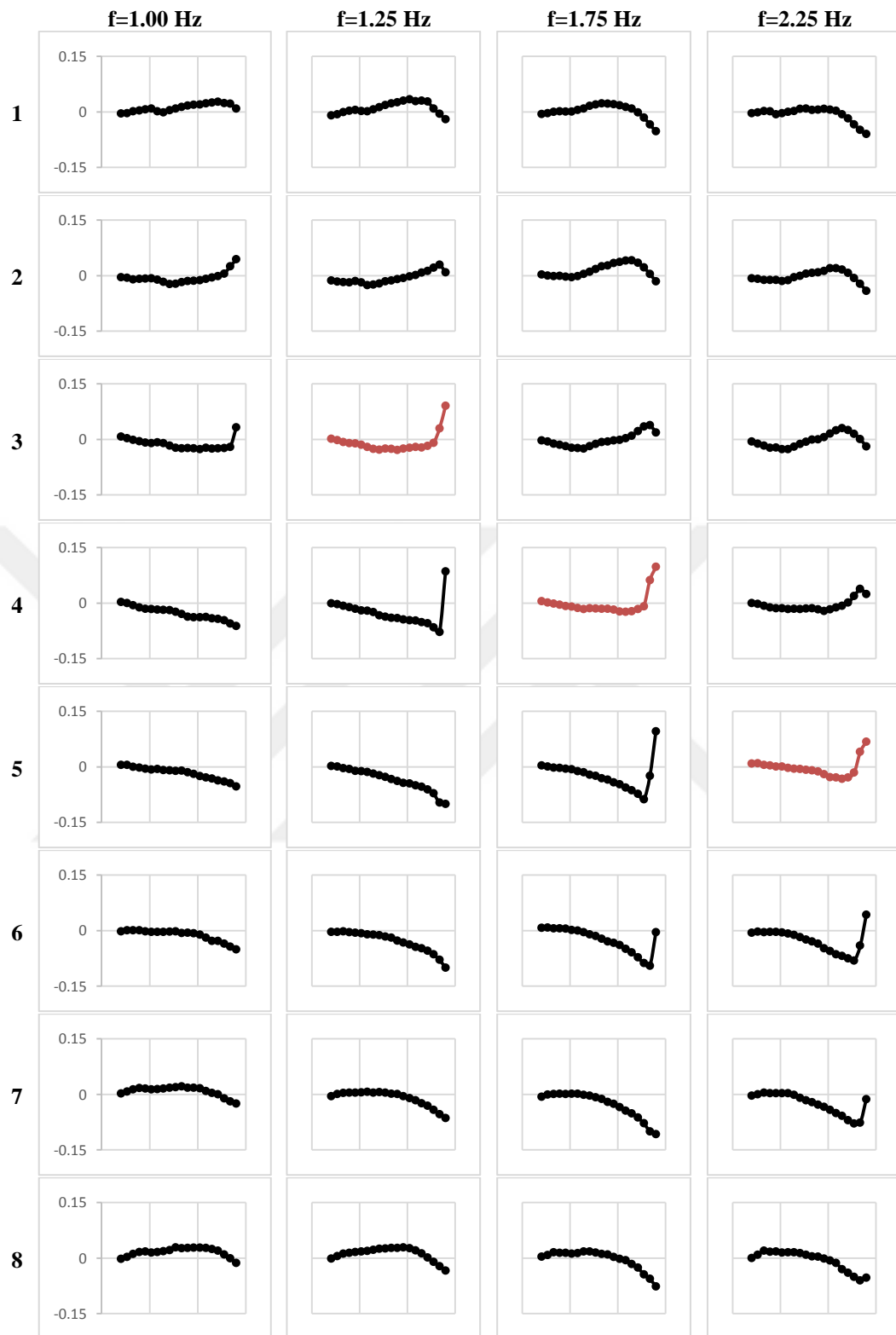


Figure 3.74 : Cross-stream velocity (v) profiles in a period for the printed wing plunging at an amplitude of $a/c=0.05$.

Similar to the u velocity distributions, v velocity distributions extracted on the same line are presented in Figure 3.74 for four flapping frequencies. Red lines again indicate TEV occurrence. At the lowest LE position (position #5), the cases of $f=1.00$ Hz and

$f=1.25$ Hz have distributions starting around zero near the LE and decreasing continuously to negative values towards the TE. As the LE moves upwards, these negative velocities recover to positive as can be seen in position #8, especially around half chord. When the LE reaches its maximum position at position #1 this positive velocity zone is shifted towards the TE, and finally, just before the TE vortex occurrence, velocities peak at the TE as can be seen in position #2. For frequencies of $f=1.75$ Hz and $f=2.25$ Hz, at position #5, continuous velocity decrease from LE to TE is also observed, however a high positive velocity peak is evident above the TE due to the shed vortex. Recovery from this state takes a long time for $f=2.25$ Hz, even at position #8 decrease and increase in the velocities can be observed at the TE. As a consequence, positive velocity zone cannot be formed for the case of $f=2.25$ Hz at position #1, whereas the other cases have it. For $f=2.25$ Hz, the positive velocity zone can only be observed in a small region near the TE at position #2 and position #3. Afterwards, the TEV is shed and indicated in position #5 by the red line. Peak value on the red line for the case of $f=2.25$ Hz is lower than other cases. The peak value on the velocity distribution obtained at the position just after that of the red line is also lower than those attained for other frequencies. The case of $f=2.25$ Hz is the highest frequency case among other cases and higher transverse velocities are expected due to high velocity of the wing. However, the case of $f=2.25$ Hz cannot yield higher velocities, possibly due to the phase difference between LE and TE hence the wing shape is not suitable for exploiting the high velocity zones created around the wing during flapping motion. Consequently, efficiency is negatively affected and the case of $f=2.25$ Hz yields lower value compared to that of other cases.

4. CONCLUDING REMARKS AND RECOMMENDATIONS

4.1 Summary of Major Contributions

Two different motion types, namely impulsive pitch-up and plunging motions are investigated on rigid and flexible wings. The flow structures in the near-wake of an impulsively pitching flat plate at different rates and associated loadings have been studied experimentally to reveal the effect of the AR on the three dimensionality of the flow.

Whether the plate pitches up fast or slow, the flow remains mostly 2D along the span for plates with $AR = 4$ and above. During the motion, the effect of the AR is to shift the force variation in amplitude without changing its variation character. The effect of AR, hence, the three-dimensionality of the flow becomes pronounced after the motion ends. The formation of a local maximum in the force variations after the motion ends was evident for wings with $AR > 2$. There exist two peaks for wings with $AR \geq 6$. These secondary or even tertiary peaks occur because of the formation of a new LEV.

Even if the effective ARs of the wings are the same, the one with a symmetry plane did not yield exactly the same flow topology and hence the same force-time histories as the fully submerged wing. There were slight differences due to the three-dimensionality of the flow. Therefore, an endplate representing the symmetry plane should carefully be placed with special care to ensure that the gap between the wing root and the endplate is approximately 2 mm (i.e., 2% of the chord).

Although wings are flexible, most of them do not deflect considerably during pitch-up motions. Major deflection is due to oncoming flow at the end of the motion where the wing stays at an angle of attack of 45° . The deflection is only high for the most flexible acetate wing, which results in a lower angle of attack. As a consequence, low C_D is obtained for the acetate wing. When flow structures are examined, streamline topology of the acetate wing shows differences due to the reduced angle of attack both in fast and slow motion cases. Continuous LEV and TEV vortex shedding can be observed for the acetate wing.

Investigations on plunging rigid wings are focused on the phase relations between the motion and the measured forces to fill the gap in the literature. It is found that the phase lag for the cross-stream force component decreases as the reduced frequency increases, and for a given reduced frequency, the phase lag increases as the plunging amplitude increases. The variation of the horizontal spacing between vortex cores with the reduced frequency follows the same characteristics as those of the phase lag for the cross-stream force. On the other hand, the phase lag for the streamwise force component decreases as the plunging amplitude increases for low reduced frequencies. The decrease converges to a phase lag value of 90° , which coincides with the maximum velocity of the wing. After the minimum is reached, the phase lag for the streamwise force component starts to increase. The minimum phase lag coincides with the reduced frequency where the crossover from drag to thrust is observed and maximum flapping efficiency is obtained. When the thrust is produced, the phase lag for the streamwise force component increases. Moreover, according to the vortex structures, the crossover from drag to thrust is observed when the LEV starts to hold around the leading edge and does not convect downstream along the plate.

The present rigid wing study, being in agreement with Theodorsen's theory, extends it for the phase lag variation for the cross-stream force component when plunging amplitude also varies. Besides, the phase lag for the streamwise component is also investigated and compared to Garrick's theory. In this perspective, the contribution of the present study is expected to especially be revealed in the flexible flapping wing investigations where extra body motion affects the force timing entirely.

In flexible flapping wings, trailing edge amplitude makes a peak when the oscillations are performed near the natural frequency of the wing ($f/f_n \sim 1$). For the acetate wing, frequencies beyond the natural frequency can be tested and after $f/f_n = 2$, trailing edge amplitudes start to increase again. The values are in a continuous increase in the measurement range up to $f/f_n = 4.4$. This finding suggests that, higher trailing edge amplitudes can be reached when the flapping frequencies are beyond the resonant frequency.

When Φ_y phases are considered, it is observed that the flexible wings have completely different phase variations compared to those of the rigid wings. Natural frequency appears to have an effect on Φ_y phase variations. Phase values increase approximately up to the natural frequency, and then exhibit a decrease followed by an increase

behavior at higher flapping frequencies (can be observed for acetate wing). Besides the natural frequency, flapping amplitude also has an effect on phases such as the peak obtained near the natural frequency diminishes at higher amplitudes for the acetate wing. This implies that natural frequency and flapping amplitude should be interpreted together.

An interesting result is obtained from the graph of combined $\Phi_y - \Phi_{TE}$ phases; trailing edge phases and force phases are intersecting at different plunging frequencies for different wings. The intersecting frequencies coincide with the natural frequency of the wing. In other words, cross-stream force phases and trailing edge phases are equal when the wings are plunged near their natural frequencies. Flexible wings have peak efficiency around their natural frequencies where their trailing edge phases and F_y force phases also coincide.

Unlike the rigid wing, the distribution of Φ_x phases have similar characteristics with those of Φ_y phases for flexible wings. This similarity indicates that the flexibility effects are not only observed in cross-stream direction, however flexibility also affects forces in streamwise direction. In flexible wings, elastic forces emerge in both streamwise and cross-stream directions coupled with the trailing edge deflection. The similarity between the streamwise and the cross-stream force phases is a result of these prevailing elastic forces over the other existing forces, namely circulatory and added mass forces.

The efficiency peaks shift towards high Strouhal numbers when the flapping amplitude is increased. For the flexible wings, the peak efficiencies are obtained in a Strouhal number range of 0.1 – 0.6. High efficiency zone in the literature is expressed in a Strouhal number range of 0.2 – 0.4 and for the flexible wings this range is generally valid. The boundaries of the range are slightly extended for the flexible wings in different flapping amplitudes.

Same flow structure topologies are attained at different stages of the motion cycle for the flexible wings. It is observed that the TE motion determines the timing of vortex shedding. As the wing gets more flexible, vortex shedding from the TE delays and similar vortex structures around the TE are observed later in the flapping period. Chordwise flexibility under parameters presented herein, alters the timing of TEV

shedding and its strength, however it does not have a pronounced effect on LEV shedding.

For the rigid wing, the vortices burst after one chord length in the wake. As the wing gets more flexible, the vortices start to burst later. The vortices in the wake of the most flexible acetate wing preserve their coherency and can be tracked in full field of view. Also number of vortices observed in the wake increases when the wing gets more flexible.

The flexibility for the wing flapping around its natural frequency exploits and enhances the high velocity zones created around the wing with the correct TE timing, yielding high efficiency. This can be considered as “catching” the flow and transferring the kinetic energy of the flow to the wake in the form of shed vortices, which is found to be crucial for high efficiency.

4.2 Recommendations for Further Study

Oscillations of the flexible wings near their natural frequency lead to efficiency peaks as presented in the results section. Higher than natural frequency oscillations could be also investigated for the most flexible acetate wing. Efficiencies exceeding those obtained at the natural frequency flapping are observed in this zone. At those high frequencies, mode shape of the wings starts to change and the motion of the wing becomes undulatory. The physics of the undulatory motion is different than the oscillatory motion and these two modes can be observed in aquatic animals. Higher frequency zone exceeding the resonant frequency can be investigated in detail using wings having low natural frequencies.

The lowest flapping frequency in this study was 0.25 Hz. Around this flapping frequency, contributions of the circulatory and non-circulatory components of the lift are close to each other. Lower flapping frequencies, where the circulatory forces are dominant, are worthwhile to investigate, possibly to study the gust effect on flapping wings. However, wings with high flexibility should be used in these low flapping frequency cases to observe the flexibility effects.

Pressure estimation from PIV images is also a current interest. The applications of the method on flexible wing studies can be assistive for understanding the flow physics around flexible wings and determining the loadings on wing surfaces.

Gust effect on flapping or pitching wings is a popular subject recently. Aerodynamic performance of the flexible wings is different from the rigid ones as presented in the current investigation. Flexible wings have shape deformations, and distinct interactions with the surrounding fluid compared to the rigid wings. Periodic or single vortex gusts alter the oncoming flow to the wing and change the flow structures around and loading on the wing. As a biomimetic study, flexible wings under gust effect can be an interesting investigation task.





REFERENCES

- Adrian, R. J.** (1991). Particle-imaging techniques for experimental fluid mechanics. *Annual Review of Fluid Mechanics*, 23(1), 261-304.
- Anderson, J. M., Streitlien, K., Barrett, D. S., & Triantafyllou, M. S.** (1998). Oscillating foils of high propulsive efficiency, *Journal of Fluid Mechanics*, 360, 41-72.
- Ansari, S. A., Żbikowski, R., & Knowles, K.** (2006). Aerodynamic modelling of insect-like flapping flight for micro air vehicles. *Progress in Aerospace Sciences*, 42(2), 129-172.
- Aydın, B. T., Cetiner, O., & Unal, M. F.** (2010). Effect of self-issuing jets along the span on the near-wake of a square cylinder, *Experiments in Fluids*, 48(6), 1081-1094.
- Baik, Y. S., Aono, H., Rausch, J. M., Bernal, L. P., Shyy, W., & Ol, M. V.** (2010). Experimental study of a rapidly pitched flat plate at low Reynolds number. *40th AIAA Fluid Dynamics Conference*. Chicago, USA, 28 June - 1 July.
- Betz, A.** (1912) Ein beitrage zur erklarung des segelfluges, *Zeitschrift fuer Flugtechnik und Motorluftschiffahrt*, 3, 269–272.
- Bratt, J. B.** (1953). *Flow patterns in the wake of an oscillating aerofoil* (Report No. 2773). UK: HM Stationery Office.
- Carr, Z. R., Chen, C., & Ringuette, M. J.** (2013). Finite-span rotating wings: three-dimensional vortex formation and variations with aspect ratio, *Experiments in Fluids*, 54, 1-26.
- Combes, S. A., & Daniel, T. L.** (2003a). Flexural stiffness in insect wings I. Scaling and the influence of wing venation, *Journal of Experimental Biology*, 206(17), 2979-2987.
- Combes, S. A., & Daniel, T. L.** (2003b). Flexural stiffness in insect wings II. Spatial distribution and dynamic wing bending, *Journal of Experimental Biology*, 206(17), 2989-2997.
- Combes, S. A., & Daniel, T. L.** (2003c). Into thin air: contributions of aerodynamic and inertial-elastic forces to wing bending in the hawkmoth *Manduca sexta*, *Journal of Experimental Biology*, 206(17), 2999-3006.
- Cory, R., & Tedrake, R.** (2008). Experiments in fixed-wing UAV perching, *In Proceedings of the AIAA Guidance, Navigation, and Control Conference*, (pp. 1-12). Reston, USA.
- Daniel, T. L., & Combes, S. A.** (2002). Flexible wings and fins: bending by inertial or fluid-dynamic forces?, *Integrative and Comparative Biology*, 42(5), 1044-1049.

- DeLaurier, J. D.** (1993). An aerodynamic model for flapping-wing flight, *Aeronautical Journal*, 97(964), 125-130.
- Dickinson, M. H., Lehmann, F. O., & Sane, S. P.** (1999). Wing rotation and the aerodynamic basis of insect flight, *Science*, 284(5422), 1954-1960.
- Eberle, A. L., Reinhall, P. G., & Daniel, T. L.** (2014). Fluid–structure interaction in compliant insect wings, *Bioinspiration & Biomimetics*, 9(2), 025005.
- Ellington, C. P.** (1984). The aerodynamics of hovering insect flight. I. The quasi-steady analysis, *Philosophical Transactions of the Royal Society of London B: Biological Sciences*, 305(1122), 1-15.
- Ellington, C. P.** (1984b). The aerodynamics of hovering insect flight. II. Morphological parameters, *Philosophical Transactions of the Royal Society of London B: Biological Sciences*, 305(1122), 17-40.
- Ellington, C. P.** (1984c). The aerodynamics of hovering insect flight. III. Kinematics, *Philosophical Transactions of the Royal Society of London B: Biological Sciences*, 305(1122), 41-78.
- Ellington, C. P.** (1984d). The aerodynamics of hovering insect flight. IV. Aerodynamic mechanisms. *Philosophical Transactions of the Royal Society of London B: Biological Sciences*, 305(1122), 79-113.
- Ellington, C. P.** (1984e). The aerodynamics of hovering insect flight. V. A vortex theory. *Philosophical Transactions of the Royal Society of London Series B-Biological Sciences*, 305(1122), 115-144.
- Ellington, C. P.** (1984f). The aerodynamics of hovering insect flight. VI. Lift and power requirements. *Philosophical Transactions of the Royal Society of London B: Biological Sciences*, 305(1122), 145-181.
- Ellington, C. P.** (1999). The novel aerodynamics of insect flight: applications to micro-air vehicles. *Journal of Experimental Biology*, 202(23), 3439-3448.
- Ellington, C. P., Van Den Berg, C., Willmott, A. P., & Thomas, A. L.** (1996). Leading-edge vortices in insect flight. *Nature*, 384, 626-630.
- Floreano, D., Zufferey, J. C., Srinivasan, M. V., & Ellington, C.** (2009). *Flying insects and robots*. Heidelberg: Springer.
- Ford, C. P., & Babinsky, H.** (2013). Lift and the leading-edge vortex. *Journal of Fluid Mechanics*, 720, 280-313.
- Freytmuth, P.** (1988). Propulsive vortical signature of plunging and pitching airfoils. *AIAA Journal*, 26(7), 881-883.
- Garcia, H., Abdulrahim, M., & Lind, R.** (2003). Roll control for a micro air vehicle using active wing morphing. *AIAA Guidance, Navigation and Control Conference and Exhibit*, Austin, Texas, 11-14 August.
- Garmann, D. J., & Visbal, M. R.** (2011). Numerical investigation of transitional flow over a rapidly pitching plate. *Physics of Fluids*, 23(9), 094106.
- Garmann, D. J., Visbal, M. R., & Orkwis, P. D.** (2013). Three-dimensional flow structure and aerodynamic loading on a revolving wing. *Physics of Fluids*, 25(3), 034101.

- Garrick, I. E.** (1937). *Propulsion of a flapping and oscillating airfoil* (NACA TR No. 567).
- Gordon, J. E.** (1978). *Structures: or why things don't fall down*. New York: Penguin Books.
- Granlund, K., Ol, M., & Bernal, L.** (2013). Quasi-steady response of free-to-pivot flat plates in hover. *Journal of Fluids and Structures*, 40, 337-355.
- Granlund, K., Ol, M. V., & Bernal, L. P.** (2013). Unsteady pitching flat plates. *Journal of Fluid Mechanics*, 733, R5.
- Gülçat, Ü.** (2016). *Fundamentals of modern unsteady aerodynamics*. Springer.
- Gursul, I., Cleaver, D. J., & Wang, Z.** (2014). Control of low Reynolds number flows by means of fluid–structure interactions. *Progress in Aerospace Sciences*, 64, 17-55.
- Hartloper, C., Kinzel, M., & Rival, D. E.** (2013). On the competition between leading-edge and tip-vortex growth for a pitching plate. *Experiments in Fluids*, 54(1), 1447.
- Heathcote, S., & Gursul, I.** (2007). Flexible flapping airfoil propulsion at low Reynolds numbers. *AIAA Journal*, 45(5), 1066-1079.
- Heathcote, S., Martin, D., & Gursul, I.** (2004). Flexible flapping airfoil propulsion at zero freestream velocity. *AIAA Journal*, 42(11), 2196-2204.
- Hu, H., Kumar, A. G., Abate, G., & Albertani, R.** (2010). An experimental investigation on the aerodynamic performances of flexible membrane wings in flapping flight. *Aerospace Science and Technology*, 14(8), 575-586.
- Ifju, P. G., Jenkins, D. A., Ettinger, S., Lian, Y., Shyy, W., & Waszak, M. R.** (2002). Flexible-wing-based micro air vehicles. *40th AIAA Aerospace Sciences Meeting & Exhibit*. Reno, NV, USA.
- Jantzen, R. T., Taira, K., Granlund, K. O., & Ol, M. V.** (2014). Vortex dynamics around pitching plates. *Physics of Fluids*, 26(5), 053606.
- Jones, A. R., & Babinsky, H.** (2010). Unsteady lift generation on rotating wings at low Reynolds numbers. *Journal of Aircraft*, 47(3), 1013-1021.
- Jones, K. D., & Platzer, M. F.** (2009). Design and development considerations for biologically inspired flapping-wing micro air vehicles. *Experiments in Fluids*, 46(5), 799-810.
- Jones, K. D., Dohring, C. M., & Platzer, M. F.** (1998). Experimental and computational investigation of the Knoller-Betz effect. *AIAA Journal*, 36(7), 1240-1246.
- Kancharala, A. K., & Philen, M. K.** (2016). Optimal chordwise stiffness profiles of self-propelled flapping fins. *Bioinspiration & Biomimetics*, 11(5), 056016.
- Kang, C. K., Aono, H., Cesnik, C. E., & Shyy, W.** (2011). Effects of flexibility on the aerodynamic performance of flapping wings. *Journal of Fluid Mechanics*, 689, 32-74.

- Katz, J., & Weihs, D.** (1978). Hydrodynamic propulsion by large amplitude oscillation of an airfoil with chordwise flexibility. *Journal of Fluid Mechanics*, 88(03), 485-497.
- Katzmayr R.** (1922) *Effect of periodic changes of angle of attack on behaviour of airfoils* (NACA TM No.147).
- Knoller, R.** (1909) Die gesetze des luftwiderstandes. *Flug- und Motortechnik* 3, 1-7.
- Koochesfahani, M. M.** (1989). Vortical patterns in the wake of an oscillating airfoil. *AIAA Journal*, 27(9), 1200-1205.
- Lee, K. B., Kim, J. H., & Kim, C.** (2011). Aerodynamic effects of structural flexibility in two-dimensional insect flapping flight. *Journal of Aircraft*, 48(3), 894-909.
- Leishman, J.** (2006). *Principles of helicopter aerodynamics* (2nd Ed.). Cambridge University Press.
- Lentink, D., & Dickinson, M. H.** (2009). Rotational accelerations stabilize leading edge vortices on revolving fly wings. *Journal of Experimental Biology*, 212(16), 2705-2719.
- Lighthill, M. J.** (1969). Hydromechanics of aquatic animal propulsion. *Annual Review of Fluid Mechanics*, 1(1), 413-446.
- Liu, H., & Kawachi, K.** (1998). A numerical study of insect flight. *Journal of Computational Physics*, 146(1), 124-156.
- Mancini, P., Manar, F., Granlund, K., Ol, M. V., & Jones, A. R.** (2015). Unsteady aerodynamic characteristics of a translating rigid wing at low Reynolds number. *Physics of Fluids*, 27(12), 123102.
- Miao, J. M., & Ho, M. H.** (2006). Effect of flexure on aerodynamic propulsive efficiency of flapping flexible airfoil. *Journal of Fluids and Structures*, 22(3), 401-419.
- Michelin, S., & Smith, S. G. L.** (2009). Resonance and propulsion performance of a heaving flexible wing. *Physics of Fluids (1994-present)*, 21(7), 071902.
- Molina, J., & Zhang, X.** (2011). Aerodynamics of a heaving airfoil in ground effect. *AIAA Journal*, 49(6), 1168–1179.
- Monnier, B., Naguib, A. M., & Koochesfahani, M. M.** (2015). Influence of structural flexibility on the wake vortex pattern of airfoils undergoing harmonic pitch oscillation. *Experiments in Fluids*, 56(4), 80.
- Moryossef, Y., & Levy, Y.** (2004). Effect of oscillations on airfoils in close proximity to the ground. *AIAA Journal*, 42(9), 1755–1764.
- Mountcastle, A. M., & Daniel, T. L.** (2009). Aerodynamic and functional consequences of wing compliance. *Experiments in Fluids*, 46(5), 873-882.
- Mueller, T. J.** (2001). *Fixed and flapping wing aerodynamics for micro air vehicle applications*. American Institute of Aeronautics and Astronautics.

- NATO STO-TR-AVT-202.** (2016). *Extensions of fundamental flow physics to practical MAV aerodynamics*. North Atlantic Treaty Organization.
- Ol, M. V., Bernal, L., Kang, C. K., & Shyy, W.** (2009). Shallow and deep dynamic stall for flapping low Reynolds number airfoils. *Experiments in Fluids*, 46(5), 883–901.
- Ol, M. V., Eldredge, J. D., & Wang, C.** (2009). High-amplitude pitch of a flat plate: an abstraction of perching and flapping. *International Journal of Micro Air Vehicles*, 1(3), 203-216.
- Paraz, F., Schouveiler, L., & Eloy, C.** (2016). Thrust generation by a heaving flexible foil: resonance, nonlinearities, and optimality. *Physics of Fluids (1994-present)*, 28(1), 011903.
- Park, H., Park, Y. J., Lee, B., Cho, K. J., & Choi, H.** (2016). Vortical structures around a flexible oscillating panel for maximum thrust in a quiescent fluid. *Journal of Fluids and Structures*, 67, 241-260.
- Park, Y. J., Jeong, U., Lee, J., Kwon, S. R., Kim, H. Y., & Cho, K. J.** (2012). Kinematic condition for maximizing the thrust of a robotic fish using a compliant caudal fin. *IEEE Transactions on Robotics*, 28(6), 1216-1227.
- Percin, M., & Van Oudheusden, B. W.** (2015). Three-dimensional flow structures and unsteady forces on pitching and surging revolving flat plates. *Experiments in Fluids*, 56(2), 47.
- Prempraneerach, P., Hover, F. S., & Triantafyllou, M. S.** (2003). The effect of chordwise flexibility on the thrust and efficiency of a flapping foil. In *Proc. 13th Int. Symp. on Unmanned Untethered Submersible Technology: special session on bioengineering research related to autonomous underwater vehicles*, (pp. 152-170). New Hampshire.
- Quinn, D. B., Lauder, G. V., & Smits, A. J.** (2015). Maximizing the efficiency of a flexible propulsor using experimental optimization. *Journal of Fluid Mechanics*, 767, 430-448.
- Raffel, M., Willert, C. E., & Kompenhans, J.** (2007). *Particle image velocimetry: a practical guide*. Springer Science & Business Media.
- Ramananarivo, S., Godoy-Diana, R., & Thiria, B.** (2011). Rather than resonance, flapping wing flyers may play on aerodynamics to improve performance. *Proceedings of the National Academy of Sciences*, 108(15), 5964-5969.
- Rao, S. S.** (2011). *Mechanical vibrations* (5th ed.). Pearson.
- Reich, G., Wojnar, O., & Albertani R.** (2009). Aerodynamic performance of a notional perching MAV design. *47th AIAA Aerospace Sciences Meeting*, Orlando, USA, 5-8 January.
- Richards, A. J., & Oshkai, P.** (2015). Effect of the stiffness, inertia and oscillation kinematics on the thrust generation and efficiency of an oscillating-foil propulsion system. *Journal of Fluids and Structures*, 57, 357-374.

- Rival, D., Prangemeier, T., & Tropea, C.** (2009). The influence of airfoil kinematics on the formation of leading-edge vortices in bio-inspired flight. *Experiments in Fluids*, 46(5), 823–833.
- S. Lai, J. C., & Platzer, M. F.** (1999). Jet characteristics of a plunging airfoil. *AIAA Journal*, 37(12), 1529-1537.
- Sane, S. P.** (2003). The aerodynamics of insect flight. *Journal of Experimental Biology*, 206(23), 4191-4208.
- Schlueter, K. L., Jones, A. R., Granlund, K., & Ol, M.** (2014). Effect of root cutout on force coefficients of rotating wings. *AIAA Journal*, 52(6), 1322-1325.
- Sfakiotakis, M., Lane, D. M., & Davies, J. B. C.** (1999). Review of fish swimming modes for aquatic locomotion. *IEEE Journal of Oceanic Engineering*, 24(2), 237-252.
- Shyy, W., Aono, H., Kang, C. K., & Liu, H.** (2013). *An introduction to flapping wing aerodynamics*. Cambridge University Press.
- Shyy, W., Ifju, P., & Viieru, D.** (2005). Membrane wing-based micro air vehicles. *Applied Mechanics Reviews*, 58(4), 283-301.
- Smith, M. J.** (1996). Simulating moth wing aerodynamics-towards the development of flapping-wing technology. *AIAA Journal*, 34(7), 1348-1355.
- Son, O., & Cetiner, O.** (2015). Effect of aspect ratio and leading and trailing edge form on the flow around an impulsively pitching flat plate. *In 53rd AIAA Aerospace Sciences Meeting*, (p. 1296), Kissimmee, Florida, 5 - 9 January 2015.
- Son, O., & Cetiner, O.** (2016). Effect of chordwise flexibility on flapping wing aerodynamics. *In Proceedings of the 5th International Conference on Jets, Wakes and Separated Flows (ICJWSF2015)*, (pp. 203-210). Springer.
- Son, O., & Cetiner, O.** (2017). Three-dimensionality effects due to change in the aspect ratio for the flow around an impulsively pitching flat plate. *Journal of Aerospace Engineering*, 30(5), 04017053.
- Son, O., & Cetiner, O.** (2018). Force-motion phase relations and aerodynamic performance of a plunging plate. *Experiments in Fluids*, 59(2), 28.
- Stevens, R. J., & Babinsky, H.** (2014). Low Reynolds number experimental studies on flat plates. *In 52nd Aerospace Sciences Meeting*, (p. 0743). National Harbor, Maryland, 13 - 17 January 2014.
- Stevens, R., Pitt Ford, C., & Babinsky, H.** (2013). Experimental studies of an accelerating, pitching, flat-plate at low Reynolds number. *In 51st AIAA Aerospace Sciences Meeting including the New Horizons Forum and Aerospace Exposition*, (p. 677), Texas, USA, 7-10 January.
- Taira, K., & Colonius, T. I. M.** (2009). Three-dimensional flows around low-aspect-ratio flat-plate wings at low Reynolds numbers. *Journal of Fluid Mechanics*, 623, 187-207.

- Tarascio, M. J., Ramasamy, M., Chopra, I., & Leishman, J. G.** (2005). Flow visualization of micro air vehicle scaled insect-based flapping wings. *Journal of Aircraft*, 42(2), 385-390.
- Theodorsen T.** (1935). *General theory of aerodynamic instability and the mechanism of flutter* (NACA TR No. 496).
- Triantafyllou, M. S., Triantafyllou, G. S., & Gopalkrishnan, R.** (1991). Wake mechanics for thrust generation in oscillating foils. *Physics of Fluids A: Fluid Dynamics (1989-1993)*, 3(12), 2835-2837.
- Tuncer, I. H., & Platzer, M. F.** (2000). Computational study of flapping airfoil aerodynamics. *Journal of Aircraft*, 37(3), 514-520.
- Url-1** <<https://www.flickr.com/photos/kaddy/68441021>>, date retrieved 08.11.2018.
- Url-2** <<https://dantecdynamics.com/measurement-principles-of-piv>>, date retrieved 08.11.2018.
- Vanella, M., Fitzgerald, T., Preidikman, S., Balaras, E., & Balachandran, B.** (2009). Influence of flexibility on the aerodynamic performance of a hovering wing. *Journal of Experimental Biology*, 212(1), 95-105.
- Venkata, S. K., & Jones, A. R.** (2013). Leading-edge vortex structure over multiple revolutions of a rotating wing. *Journal of Aircraft*, 50(4), 1312-1316.
- Vest, M. S., & Katz, J.** (1996). Unsteady aerodynamic model of flapping wings. *AIAA Journal*, 34(7), 1435-1440.
- von Karman, T., & Burgers, J. M.** (1935). General aerodynamic theory-perfect fluids. *Aerodynamic Theory*, 2, 346-349.
- Wang, Z. J.** (2005). Dissecting insect flight. *Annual Review of Fluid Mechanics*, 37, 183-210.
- Widmann, A., & Tropea, C.** (2015). Parameters influencing vortex growth and detachment on unsteady aerodynamic profiles. *Journal of Fluid Mechanics*, 773, 432-459.
- Willis, D. J., Israeli, E. R., Persson, P. O., Drela, M., Peraire, J., Swartz, S. M., & Breuer, K. S.** (2007). A computational framework for fluid structure interaction in biologically inspired flapping flight. In *25th AIAA Applied Aerodynamics Conference* (p. 3803).
- Wu, P., Stanford, B. K., Sällström, E., Ukeiley, L., & Ifju, P. G.** (2011). Structural dynamics and aerodynamics measurements of biologically inspired flexible flapping wings. *Bioinspiration & Biomimetics*, 6(1), 016009.
- Yilmaz, T. O., & Rockwell, D.** (2012). Flow structure on finite-span wings due to pitch-up motion. *Journal of Fluid Mechanics*, 691, 518-545.
- Zhao, L., Deng, X., & Sane, S. P.** (2011). Modulation of leading edge vorticity and aerodynamic forces in flexible flapping wings. *Bioinspiration & Biomimetics*, 6(3), 036007.
- Zhao, L., Huang, Q., Deng, X., & Sane, S. P.** (2010). Aerodynamic effects of flexibility in flapping wings. *Journal of the Royal Society Interface*, 7(44), 485-497.

Zhu, Q. (2007). Numerical simulation of a flapping foil with chordwise or spanwise flexibility. *AIAA Journal*, 45(10), 2448-2457.



CURRICULUM VITAE

Name Surname : Onur SON
Place and Date of Birth : Şişli – 13.05.1986
E-Mail : sononurson@gmail.com

EDUCATION:

- **B.Sc.** : 2008, Istanbul Technical University, Faculty of Aeronautics and Astronautics, Department of Astronautical Engineering
- **M.Sc.** : 2010, Istanbul Technical University, Graduate School of Science Engineering and Technology, Aeronautics and Astronautics Engineering Program

PROFESSIONAL EXPERIENCE:

- 2010-2016 Research & Teaching Assistant at Department of Astronautical Engineering, Istanbul Technical University.
- 2016-2018 Project Assistant at Trisonic Laboratory, Istanbul Technical University.

PUBLICATIONS, PRESENTATIONS AND PATENTS ON THE THESIS:

- **Son, O., & Cetiner, O.** (2018). Force-motion phase relations and aerodynamic performance of a plunging plate. *Experiments in Fluids*, 59(2), 28.
- **Son, O., & Cetiner, O.** (2017). Three-Dimensionality Effects due to Change in the Aspect Ratio for the Flow around an Impulsively Pitching Flat Plate. *Journal of Aerospace Engineering*, 30(5), 04017053.
- **Son, O., & Cetiner, O.** (2016). Effect of Chordwise Flexibility on Flapping Wing Aerodynamics. *In Proceedings of the 5th International Conference on Jets, Wakes and Separated Flows (ICJWSF2015)* (pp. 203-210). Springer Proceedings in Physics vol.185.

- Karakas, F., Paca, O., Köse, C., **Son, O.**, Zaloglu, B., Fenercioglu, İ., & Cetiner, O. (2014). Effect of Cross Sectional Shape Variation for an Oscillating Wing (Turkish). *Journal of Aeronautics and Space Technologies*, 7(2), 55-70.
- **Son, O.**, Cetiner, O., Stevens, P.R.R.J., Babinsky, H., Manar, F., Mancini, P., Jones, A., Ol, M.V., & Gozukara, A.C. (2016). Parametric Variations in Aspect Ratio, Leading Edge and Planform Shapes for the Rectilinear Pitch Cases of AVT-202 (Invited), 54th AIAA Aerospace Sciences Meeting, San Diego, California, USA, 4-8 January.
- Kose, C., **Son, O.**, & Cetiner, O. (2015). Effect of Planform Shape on the Flow Around an Impulsively Pitching Flat Plate, 8th Ankara International Aerospace Conference (AIAC 2015), Ankara, Turkey, 10-12 September.
- **Son, O.**, & Cetiner, O. (2015). Effect of Chordwise Flexibility on Flapping Wing Aerodynamics, The International Conference on Jets, Wakes and Separated Flows, Stockholm, Sweden, 16-18 June.
- **Son, O.**, & Çetiner, O. (2015). Effect of Aspect Ratio and Leading and Trailing Edge Form on the Flow around an Impulsively Pitching Flat Plate, 53rd AIAA Aerospace Sciences Meeting, Kissimmee, FL, USA, 5-9 January.

OTHER PUBLICATIONS, PRESENTATIONS AND PATENTS:

- **Son, O.**, & Cetiner, O. (2016). Drag Prediction in the Near Wake of a Circular Cylinder Based on DPIV Data. *Journal of Applied Fluid Mechanics*, 9(4), 1963-1968.
- Kal, I., **Son, O.**, Zaloglu, B., & Cetiner, O. (2018). Gust Effect on a Plunging Flexible Wing, *5th International Conference on Experimental Fluid Mechanics* (ICEFM 2018 Munich), Bundeswehr University Munich, Germany, July 2-4.
- **Son, O.**, Zaloglu, B., & Cetiner, O. (2017). Experimental Investigation of a Wing Performing Pitch-Up Motion under Gust Environment, *9th Ankara International Aerospace Conference* (AIAC 2017), Ankara, Turkey, 20-22 September.
- **Son, O.**, Zaloglu, B., Percin, M., & Cetiner, O. (2016). Force Measurement and Load Estimation Studies at ITU for Flexible Flapping Wings and Maneuvering Wings under Gust”, *NIOPLEX International Workshop on Non-Intrusive Optical Flow Diagnostics*, Delft, The Netherlands, 25 - 26 October.
- Dönerkaya, G.R., Tunalı, G.G., **Son, O.**, & Cetiner, O. (2012). Flow Structures in the Near-Wake of a Wing Pitching Up in Steady Current, 15th International Symposium on Flow Visualization, Minsk, Belarus, June 2012.
- **Son, O.**, Cetiner, O., Tevrizci, G., & Atalik, K. (2009). Effects of Polymer Addition to Structure and Properties of the Flow Around A Circular Cylinder, 5th Ankara International Aerospace Conference (AIAC 2009), METU Ankara, Turkey, August 2009.
- Turam, E., **Son, O.**, & Cetiner, O. (2014). Sensitivity Analysis of the Experimental Parameters for Force Prediction Using DPIV Data, V. National Aerospace Conference, UHUK-2014-112, Erciyes University, Kayseri, Turkey, 8-10 September.

- Paca, O., **Son, O.**, & Cetiner, O. (2014). Experimental Investigation of a Flat Plate Undergoing Ramp-Type Pitch-up Motion, III. National Conference on Advanced Technologies in Aerospace, HITEK-2014-093, Istanbul, Turkey, June.
- Karakas, F., Paca, O., Köse, C., **Son, O.**, Zaloglu, B., Fenercioglu, I., & Cetiner, O. (2014). Effect of Airfoil Profile in Flapping Wings, III. National Conference on Advanced Technologies in Aerospace, HITEK-2014-095, Istanbul, Turkey, June.
- Çaylan U., Seckin, S., Köse, C., **Son, O.**, Zaloglu, B., Fenercioglu, I., & Cetiner, O. (2014). Three-dimensionality Effects in Flapping Wings, III. National Conference on Advanced Technologies in Aerospace, HITEK-2014-094, Istanbul, Turkey, June.
- **Son, O.**, Cetiner, O., & Atalık, K. (2009). Effect of Polymer Addition on the Flow Structures around a Square Cylinder at High Reynolds Numbers, XVI. National Mechanics Congress, Kayseri, Turkey, June 22 – 26.

